SIMULATIONS OF SPACE RADIATION INTERACTIONS WITH MATERIALS AND DOSE ESTIMATES FOR A LUNAR SHELTER AND ABOARD THE INTERNATIONAL SPACE STATION

TAI T. PHAM AND MOHAMED S. EL-GENK

Institute for Space and Nuclear Power Studies and the Department of Chemical and Nuclear Engineering, The University of New Mexico
MSC01 1120
1 University of New Mexico, Albuquerque, NM 87131-0001

Technical Report ISNPS-UNM-1-2013
Institute for Space and Nuclear Power Studies (ISNPS)

August 2013

ACKNOWLEDGEMENT

This Research is funded partially by the United States Nuclear Regulatory Commission Graduate Fellowship Grant # NRC-38-09-931-MO1, to the University of New Mexico (UNM) and UNM's Institute for Space and Nuclear Power Studies.

ABSTRACT

In the past decade, there had been a strong renewal of the space exploration spirit. Particularly, is the push for manned mission to the Moon and Mars, and eventually establishing permanent settlement on the lunar surface within the next 20-30 years. With more than 40 years of experience human space flight remains a major challenge, especially the concern of health safety to the crew. Once leaving the Earth's protective atmosphere, space travelers face significant hazard due to the complex space radiation environment of Trapped Protons and Electrons, high energy and intensity of Solar Particles Event, and bombardment from Galactic Cosmic Radiation. Astronauts and cosmonauts aboard the International Space Station are constantly under the threat of such radiation, though the geomagnetic fields still provide significant protection to the crew. For future manned missions to the Moon and beyond, astronauts will be exposed to galactic cosmic radiation (GCR) and solar energetic particles (SEPs). Assessment of radiation risk must, therefore be performed to ensure the safety of the crew. Direct dose or energy deposition measurements represent the best method of quantifying the exposure risk to high-energy radiation. However, since such measurements for all the radiation components and combinations of projectile-target and energy-geometry are not possible, validated computer simulations could effectively help assesses the radiation risk in space.

This research performed simulations using the state-of-art three dimensional computer codes to investigate the interactions of space radiation with materials and quantify the biological dose onboard the International Space Station (ISS) and in a lunar shelter for future manned missions. High-energy space radiation of Trapped Protons, Solar Particle Events, and GCRs particles interactions are simulated using MCNPX and PHITS probabilistic codes. The energy loss and energy deposition within the shielding materials and in a phantom are calculated. The contributions of secondary particles produced by spallation reactions are identified. Recent experimental measurements of absorbed dose in a phantom aboard the International Space Station (ISS) are simulated.

Results show that the interactions of high energy protons with different materials generate large quantities of secondary particles including: secondary protons, neutrons, deuterons, alphas, etc. Depending on the shielding material, secondary neutrons can contribute > 20% to the total dose. For a typical Solar Particle Event (SPE), more than 30 g/cm^2 of materials are needed to shield the lunar shelter inhabitants from reaching a 30-days dose limits of 250 mSv. For the same thickness, the lunar regolith is slightly more effective than aluminum for shielding solar energetic particles (SEPs). Three different modes of incidence of the source particles are considered. The center-seeking yield the most conservative estimates, while isotropic and planar mode of incidence produced much lower estimates. The planar mode of incidence results in the lowest dose estimates inside the lunar shelter, followed by that of the isotropic source incidence.

This research simulated the MATROSHKA-R spherical phantom experiment performed onboard the Russian module Zvezda of the ISS. The exact geometry and dimensions of the space station module was not available and often too complicated to implement in the simulation. A simplified cylindrical aluminum structure is used in the current simulations. The absorbed dose are calculated for two detector arrangements (cylinder 13 - Wall facing and cylinder 3 - Interior facing), and compared with experimental results.

With a spherical isotropic radiation environment, as suggested in the literature to simulate the isotropic radiation environment, the simulations capture well the trend of dose distribution inside the phantom, though results can be 1.5 – 2 times higher without a detector efficiency correction. When corrected with an average detector efficiency of 63.5%, the simulated dose rates for the Wall facing arrangement agree well with experimental measurements. For the Interior facing detector layout, results over estimate the absorbed dose rate distribution near the phantom surface. In this detectors layout, experimental measurements reported a relatively flat distribution from the phantom surface moving inward into the phantom center, with a relative dose rates difference of ~0.01 mGy/day. However, simulation results show a strong dependence on radial distance, where the dose rates are ~0.15 mGy/day at 6.5cm from phantom center and increasing to ~0.22 mGy/day at 16.5cm from phantom center.

To rectify this divergence between the estimates and experimental measurements of the absorbed dose rates, the simulation methodology using a spherical domain is modified to a cylindrical domain of source particles. For the Wall facing detector layout, the absorbed dose rates are similar, regardless of the simulation domain of the source particles. Using a limited 70 cm long cylindrical isotropic source, the estimated absorbed dose rates for the Interior facing detectors layout are ~0.15 mGy/day at 6.5cm from phantom center and ~0.17 mGy/day at 16.5cm from phantom center. The dose distribution throughout the phantom decreases to ~0.02 mGy/day from the inner detector point to the phantom surface, comparable to the ~0.01 mGy/day in the experimental measurements.

The analysis performed in this dissertation clearly show the strong dependence of the dose rate estimates for the detectors facing away from the station wall on the selected dimension and geometry of the source particles domain. Based on the presented results, it is recommended that cylindrical source particles domain be used for accurate estimates of the dose rate in ISS and for future space flights. Such a domain provides better estimates of the dose rate to interior organs as well as at the surface of the astronaut body. This finding is important for future space flights to Mars, for which no direct measurements for a phantom are available.

TABLE OF CONTENTS

LIST OF FIGURES

LIST OF TABLES

NOMENCLATURES

A	=	mass number of a material
A_1	=	mass number of incident particle
A_2	=	mass number of the lattice atom
c	=	velocity of light (2.997925 x 10^8 m/s)
D	=	energy deposition with shield (MeV/g)
D_a	=	absorbed dose (J/kg or Gy)
D_o	=	energy deposition without shield (MeV/g)
D_T	=	absorbed dose of specific tissue
e	=	electron charge (1.6022 x 10^{-19} C)
E	=	incident particle energy (MeV)
E_d	=	Displacement energy deposition (MeV/g)
E_{th}	=	Energy Threshold for spallation reactions
F	=	particle fluence (#/cm^2)
ħ	=	Planck's constant ($h/2\pi$ = 1.1734 x 10^{-44} C^2-s/m)
H_T	=	equivalent dose (Sv)
L	=	linear energy transfer (LET)
$L(T)$	=	Lindhard energy partition function
m_1	=	incident particle mass (kg)
M	=	lattice atom mass (kg)
N	=	Avogadro's number (6.022 x 10^{23} /mole)
N_V	=	target atom density (#/cm^3)
$NIEL$	=	Non-Ionizing Energy Loss (MeV-cm^2/g)
p	=	source particle proton
$Q(L)$	=	radiation quality factor
T	=	recoiling atoms energy (MeV)
T_d	=	threshold energy transferred to lattice atoms (MeV)
T_{dam}	=	damage energy transferred to lattice nuclei (MeV)
T_{max}	=	maximum permissible energy transferred to lattice atom (MeV)
w_T	=	tissue weighting factor

x = target thickness (cm)

X = spallation products

z = atomic number of charged particle

z_1 = atomic number of incident particle

z_2 = atomic number of lattice atom

Greek letters

α = coefficient, Eq. (B9)

β = coefficient, Eq. (B9)

γ = coefficient, Eq. (B9)

ϕ = fluence per source particle (#/cm^2)

ρ = material density (g/cm^3)

σ_d = damage energy cross section (cm^2)

$\sigma_{d,\ Coulomb}$ = Coulombic interaction damage cross section (MeV-cm^2)

$\sigma_{d,\ Nuclear}$ = Nuclear interaction damage cross section (MeV-cm^2)

σ_i = cross section of the ith interaction (cm^2)

Subscripts

1 = incident particle

2 = target atom

a = absorbed

coulomb = coulomb

d = displacement

dam = damage

L = Lindhard partition function

max = maximum

nuclear = nuclear

T = Tissue

ν = target atom

1. INTRODUCTION

Fifty years ago, President John F. Kennedy challenged the country to send astronauts to the Moon, and return them safely to Earth, before the end of the 1960s. The Apollo program of the National Aeronautics and Space Administration (NASA) achieved this goal less than seven years later, sending the first humans to the Moon, and firmly establishing the United States as the leader in space technology. Since the last manned lunar mission four decades ago, the space program has enjoyed many successes. NASA has flown hundreds of missions and have provided significant scientific observations and discoveries, as well as great commercial return [Dordain 2010]. The US competitive space program shifted to a space cooperation program with international partners that have changed human space experience in a profound way. Space based scientific observatories, such as the Hubble Space Telescope; have made unprecedented contributions to enhancing scientific understanding in astronomy and astrophysics. Robotic studies of the solar system produced a revolution in scientific understanding of the Sun, the planets, asteroids, comets, and the Earth's immediate environment. Technologies developed as a result of investment in space-based research and exploration have greatly improved modern communications, weather forecasting, climate-change prediction, international commerce, and the nature of news reporting [Abbey and Lane 2005]. The past five decades have transformed space from an intrigue of human imagination into an international endeavor and from novelty into a necessity.

Since the last manned mission to the Moon in December 1972, human space flight has continued with numerous missions, though none have left Earth orbit. Most notable are the establishment of stations as space science research bases. The Soviet Union had built the first space station, Salyut 1 in 1971, followed by the US first space station Skylab in 1973 [Abbey and Lane 2005]. In 1986, the Soviet's space station Mir, replaced the existing Salyut and the US began the Freedom program to replace Skylab, which evolved into the International Space Station Program. In 1998, the International Space Station (ISS) was launched as the 11^{th} station, and is being jointly operated by 16 nations [Dordain 2010].

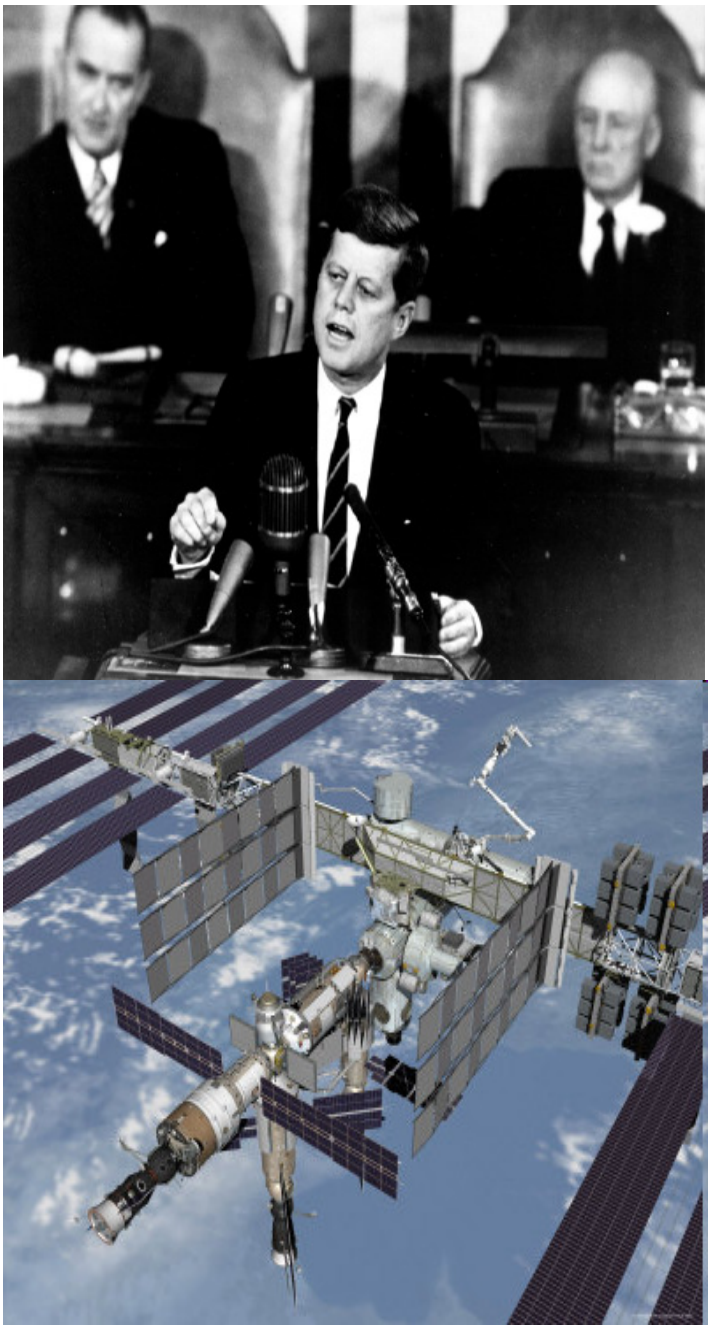

Figure 1.1. President John F. Kennedy addressing the nation (above). The International Space Station (below).

Even with more than 40 years of experience, human space flights remains a challenging task, with the safety and health of the crew are the primary concerns of every mission. One of the major health concerns is the continual exposure of the crew to the energetic space radiation. Once they leave the Earth's protective environment, astronauts face radiation levels that exceed those routinely received by terrestrial radiation workers. It was soon recognized that for future interplanetary and long duration missions, the effects of protracted radiation exposure must be considered in the context of other inherent risks of human operation in space [Wilson et. al. 1997; NCRP 1998]. Astronauts aboard the ISS and space vehicles encounter radiation exposure that includes: galactic cosmic radiation (GCR), solar-particle events (SPEs), energetic protons and electrons in the trapped radiation belts, and onboard radiation sources. In Low-Earth orbit (LEO), the atmosphere and geomagnetic field deflects the low energies protons and heavy ions back to space, shielding the crew from the full extend of the GCR and SPE particles [Wilson et. al. 1997; NCRP 1998]. At higher inclination orbits, the numbers of GCR and SPE particles are likely to increase, due to the less favorable magnetic field intensity and orientation; though significant shielding are still provided by the Earth's magnetic field and the shadow shield from the Earth itself [Wilson et. al. 1997; Tylka et. al. 1997].

In the past decade, there has been a strong renewal of interest in the exploration and eventual colonization of space. In 2004, President G.W. Bush announced a plan for returning human to the Moon and eventually flying a manned mission to Mars [NASA 2004; Abbey and Lane 2005]. Several other nations, including China, India, Russia, Japan, as well as the European Union, have expressed interest in sending crewed missions to the Moon in the coming decades, with the eventual goal of establishing permanent outposts on the lunar surface [Day 2009]. In 2010, President Obama extended the operation of ISS to 2020 and possibly beyond, and echoed ex-president Bush of sending manned mission to the Moon and Mars. [Dordain 2010]. With the success of the jointly operated ISS, the Moon represents a logical destination for future human exploration and development efforts.

For missions beyond LEO, such as missions to the Earth's Moon and Mars, the fluence of GCR and SPE could be three times that of the ISS [Wilson et. al. 2001; NCRP 2000]. Measurements onboard the ISS showed that astronauts and cosmonauts could

have received dose ranging from 0.5 to 1.2 mSv/day, primarily from exposure to GCR and high-energy trapped protons. For missions at higher inclinations, or beyond LEO, the astronaut's doses are expected to be a factor of two higher [NCRP 2000]. In a recent study, the measurements of the energetic particle radiations were performed using the probe of the Mars Science Laboratory (MSL) during its' cruise to Mars. Results showed that a one-way trip to Mars netted a total of 466 ± 84 mSv for the 253 days trip, with an estimated dose for the return trip being equal, if not greater than the measured dose to Mars [Zeitlin et al. 2013]. The findings suggested that the exposure to the human crew, during the cruise phase to and from Mars alone, would exceed the current astronauts career exposure limit [Zeitlin et al. 2013]. This finding is problematic in that it exceeds previous estimate of crew exposures during a mission to Mars. It further accentuated the needs for accurate modeling using transport models to estimates astronaut exposures and the effectiveness of radiation shielding options [O'neill 2010; Cucinotta et al. 2006; Zeitlin et al. 2013].

Shielding provided by the spacecraft structure can mitigate the full intensities of space radiation. However, when passing through materials, such as shielding (or body tissue), high-energy particles interact with the atoms and nuclei of the target materials. At the atomic level, interactions results in energy transfer by the radiation fields (Coulombic interaction), exciting and ionizing the atoms of target materials [Littmark and Ziegler 1980]. However, this interaction preserves and does not alter the identities of the incident particles. On the other hand, spallation interactions with the atomic nuclei can be violent and often result in the breakup of the incident and the target nuclei. Thus, spallation interactions of the high-energy charged particles with structure materials can generate significant amount of secondary particles. This alters the energy spectra and the composition of the transmitted radiation, further complicating the radiation environment inside the spacecraft and hence, the shielding requirements.

The assessment of radiation risk requires a detailed knowledge of the composition and spectra of the radiation environment. Experimental evaluation of the absorbed dose and the dose equivalent due to a complex radiation field requires measuring the charged particle fluences and other spectral information, which can be used to deduce the radiation quality [Badhwar et. al. 2000; Badhwar 2002]. Onboard the ISS and the Space

Shuttle, passive and active detectors are mounted to measure the radiation environment inside the crew quarters [Badhwar 2002; Cucinottta et. al. 2002; NCRP 2000; NCRP 2002]. However, the measurements of all components of the radiation spectrum in a spacecraft is difficult because: (1) no detector is efficient enough to collect all the necessary characteristics [Badhwar et. al. 1998; Badhwar et. al. 2001; NCRP 2002], and (2) the complex composition and wide range of energies of space radiation and the dynamical nature of the angular spectra in habitable compartments of the space stations do not permit accurate enough data on radiation conditions based on dosimetric values [Qualls et. al. 2001; Shurshakov et. al. 2008]. Since it is not possible to perform measurements of all possible projectile-target and energy-geometry combinations, computer simulations using particles and heavy-ions transport codes are necessary [Badhwar et. al. 2001; Badhwar and Cucinotta 2000; NCRP 2000].

The description of particle propagation through radiation shielding materials is a complex problem. The radiation field behind the shielding (or inside a spacecraft), is a result of transformation of the external radiation field by ionization losses, nuclear and spallation reactions in the shield material [Sato et. al. 2004; Satoh et. al. 2009; Wilson et. al. 2005]. Computer codes describing coupled proton, high charge and energy (HZE), and neutron transport are important tools for understanding the interaction of space radiation on shielding materials, space radiation biology and dosimetry. The current NASA space radiation transport tool of choice is the High Z and Energy TRaNsport (HZETRN) code system, which is not available to the public. HZETRN is a suite of codes containing a numerical solution of the Boltzmann transport equation employing the continuous slowing down and straight ahead approximation [Wilson et. al. 2005]. The code is capable of transporting protons, neutrons, and heavy ions and calculating dose at critical tissue sites, using simple slab geometry. The deterministic 1-D HZETRN code allows high-speed computational procedure suitable for early stages of design and optimization of radiation shielding calculations [Wilson et. al. 2002]. Though HZETRN can efficiently estimate the dose at a point in a simple geometry; the propagation of particles through shielding materials are anything but one-dimensional [Sato et. al. 2004; McKinney et. al. 2008]. In a more complex environment, such as shielding a lunar habitat, the radiation field inside is complex, and the dose rate calculation for neutron

contributions cannot be described by a one-dimensional approach [Sato et. al. 2004; Satoh et. al. 2009]. Therefore, computer simulation operating with three-dimensional geometry and transport processes should be used in conjunction with measurements and 1-D deterministic codes. However, the relevancy and accuracy of the transport models must be validated or benchmarked through the iterative process of direct comparisons with measurements data.

In 2004, the Institute for Biomedical Problems in Moscow (IBMP) developed and flown an advanced spherical phantom MATROSHKA-R (MTR-R) aboard the Russian segment of the ISS. The phantom was equipped with thermo-luminescent detectors (TLDs), plastic nuclear track detectors (PNTDs) and biological samples [Semkova et. al. 2003; Kireeva et. al. 2007; Kartsev et. al. 2009; Sihver et. al. 2009; Jadmickova et. al. 2010]. This is one of the first long-duration experiments for determining the dose distribution onboard the ISS [Semkova et. al. 2003; Kireeva et. al. 2007; Kartsev et. al. 2009; Sihver et. al. 2009; Jadmickova et. al. 2010]. The initial data were collected during space flights of crews ISS-8,9 in the Russian Service Module/Crew Cabin "Zvezda" of the ISS, for the duration from August 2004 – October 2005 [Kireeva et. al. 2007; Kartsev et. al. 2005; Akatov et. al. 2007; Sihver et. al. 2009]. These measurements represent the best available data for estimating the incurred doses to the astronauts aboard the ISS.

1.1 Objectives

1. Investigate the interactions of space radiation with potential shielding materials and estimate the biological dose onboard the ISS and in a lunar shelter. The interactions of high-energy space trapped particles, Solar Particles Events, and GCR heavy ions spectrum with potential shielding material is simulated using the state-of-art, three-dimensional probabilistic MCNPX and PHITS computer codes [Sato et. al. 2004; Pelowitz 2011]. The simulation codes PHITS and MCNPX are widely used transport codes capable of treating many components of the primary and secondary spectra of the space radiation environment, including: protons, neutrons, light ions, and heavy ions. The calculated energy loss and energy deposition within different shielding materials are compared; and the contribution of the secondary particles produced by spallation reactions are quantified.

2. Perform dose estimates in a lunar shelter, shielded using lunar regolith, during a large solar energetic particles event. The fluence and energy spectra of large events are used as the primary source particles incidence on a simulated semi-cylindrical lunar shelter. The dose estimates inside a representative lunar shelter are calculated as a function of the type and thicknesses of the shielding materials. The contributions of the primary and secondary protons, and the secondary particles to the doses estimates are calculated. The regolith thickness required to reduce the dose in the shelter to those recommended for 30-day operation in LEO (250 mSv) by NASA, and for radiation workers (50 mSv) are determined. The effect of anisotropy of the source event could significantly influence the doses estimates inside the lunar shelter. This effect on the dose distributions inside the representative lunar shelter is investigated with different modes of incidence particles and obtained results are compared.

3. Compare simulation results of PHITS and MCNPX. Though each code incorporates high energy physics models, the comparisons of the two transport codes predictions for a variety of space radiation protection scenarios provide relevancy of their predictive capability.

4. Obtain energy deposition and organ absorbed dose estimates and compare with recent measurements onboard the ISS. A spherical phantom model similar to that of the experiment is developed in MCNPX and PHITS, and configured with the ISS module to reproduce the experimental conditions. The energy deposition and absorbed dose rates are estimated and the secondary particles produced inside the ISS module and tissue equivalent phantom are determined.

2. BACKGROUND

The most notable difference between the occupational radiation exposure on Earth and in space is that the latter is due to a persistent field of mixed radiation types. Space radiation environment has three main components: trapped particles, solar particles, and galactic cosmic rays (Fig. 2.1) [Wilson et. al. 1997; Wilson 2000; NCRP 2000]. The trapped particles are comprised primarily of electrons and protons in closed orbits by the Earth's magnetic field. Solar particles and GCR consists primarily of protons with small mixture of helium ions, and even smaller composition of heavier charge particles [Wilson et. al. 1997; Wilson 2000; NCRP 2000]. While Solar Particles Events (SPEs) are sporadic, the particles' energy distribution and high flux are of major concerns. The energetic heavy ions comprising part of the galactic cosmic rays can cause large amount of damage, even though they have very low flux intensity [Wilson et. al. 1997; Wilson 2000; NCRP 2000]. The relative importance of the components of space radiation environment is highlighted by their contributions to the radiation risk to the crew. This risk depends strongly on the details of a given mission. Substantial contributions have been made by ground-based measurements and data from both manned and unmanned spacecraft, further expanding our knowledge of the space radiation environment.

2.1 Trapped Radiation

The Earth is surrounded by magnetically trapped radiation. Trapped radiation exists above the atmosphere from an altitude of approximately 200 km to around synchronous orbit altitude [Wilson et. al. 1997; Wilson 2000; NCRP 2000]. This radiation consists primarily of protons and electrons, but energetic helium, carbon, and other ions are also observed [Wilson 2000; NCRP 2000]. Albedo neutrons are also observed along with the high-energy protons and electrons at lower altitude, likely due to the interactions of GCR with the constituents of the earth atmosphere. At higher altitude, the ionosphere, solar wind particles, and cosmic rays components are the primary sources of the trapped particles [Wilson et. al. 2001]. Figure 2.2 gives a pictorial distribution of the trapped protons and electrons in the Van Allen belts. It shows an approximate extent of the trapped radiation region, and two distinct regions as the "inner" and "outer" belt.

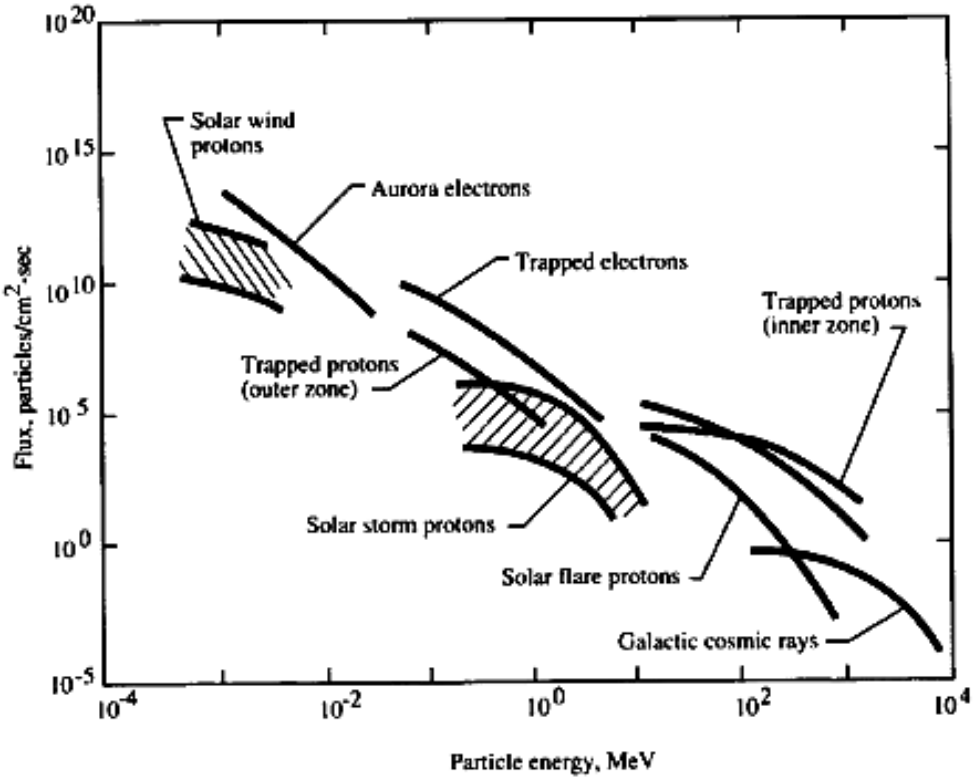

Figure 2.1. Depiction of the space radiations environment. Comparing the relative abundances and energy of the many components of the radiation environment [Wilson et. al. 1997; NCRP 2000].

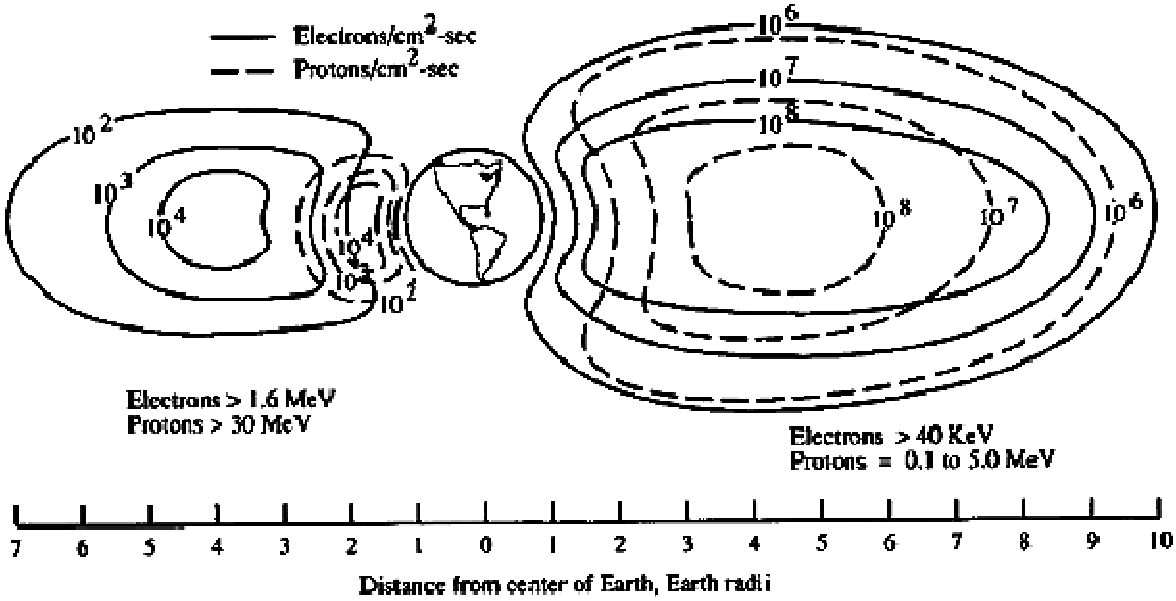

Figure 2.2. Pictorial distribution of the trapped protons and electrons in the Van Allen belts [Wilson 2000].

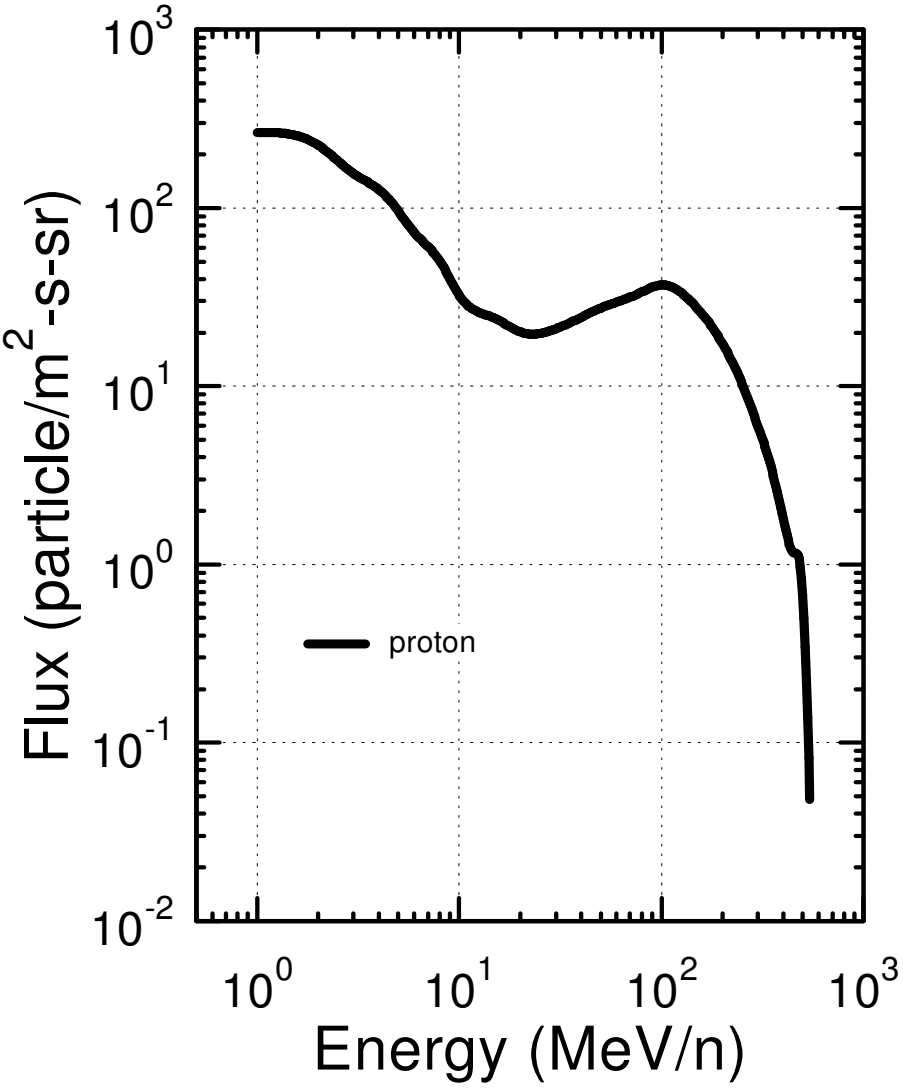

Figure 2.3. Fluxes of trapped protons for apogee 364 km, perigee 347 km, and inclination of 52^0 [Tylka et al. 1997].

The trapped radiation flux intensity and energy distribution are time dependent. The general variations are associated with the 11-year solar cycle and it's anomalous solar storm. The high-energy trapped protons are relatively constant, though can vary by as much as a factor of 2 during solar storms [Badhwar 1997; Wilson et. al. 1997; NCRP 2000]. The trapped electrons flux is much more variable, with the largest changes occurring at high altitudes. The electrons can be easily shielded, leaving the protons as the most important contributor to the dose.

Figure 2.3 shows a representative trapped protons energy spectrum for the ISS orbit of 51.6 degrees inclination at ~400km altitude. The protons form a continuous distribution that decreases sharply over 500 MeV. This is because high-energy protons are not easily controlled by the magnetic field [Tylka et. al. 1997; Badhwar 2000]. Generally, within moderately shielded spacecraft the dose incurred during transit through the trapped belts is not significant. Though cumulative exposures can results from sustained operations in low Earth orbit (LEO) and extravehicular activities. However, exposure time must be minimized to avoid incurring large exposure dose [Badhwar 1997; Badhwar 2002].

An important feature of the trapped radiation belt is the South Atlantic Anomaly (SAA). The SAA feature is the result of the magnetic field lines dipping closer to Earth due to the eccentricity of the geomagnetic field with respect to Earth's center [Badhwar 1997; Badhwar 2002]. This feature enhances atmospheric scattering of the particles, increasing their intensity within this region. Consequently, the encountered denser particles within this region increase the radiation exposure to the spacecraft orbiting at a low altitude and a low inclination.

2.2 Solar Energetic Particles

Solar Energetic Particles (SEPs) are high-energy particles originating on or near the sun. They lead to extraordinary large increase in the high-energy particle fluence into the surrounding space environment, and composed of protons, electrons, and alpha particles (helium nuclei), and small amounts of ions of heavier elements (<3%) [Wilson et. al. 2001; Sauer et. al. 1990]. Protons contribute over 80% of the total mass ejection of a solar event [Wilson et. al. 2001; Sauer et. al. 1990], with energy ranging between ten's

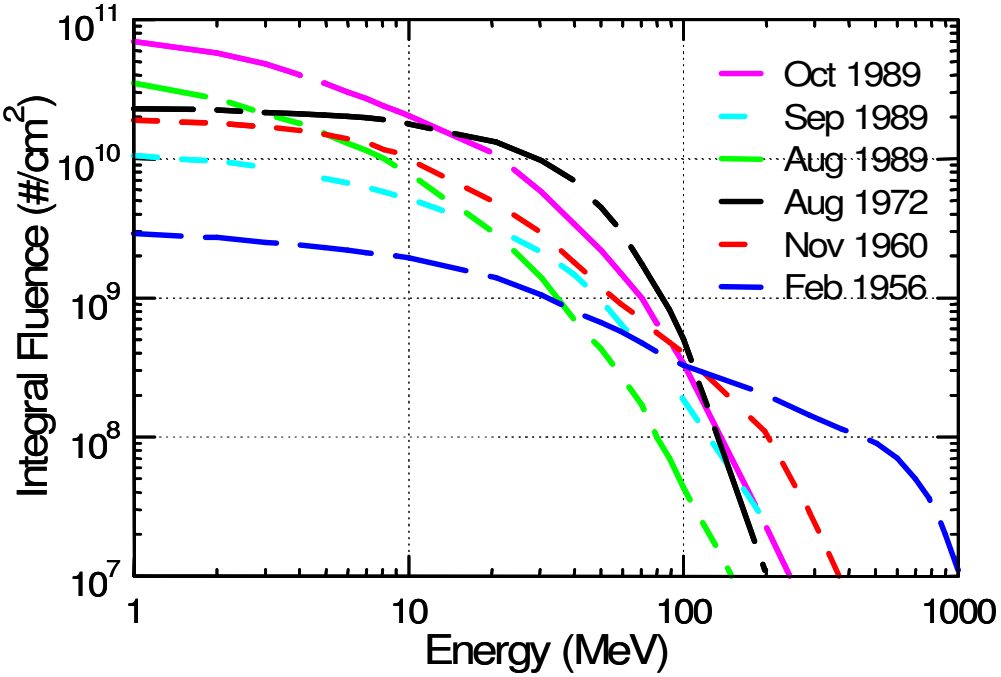

Figure 2.4. Protons Integral Fluence of Larger Solar Particle Events from 1956 to 1989 [Sauer et. al. 1990; Shea and Smart 1996].

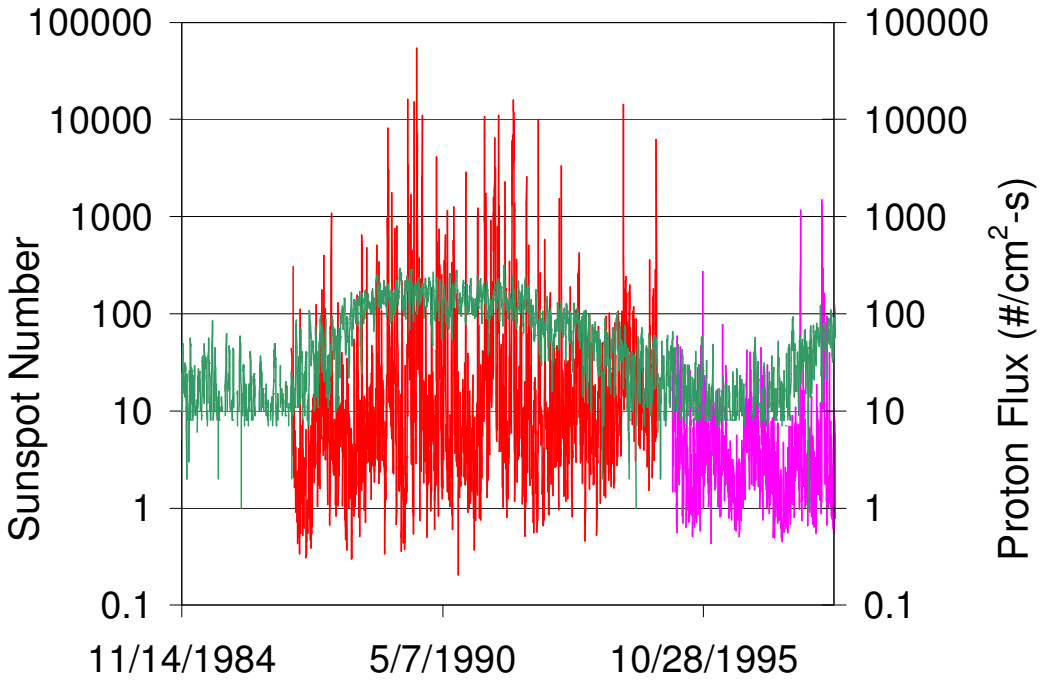

Figure 2.5. Protons Flux Superimposed Over Sunspot Number for Solar Cycle 22 [NNDC, GOES].

of MeV up to GeV and a fluence up to 10^{11} particles/cm^2. Figure 2.4 shows some of the largest particle events from 1956 to 1989 [Sauer et. al. 1990; Shea and Smart 1990]. The 1972 event are most famous as it occurred between two Apollo missions (Apollo 16 and 17). The events in 1989 delivered among the highest fluences ever recorded, and happened within close successions of each other, raising major risk concerns to astronauts. The 1956 event emitted much fewer particles than the 1989s and 1972 events, but had an unusually higher concentration of protons with energies E > 200 MeV and upto GeV. These events are considered the worse-case scenario for risk assessment [Sauer et. al. 1990; Shea and Smart 1990; NCRP 2000].

For future manned missions, a concern is that an SPE could, in short period of time (hours to days), deliver a large fluence with energies in excess of 100s' of MeV [NCRP 2000; NCRP 2002]. SEPs are usually associated with two solar events; the solar flare and interplanetary shock corona mass ejection (CME). Both events are primarily sporadic, but scientists generally associate the frequencies of particles events with the solar activity of an approximately 11 years cycle. The proton flux data from the Geostationary Operational Environment Satellites for a series of events, superimposed over the sunspot number of solar cycle 22 is shown in Figure 2.5. Solar activities are predominant in the years of high sunspots numbers, referred to as solar maxima. In the years of low sunspot numbers, or solar minima, from 1995-1997, very few events occurred and the solar protons environment was normally low.

2.3 Galactic Cosmic Radiation

Space is filled isotropically with background high-energy charged particles, collectively known as galactic cosmic radiations (GCR). GCR consists of charged particles ranging from hydrogen to uranium, arriving from outside the heliosphere [Wilson et. al. 2001; Badhwar and O'Neill 1996; NCRP 2000]. GCR consists of over 98% protons and heavier ions and less than 2% electrons and positrons. The GCR energy spectrum, outside the influence of the Earth's magnetic field, can vary from tens of MeV/n to ~10^{12} MeV/n [Badhwar and O'Neill 1996; NCRP 2000; Wilson et. al. 2001]. In the range where the flux is greatest, the GCR comprises 89% protons and 10% helium ions, and 1% of heavier ions [Wilson et. al. 2001; Badhwar and O'Neill 1996; NCRP

2000; NCRP 2002]. Figure 2.6 show the relative ion abundances in the GCR and of components up to Nickel (Z = 28) ions. Above Nickel ions, the relative abundance of the heavier elements are negligibly small [Badhwar and O'Neill 1996; NCRP 2000; Wilson et. al. 2001]. Figure 2.7 displays the flux energy spectrum for a few representative ions. It is interesting to notes the slight increase in the spectrum of some ions at low energy (<50 MeV/n). This sharp increase in intensity is the "anomalous" component of GCR, called ACR. The ACR is known to consist of six elements: helium, carbon, nitrogen, oxygen, neon, and argon, and suspected to be of a different origin than that of the high-energy components [Badhwar and O'Neill 1996; NCRP 2002]. The cyclic variation of the solar magnetic field and changes in the solar wind environment can cause changes in the GCR spectrum within the heliosphere. Measurements have indicated that the particle fluxes could vary by a factor of 2 between a solar minimum and a solar maximum. Due to the vast energy range difference of the GCR components, these particles are difficult to shield against, ever present as the background radiation and a constant source of low dose radiation to astronauts.

2.4 Interactions of High Energy Particles with Materials

When high-energy particles pass through materials, such as shielding or body tissue, some of the radiation may be absorbed completely, some may be scattered and some may pass straight through without any interaction at all. There are two basic energy loss mechanisms in materials for charged particles, such as protons: Electromagnetic and Nuclear interactions.

Charged particles traveling through materials lose energy to the orbital electrons setting them into motion and transporting the energy away forming ions and emitting x-ray. The intensity of the ionization depends on the square of the ion effective charge and speed of the incident particle [Littmark and Ziegler 1980]. There are several ways of describing the net effects of charged particles interaction. The most common is the rate of energy loss along the particle's path, referred to as stopping power, expressed in MeV/cm. It is also referred to as the *linear energy transfer* (LET) from the incident particles to the atoms of the target material and closely associated with the dose delivered. A more common quantity for expressing the ionizing energy loss is the mass

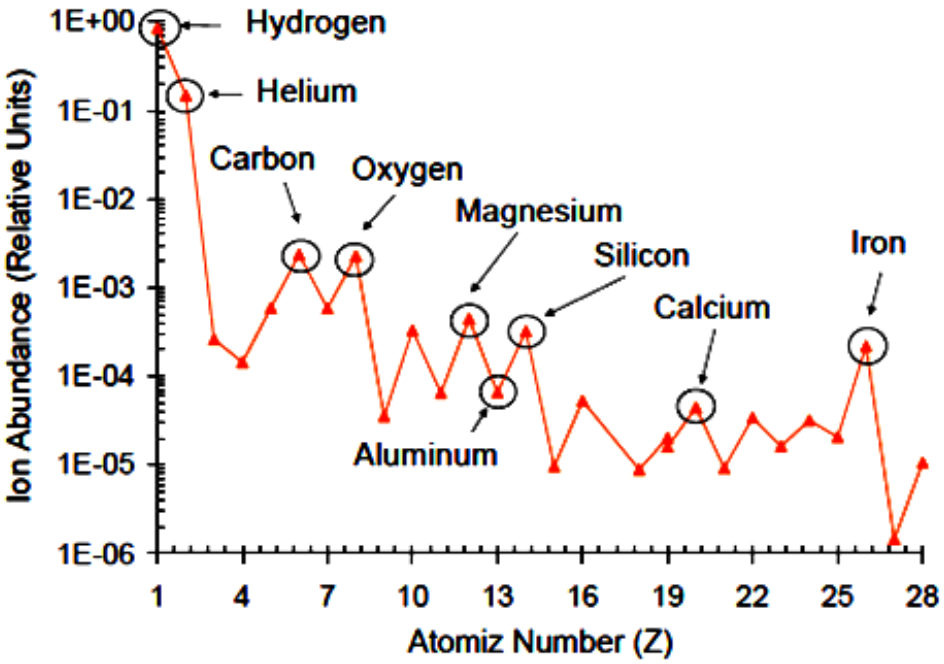

Figure 2.6. Relative ion abundances of the GCR component up to Nickel (Z=28) [NCRP 2000].

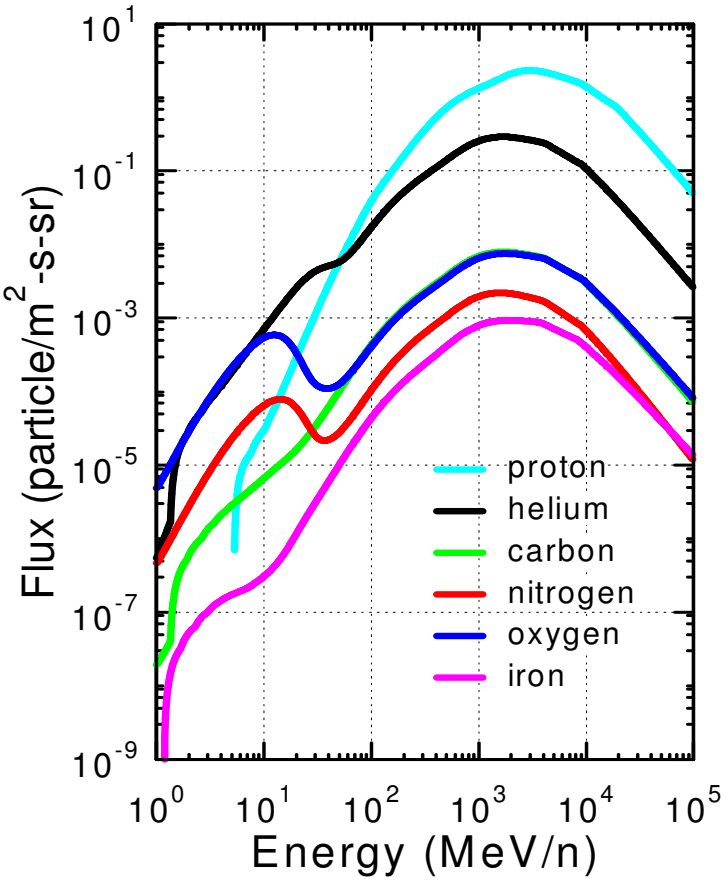

Figure 2.7. Flux spectra of GCR ions with the highest radiation weighting factors [Tylka et. al. 1996; NCRP 2000].

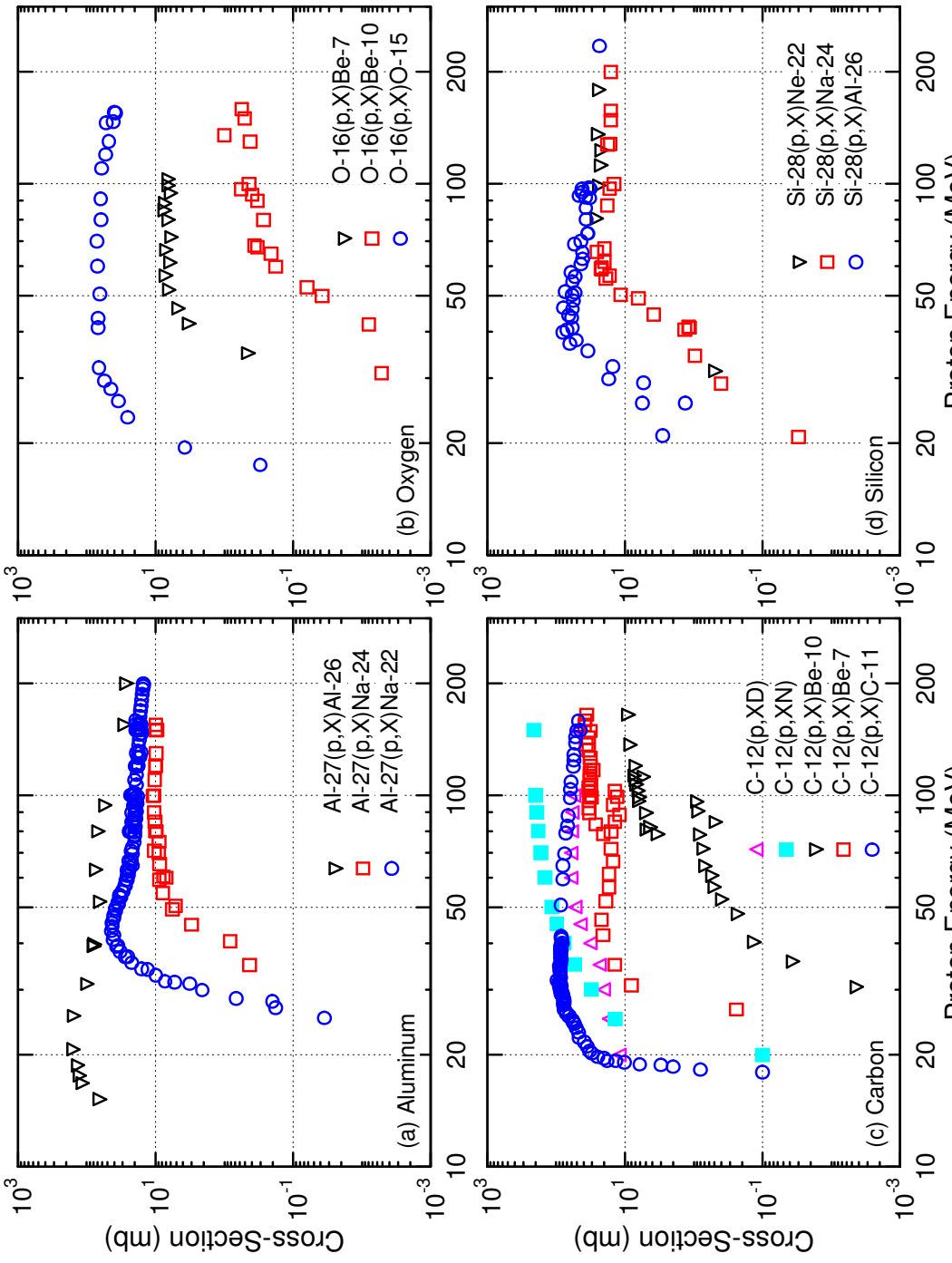

Figure 2.8. High Energy Protons Spallation Interactions Cross-Sections in Aluminum, Oxygen, Carbon, and Silicon [Chadwick and Young 1997; Kitazawa et. al. 2002].

stopping power expressed in units of MeV-cm^2/g [Littmark and Ziegler 1980]. It is obtained from dividing the LET by the density (ρ) of the target material. This quantity accounts for the density of electrons within the materials. Electromagnetic interaction between moving charged particles and the atoms of the target material is by far the dominant mechanism of interactions. Since the electromagnetic interaction extends over some distance, it is not necessary that charged particles make a direct collision with the material atom. They can transfer energy simply by passing close by. At this level, the interactions occur very frequently (~10^8/cm of travel). Although the amount of energy transfer at each interaction may be small, the cumulative effect can be considered as a continuous slowing down effect within the target material [Littmark and Ziegler 1980].

In nuclear reactions, the incident particles collide with the nucleus of the target material, and can results in the breakup of both the incident and targeted nuclei. Nuclear collisions are much less frequent, occurring only once or twice every few centimeters of travel through target material. Conversely, in spallation reactions, secondary particles, such as high-energy protons and neutrons, deuterons, alphas, etc., are ejected from the nuclei of the target material. They create cascades of events and defects along their tracks within the target material and atom clusters at the end of their tracks [Srour et. al. 2003]. High-energy protons and neutrons interact through knockout and light particles production, leading to a large buildup of secondary light particles and the localized production of heavy-ion target fragment [Hufner 1985]. As an example, Figure 2.8a-2.8d compares the most probable cross-section of spallation interactions of high energy protons in Aluminum, Oxygen, Carbon, and Silicon targets [Chadwick and Young 1997; Kitazawa et. al. 2002]. The spallation reactions, leading to production of secondary particles are highly dependent on the incident particles and the threshold energy of the target materials. All reactions shown in Figure 9a-9d have a threshold energy of >10 MeV, while Aluminum have the lowest spallation threshold energy of ~11 MeV, making it the most likely shielding materials to generate large amount of secondary particles. The spallation reactions can transfers large kinetic energy of incident particles into the recoiling secondary particles; thus, further spallation reactions can be initiated by the recoiling secondary particles [Hufner 1985]. The secondary neutrons are especially of concern, due to it being a neutral charge particle (or lack of a coulomb field), the

reactions threshold energy for absorption and spallation are much lower than those of protons.

2.5 Radiation Dose Assessment and Recommendation Limits

No real physical system is able to measure the dosimetric quantities directly. These quantities are defined for radiation protection as the energy deposited by radiation on the atomic composition of the irradiated materials. The absorbed dose, D_a, of radiation represents the amount of energy deposited in bulk material, and is expressed in units of joules per kilogram (J/kg) or Gray (Gy). It is expressed as the product of the fluence of particles (#/cm^2), F, and the linear energy transfer (LET), L, as:

$$D_a = F \cdot L \tag{2.1}$$

It is well established that radiation with different qualities has different effectiveness for producing biological effects [ICRP 1991]. The dose equivalent, H_T, is defined as the product of the radiation quality factor Q(L) and the absorbed dose averaged over a specific tissue (D_T) and summed over the LET distribution:

$$H_T = \int D_T Q(L) dL \tag{2.2}$$

The unit of dose equivalent is denoted as Sievert (Sv).

The International and National Commissions on Radiological Protection introduced an effective dose for a radiation risk assessment of individual tissue [ICRP 1991; NCRP 1989]. The effective dose, E, is defined as:

$$E = \sum w_T H_T \tag{2.3}$$

where w_T is the tissue weighting factor representing the proportionate detriment of tissue is irradiated uniformly, and H_T is the equivalent dose received by the tissue. The tissues weighting factors are estimates of the average contribution of specific tissues to the overall cancer burden with the major sites, including the blood forming organs (BFO), stomach, bladder, breast, lung, and gonads. The tissue weighting factors reflect the total detriment from radiation exposure, which includes consideration of the years of life-loss expected for different types of cancer deaths, cancer morbidity and hereditary effects [ICRP 1991].

Table 2.1. Recommended Dose Limits for Flight Crew on Space Missions, cSv [NCRP 2000].

Duration	BFO	Eye	Skin
Career	100 - 400	400	600
Annual	50	200	300
30-Day	25	100	150

Early radiation effects are deterministic in nature and occur only above dose thresholds, usually after a significant fraction of cell loss in a tissue. Short-term dose limits ensure that no clinically significant deterministic effects occur [ICRP 1991; NCRP 2000]. Table 1 lists the recommended dose limits for flight crew on space mission [NCRP 2000]. The short-term 30-days limits are designed to prevent the effects that can lead to significant clinical conditions. The annual limit is for a 1 year, not repeated year after year. As the biological effects of space radiation are not well established, the values listed in Table 1 are given as recommendations, not as established limits.

2.6 Phantom Experiment in Space

The dosimetric surveillance of astronauts and cosmonauts have generally been performed with personal passive thermolunescent dosimeters (TLDs) worn by the crewmembers, as well as from monitoring instruments at fixed locations within the crew compartment of the Space Shuttle and the ISS [Badhwar 2000; Badhwar et. al. 2001; Lyagushin et. al. 2001]. This only allowed the determination of the skin dose, but no information is provided about dose distribution inside the body [Badhwar 2000; Lyagushin et al. 2001; NCRP 2000; NCRP 2002]. The assessments of radiation risk to astronauts are currently based on the dose to the radiosensitive organs and blood-forming organs (BFO) from all the sources of radiation [ICRP 1993; NCRP 2000; ICRP 2003; NCRP 2002]. This raises the question of whether the skin dose provides sufficient information to determine the radiation risk inside the crewmembers' body [Badhwar 2000]. Since radiosensitive organs are located inside the body, direct measurements of dose in these organs are impossible, not to mention the measurements inside living subjects. To increase the knowledge of dose deposition and distribution inside the human

body, phantom experiments, simulating the human body, has been employed in-flight on the Space Shuttle and ISS.

Although measurements inside tissue equivalent phantoms are used routinely in radiotherapy for the treatment of patients, the first experiments with phantoms for the evaluation of the organ dose and the dose distribution inside the human body in space had to wait til the 1990 [Badhwar et al. 1990; Konradi et al. 1992]. The first measurements were for a human phantom head, performed in 1989 and 1990 onboard three Space Shuttle missions [Badhwar et al. 1990; Konradi et al. 1992]. This was a joint NASA and DoD project to help validate the used of tissue equivalent for dose measurements and investigate the radiation distribution inside the brain. The phantom head was constructed around a real human skull. Over 200 thermo-luminescent dosimeters (TLDs) were inserted into the phantom to measures the possible dose distribution in the brain.

NASA expanded space radiation research in the late 1990s, by designing a human torso phantom (nickname FRED), which was exposed to space radiation in the year 1998 aboard the Shuttle-MIR space flight [Yasuda et al. 2000; Yasuda and Fujitaka 2002; Badhwar et al. 2002; Cucinotta et al. 2008; Yasuda 2009]. FRED is the first fully instrumented Alderson RANDO phantom torso (with head) in a flight inside the single-module SpaceHab during STS-91 Shuttle-MIR mission. The phantom was composed of a human male skeleton and tissue-equivalent polyurethane resin. The soft tissue comprised of 8.8% hydrogen, 66.8% carbon, 3.1% nitrogen and 21.1% oxygen, with a density of 1.0 g/cm^3; and the lung is composed of 5.7% hydrogen, 74.0% carbon, 2.0% nitrogen, and 18.1% oxygen with a density of 0.320 g/cm^3 [Yasuda et al. 2000; Badhwar et al. 2002; Cucinotta et al. 2008; Yasuda 2009]. The phantom body was sectioned into 34 equal slices (2.5cm thick) from the head to the thigh. A total of 59 detector cases were placed into critical organ/tissue positions and were designed to provide measurements for: the brain, thyroid, bone surface, esophagus, heart, lung, stomach, liver, spinal cord, bone marrow, descending colon, bladder and gonad [Yasuda et al. 2000; Badhwar et. al. 2002; Cucinotta et al. 2008; Yasuda 2009]. Figure 2.9 show an illustration of the human phantom torso, indicating the positions of the detector cases [Yasuda et al. 2000; Badhwar et. al. 2002; Cucinotta et al. 2008; Yasuda 2009]. The phantom was fixed onto a rack at the starboard side in the SpaceHab module onboard the Space Shuttle. The

shuttle Discovery was launched on June 2, 1998, and landed on June 12, 1998, for total flight duration of 9.8 days [Yasuda et al. 2000; Badhwar et. al. 2002; Cucinotta et al. 2008; Yasuda 2009]. Though relatively short, the dose measurements in FRED are the most comprehensive at the time.

In the same time period, the Institute for Biomedical Problems in Moscow (IBMP) developed a water filled spherical phantom with a 35cm diameter. This phantom was placed at three different locations onboard the space station MIR in the years 1997 – 1999 [Berger et. al. 2001; Berger et. al. 2002; Berger et. al. 2004; Semkova et. al. 2003]. The phantom is rather simple, having only four detector channels, positioned in right angle in one plane inside the phantom. In those channels, different dosimeter types are inserted to measure the depth dose distribution. Due to it small dimensions, the phantom was easy to handle and move, and experimental measurements could be measured in different compartments with different phantom orientation [Berger et. al. 2001; Berger et. al. 2002; Berger et. al. 2004; Semkova et. al. 2003].

Building on their success, the Institute for Biomedical Problems in Moscow (IBMP) developed and flown a more advanced spherical phantom (MATROSHKA-R) in 2004. The MATROSHKA-R (MTR-R) phantom is a multi-user unit for studies of the depth dose distribution of the onboard radiation field inside the compartments of the ISS. The phantom consists of 13 slices made of the tissue equivalent prepolymer Diafor-TDI, with a chemical composition of: 8.63% Hydrogen, 2.6% Nitrogen, 32.3% Oxygen, and 56.5% Carbon [Kartsev et. al. 2005; Akatov et. al. 2007]. The slices are stacked together forming the spherical phantom with an outer diameter of 35 cm and an inner spherical air cavity of 10 cm diameter, and the total weight of the unit is about 32 kg [Kartsev et al. 2005; Akatov et al. 2007; Shurshakov et al. 2008]. Additional cylindrical channel pierce into the phantom for the placement of detectors; with the main four perpendicular channels across the equatorial plane. Passive thermo-luminescent detectors (TLDs), and solid state Plastic Nuclear Track Detectors (PNTDs), were installed inside tissue equivalent containers, and in turn, the containers were inserted into the corresponding detector channels inside the phantom. About 300 detectors filled the phantom at regular intervals to measures the absorbed dose at their designated position [Kartsev et al. 2005; Akatov et al. 2007; Shurshakov et al. 2008].

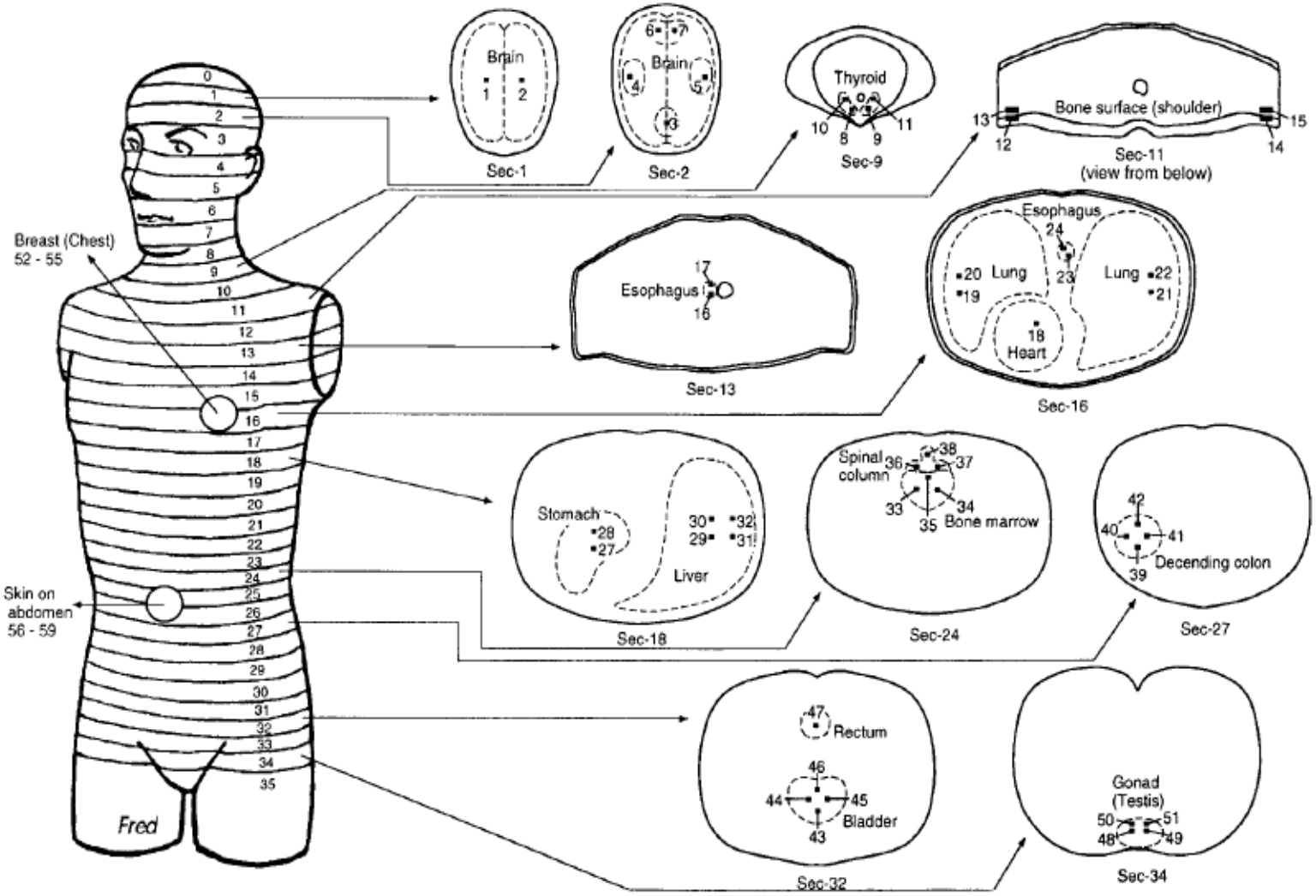

Figure 2.9. Illustration of the human phantom torso with indicating positions of the detector [Yasuda et al. 2000; Badhwar et al. 2002].

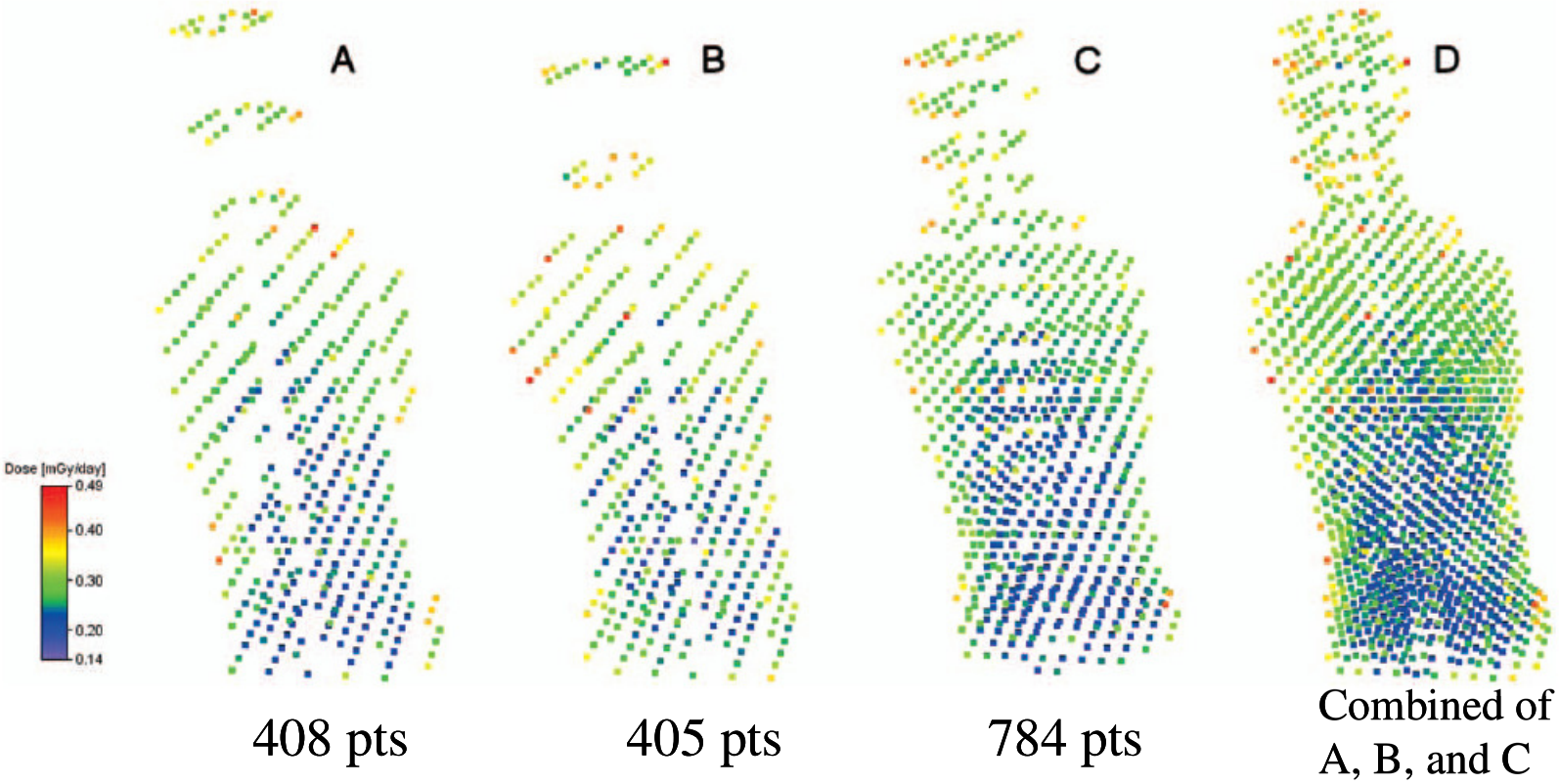

Figure 2.10. Distribution of measure absorbed dose-rate in the MATROSKA phantom. A, B, and C refer to the different research group. D is the combine of A, B, and C detectors group [Dettman et al. 2007; Kireeva et al. 2007; Zhou et al. 2010].

The configuration of the cylindrical channels were designed so that it could be removed and replaced without disassembling of the entire phantom, making the phantom very versatile to accommodate different detector types and biological samples [Kartsev et al. 2005; Akatov et al. 2007; Shurshakov et al. 2008]. Since 2004 till present, the MATROSHKA-R spherical phantom took it place aboard the Russian module Zvezda of the International Space Station; and is one of the first long-duration experimental measurements in space.

The most recent and most comprehensive phantom experiment is the MATROSHKA human phantom experiment; headed by ESA and with cooperation from 16 international research organizations. The objectives of the MATROSHKA experiment is to determine the empirical relations between measurable absorbed doses and the tissue absorbed doses in a realistic human phantom exposed to the radiation field in orbits of the ISS; particularly the depth dose distribution at different organs of astronauts during an extravehicular activity (EVA) [Reitz and Berger 2004; Dettmann et. al. 2007]. The MATROSHKA facility consists of a RANDO human phantom, a base structure and a container. The phantom body consists of natural bones embedded in tissue-equivalent polyurethane resin, with different density for tissue, lungs and organs [Reitz and Berger 2004; Dettmann et. al. 2007]. The phantom body is made up of 33 slices, each with 25mm thickness, stacked together over a mandrel to stabilize the whole body. The slices are equipped with 356 channels, where the TLDs/detectors from different participating groups are located, at a total of 1634 positions arranged in 1-in grid. The phantom also accommodated five nuclear track detector packages, each consisting of 60 detectors of varieties, locating in five specific organs locations (Eye, Lungs, Stomach, Kidney, and Intestine). The phantom was covered in a poncho and hood with sewn on polyethylene stripes and detectors to measure the skin dose and for thermal protection [Reitz and Berger, 2006; Kireeva et. al. 2007; Zhou et. al., 2010]. The phantom was enclosed inside a carbon fiber reinforced plastic container, with a mean mass thickness similar to the astronauts spacesuit during EVA, and to protect the phantom against space vacuum, debris, and material off-gassing [Reitz and Berger, 2006; Kireeva et. al. 2007; Zhou et. al., 2010]. The phantom was launched to the ISS in 2005 and was transferred into the Russian module Zvezda of the ISS. The MATROSHKA

phantom facility was installed outside the Zvezda module, simulating measurement of an astronaut during EVA. The MATROSHKA experiment spent 616 days in orbit, both inside and outside the Russian module. Figure 2.10 show a color coded distribution of the measure absorbed dose rate in the MATROSHKA phantom [Reitz and Berger, 2006; Kireeva et. al. 2007; Zhou et. al. 2010]

2.7 Simulations of Phantom Experiments in Space

Reliable risk estimations and shielding optimization studies are mandatory in the field of manned space flights. Such estimations can be performed using measured data of dose distributions in the spacecraft compartments in real space flight or through computer simulations. However, due to the complex space radiation environment of space radiation, it is impossible to perform measurements for all possible combinations of space radiations. In this framework, models and computer codes, which simulate particle and heavy ion transport and interactions, are needed to aid in prediction of radiation risks in human space flights.

Many authors have performed dose estimate predictions for astronauts by performing radiation transport simulation in computational phantoms, with deterministic (HZETRN) or Monte-Carlo codes (GEANT, FLUKA, PHITS, MCNPX) [Ballarini et al. 2006; Trovati et al. 2006; Niita et al. 2007; Cucinotta et al 2008; Slaba et al. 2010; McKinney et al. 2006; McKinney et al. 2008]. But direct comparisons with phantom experiment in space are limited to two simulation codes, NASA High Z and Energy TRaNsport (HZETRN) and Particle and Heavy-Ion Transport System (PHITS). The NASA HZETRN simulation was primarily limited to the FRED STS phantom experiment, and the PHITS code was used in conjunction with the ESA MATROSHKA experiment program [Cucinotta et al. 2008; Shurshakov et al. 2008; Sihver et al. 2009; Gustafsson et al. 2010].

2.7.1 HZETRN Simulations

Badhwar et al. compared the HZETRN code predictions with the measurements from the FRED phantom experiment. They coupled a computerized anatomical model to the code by computing the shielding mass thickness of the body in relation to the detector

points. Five detector points of brain, colon, heart, stomach, and thyroid were taken, and the dose estimates were calculated and compared to experimental values. The calculation shows an almost constant GCR dose rate that is almost independent of the organ or tissue location [Badhwar et al. 2002]. Thus, the changes of the dose rates throughout the body tissue/organs are dependent of the trapped particles. Result showed that the calculated equivalent dose rates are 20% higher than the measurements for colon and skin location [Badhwar et. al. 2002]. However, the large differences in the skin dose estimate made it difficult to assess the relationship between the organ doses and skin dose. The differences are thought to be due to those between the trapped-proton flux AP-8MIN model and the actual experimental conditions [Badhwar et. al. 2002]. The model calculations are for trapped-proton fluxes at a solar minimum and solar maximum, while the experimental condition is not specific for the minimum or maximum condition [Badhwar et. al. 2002].

In 2008, Cucinotta et al.(2008) re-analyzed the transport code assessment of the organ dose and dose equivalent, using an update version of the code and model. They compared estimates with measurements for the phantom experiment aboard STS-91 mission [Cucinotta et al. 2008]. The simulation analysis implemented the update HZETRN/QMSFRG model, coupled to a Computerized Anatomical Man model by approximating the shielding thickness of the detector position for the 1-D HZETRN transport model. The updated model showed good agreement, reducing the differences in the skin dose [Cucinotta et al. 2008]. The largest differences were for the calculated bone surface dose, with differences > 20%. Cucinotta et. al. found that organ dose equivalents for the brain, thyroid, heart, stomach, and colon have a relatively flat distribution, despite the varying depths of these organs from the skin. Such flat distribution of internal dose was not expected based on previous model calculations [Badhwar et. al. 2002; Cucinotta et al. 2008].

These two simulations represent the main benchmarking and validation effort of the HZETRN code with experimental measurements. The results demonstrated the promising predictive capability of the code. Though it is a fast running, 1-D deterministic code is unsuitable for shielding optimization and dose estimate in 3-

dimensional geometry. Besides, HZETRN is an in-house NASA code that is not available to the public.

2.7.2 PHITS Simulations of the MTR-R and MTR experiments aboard the International Space Station

In conjunction with the MATROSHKA experiment, Shiver et al. 2009 examined the applicability of the Particle and Heavy Ion Transport code system (PHITS) for estimating the dose to astronauts by comparing calculations with the phantom measurements. In the MTR simulations, Sihver et al. (2009) simulated a spherical phantom located in a cylindrical shape spacecraft with inner dimensions approximately that of the crew cabin, where the spherical phantom was located [Sihver et. al. 2009]. The spacecraft was assumed to be freestanding, surrounded by a spherical radiation source of trapped protons and GCR particles, simulating the external radiation environment. The Trapped Protons and GCR fluxes and energies were obtained from the Cosmic Ray Effects on Micro-Electronics Code [Tylka et al. 1997], based on the average orbital data of the ISS. They reported that the absorbed dose rate is highest at the surface of the phantom, decreasing with increasing distance into the phantom. However, the simulated dose values were found to be ~2 times higher than the measurement values [Sihver et al. 2009]. They also performed simulations of the MATROSHKA human phantom experiment using simplified oval shape discs, shaped the phantom. The simulations positioned the simplified phantom on an aluminum support structure, enclosed in a carbon fiber container in vacuum, and surrounded by a spherical radiation source; but without the ISS structure [Sihver et al. 2009]. The simulation dose rates were found to be also 1.5-2 times larger than the measured values [Sihver et al. 2009]. They suggested that the difference in both simulations could be due to the lack of detector efficiency correction and incorrect estimation of shielding thickness [Sihver et al. 2009].

In 2010, Sihver et al. (2010) performed a more extensive analysis of their earlier work, by incorporating a more realistic human phantom. Their simulation incorporated a numerical voxel model of the RANDO phantom developed at the Institute of Nuclear Physics (IFJ) in Krakow [Puchalska et al. 2010]. The voxel phantom was constructed based on computed tomography (CT) scans. It was scaled to those of the ICRP reference

man [ICRP 2002]. The phantom was placed inside a container made of carbon fiber and was placed on an aluminum foundation of 1 g/cm^2 thickness. The container and foundation was mounted on a simplified cylindrical ISS module with 12.5 g/cm^2 aluminum wall thickness [Sihver et al. 2010; Gustafsson et al. 2010]. The external space radiation environment was simulated with the spherical source emitting inward simulating an isotropic environment. Both the simulations and measurements showed a general trends of decreasing dose from the surface into the center of the phantom, though the dose calculations by PHITS was ~20% higher than the experimental values.

3. SIMULATION OF SPACE RADIATION INTERACTIONS WITH MATERIALS

High-energy particles traversing a shielding material lose energy by interactions with the atomic electrons and collisions with atomic nuclei. Such collisions generally result in cascaded events that produce secondary particle such as protons, neutrons, gammas, etc., with fluxes often exceeding that of the primary particles [Jun 2001]. This chapter investigates important modes of interaction of high energy protons with structure materials or potential shielding materials. The components of the total energy deposition are calculated and compared.

This work investigates the interaction of monoenergetic, 100-MeV protons with aluminum, enriched B_4C, a $C_{29}H_{28}O_8$ polymer resin for shielding electronic devices and calculates the contributions to the total energy deposition of the incident primary protons and secondary particles in a 1-cm-diameter silicon sphere, which represents the electronic device. The potential of the lunar regolith, as shielding material for electronic devices is also investigated. The energy spectrum and the relative contributions of the primary and secondary radiations to the displacement and ionizing doses are calculated and the threshold energies for the spallation reactions by primary and secondary protons and secondary neutrons are determined and compared. In addition to determining the type and concentration of the secondary particles generated, the calculated effectiveness of the different shielding materials investigated in this work are compared.

3.1. Introduction

Beyond the Earth's protective magnetic field, space radiation and meteoroids represent serious threats to human space travel and avionics. Space travel involves exposure to Solar Energetic Protons (SEPs) and Galactic Cosmic Rays (GCRs). The SEPs could have energies >100 MeV, and the GCRs include protons with energies >1000 MeV and heavier ions with higher energies [Wilson 2000; NCRP 2005]. Protective shielding of avionics and astronauts from GCRs and SEPs on long-duration space travel is necessary. As the incident high-energy protons pass through the shielding materials, the spallation reactions with the nuclei of the elements comprising these materials

generate secondary protons, neutrons, gammas, deuterons, and alpha particles. The secondary particles increase the overall dose beyond that due to the incident high-energy protons [Jun 2001]. The energy thresholds for the spallation reactions depend on the elements in the shielding materials and the energies of the protons and neutrons.

High-energy particles lose energy in shielding materials through Coulomb interactions and nuclear (or spallation) reactions. A proton traversing an electronic device can induce sufficient ionization to cause single-event effects. The interactions of these particles can also displace atoms, causing performance degradation and changing the operation characteristics of the electronic devices. For example, the semiconductor space photovoltaic solar panels are generally oversized to compensate for the degradation of the electrical power output over their operation life due to the exposure to both SEPs and GCRs [Wilson 2000; Jun 2001]. Therefore, it is important to understand the interaction of high-energy protons with candidate shielding materials and calculate the amount and type of secondary particles generated as well as the displacement and ionizing energy deposition in the electronic devices protected by these materials.

3.2 Radiation Shielding Materials

High energy protons traversing a shielding material lose energy by interactions with the atomic electrons and the collisions with the atomic nuclei. Such collisions generally result in cascaded spallation events that produce secondary particle such as protons, neutrons, gammas, etc. (see Appendix A), with fluxes often exceeding that of the primary protons [Wilson 2000; Jun 2001]. The number of the secondary nucleons generated by the spallation reactions is related to the atomic weight of the elements comprising the shielding material.

There are two important parameters for selecting a suitable shielding material of SEPs: the ability to stop the low energy secondary protons and the low production of secondary particles. On per-unit-mass basis, materials with low atomic weights and high hydrogen contents are relatively more effective for shielding high energy protons. However, aluminum with a density of 2.7 g/cm^3, has been the standard shielding and structural material for space applications. When aluminum is used for shielding high-

Table 3.1. Density of Shield Materials.

Material	Density (kg/m^3)
Aluminum	2700
Enriched $^{10}B_4C$	2520
Polymer $C_{29}H_{28}O_8$	1060
Regolith	1200

Table 3.2. Lunar Regolith Composition used [Kang et. al. 2006, McKay 1994].

Material	wt %
SiO_2	47.71
TiO_2	1.59
Al_2O_3	15.02
Fe_2O_3	3.44
FeO	7.35
MgO	9.01
CaO	10.42
MnO	0.18
Na_2O	2.7
K_2O	0.82
Cr_2O_3	0.04

energy protons (> 20 MeV), spallation reactions generate a slew of secondary particles including protons and neutrons [Wilson 2000; Jun 2001].

The enriched B_4C is investigated in this work as a potential shielding material of incident monoenergetic 100 MeV protons, for a number of favorable considerations. These are the low density, high melting point, structural strength, and the high contents of boron-10 isotope, with a large absorption cross-section for neutrons, particularly those with low energies. The polymer resin $C_{29}H_{28}O_8$ is also considered because of the very low density (1.06 g/cm^3) and the high hydrogen density (5.28 x 10^{21} cm^{-3}) for slowing incident protons and secondary neutrons.

In addition to the three shielding materials indicated earlier (aluminum, enriched $^{10}B_4C$, and polymer resin $C_{29}H_{28}O_8$), this work also investigated using lunar regolith for shielding silicon-based electronic devices from SEPs. Table 3.1 compares the densities of aluminum, $^{10}B_4C$, Polymer resin $C_{29}H_{28}O_8$, and the Regolith and Table 3.2 presents the regolith composition used in this work for shielding silicon-based electronics from incident monoenergetic 100 Mev protons [McKay et. al. 1994; Kang et. al. 2006]. Although not representative of an actual space radiation energy spectrum, the 100 Mev energy protons is high enough to investigate important modes of interaction with potential shielding materials, including the production and attenuation of secondary particles.

3.3 Energy Loss Mechanisms

There are three basic energy loss mechanisms for charged particles, such as protons, in potential shielding materials: ionizing, non-ionizing or displacement damage, and spallation. In the first, charged particles lose energy by exerting electromagnetic forces on and transferring energy to the atomic electrons; knocking out electrons, forming ions and emitting x-ray. The energy loss caused by the interaction of the energetic particles with the atoms of the target material is known as the Non-Ionizing Energy Loss (NIEL) or displacement energy loss. NIEL has the units of MeV-cm^2/g and describes the collision stopping power, or the rate of energy loss due to the displacement of the lattice atoms of the shield material. The spallation energy loss is due to the elastic and non-elastic collisions of energetic particles with the atoms nuclei of the shield material. These

losses are typically dominant at > 10 MeV. These energy loss mechanisms are discussed briefly next.

3.3.1 Ionizing Energy Losses

Ionizing energy loss creates hole-electron pairs within the silicon oxide layer in the electronic devices. Due to their high mobility, electrons escape, leaving behind a net positive charge that increases the leakage current, causing a loss of noise immunity and an eventual failure of the circuit. When a large enough number of hole-electron pairs is generated within the silicon oxide layer, the resulting large electrical pulse could short-circuit or burnout the electronic device. Ion creation also ruptures the chemical bond, thus influencing the behavior and the characteristics of the materials [Hawari et. al. 2007]. The stopping power, expressed in MeV/cm is conveniently used to express the ionizing energy loss. It is also referred to as the *linear energy transfer* (LET) from the incident particles to the atoms of the target material and closely associated with the dose delivered. A more common quantity for expressing the ionizing energy loss is the mass stopping power expressed in units of MeV-cm^2/g [Littmark and Ziegler 1980]. It is obtained from dividing the LET by the density (ρ) of the target material.

3.3.2 Non-Ionizing Energy Loss (NIEL) or Displacement Damage

The Non-Ionizing Energy Loss (NIEL) by the incident energetic charged particles is caused by the displacement of the lattice atoms from their sites. The displaced atoms lodged out of lattice plane form interstitials. Displacements caused by low energy and irradiation intensity primarily create point defects. However, as the energy of the incident particles increases to ~ 1 MeV, a large fraction of their energy is transferred to the displaced knock-on atoms, displacing surrounding atoms and creating a disordered region or cluster [Srour et. al. 2003]. The displacement energy deposition per unit mass (E_d) in silicon is calculated as $E_d = NIEL \cdot \phi$. The fluxes of the primary and secondary particles are determined in this work using the particle transport code MCNPX. The NIEL values are based on those reported in literature for the different particle species in

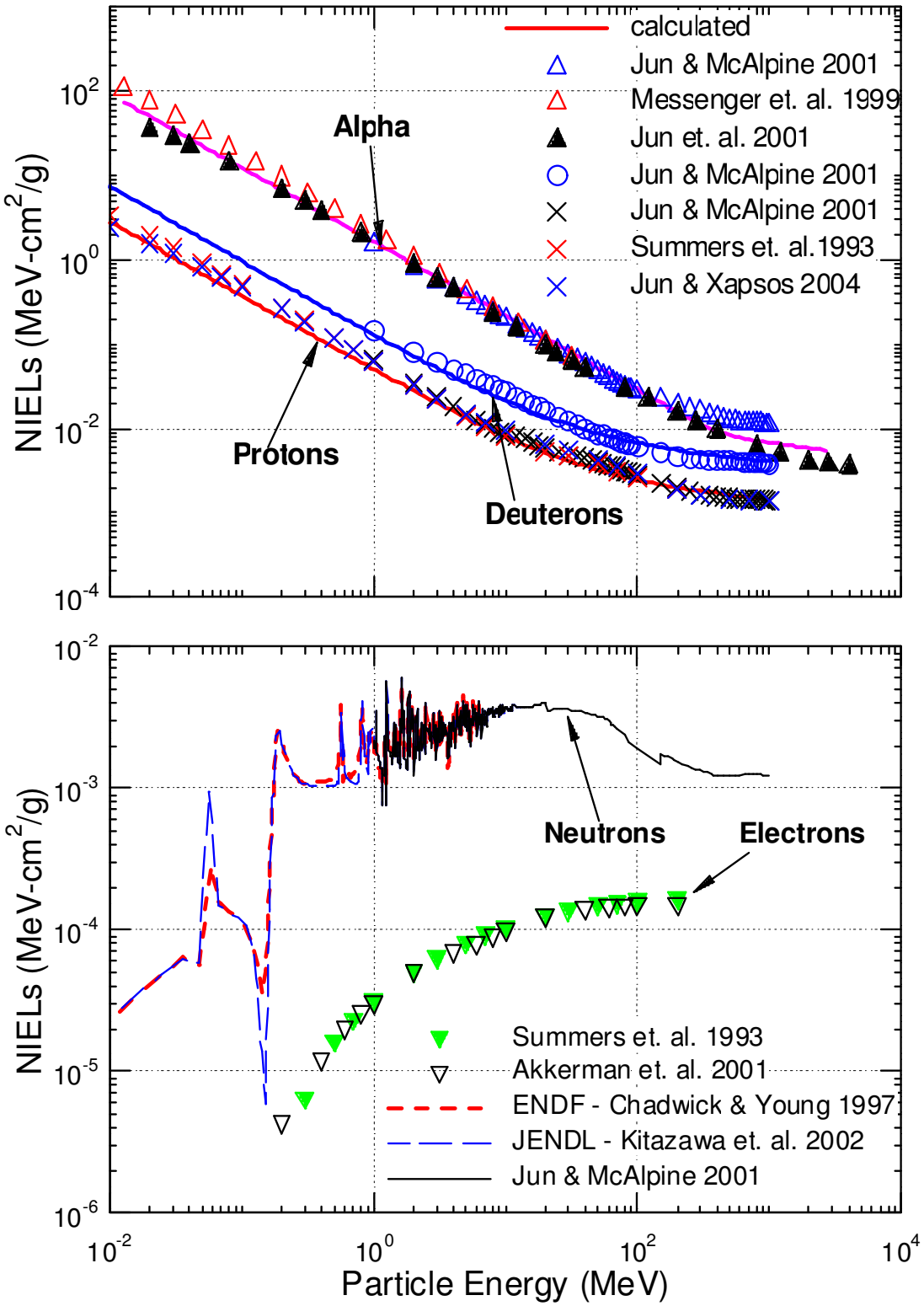

Figure 3.1. Non-Ionizing Energy Loss (NIEL) for protons, neutrons, electrons, deuterons, and alphas.

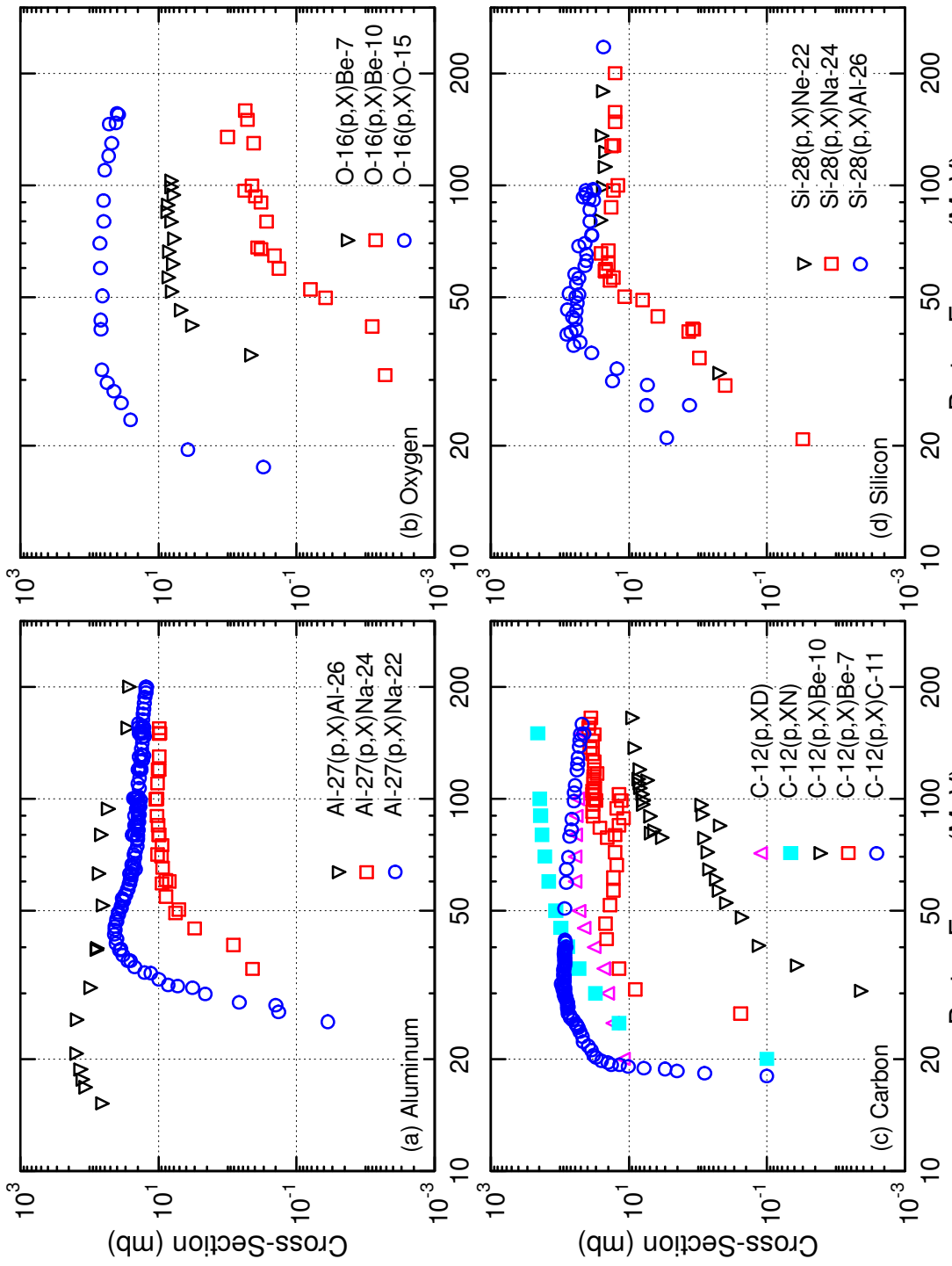

Figure 3.2. High Energy Protons Spallation Interactions Cross-Sections in Aluminum, Oxygen, Carbon, and Silicon [Chadwick and Young 1997; Kitazawa et. al. 2002].

the range of energies of interest. However, additional calculation are performed to confirm the continuity of the NIEL values for energetic protons from separate calculations and to generate NIEL values for deuterons, which are limited in the literature. The NIELs from neutrons and electrons are shown in Figure 3.1a and those for protons, deuterons, and alphas are shown in Figure 3.1b. The compiled NIELs in these figures are obtained from many sources [Summers 1993; Jun and McAlpine 2001; Jun et. al. 2004; Messenger et. al. 1999; Chadwick and Young 1997; Kitazawa et. al. 2001; Akkerman et. al. 2001].

3.3.3 Spallation Energy Loss

Nuclear or spallation reactions of incident energetic particles with > 10 MeV can cause severe displacements and damages in the crystal lattice. Secondary particles, such as high-energy protons and neutrons, deuterons, alphas particles, and gamma photons are ejected from the nuclei of the target material. They create cascades of events and defects along their tracks within the target material and atom clusters at the end of their tracks [Srour et. al. 2003]. Spallation reactions and inelastic nuclear interactions transform the target nuclei into other nuclei and generate high energy secondary particles. Appendix – A lists the most probable protons and neutrons inelastic nuclear reactions with target atoms, along with the threshold energies for the spallation interactions. The threshold energy is the minimum energy that required for a spallation reaction to occur.

Figures 3.2a – 3.2d, compare the most probable cross-sections of the spallation interactions of high energy protons in Aluminum, Oxygen, Carbon, and Silicon targets [Chadwick and Young 1997; Kitazawa et. al. 2001]. Aluminum (Fig. 3.2a) has the highest interaction cross-section along with the lowest spallation reaction threshold energy of ~11 MeV, making it the most likely material to produce large amount of secondary particles. Carbon, Oxygen, and Silicon have lower proton spallation interaction cross sections (Figs. 3.2b – 3.2d), and higher energy threshold of ~14-20 MeV, compared with Aluminum. All energy thresholds are below that of the incident primary protons (100 MeV) in the present analysis. Thus, all the interactions listed in the Appendix A could occur, but the most probable are those with the lowest energy threshold (Figs. 3.2a – 3.2d). For Aluminum, the likely spallation interaction is that of

^{27}Al (p, X) ^{26}Al, where X could be a Deuteron ($_1^2D$) or a proton ($_1^1p$) – neutron ($_0^1n$) pair, with energy thresholds of 11.237 and 13.454 MeV, respectively (see Appendix A). The reaction ^{16}O (p, X) ^{15}O is also highly probable, yielding a Deuteron ($_1^2D$), with a threshold energy of 14.280 MeV, or both a proton ($_1^1p$) – neutron ($_0^1n$) pair with an energy threshold of 16.600 MeV. The carbon spallation reaction ^{12}C (p, X)^{11}C, with a energy threshold of 17.882 MeV, produce a Deuteron, and with an energy threshold of 20.292 MeV produces a proton – neutron pair.

In these spallation reactions, only a fraction of the energy of the primary protons is transferred into kinetic energy of the recoiling secondary particles and target nuclei. The energies of the secondary particles are typically higher than the threshold energies for the spallation reactions. Thus, further spallation reactions can be caused by the secondary particles. Once the energies of the secondary particles fall below the applicable energy thresholds, spallation reactions cease. At lower energies, the shielding materials behave like a moderator, slowing down the protons and neutrons by elastic collisions and by coulombic interaction with the atoms of the shield material. Secondary neutrons with high enough energy would initiate additional spallation reactions, depending on the type of target nuclei and the interaction thresholds energy (see Appendix – A). In many cases, the energy thresholds for the neutrons spallation reactions are lower than those for the protons. Neutrons lose their energy primarily by nuclear interactions with the nuclei of target material. The caused disruptions in the crystal lattice of Si by high-energy protons and neutrons could significantly affect the silicon's thermal, optical, and mechanical properties and the operation characteristic of the electronic devices. In a space environment, spallation by SEPs and the GCR protons would generate high-energy secondary particles that must be accounted for in the shielding calculations.

3.4 Problem Setup and Methodology

The present calculations are for a spherical shell of the shield materials surrounding a 1.0 cm diameter silicon sphere, representing an electronic device or sensor (Fig. 3.3). The thickness is increased incrementally up to 20 g/cm^2 for all shield materials

investigated. The primary 100 MeV monoenergetic protons are assumed incident isotropically onto the outer surface of the shielding spherical shell of the 1 cm diameter silicon sphere (Fig. 3.3).

The present shielding calculations are performed using the three-dimensional (3-D) general purpose Monte Carlo radiation transport code MCNPX version 2.5.0 [Pelowitz et. al. 2005]. This code tracks a wide range of light particles such as: protons, neutrons, photons, electrons, muons, pions, kaons, deuterons, tritons, alphas, and their respective anti particles over a wide range of energies >1000 MeV. The fluences of the primary and secondary protons and of the secondary neutrons, deuterons, alphas, and electrons generated in the shield material are all tallied over the silicon sphere volume. For 100 MeV incident protons does not produce muons, kaons, and pions. Since MCNPX 2.5.0 cannot explicitly distinguish between the primary and the secondary protons resulting from the nuclear reactions in the shield materials, the present calculations consider all protons not having the incident 100-MeV to be secondary protons.

All shielding calculations with MCNPX 2.5.0 used 10 to 15 millions source particles to reduce the statistical uncertainties in the results below 5% for shield material less than the threshold thickness. The latter is defined as the shield thickness beyond which there are precipitous drops in the fluences of the primary and secondary protons in the shielding material (Fig. 3.4). The total energy deposition in the Silicon sphere is the sum of the Non-ionizing or displacement damage and ionizing energy losses. The statistical uncertainties in the MCNPX 2.5.0 calculations for the secondary protons, deuterons, alphas, and electrons increase as the shield thickness increases. However, as will be shown next in the results section, the contributions of these secondary particles to the total energy deposition in the silicon sphere are minimal. Conversely, the contributions of the secondary neutrons dominate the displacement damage energy deposition and remain fairly constant beyond the threshold thickness of the shield; the contributions of the secondary neutrons for the different materials are determined next.

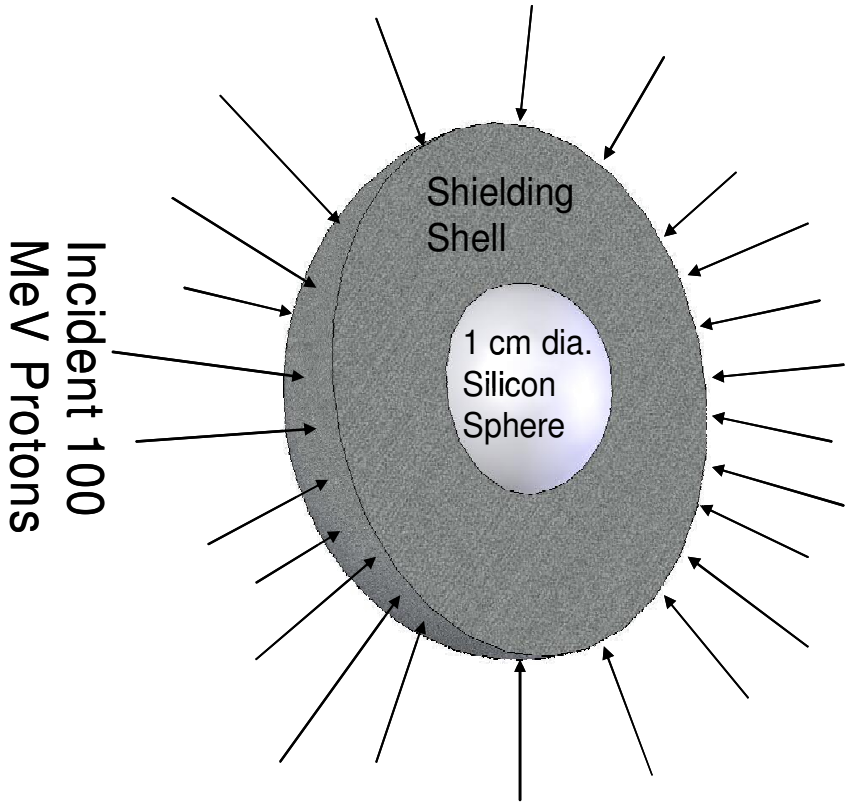

Figure 3.3. Shielding Model in Simulations.

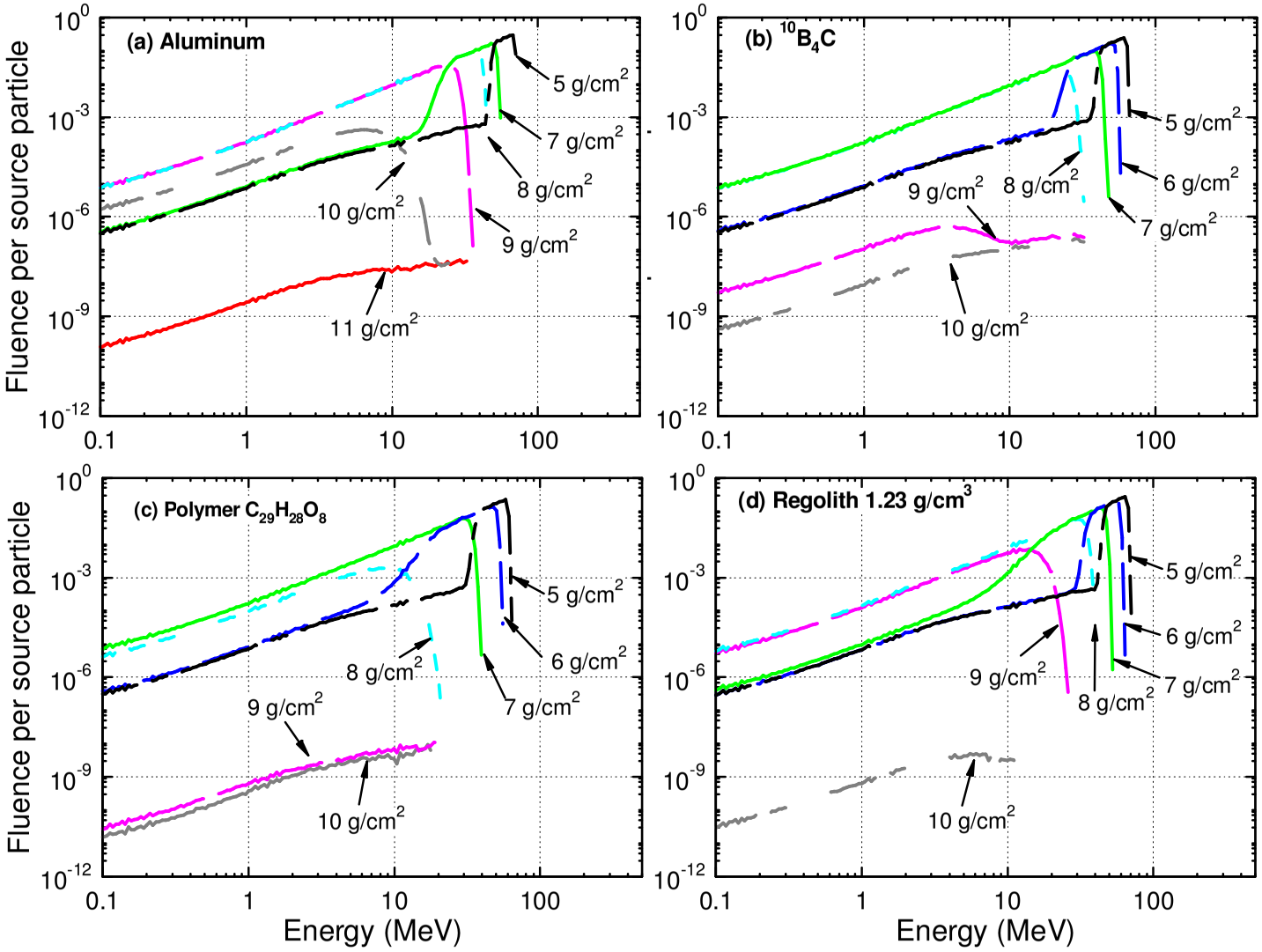

Figure 3.4. Calculated Energy Spectra of Protons in Different Shield Materials.

3.5 Results and Discussion

This section presents the results of the interaction of monoenergetic, 100 Mev protons with the shielding materials of Aluminum, commonly used also for structure in spacecraft, enriched B_4C, $C_{29}H_{28}O_8$ polymer, and Lunar Regolith. The calculations track the changes in the energy spectrum and the total energy deposition by the incident and secondary protons as well as by the secondary neutrons, deuterons, and electrons as functions of the thickness and type of shielding material. The calculated energy loss by spallation, ionizing energy loss, and non-ionizing (displacement) energy loss are presented and discussed.

3.5.1 Interaction of Primary Protons with Shield Materials

When the shielding material thickness is < 7 g/cm^2, total energy deposition in the silicon sphere by the primary and secondary protons is directly related to the fluence and the energy spectrum of the protons in the shield. The interactions of the high-energy protons with various shield materials are dominantly through spallation. This is evident by the generation of the secondary protons, neutrons, deuterons, and alphas. Figures 3.4a – 3.4d compares the calculated protons' energy spectra with different thicknesses in g/cm^2 of the shielding materials.

The precipitous drop in the fluence of the high energy primary protons to that of the secondary protons occurs at different energies in the different materials; the highest is in aluminum and the lowest is in $C_{29}H_{28}O_8$ polymer. Such a sharp drop in the protons' energy is indicative of the large energy transfer from the primary protons to the lattice atoms, in contrast to the continuous slowing down caused by Coloumbic interactions at lower energy.

The energy spectra of the secondary protons in the different shield materials are very similar (Fig. 3.4a – 3.4d). The secondary protons are dominanted by those with energies > 43 MeV in aluminum, > 40 MeV in lunar regolith, > 36 MeV in $^{10}B_4C$, and > 30 MeV in the $C_{29}H_{28}O_8$ polymer. Thus the smallest proton energy loss per collision is that in aluminum, followed by the lunar regolith, and $^{10}B_4C$, while the highest energy deposition is in the $C_{29}H_{28}O_8$ polymer. The harder energy spectrum of the secondary

protons in aluminum is indicative of the low energy thresholds for the spallation interactions of protons in Aluminum (see Appendix – A).

The most probable nuclear reactions in aluminum is ^{27}Al (p, X) ^{26}Alwith a cross-section of ~ 100 mb. Its energy threshold for the production of a secondary proton – neutron pair is 13.454 MeV (see Appendix – A). The excess 86.546 MeV is the recoil energy of the generated secondary particles. The energies of the secondary protons and neutrons is above the spallation energy thresholds for aluminum (see Appendix – A) and could cause additional spallation reactions. The low-energy secondary particles are generated at the tail of the energy spectrum (Fig. 3.4a – 3.4d).

At low energy, secondary neutrons dominate the spallation reactions such as ^{27}Al (n, n + p) Mg and ^{27}Al (n, 2n) ^{26}Al, with cross-sections of ~ 400 mb and 170 mb, and energies thresholds of 8.580 and 13.057 MeV, respectively (see Appendix – A). Carbon in $^{10}B_4C$ and the $C_{29}H_{28}O_8$ polymer have low proton interaction cross-sections of ~ 60 mb for ^{12}C (p, X) ^{11}C and a higher spallation energy threshold of 20.292 MeV for the production of a secondary proton – neutron pair (see Appendix – A). Similarly, Oxygen has a low proton interaction cross-section of ~ 62 mb for the ^{16}O (p, X) ^{15}O reaction, which has a higher energy threshold of 16.60 MeV.

With a shield thickness of 6 g/cm^2, the secondary protons in aluminum are predominantly with > 35 MeV, compared to > 30 MeV in regolith. The proton energy spectrum in enriched $^{10}B_4C$ is dominated by particles with energies > 20 MeV; which are higher than the spallation energy thresholds. When the energies of the protons drop below the spallation thresholds, the ionizing energy loss dominates, which results in a continuous energy loss spectrum. This occur when using 6 g/cm^2 of enriched $^{10}B_4C$ or $C_{29}H_{28}O_8$ polymer shield and is not exhibited in aluminum and the lunar regolith until a shield thickness of ~ 7 g/cm^2. For a thickness of 8 g/cm^2, the energy losses by inelastic scattering and coloumbic interactions dominate in all shielding materials.

With shield thicknesses $\geq$ 9 g/cm^2, the fluence of the secondary protons drops several decades and shifts toward lower energy, insignificantly contributing to the total energy deposition in the silicon sphere. The energy spectrum and fluence of the secondary proton are hardest and highest in Aluminum, followed by those in the lunar regolith. The results delineated in Figures 3.4a – 3.4d show that the lowest fluence of the

secondary protons is by far that in the $C_{29}H_{28}O_8$ polymer, followed by that in $^{10}B_4C$ at 9 g/cm^2. Thus, using either enriched $^{10}B_4C$ or $C_{29}H_{28}O_8$ polymer as shielding materials could result in a mass saving of ~ 2 g/cm^2.

3.5.2 Effect of Shield Material on Ionizing Energy Deposition

The calculated ionizing energy depositions in the silicon sphere, using different shielding materials, are compared in Figures 3.5a – 3.5d. For aluminum, the primary and secondary protons dominate the ionization energy deposition up to the thickness of 10 g/cm^2. With shield thickness < 10 g/cm^2, the secondary deuterons, alphas and the electrons contribute minimally to the total energy deposition. Similar results are obtained for the different shielding materials, where the primary and secondary protons dominate the ionizing energy deposition up to a thickness of 8 g/cm^2 for B_4C and $C_{29}H_{28}O_8$ polymer, and 9 g/cm^2 for the regolith shield.

The aluminum shield results in the highest ionizing energy deposition, which peaks at a thickness of 8 g/cm^2. The second highest ionization energy deposition is that with the B_4C shield, peaking at a thickness of 7 g/cm^2, followed by that of $C_{29}H_{28}O_8$ polymer with a peak at a thickness of 6.5 g/cm^2. The lowest increase in the ionization energy deposition is with the regolith shield, peaking at a thickness of 7.5 g/cm^2. This is due to the higher contribution of the low energy particles to the ionization energy deposition. The calculated total ionizing energy depositions in silicon with all shield materials are comparable, with the primary contributors being the primary and secondary protons. The $C_{29}H_{28}O_8$ polymer shield is the most promising with a smaller threshold thickness of ~ 8 g/cm^2, representing a 2 g/cm^2 saving compared to aluminum.

3.5.3 Effect of Shield Material on Displacement Energy Deposition

Figures 3.6a – 3.6d show the thickness of the different shield materials beyond which the contribution of the protons become insignificantly small. The single most significant contributor to the displacement energy deposition in the silicon sphere with a shield thickness of 20 g/cm^2 is the secondary neutrons. This is also true with aluminum and regolith shields having thicknesses > 10 g/cm^2 and for $^{10}B_4C$ and $C_{29}H_{28}O_8$ polymer with thicknesses > 7 g/cm^2 and 8 g/cm^2, respectively.

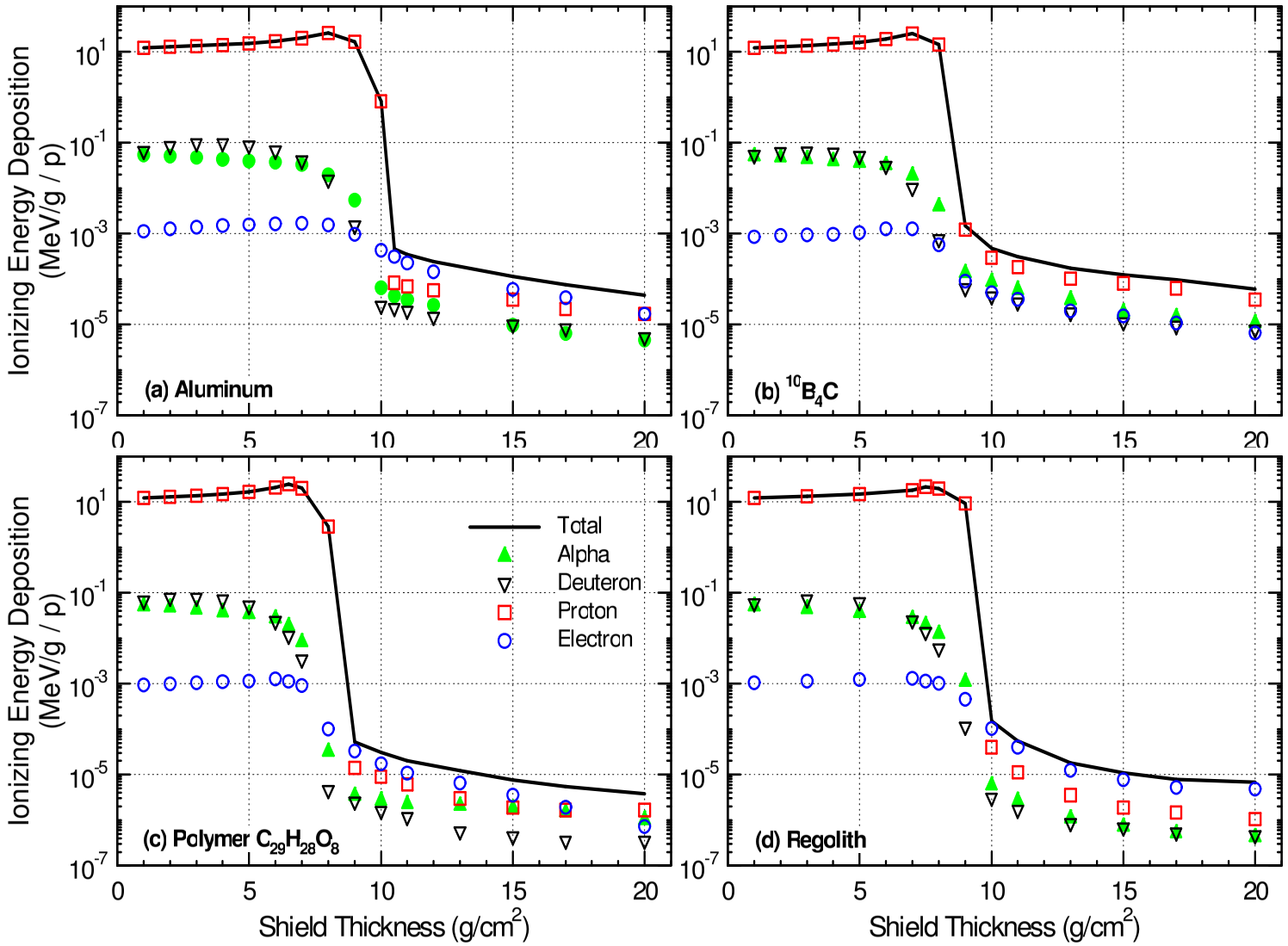

Figure 3.5. Calculated Ionizing Energy Deposition in Silicon with Different Shielding Materials.

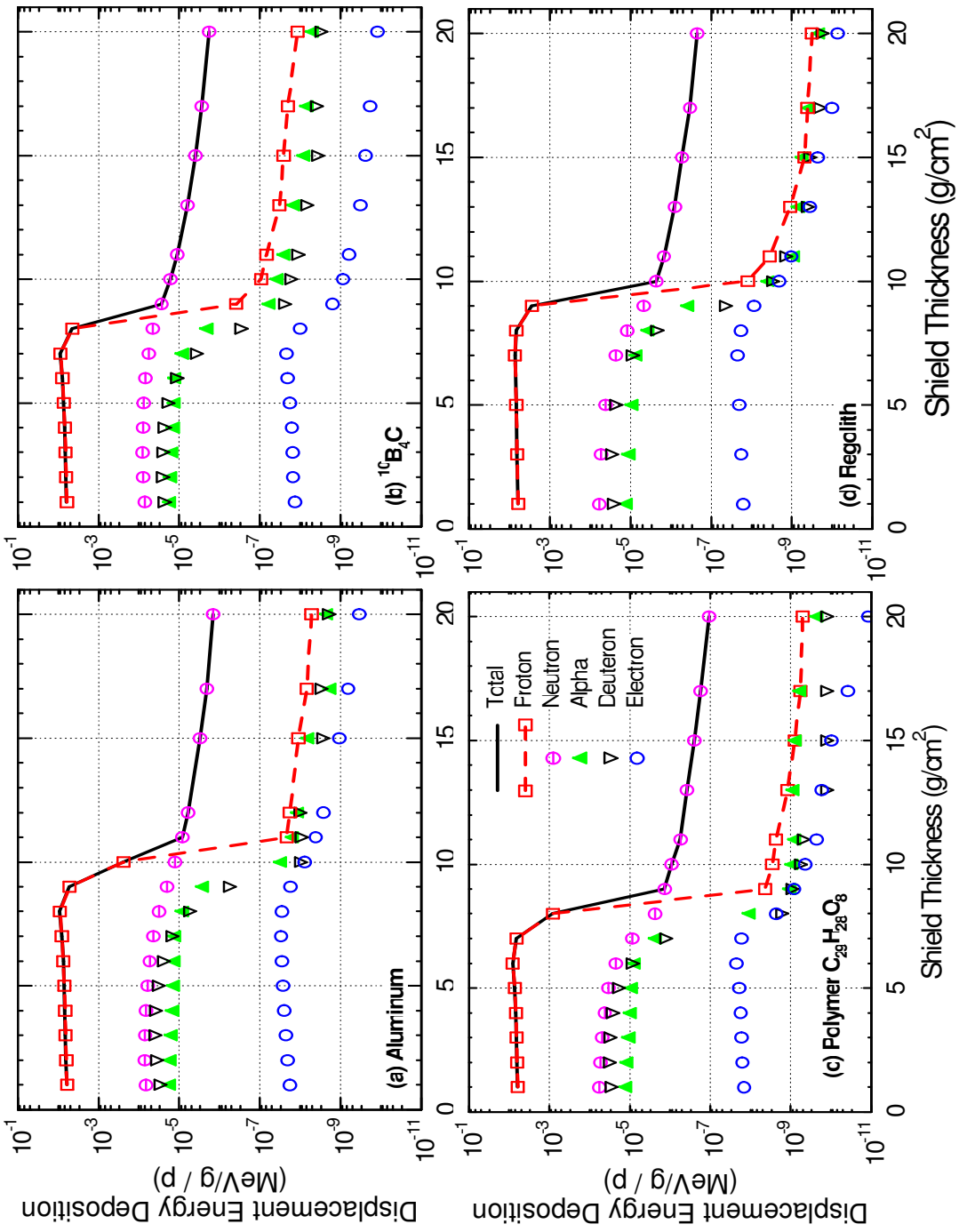

Figure 3.6. Calculated Non-Ionizing or Displacement Damage Energy Deposition in Silicon with Different Shielding Materials.

For aluminum thicknesses < 10 g/cm^2, the displacement energy deposition in the silicon sphere is almost constant and dominated by those due to the primary and secondary protons. The secondary neutrons, deuterons, and alphas contribute ~ 5% of the total displacement energy deposition. With an aluminum shield thickness of 10 g/cm^2, the contribution of the primary protons to the total displacement energy deposition drops precipitously, becoming infinitesimally small, while the secondary neutrons become the primary contributor to the displacement energy deposition. The combined total energy deposition in the silicon sphere due to secondary protons, deuterons and alphas is < 5% (Fig. 3.6a).

Figure 6b shows that with $^{10}B_4C$ shield thicknesses < 8 g/cm^2, protons dominate the total displacement energy deposition in the silicon sphere. This thickness is 20% lower than the threshold thickness for aluminum (10 g/cm^2); this is likely because the lighter nuclei in B_4C gain higher energy per collision by the incident protons. The contributions of the secondary neutrons, deuterons, electrons and alphas are similar to if not slightly higher than those with the aluminum shield. Though $^{10}B_4C$ is considered because of the high absorption cross-section of ^{10}B for thermalized neutrons, the secondary neutrons are not moderated enough to take advantage of this cross section. However, the smaller atomic weights of Boron and Carbon in B_4C have been a factor in reducing the threshold thickness for shielding the incident high-energy protons.

The $C_{29}H_{28}O_8$ polymer is a promising shielding material. The calculated displacement energy deposition due to the secondary neutrons, deuterons, and alphas in the silicon sphere, are all smaller (Fig. 3.6c) than with Aluminum and $^{10}B_4C$ shields (Figs. 3.6a and 3.6b). For polymer thicknesses > 9 g/cm^2, the contribution of the protons to the displacement energy deposition in the silicon sphere is negligible and the contributions due to the secondary neutron, deuterons, alphas, and electrons are about two orders of magnitude lower than with aluminum, $^{10}B_4C$, and the lunar regolith shields.

With lunar regolith (1.2 g/cm^3) shield thicknesses < 9 g/cm^2 (Fig. 3.6d), the primary protons dominate the total displacement energy deposition in the silicon sphere. With thicknesses > 10 g/cm^2, the secondary neutrons are the primary contributor to the total displacement energy deposition, and the combined contribution of the protons and secondary deuterons and alphas is insignificantly small (Fig. 3.6d).

Shielding monoenergetic 100-MeV protons requires a thickness larger than the determined threshold for the different materials: 10 g/cm^2 of Aluminum and Regolith and 8 g/cm^2 and 7 g/cm^2 of $^{10}B_4C$ and $C_{29}H_{28}O_8$ polymer. The required thickness of $C_{29}H_{28}O_8$ polymer is the smallest, and the total displacement energy deposition in the silicon sphere is the lowest. The calculated values of the total energy deposition with $C_{29}H_{28}O_8$ polymer and regolith shielding are about two orders of magnitude lower than with aluminum and $^{10}B_4C$ shields (Figs. 3.6a – 3.6d).

3.5.4 Shielding Effectiveness

The shield effectiveness for the different materials investigated is defined as: $(1 – D/D_o)$. The calculated total displacement energy deposition in the silicon sphere and the corresponding effectiveness of all four shielding materials investigated are compared in Figures 3.7a – 3.7b. Up to the threshold thicknesses of these shield materials, there is a net increase in the total displacement energy deposition in the silicon sphere (Fig. 3.7a), or a decrease in the shielding effectiveness (Fig. 3.7b). Such a decrease in the shielding effectiveness is a direct result of the spallation reactions of the primary protons with the nuclei of the target materials and the contribution of the low energy protons. For the four materials investigated, the shielding effectiveness becomes negative because of the production of the secondary particles, up to the threshold thicknesses. The threshold thickness is directly related to the increase in the total displacement energy deposition in the silicon sphere in Figure 7a. Aluminum has the lowest shielding effectiveness of approximately - 50%, followed by that of enriched B_4C at approximately - 45%, the polymer $C_{29}H_{28}O_8$ at approximately - 40%, and finally the regolith with a shielding effectiveness of approximately - 25%. These values of the shielding effectiveness correspond to the threshold thicknesses of 8 g/cm^2 for aluminum, 7 g/cm^2 for enriched B_4C, 6.5 g/cm^2 for the polymer $C_{29}H_{28}O_8$, and 7.5 g/cm^2 for the regolith.

Figure 3.8a and 3.8b compare the calculated total ionizing energy depositions in the silicon sphere and the corresponding effectiveness of the shielding materials. Similar to the results of the total displacement energy depositions, aluminum results in the highest ionizing energy deposition and has the lowest effectiveness of approximately -120%; followed by effectiveness of enriched B_4C at approximately -110%, effectiveness

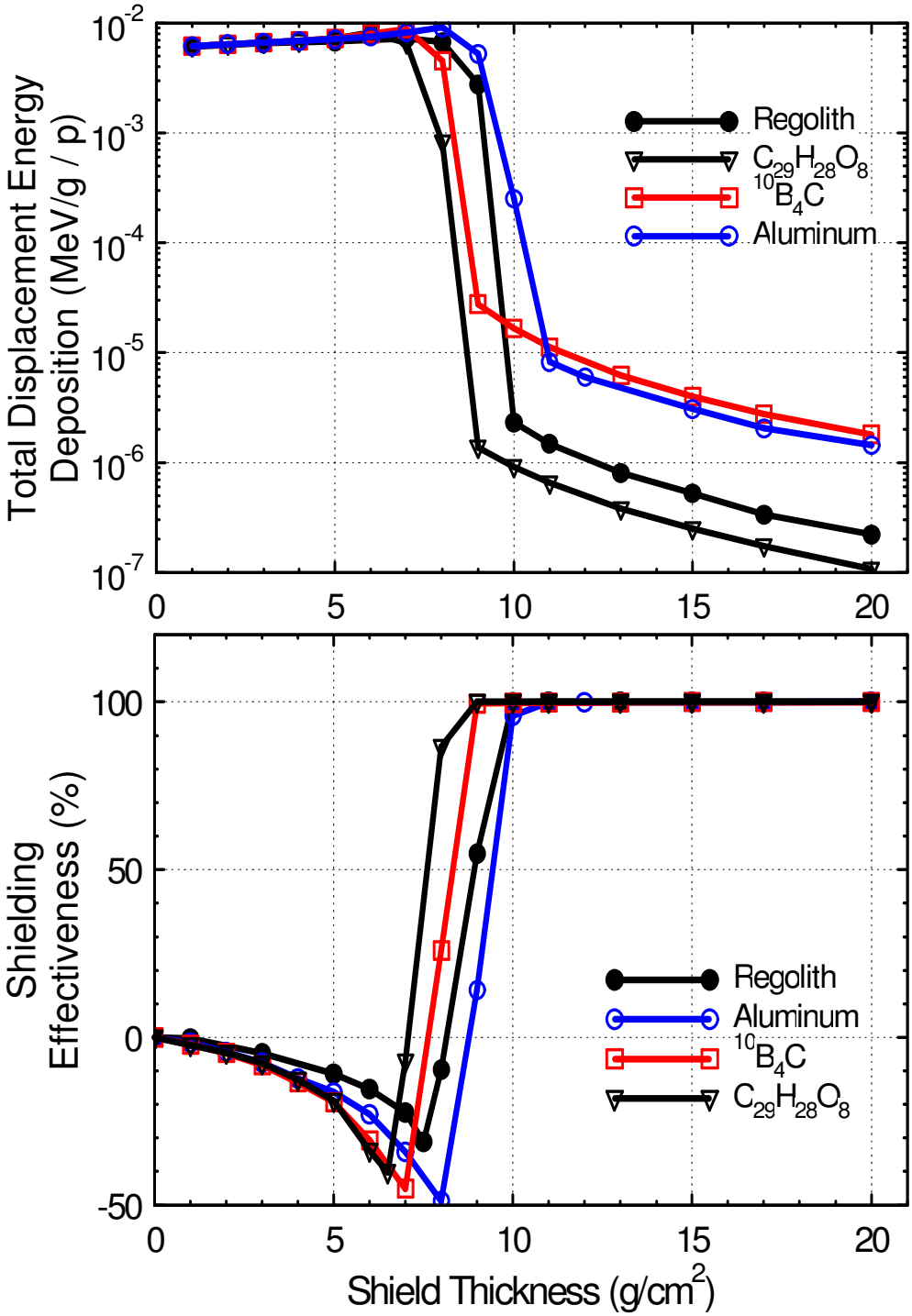

Figure 3.7. Calculated Total Displacement Energy Deposition in Silicon and Effectiveness of Different Shielding Materials.

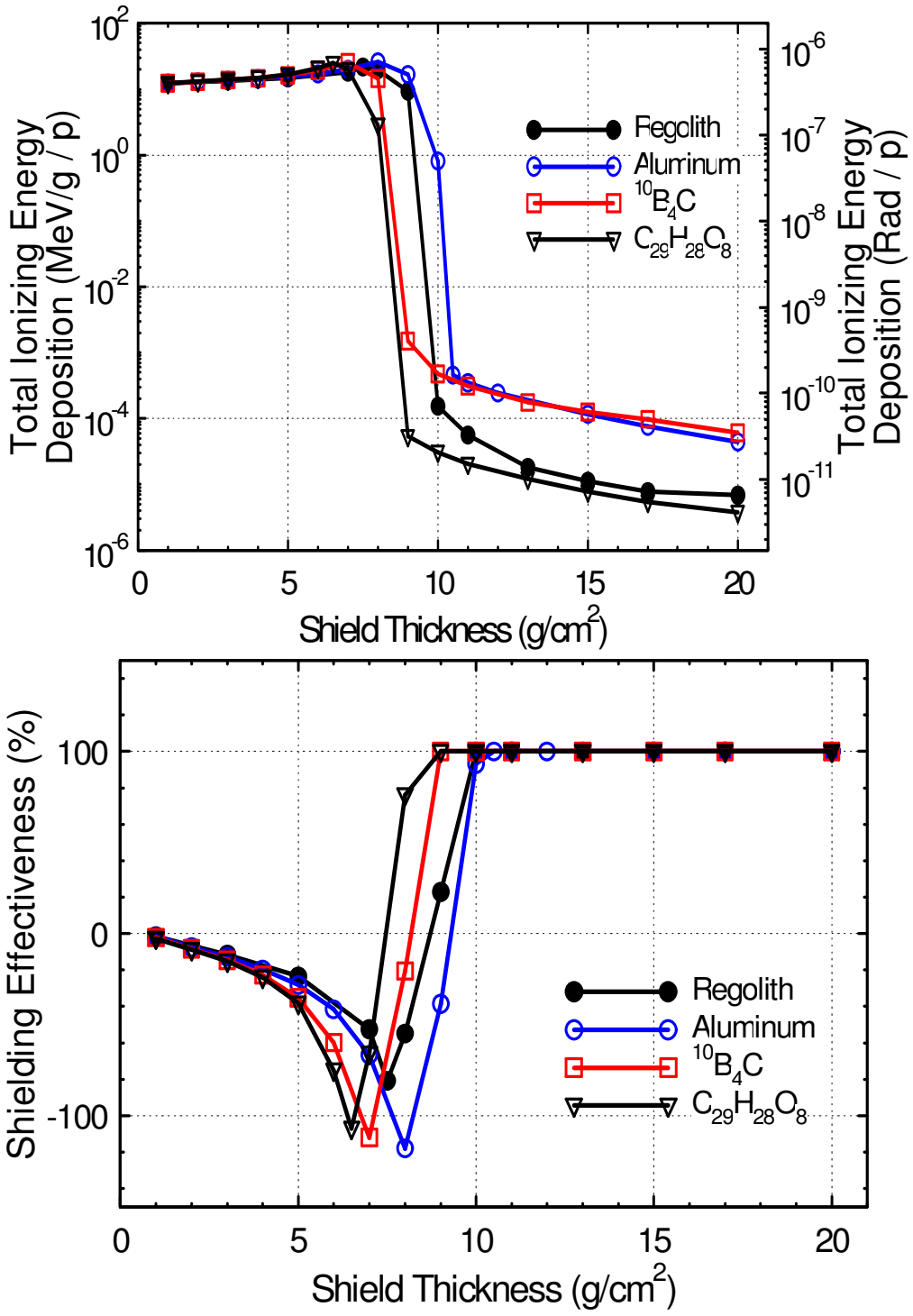

Figure 3.8. Calculated Total Ionizing Energy Deposition in Silicon and Effectiveness of Different Shield Materials.

of $C_{29}H_{28}O_8$ polymer, of approximately -105%, and effectiveness of regolith of approximately -80%. These larger decreases in the shielding effectiveness are due to the large ionizing energy deposition by the low energy protons. Figure 7b and 8b also show that the quickest decreases in the shield effectiveness with increasing thicknesses are of the $C_{29}H_{28}O_8$ polymer. This is because of the large energy transfers from the primary protons to the light atoms in the polymer, which make it the best material for shielding the incident primary 100 MeV protons. The polymer has the smallest threshold thickness for shielding these protons.

Compared to aluminum, the enriched B_4C, lunar regolith, and the $C_{29}H_{28}O_8$ polymer shield are more effective in reducing the total displacement and ionizing energy deposition in the silicon sphere. The lunar regolith, although not as effective as the polymer resin, is better than aluminum. For spacecraft applications, the $C_{29}H_{28}O_8$ polymer is an attractive shielding option compared to aluminum because of its higher shielding effectiveness. In addition to being light weight, when reinforced with carbon nanotubes, the polymer resin becomes multi-functional. Besides shielding high energy protons, it is a strong and light weight structure material for protection from space debris, and is also effective in reducing electromagnetic interference. For best results (low energy deposition in silicon and shielding effectiveness of about 100%) the shield thickness for the electronic devices should be larger than the threshold values determined in this study for the different shielding materials.

3.6 Summary

The interactions of monoenergetic 100-MeV protons with potential shielding materials of Aluminum, enriched B_4C, polymer $C_{29}H_{28}O_8$, and lunar regolith are investigated using MCNPX 2.5.0. The contributions of the primary and secondary protons, and of the secondary neutrons, deuterons, alphas and electrons to the total energy deposition in 1 cm diameter sphere silicon, representing of an electronic device, are calculated for different thickness of the five shielding materials. The total energy deposition in the silicon sphere, a measure of the potential damage to the electronic devices, is the sum of those due to displacement and ionizing energy losses. The latter is several orders of magnitude higher than the former per incident primary particle.

The primary and secondary protons and the secondary neutrons are the primary contributors to the displacement energy deposition in the silicon sphere. The total contribution of the secondary electrons, deuterons, and alphas particles is ~5% of the total displacement energy deposition. Up to the threshold shield thickness of 10, 8 and 7 g/cm^2 for aluminum and regolith, for B_4C, and for $C_{29}H_{28}O_8$ polymer, respectively, the primary and secondary protons dominate the total displacement energy deposition in the silicon sphere. With larger shield thicknesses, the secondary neutrons are the dominant contributor to the total displacement energy deposition in the silicon sphere. The primary and secondary protons are also the major contributors to the total ionizing energy deposition. With shield materials less than the calculated threshold thicknesses, the contribution of the secondary electrons, deuterons and alphas particles are minimal compared to that of the protons.

The $C_{29}H_{28}O_8$ polymer and the lunar regolith are better materials than aluminum for shielding electronic devices from high energy protons. The light atoms of the polymer are effective in slowing down the primary protons and reducing the amount of secondary particles generated by spallation reactions. The threshold thickness of this material for shielding the primary protons represents a mass saving of about ~2 g/cm^2, compared with aluminum. However, a polymer thickness of 8 g/cm^2 correspond to twice the thickness and about nine time the volume of 10 g/cm^2 thick aluminum. Second, the radiation effects on the polymer are not well established [Rodriguez et. al. 2006]. The large energy transfer to the lattice atoms and the knock out of the hydrogen atoms in the polymer could change its characteristic and structural integrity.

The oxygen in the lunar regolith reduces the generated secondary particles and lowers the total energy deposition in the silicon sphere, compared to aluminum. Though not as effective as the polymer resin in shielding high energy protons, the regolith is abundant on the lunar surface. With enriched B_4C shield, the total energy deposition in the silicon sphere is higher than with either the lunar regolith or the polymer, but lower than with aluminum. The threshold thickness of the B_4C shield represents a mass saving of 1 – 2 g/cm^2 compared to Aluminum. The regolith is an effective shielding material for lunar outpost applications; while the $C_{29}H_{28}O_8$ polymer is best for protecting electronics from incident high-energy protons in spacecraft for future space exploration missions.

4. INVESTIGATION OF DOSE ESTIMATES INSIDE A SPACE STATION USING SOLAR PROTONS SPECTRUM

This section investigates the interaction of energetic solar protons measured by the Geostationary Operational Environmental Satellites (GOES), with the aluminum shielding structure of different thicknesses and calculates the dose distribution inside an tissue equivalent phantom inside the aluminum structure. In addition to the incident energetic protons, the major contributors to the total dose inside the phantom are the secondary protons and neutrons generated by spallation reactions in the aluminum structure and the phantom. Three modes of incidence of source protons are considered: center seeking, planar, and isotropic.

4.1 Introduction

Human space flight face significant hazard from natural space radiation of energetic electrons, protons, heavy charged particles, and Galactic Cosmic rays (GCR) [Wilson 2000; Wilson et al. 2001; Wilson et al. 2004]. Energetic protons make up over 85% of Solar Energetic Particles (SEP) and GCR and having energies ranging between ten's of MeV up to a GeV. Thus, they represent the greatest threat due to both it energy and intensity for mission in earth orbit such as in the International Space Station.The Energetic heavy nuclei could cause larger radiation damage due to their high Z and high energy, though their flux intensity is typically very low precluding them in the Dose estimates in shorter duration mission [Wilson et al. 2001; Wilson et al. 2004].

Solar protons monthly average flux measured by Geostationary Operational Environmental Satellites (GOES) for the months of November and December, 2010, and January, February and March, 2011 together with the fitted spectrum for the presented data are presented in Fig. 4.1 [NNDC, GOES]. The data in this figure show that the low energy protons E<10 MeV dominates, which could be easily attenuated and mitigated with thin aluminum shielded structure. The flux of the high energy protons is about three orders of magnitude lower, but with protons energy in excess of 500 MeV. These high energy protons could potentially deliver a significant dose to biological body or human inside the spacecraft structure.

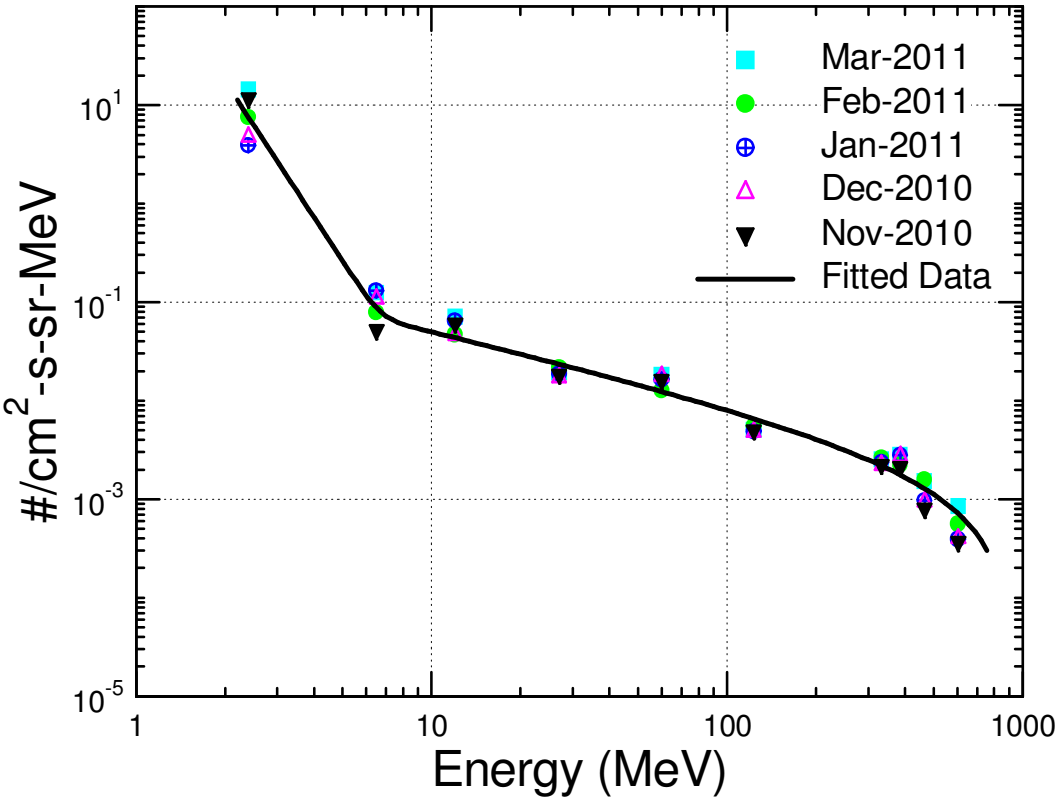

Figure 4.1. Solar protons average monthly measurements by GOES-13 and GOES-15 satellites [NNDC, GOES].

The high energy protons are highly penetrative and interact primarily through spallation collisions with atomic nuclei of the target materials. Such collisions by spallation reactions generate large numbers of secondary radiation such as protons, neutrons, gamma photons, deuterons, and alphas. The fluences of the secondary neutrons and protons could be higher than that of the incident high energy protons, and increase the complexity of the radiation interaction and resulting radiation dose [Wilson et al. 2001; Saganti et al. 2002].

The high energy secondary particles interact with molecules of living tissues, strip away electrons and generate charged radicals, which cause adverse changes in the chemistry of the tissue cells [Wilson 2000]. The high energy secondary protons and neutrons from the interaction of incident high energy protons with the aluminum shield structure further increases the biological dose.

Depending on the energy of the secondary particles and mode of incidence, secondary particles generated by the spallation reactions within the phantom strongly affect not only the dose values but also spatial distribution in the phantom. The dose values at the surface could be comparable or much higher than inside the phantom [Machrafi et al. 2009]. Therefore, it is important to characterize the contributions of the secondary particles to the values and spatial distribution of the biological dose inside the phantom as well as the effectiveness of the aluminum shield structure of different thicknesses.

The objectives of this work are to (a) investigate the interaction of the measured solar protons spectrum (Fig. 4.1) with the spacecraft aluminum shield structure and (b) calculate the values and spatial distributions of biological dose in a spherical tissue phantom, simulating an astronaut inside the spacecraft. The calculated dose estimates inside and at surface of the phantom are for aluminum structure thicknesses of 10.5 g/cm^2 and 14 g/cm^2 and three different incidence modes of source protons onto the spherical spacecraft: center seeking, isotropic, and planar. The spherical phantom is located concentric with the spacecraft structure.

4.2 Problem Setup and Methodology

As shown in Figure 4.2, the spherical aluminum structure with 3 m inner diameter is filled with air. The thickness of the aluminum varied from10.5 g/cm^2 and 14 g/cm^2. A 35 cm diameter phantom with natural tissue composition (see Table 4.1), is concentric with the aluminum structure.

The dose calculations employed a 3-D, general purpose Monte Carlo radiation transport code MCNPX version 2.7C to track the primary and secondary particles throughput the computation domain (Fig. 4.2) [Pelowitz et al. 2010]. This code tracks a wide range of particles including, protons, neutrons, photons, electrons, deuterons, alphas, and pions, as well as their respective anti particles over a wide range of energies. The fluences of the primary and secondary particles inside both the aluminum shield structure and the phantom are all tallied, along with the optional energy depositions in the phantom volume, which contribute to the calculated biological doses.

The normalized particle currents are tallied for both inward and outward passing particles. The results presented in this paper only consider inward normalized particle current passing into the inner volume of the craft, directly impacting dose estimates in the phantom. The spatial dose distribution inside the phantom is calculated using tallies for 5 mm cubical elements of a cubical grid that encloses the spherical phantom. The present MCNPX simulations and dose estimates are performed with 300 millions incident particles on the outer surface of the aluminum structure of the craft.

Three different incidence modes of the source protons on the outer surface of the craft's aluminum structure are considered: center seeking (Fig. 4.2a), isotropic (Fig. 4.2b), and planar (Fig. 4.2c). The base case is that of the most conservative incidence mode and with 10.5 g/cm^2 aluminum shielding thickness.

The effective dose, expressed as the weighted sum of the equivalent dose received by body organs and tissue, is a useful quantity for radiation protection purposes[9]. It is determined based on the fluence and the energy spectrum of the incident particles on the organ or tissue. Thus, the effective dose inside the phantom is calculated as the particle fluence times the fluence-to-dose conversion coefficient of the respective particle type.

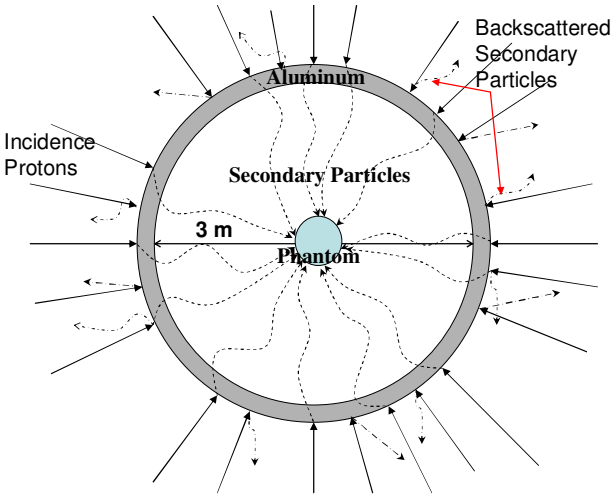

(a) Center-Seeking Incidence Mode

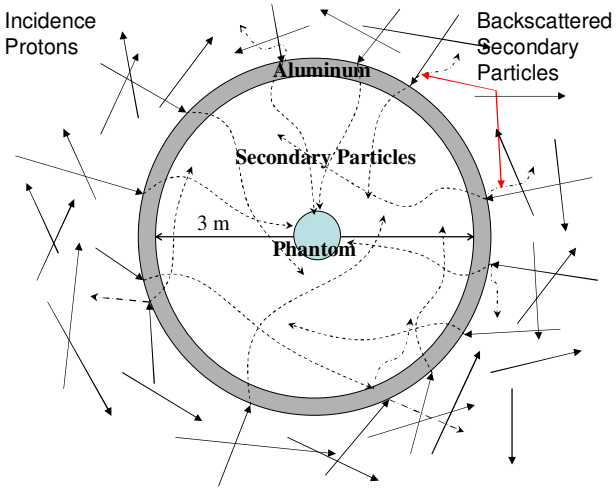

(b) Isotropic Incidence Mode

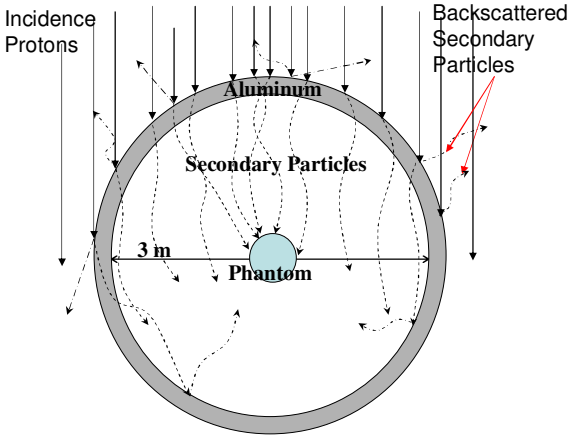

(c) Planar Incidence Mode

Figure 4.2. Schematic of simulated space station with (a) center seeking, (b) Isotropic, and (c) Planar mode of Incidence of source particles.

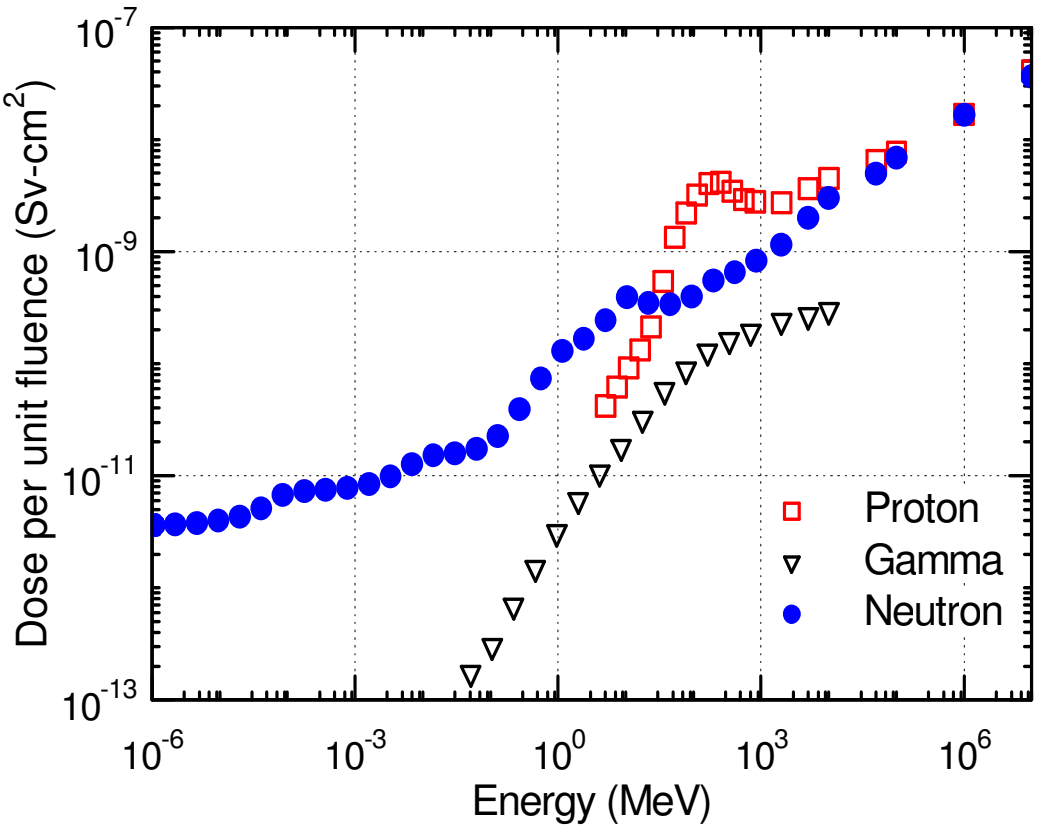

Figure 4.3. Fluence-to-Dose Conversion Coefficients for Protons, Neutrons, and Gamma Photons [Ferrari et al. 1996; Ferrari et al. 1997; Ferrari et al. 1997].

Table 4.1. Tissue Composition for Dose Estimates

Elements	Atom %	Elements	Atom %
H	63.045	C	11.759
O	23.960	N	1.080
Na	0.030	P	0.026
S	0.038	Cl	0.023
K	0.031	Ca	0.008

Figure 4.3 plots the fluence-to-dose conversion coefficients for protons, neutrons and gammas as a function of energy. The conversion coefficient for neutrons cover a range of energies up to 10 TeV, while the coefficients for protons cover energies from 5 MeV to 10 TeV [Ferrari et al. 1997; Ferrari et al. 1997]. The coefficients for gamma photons cover an energy range from 50 keV to GeV, much wider than the energy range of the secondary gamma photons within the present dose simulation [Ferrari et al. 1996].

4.3 Results and Discussion

The low energy protons of the measured solar protons spectrum by the GOES satellites (Fig. 4.1) incident on the outer surface of the aluminum structure were easily stopped, while the higher energy protons penetrated past the aluminum structure and into the phantom (Fig. 4.2).

Figure 4.4 compares the primary protons and calculated secondary particles and photons generated by the spallation reactions of incident protons in 10.5 g/cm^2 thick aluminum structure, assuming a center seeking incidence mode. The elimination of the low energy protons reduces the number of primary and secondary protons penetrating the aluminum structure, by almost an order of magnitude. The spallation reactions of the high energy protons with aluminum generate large number of secondary particles of alphas, deuterons, neutrons, and gammas photons.

Note that within the aluminum structure, the currents of the secondary neutrons and gamma photons are very close to that the sum of primary and secondary protons. The secondary alphas and deuterons are order of magnitudes smaller and thus neglected in the dose calculations. The sharp decreases in the primary and secondary particles emerging from the inner surface of the aluminum shield are primarily caused by the reduction of the surface area with the concentric spherical geometry investigated (Fig. 4.2a). This effect and the lack of interaction in the air volume separating the aluminum structure from the phantom, cause larger reduction in the number of secondary particles impinging on the phantom outer surface.

The currents of the secondary neutrons and gamma photons increase for some distance inside the phantom before beginning to decrease (Fig. 4.4). For example, their

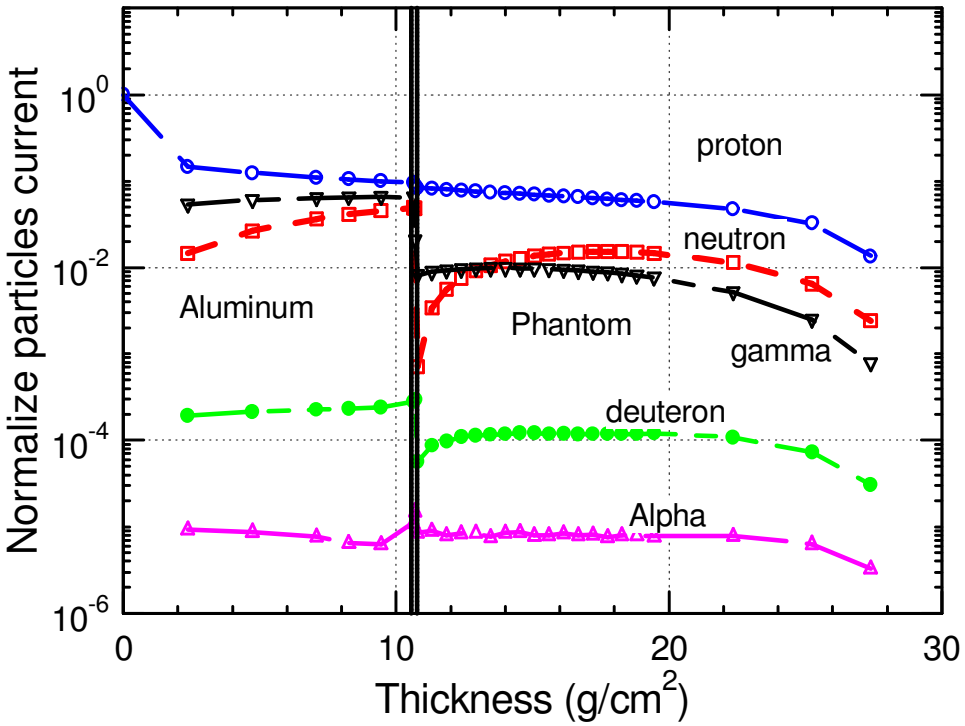

Figure 4.4. Primary and secondary particles for 10.5 g/cm^2 aluminum and center seeking incidence mode.

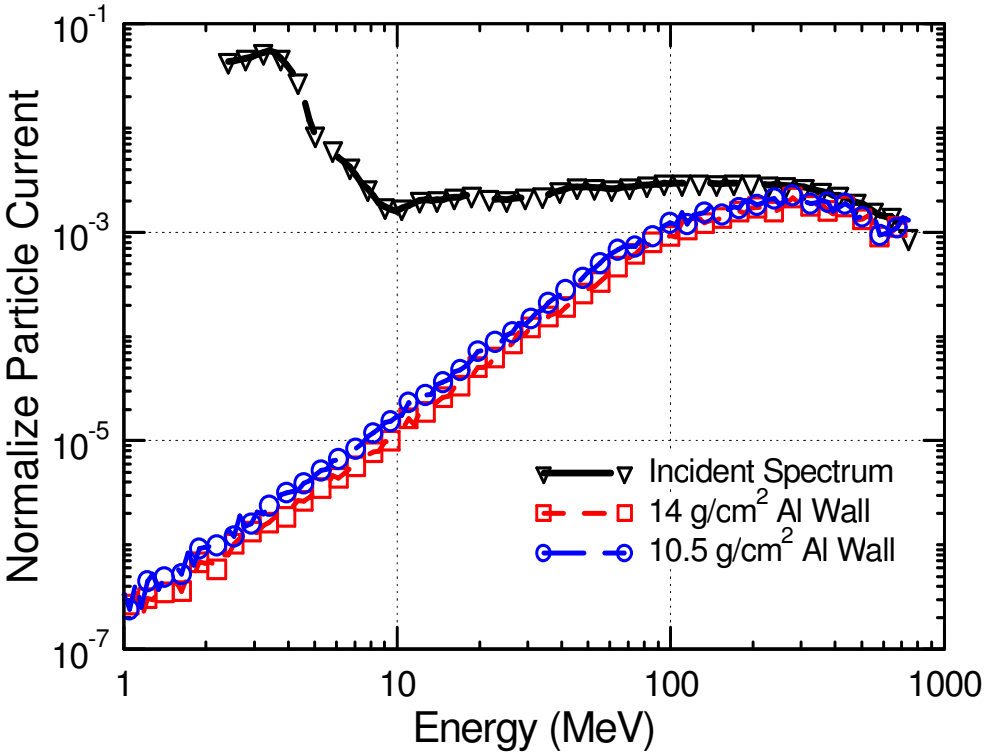

Figure 4.5. Comparison of incident and secondary protons energy spectrums at phantom's outer surface.

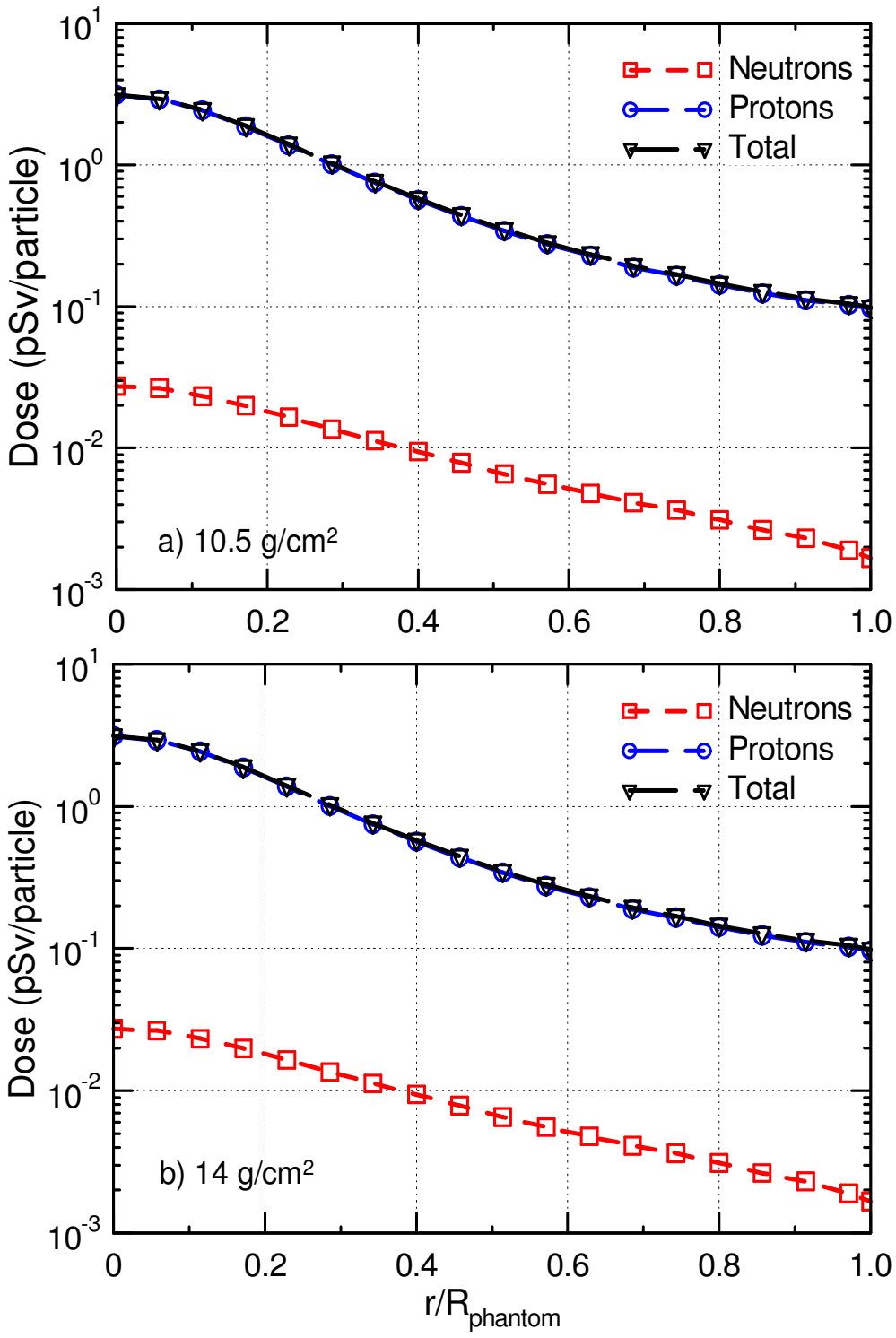

Figure 4.6. Dose spatial distribution inside phantom with center seeking incidence of source protons.

currents at a distance ~4 g/cm^2 inside the phantom are higher than at the surface. Such increases are due to the generation of additional secondary neutrons and photons by the spallation reactions of incident protons with molecules in the phantom (Table 4.1).

This can be seen in Fig. 4.5, which compares the energy spectrums of the incident source protons and secondary protons onto the surface of the phantom, with aluminum structure thicknesses of 10.5 and 14 g/cm^2. As can be seen, the protons energy spectrum at the outer surface of the phantom consists primarily of protons with energies >100 MeV, sufficiently higher than the spallation threshold energy of Oxygen and Carbon (~ 16 MeV and ~20 MeV) [Pham and El-Genk 2009; Chadwick and Young 1997; Kitazawa 2001]. These elements are the primary constituents of the human tissue (Table 4.1).

Figure 4.6 compares the calculated dose values and spatial distribution in the phantom with 10.5 and 14 g/cm^2 thick aluminum structure assuming a center seeking incidence of source protons. The calculated dose values are primarily due to the high energy protons and the secondary neutrons. The latter is about 2 orders of magnitude lower than the former.

The results delineated in Fig. 4.6 also shows that the combined effect of the penetrating high energy protons and increase in number due to the center seeking incidence mode of the source protons produce a distinct spatial dose distribution in the phantom (Fig. 4.6). The penetrating high energy protons and the assumed center seeking incidence mode produce a distinct distribution, where the dose is lowest at the surface of the phantom and monotonically increases with increasing distance from the surface. The results in Fig. 4.6 show that biological dose estimates increase with depth into the phantom, indicating a higher dose would be delivered to the internal organs of a human body.

Figure 4.7 compares the normalized current for protons and neutrons as a function of relative thickness in the aluminum shield structure and the phantom. The results in Figs. 4.7a – 4.7c show the effects of the different incidence modes of the source particles and the thickness of the spacecraft aluminum structure. The precipitous drop in the protons' current in the first few g/cm^2 of aluminum are due to the removal of the low energy protons. Results show that increasing the aluminum structure thickness from 10.5

to 14 g/cm^2 insignificantly decreases the number high energy protons at the surface of the phantom and increases the number of secondary neutrons.

With center seeking incidence mode of source particles (Fig. 4.7a), the number of high energy protons reaching the phantom surface are relatively high, almost all of the particles passing through the aluminum structure inner surface impinge onto the outer surface of the phantom, resulting in a higher dose. However, the secondary neutrons are not center-seeking, thus leads to a larger reduction from the aluminum surface to the phantom surface. The incidence mode of the primary protons strongly affects the currents of the primary and secondary energetic particles at the surface of and within the phantom. Changing from the center seeking (Fig. 4.2a) to isotropic (Fig. 4.2b) and planar (Fig. 4.2c) incidence mode of primary particles reduces the number protons reaching the surface of the phantom. For the planar and isotropic incidence modes, the current of the high energy protons reaching the surface of the phantom is ~ 2 orders of magnitudes lower than those passing through the aluminum shield structure.

Figure 4.8a and 4.8b compares the calculated dose values and spatial distributions inside the phantom for all three mode of incidence of primary protons, normalize to the 10.5 g/cm^2 thick aluminum structure. The center seeking incidence mode of source protons is the most conservative, resulting in the highest dose values. Increasing the aluminum thickness to 14 g/cm^2 decreases the total dose very little, to ~10% at the phantom surface and ~20% inside the phantom. For the planar and isotropic modes, the normalized total dose at the surface of the phantom are only ~2% and ~0.2% of those for the center seeking incidence mode and ~0.02% and 0.002% at the phantom center, respectively, (Fig. 4.8a).

With center-seeking incidence of primary protons, the dose at the center of the phantom is approximately 10 times that at the phantom surface. With isotropic and planar incidence modes of the primary particles, the normalized total dose estimates at the surface and inside the phantom are reduced significantly. This is mostly due to the decrease in the total number of the protons reaching the surface of the phantom. For these two incidence modes of the primary protons, the calculated dose values are not only significantly lower but also almost constant throughout the phantom.

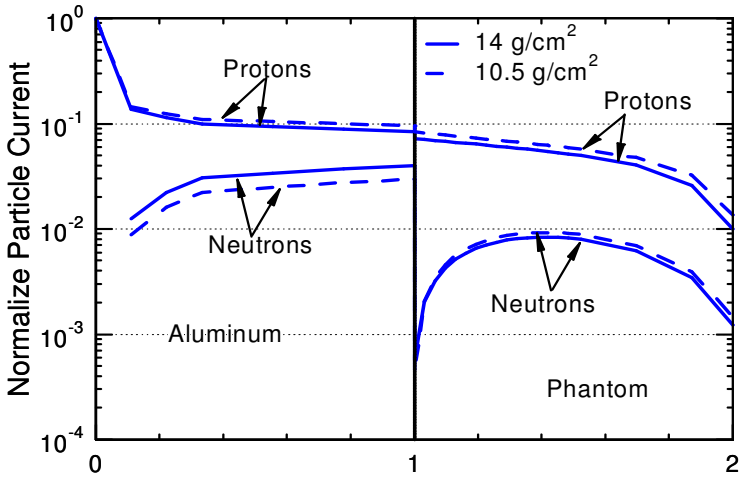

(a) Center Seeking Incidence of Source Particles

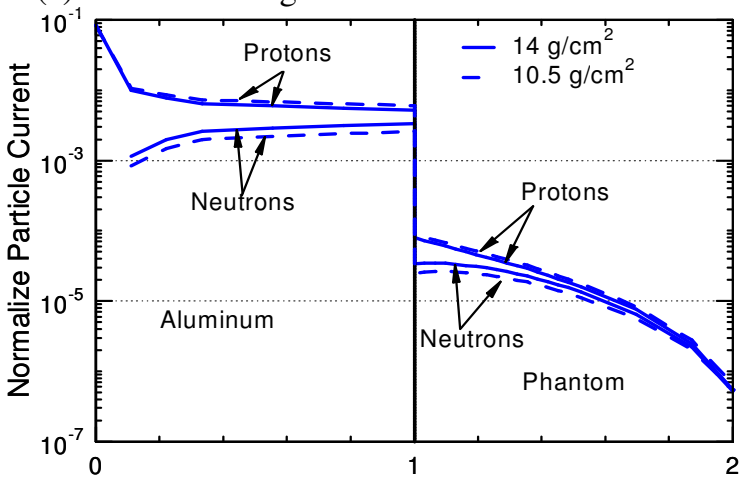

(b) Isotropic Incidence of Source Particles

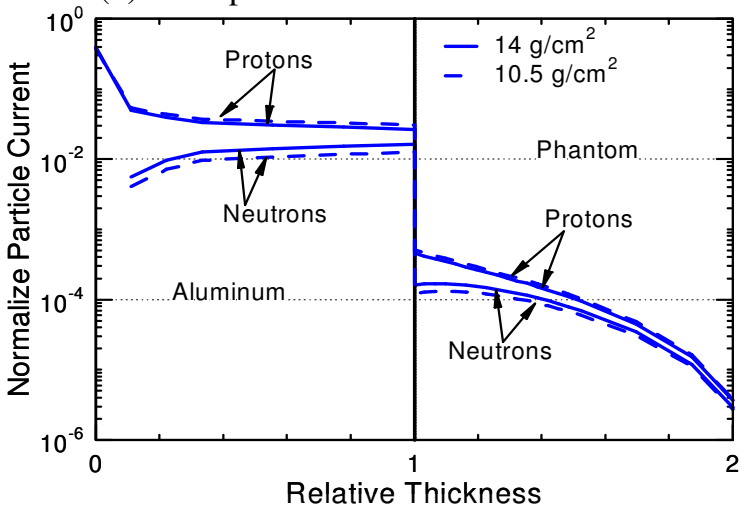

(c) Planar Incidence of Source Particles

Figure 4.7. Calculated Currents of primary and secondary protons and secondary neutrons within aluminum structure and phantom.

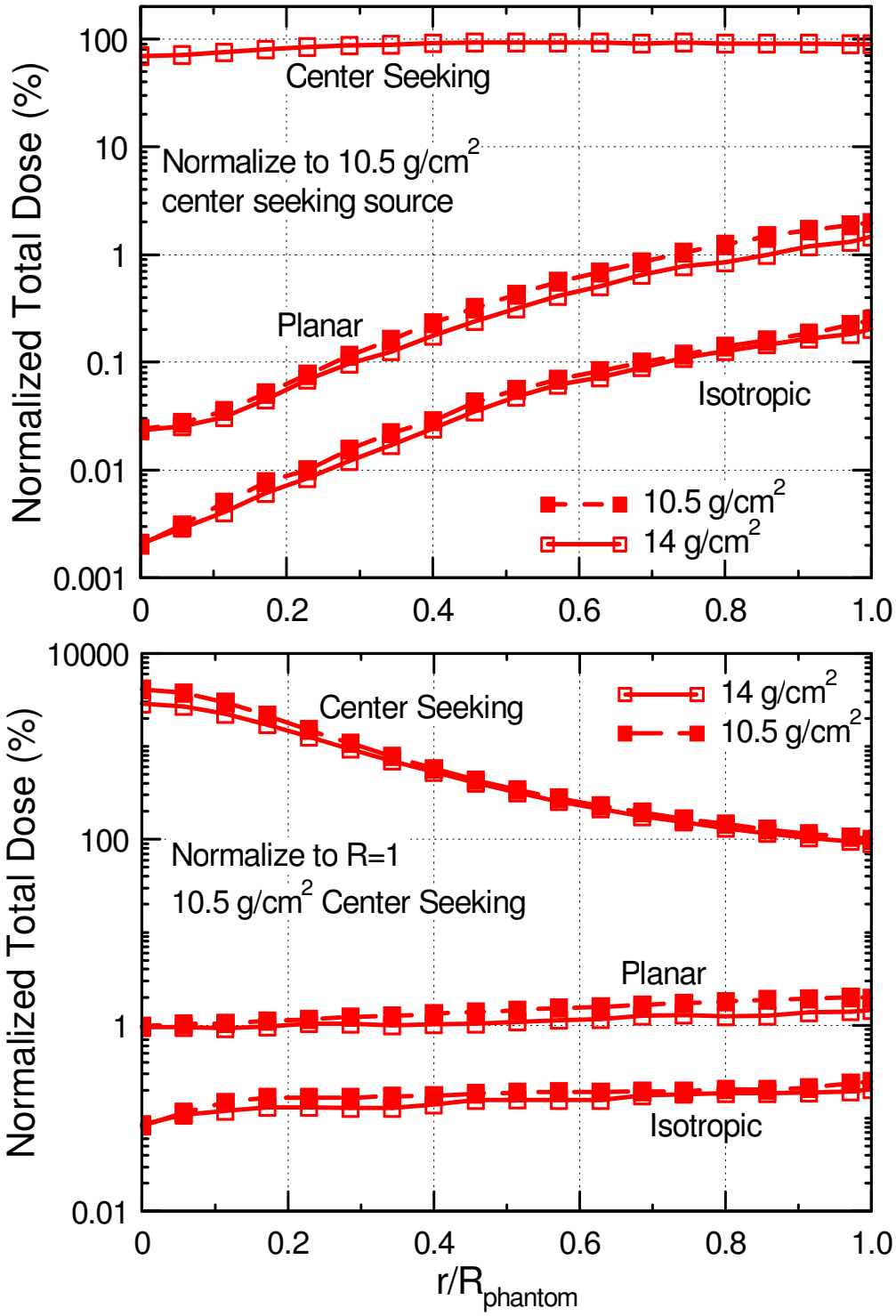

Figure 4.8. Normalized total dose distribution inside phantom for center seeking, planar, and isotropic incidence modes of source protons.

Conversely, with the center-seeking incidence mode, the calculated dose of almost 2 orders of magnitude higher and increase with distance into the phantom.

4.4 Summary

Investigated is the interaction of energetic solar protons measured by the Geostationary Operational Environmental Satellites (GOES), with spacecraft aluminum structure. The present analysis also calculated the dose distribution inside a tissue equivalent phantom concentric with the spherical aluminum structure. Results show the major contributors to the total dose inside the phantom are the secondary protons and neutrons generated by spallation reactions in the aluminum structure and the phantom. Three modes of incidence of source protons on the aluminum structure are considered: center seeking, isotropic, and planar. The center seeking mode is the most conservative, resulting in the highest dose values that increase with distance inside the phantom. Both the planar and isotropic incidence modes result in much lower dose values that are more evenly distributed throughout the phantom.

Increasing the aluminum thickness from 10.5 g/cm^2 to 14 g/cm^2 only slightly affects the overall protons energy spectrum inside the aluminum structure and reduces slightly the overall dose inside and at the surface of the phantom. Future work aims at comparing dose estimates with measurements on board the international Space Station.

5. DOSE ESTIMATES INSIDE A LUNAR SHELTER

For long duration missions on the lunar surface (months to a year) a radiation shelter is needed for dose mitigation and emergency protection in case of solar events. This chapter investigates the interaction of source protons of solar events like those of February 1956 that emitted many fewer particles with energies up to 1000 MeV and of the October 1989 event of lower protons energy but higher fluence, with the lunar regolith and aluminum shielding of a lunar shelter. The shielding thicknesses to reduce the dose solely due to solar protons in the lunar shelter below those recommended by NASA to astronauts for 30 day-operation in space (250 mSv) and for radiation workers (50 mSv) are determined and compared.

5.1 Introduction

Returning to the Moon and establishing lunar settlements are expected within the next 20-30 years. Beyond the protective shelter of the Earth atmosphere, the natural space radiation of Galactic Cosmic Radiation (GCR) and Solar Energetic Protons (SEPs) poses significant risk. The GCR, which include heavy atoms such as Iron, is the most penetrating and highest in energy [Badhwar and O'neill 1996; Wilson et. al. 2004]. Depending on the solar cycle and activity, the intensity of the GCR varies between 1 and 2.5 particles per cm^2- s [Wilson et. al. 2004]. Despite this low intensity, on a long duration mission or stay on the moon, GCR could deliver a career limiting dose, but is not a concern for short duration missions. Large solar events are rare, though several occurred in close succession in 1989, raising the safety concerns for future space operation [Shea and Smart 1990; Sauer et. al. 1990]. Solar Energetic Particles (SEPs) are primarily protons, electrons and alphas (helium nuclei), plus small amounts of heavier elements (< 1%). Protons contribute over 80% of the total mass ejections of a solar event [Shea and Smart 1990; Sauer et. al. 1990], and their energy range is between ten's of MeV to a GeV, with fluence up to 10^{11} particles per cm^2 (Fig. 2.4). The October 1989 event produced the greatest amount of protons, while the February 1956 emitted many fewer particles than the October 1989 and July 1972 events, but had a higher concentration of protons with energies E > 200 MeV and up to a GeV (Fig. 2.4).

Numerous studies have been reported on the characterization and modeling of the Moon radiation environment and of the deep space environments for future human exploration missions [Wilson 2000; Wilson et al. 2004; Tripathi et al. 2006; DeAngelis et al. 2007]. Though the occurrence of solar energetic events is largely unpredictable, it is directly related to the peak solar activity and a cycle of approximately 11 years. Solar activities are predominant in the years of high sunspots numbers (Fig. 2.5), referred to as solar maxima. In the years of low sunspot numbers, or solar minima, from 1995 - 1997, very few events occurred and the solar protons environment was normally low [Sauer et al. 1990]. The protons flux data from the Geostationary Operational Environment Satellites for a series of events, including those of August, September, and October 1989, are shown in Figure 2.5. The August 1989 event lasted for about 5 days, with the protons flux peaking in the first day then slowly decaying to a nominal level. The September 1989 SEP event lasted for about 3 days, and the protons peak flux occurred in the second day. The October 1989 event came in a series of three main pulses that lasted for a total of about 10 days [Simonsen et al. 1991; Wilson 2000; Wilson et al. 2004; Tripathi et al. 2006; DeAngelis et al. 2007]. While the August 1972 and the February 1956 events only lasted for a few hours each, the shortest was that of February 1956 [Foelsche et al 1974]. Though the October 1989 delivered the largest amount of energetic protons and had the highest fluence of low energy protons (~$7x10^{11}$ cm^{-2}), those of August 1972 and February 1956 delivered large amounts of high energy protons. The February 1956 event contained the most energetic protons with energies up to 1 GeV, but since the estimates were based on indirect measurement, thus may not be as accurate as those of the more recent events in 1989.

5.2 Lunar Environment

The Moon lacks an external dipolar magnetic field, as would be generated by a geodynamo in its core, diminishing the ability to deflect charged solar particles and GCR. The Moon is also void of any substantial atmosphere, which affects the scattering of light from the sun and the visual perception of the crew, by masking the surface terrain features and compromising the ability to judge depth and distances [Taylor 1989]. The lack of magnetic field and a substantial atmosphere also means no protection from space

radiation and no atmospheric friction to slow or burn up micrometeoroids. The poor retention of heat from the sun causes large temperature fluctuations across the lunar surface [Kang et al. 2006]. During a month long lunar day, equatorial temperatures vary from 100 K to 400 K, with a rapid 5 K/hr change from sunrise to sunset [14]. In the polar region, many of the crater floors are in constant shadow with a temperature of ~ 80 K [14]. Thus, for prolonged stay, shelters within the lunar habitats need to adequately protect the inhabitants and equipments.

The lunar surface is composed mostly of fine debris dust and small rocks, referred to as "regolith". The surface terrain is divided into two characteristic regions (Figure 5.1). The smooth darker regions, known as *maria*, account for about 17% of the lunar surface and have uncompacted regolith that is 4 – 5 meters deep. The mare regolith has high concentrations of sulfur, iron, magnesium, calcium, and nickel. The lighter color regions, known as the *highlands*, make up the remaining 83% of the lunar surface and contain regolith that is 10 - 20 meters deep in most places [Papike et al. 1982; Taylor 1989; Kang et al 2006]. The highlands regolith is predominantly composed of Fe and Ti poor rocks [McKay et al. 1994; Kang et al. 2006]. The density and composition of the regolith is just as diverse as the lunar surface terrain, varying with increasing depth from 1.2 g/cm^3 to 1.7 g/cm^3 [McKay et al. 1994; Kang et al. 2006].

The composition of two lunar samples, 14163 from Apollo 14 mission, and 64501 from Apollo 16 mission [Papike et al. 1982], as well as that of the JSC-1 Simulant [McKay et al. 1994; Kang et al. 2006] are compared in Table 5.1. Figure 5.1 shows several of the Apollo landing sites, from which regolith was returned to Earth. The Apollo 14 sample is from the mare region, while that of the Apollo 16 is a highland sample. The carbon, hydrogen, and nitrogen contents in the regolith are almost entirely due to implantations by the solar winds [Papike et al. 1982; McKay et al. 2006]. The potential of the regolith as an effective shielding material is the focus of this paper. The present analysis uses the JSC-1 Simulant to represent the lunar regolith in the shielding calculations (Table 5.1). Preliminary results showed that using the mare and the highland composition had little effect on the results, but would require conducting twice as many calculations.

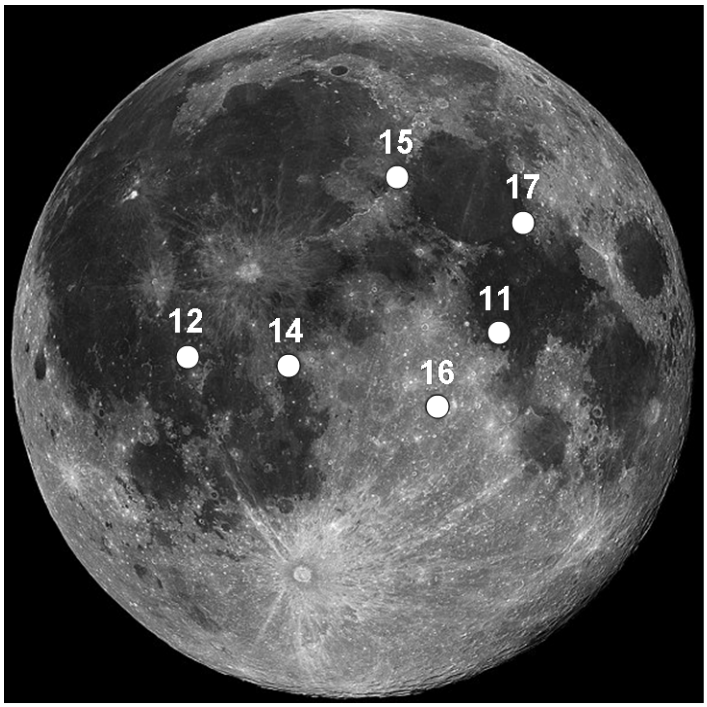

Figure 5.1. Lunar Surface and Apollo Landing Sites [McKay et al. 1994].

Table 5.1. Compositions of the lunar regolith from the Apollo 14 and Apollo 16 missions with JSC Simulant [Papike et al. 1982; McKay et al. 1994].

Material	JSC-1 Simulant (wt %)	Apollo Sample 14163 (wt %)	Apollo Sample 64501 (wt %)
SiO_2	47.71	47.3	45.3
TiO_2	1.59	1.6	0.37
Al_2O_3	15.02	17.8	27.7
Fe_2O_3	3.44	0	0
FeO	7.35	10.5	4.2
MgO	9.01	9.6	4.9
CaO	10.42	11.4	17.2
Na_2O	2.7	0.7	0.44
K_2O	0.82	0.6	0.1
MnO	0.18	0.1	0.056
Cr_2O_3	0.04	0.2	0.09

5.3 Radiation Exposure Limits

Currently, there are not firm recommendations for the radiation exposure limits to human in space travel and future lunar outposts. For planning purposes, however, the limits established for the flight crew in low-Earth orbit (LEO) may be used only as guidelines [Wilson 2000; Wilson et al. 2004; NCRP 2000; NCRP 2006]. The recommended limits for LEO are given as a dose to the skin, blood forming organ (BFO), and ocular lens [8]. They are divided into short term exposure (30-day), annual exposure, and total career exposure (Table 2.1). The recommendations in Table 2.1 are based upon a 3% lifetime excess fatal cancer risk, comparable to the fatal risk of moderately safe occupations [Wilson et al. 2004; NCRP 2000]. For the Solar Energetic Protons, not considering detailed body geometry, the computed BFO dose is often taken to be that for the whole body exposure.

Earlier mission profiles to the Moon call for a 3 days trip from Earth, with 30 days stay on the surface, eventually extending to 6 - 12 months [NASA 2004; NCRP 2006]. For a relatively short stay, the most important radiation hazard is a large solar protons event. Without an adequately shielded lunar shelter, a major solar event similar to those in Figure 2.4 could potentially deliver a dose greatly exceeding the NASA's 30-day exposure limit of 250 mSv (Table 2.1) for the astronauts. Therefore, effective shielding of a lunar shelter is needed to reduce such a dose to an acceptable level during a solar event. The required shielding thickness material depends on the type and composition of the material and the fluence, energy, and the spectral incidence of the energetic protons.

5.4 Shielding Materials

The desirable shielding material effectively attenuates the high energy primary protons and the secondary particles produced by the interactions of the primary protons with the nuclei of the material, resulting in an acceptable dose within the lunar shelter. In general, high hydrogen content materials, such as water or polyethylene, are good shielding materials, particularly for neutrons [Sato et al. 2004; Pham and El-Genk 2006]. However, water is a consumable that would deplete over time, needs special structure to contain and may raise issues of corrosion and potential freezing. A good choice is a

light-weight material that could be used both for structural support and shielding. In a recent study [Pham and El-Genk 2006], aluminum, enriched B_4C, and $C_{29}H_{28}O_8$ polymer have been investigated for shielding mono-energetic (E = 100 MeV) protons; aluminum is the standard structure and shielding material for spacecraft [Wilson et al. 2001; Sato et al. 2004]. The interaction of 100 Mev mono-energetic protons with these materials is mostly by spallation reactions [Pham and El-Genk 2006], generating large quantities of secondary protons, neutrons, gammas, deuterons, alphas, etc., increasing the dose beyond that due to the primary particles alone. Results showed that ~10 g/cm^2 of aluminum reduces the primary and secondary protons to a negligible level. Beyond such a thickness, the primary contributor to the dose is the secondary neutrons. Other secondary particles such as gammas, deuterons and alphas contribute minimally to the dose.

B_4C, considered for it high neutron cross-section, was counterproductive because the high secondary neutrons increased the dose estimate. The polymer was most promising due to it high hydrogen content, but because of the high glass (or Ductile-to-Brittle Transition (DBTT)) temperature it could not be used for structure on the lunar surface. Lighter flexible materials such as Kevlar and Vectran, usually fiber strung, are being considered for supporting structure of an inflatable habitat [NASA 2004]. Inflatable habitats, currently in the testing phase, would require a shelter to protect inhabitants during a major solar event. In any case, the polymer and aluminum would be brought from Earth, adding to the launch and mission cost, thus using lunar regolith for shielding the shelter represents significant saving in the launch and mission cost.

This chapter investigates the interactions of high energy protons from solar events like those of the February 1956 and October 1989, with aluminum and lunar regolith shielding of a lunar shelter. Although it has low protons intensity and may not be as accurately measured as the October 1989 spectrum, the February 1956 event apparently included protons with energy up to 1000 MeV (Fig. 2.4). Thus, the February 1956 event is considered to demonstrate the contribution of energetic protons (E > 100 MeV), and the 1989 event is considered to assess the contribution of the high fluence of low energy protons (E < 100 MeV). The dose estimates inside a representative lunar shelter are calculated as a function of the type and thicknesses of the shielding materials, as well as the incidence mode of the source protons. The spatial distributions of the estimated dose

inside the shelter are calculated for three different incidence modes of the primary protons on the outer surface of the shelter shielding: center seeking, planar and isotropic (Fig. 5.2). Also calculated is the shield thickness required to reduce the dose in the shelter to those recommended for 30-day operation in LEO (250 mSv) by NASA, and for radiation workers (50 mSv).

5.5 Approach and Methodology

For long duration human missions on the lunar surface (months to a year) a radiation shelter is needed for dose mitigation and emergency protection in case of solar events. This study investigates the interaction of SEPs with energy spectra like those of the February 1956 and October 1989 events (Fig. 2.4) with lunar regolith and aluminum shields and calculates the effective dose inside a shielded semi-cylindrical lunar shelter module (Fig. 5.2). The February 1956 event emitted many fewer particles with energies up to 1000 MeV, while the October 1989 event had higher particle fluence but lower protons energy. The shelter has an inner diameter of 5 m, a footprint of 5 x 8 m, and a 10 cm thick aluminum support frame [Colborn et al. 1995; Wilson et al. 2001; Sato et al. 2004], however, the actual thickness would depend on the amount of regolith piled on top, and could be as little as 1 – 2 cm. In the future, using a support frame made of indigence materials would save the cost of bringing aluminum from Earth. The thicknesses of the shielding materials to reduce the dose inside the lunar shelter below the NASA recommended 30-days operation limit for astronauts in LEO (250 mSv) (Table 2.1) and that recommended for nuclear workers in any given year (50 mSv) are calculated. The semi-cylindrical shelter is erected on a planar surface extending 30 m and is 5 m deep. The density of the planar regolith is assumed 1.7 g/cm^3, while that of the uncompacted regolith shielding is assumed 1.2 g/cm^3.

The present dose and shielding calculations used the three-dimensional, general purpose Monte Carlo radiation transport code, MCNPX version 2.6C [Pelowitz 1997]. It tracks the primary protons and the secondary protons, neutrons, gammas, deuterons, alphas particles and pions, within the shielding material and the aluminum support structure of the lunar shelter. The code also tracks secondary particles backscattered

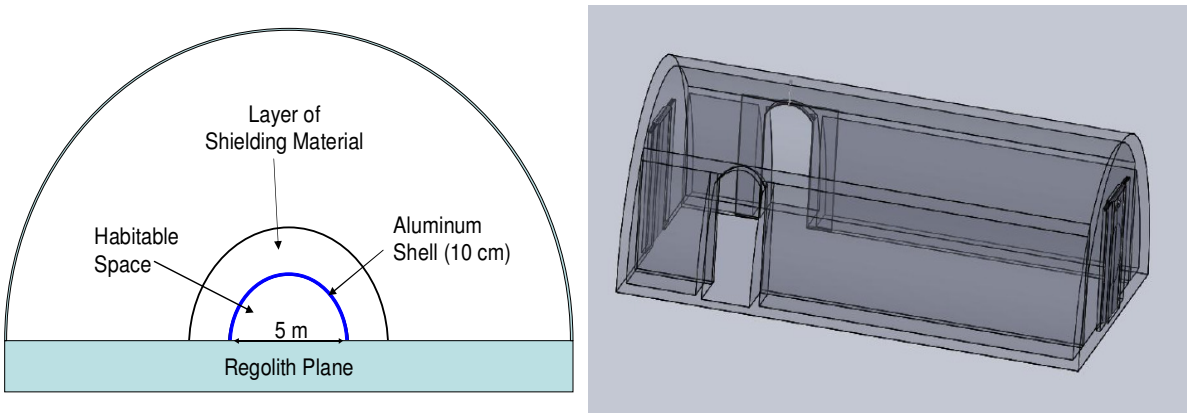

(a) Schematic (b) Isometric View

Figure 5.2. Lunar Habitat Schematic and an Isometric View.

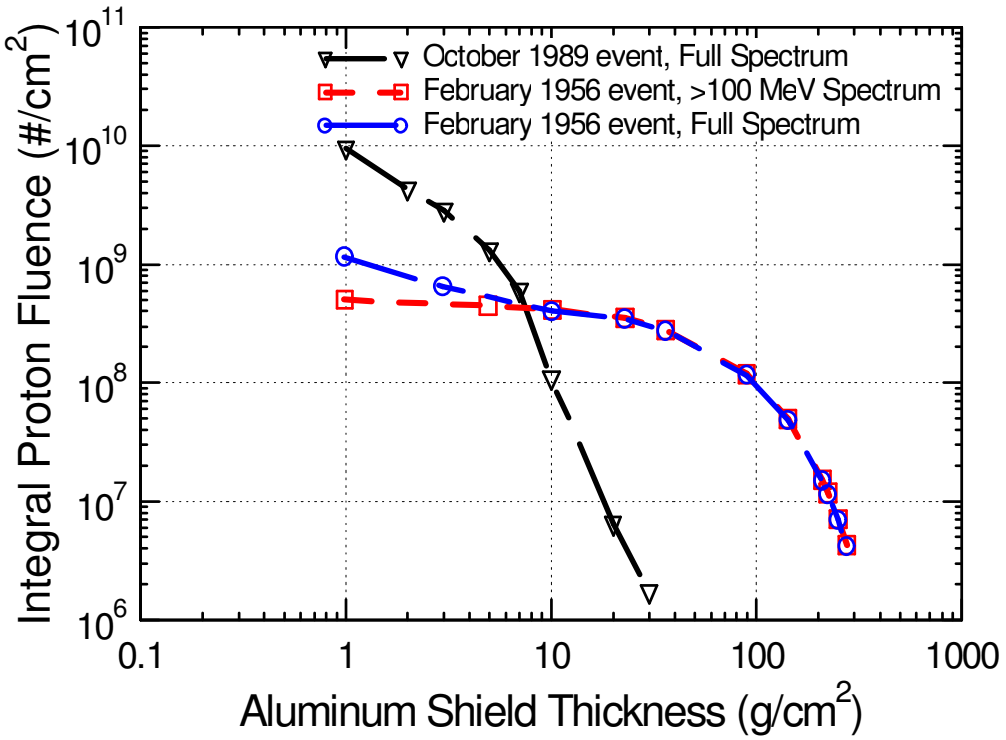

Figure 5.3. Comparison of the calculated Integral Fluence using the Full Spectrum and protons with >100 MeV from February 1956 Solar Event and for the October 1989 Solar Event.

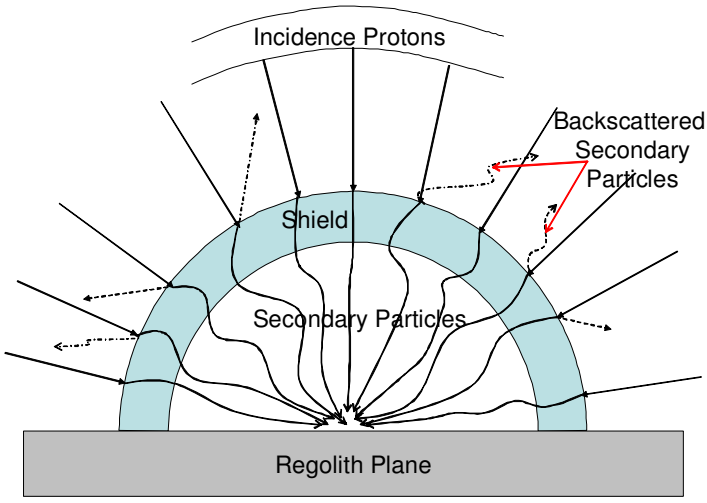

(a) Center Seeking Incidence of Source Particles

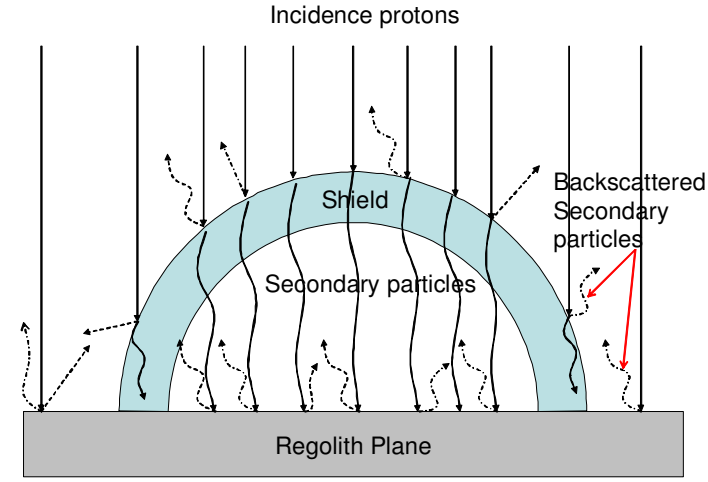

(b) Planar Incidence of Source Particles

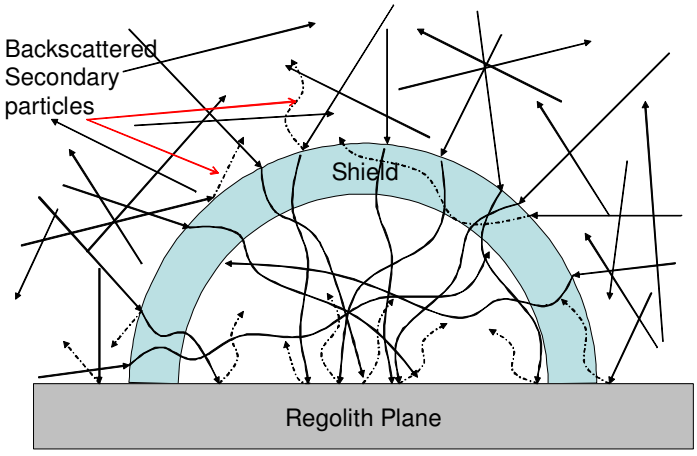

(c) Isotropic Incidence of Source Particles

Figure 5.4. Center Seeking, Planar, and Isotropic Incidence of Source Particles.

from the lunar surface. Both the October 1989 and February 1956 events are used to represents two different energy spectra of incident protons. The February 1956 solar event has the highest relative concentrations of high energy protons with E >100 MeV (Fig. 2.4); though protons with E <100 MeV constitute ~ 90% of the spectra. The October 1989 event has the highest integral fluence of low energy protons (~ $7x10^{11}$ cm^{-2}), but the protons in the spectrum are of relatively low energy (E <100 MeV).

When the full spectrum of the February 1956 event is taken into account, significant numbers of particles are required for each MCNPX simulation, requiring very long time to complete the calculations. To reduce the simulation time, while improving the calculation statistics, the February 1956 energy spectrum of incident protons (Fig. 2.4) is divided into two parts: E <100 MeV and E >100 MeV. The results in Figure 5.3 indicate that for an aluminum shield thickness greater than 10 g/cm^2, there is essentially no difference in the estimated fluence inside the lunar shelter when using the full energy spectrum or only protons with E >100 MeV. With > 10 g/cm^2 of aluminum the difference caused by the contribution of the low energy protons (E <100 MeV) is small, but increases as the shield thickness decreases. On the other hand, protons with E > 100 Mev (Fig. 2.4) require much more shielding as they dominate the protons fluence inside the lunar shelter. As long as the shield thickness is larger than 10 g/cm^2, using the portion of the 1956 energy spectrum with E >100 MeV in the shielding calculations would not compromise the dose estimates inside the lunar shelter. With the assumed 10 cm-thick (~ 27 g/cm^2) aluminum support structure, protons with E <100 MeV would not be a major contributor to the dose estimates within the lunar shelter, and thus could be eliminated from further consideration.

Although the February 1956 event spectra were obtained using ground-based measurements, which might have had large uncertainties, the high energy protons (E > 100 MeV) are the biggest challenge for shielding calculations. For comparison, the full spectrum of the October 1989 event is simulated and the results are also shown by the open triangle symbols in Figure 5.3. As expected, the integral fluence of the October 1989 event inside the shielded lunar shelter is much higher than that of the February 1956 event only with small shield thicknesses. The integral fluence of the October 1989 event decreases quickly with increasing shield thickness; with ~10 g/cm^2, it drops by two

orders of magnitude, below that due to the February 1956 event. Though large uncertainties might be associated with the February 1956 event data, it is the worst case scenario for high energy protons shielding analysis, thus subsequent dose estimates inside the lunar shelter are based on the February 1956 like solar event.

5.6 Computation Domains

The analysis is performed for three different modes of incidence of the source protons onto the outer surface of the shielding for the shelter: center seeking (Fig. 5.4a), planar (Fig. 5.4b), and isotropic (Fig. 5.4c). The center seeking incidence of the primary SEPs represents the worse case scenario for dose calculations inside the lunar shelter. The effective dose distribution inside the shelter is calculated using the mesh tallies function in MCNPX to identify any radiation hot spots inside the shelter. To reduce the computation time, the employed mesh tallies use a rectangular domain that is 8 m long and wide and more than 4 m high, depending on the shielding thickness. The rectangular box is further divided into smaller, 5 cm size meshes. To ensure good statistics, > 300 millions particles are used in the MCNPX simulations of the center seeking, planar and isotropic incidence modes of the solar source protons.

5.7 Dose Estimates

The effective dose is expressed as the weighted sum of the equivalent dose received by the organ and tissue of the body. Though a useful quantity for comparing irradiation exposures for protection purposes, it is not measurable, but can be determined using the incident particle fluence and energy spectrum [Simonsen et al. 1991; Ferrari et al. 1996; Ferrari et al. 1997; Ferrari et al. 1998; NCRP 2000; NCRP 2006]. The estimated dose equals the particle fluence inside the shelter times the fluence-to-dose conversion coefficients (Fig. 5.5). This figure plots the fluence-to-dose conversion coefficients used for protons, neutrons and gammas as a function of the particle or photon energy. Because the energy steps in this figure are very wide, the values in between are interpolated into smaller energy steps, consistent with the bin size used in the MCNPX calculations. The fluence-to-dose conversion coefficient for neutrons covers the entire

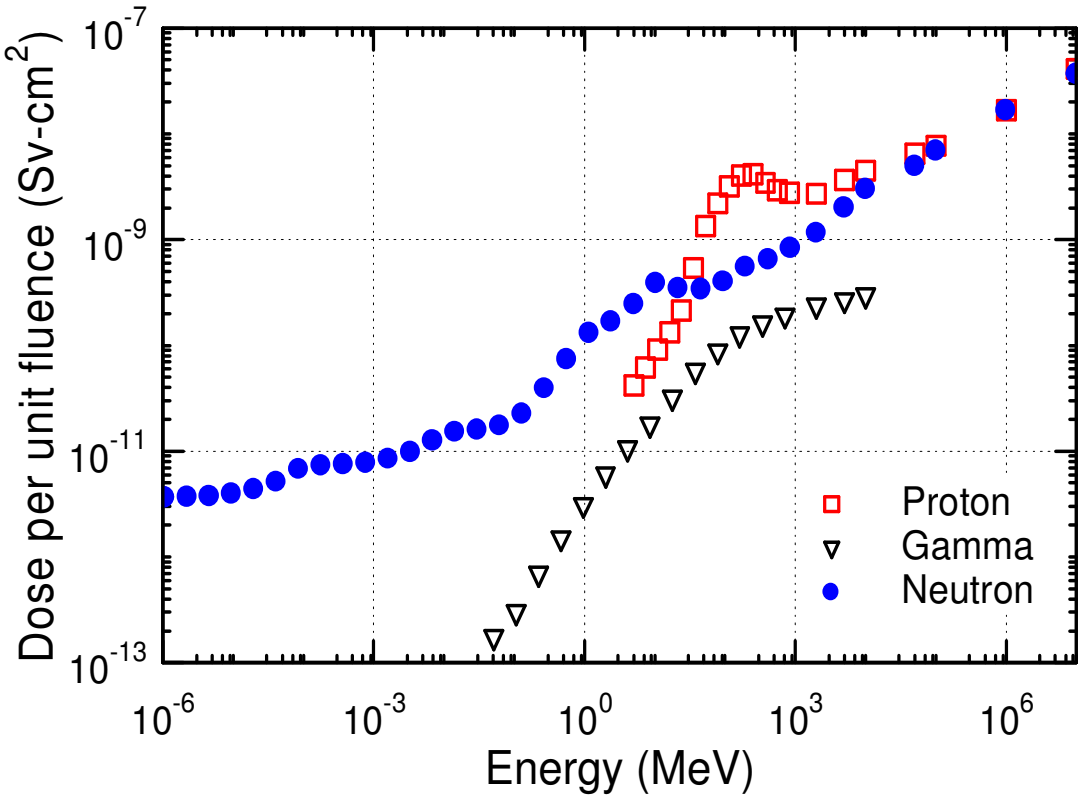

Figure 5.5. Fluence-to-Dose Conversion Coefficients for Radiation Particles and Gamma Photons [Ferrari et al. 1996; Ferrari et al. 1997; Ferrari et al. 1997].

energy range from thermal to 10 TeV, sufficiently wider than the range of interest in this study. The conversion coefficients for the photons and protons are only given for energies higher than 50 keV and 5 MeV, respectively. To avoid extrapolating beyond the range of the data in Fig. 5.5, the initial energy bin in MCNPX is set with lower limits of 50 keV and 5 MeV for the photons and the protons calculations, respectively.

5.8 Results and Discussion

This section presents the results of the shielding calculations of a February 1956 like, solar proton event. The results quantify the contributions of the source protons and those of the secondary protons and the secondary neutrons and gammas to the effective dose estimates inside the lunar shelter. The dose estimates are calculated as a function of the aluminum or the regolith shield thicknesses. Dose spatial distributions within the shelter are also calculated and discussed. As indicated earlier, the dose estimates in the lunar shelter (Figs. 5.2 and 5.4) are performed for three modes of incidence of the primary protons on the outer surface of the shield: center seeking (Fig. 5.4a), planar (Fig. 5.4b), and isotropic (Fig. 5.4c).

5.8.1 Center Seeking Incidence of Source Protons

With a 10-cm thick aluminum support structure of the lunar shelter, the additional thickness of the aluminum and regolith shield varied from 0 to 200 g/cm^2. Center seeking incidence of the sources protons results in the highest dose estimates and thus, is the worst case scenario. Figures 5.6a – 5.6d compare the calculated fluences of the source protons and secondary protons, as well as those of the secondary neutrons and gammas in the regolith shield (Figs. 5.6b – 5.6d) and in the aluminum support structure alone (Fig. 5.6a). Near the outer surface of the aluminum support structure, the integral fluence of the primary protons is almost two orders of magnitude higher than those of the secondary neutrons and gammas. Conversely, on the inside of the aluminum support structure of the shelter, the integral fluences of the secondary neutrons and gammas are more than 2 and 3 times that of the source protons (Fig. 5.6a).

With the regolith shield piled on top of the aluminum support structure, the incident source protons penetrate the regolith then the 10 cm-thick aluminum support

structure. With a 50 g/cm^2 regolith shield the integral fluences of the primary and secondary protons inside the shelter decrease, while those of the secondary neutrons and gammas increase with increased penetration distance in the regolith (Fig. 5.6b). The fluences of the secondary protons, neutrons, and gammas at a depth of 30 g/cm^2 are comparable to those inside the shelter with the aluminum support structure alone (Fig. 5.6a). These results suggest that both the aluminum and regolith of the same mass thickness are similarly effective for shielding high energy protons, which is attributed to the similarity in the average molecular weight. Thus, reducing the thickness of the aluminum support structure and replacing it with regolith of the same mass thickness would give similar results. The results in Figs. 5.6b and 5.6c show that, while increasing the regolith thickness significantly reduces the integral fluence of the primary protons, the decreases in the integral fluences of the secondary neutrons and gammas are relatively small. The dose estimates inside the shelter depend upon the fluence, energy, and type of the radiation species.

5.8.1.a Dose estimates inside the lunar shelter

Figures 5.7a and 5.7b compare the estimated dose inside the lunar shelter with aluminum and regolith shields of increasing thicknesses. With a zero shield thickness, the attenuation is solely due to the aluminum structure. As can be seen in Figures 5.7a and 5.7b, the total (taken as the sum of those due to protons, neutrons, and gammas) inside the shelter drop below the recommended 30-day limit for astronauts (250 mSv), when the thickness of the aluminum shield is ~25 g/cm^2 and of the lunar regolith shield is ~ 20 g/cm^2. The primary and secondary protons contribute ~ 180 mSv or 72%, while the secondary neutrons contribute ~ 70 mSv or 28%; the contribution of the secondary gamma rays is minimal.

The source protons and the secondary protons are the greatest contributor to the dose estimates inside the shelter with a shield thickness up to 100 g/cm^2 of aluminum or lunar regolith (Fig. 5.7a and 5.7b). Beyond this thickness, the secondary neutrons are the major contributor to the estimated dose inside the shelter. With about 20 g/cm^2 of aluminum or regolith shield, the estimated dose inside the lunar shelter equals the

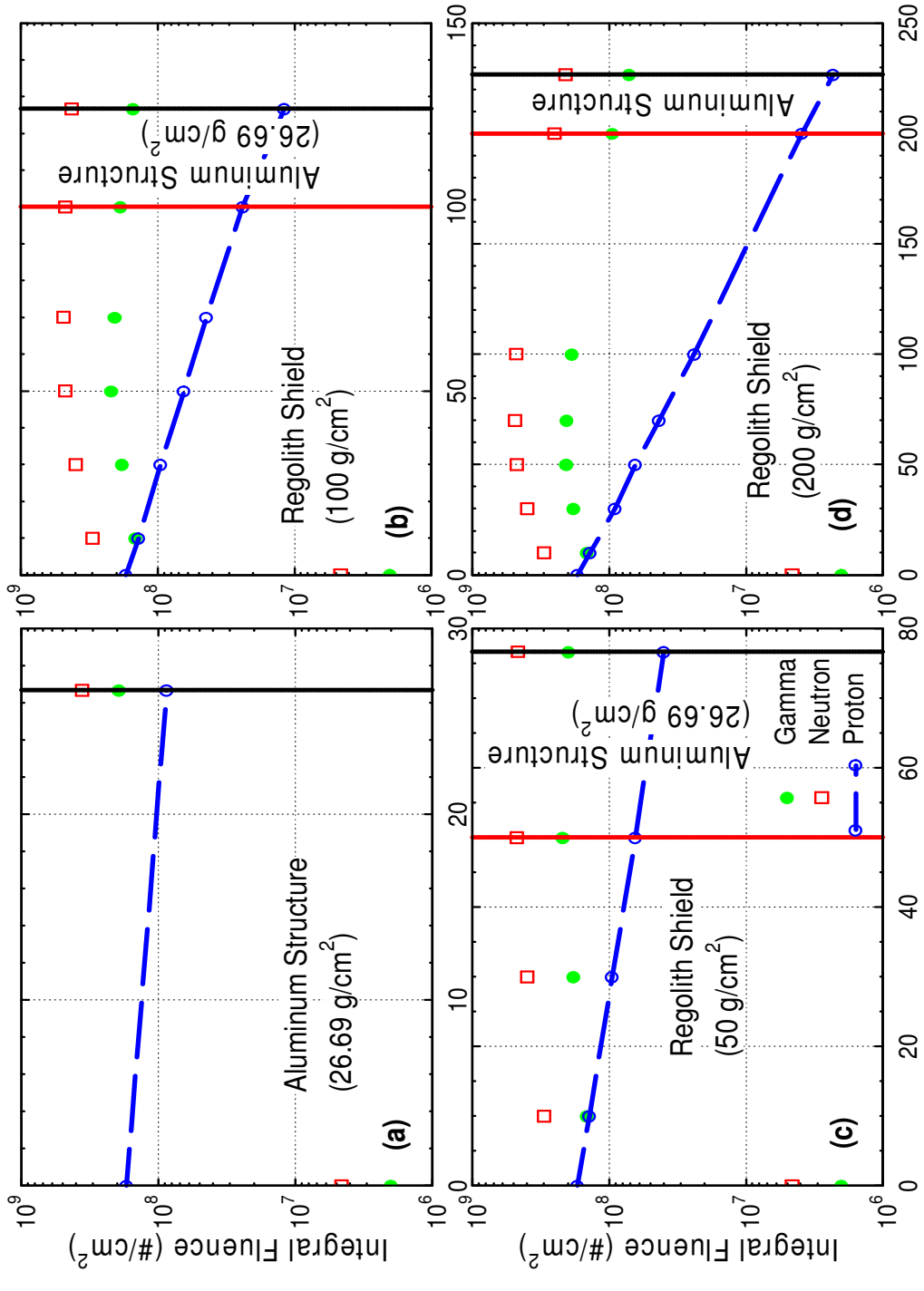

Figure 5.6. Calculated Integral Fluences of the Primary and Secondary Protons and the Secondary Neutrons and Gammas with Different Regolith Shield Thickness.

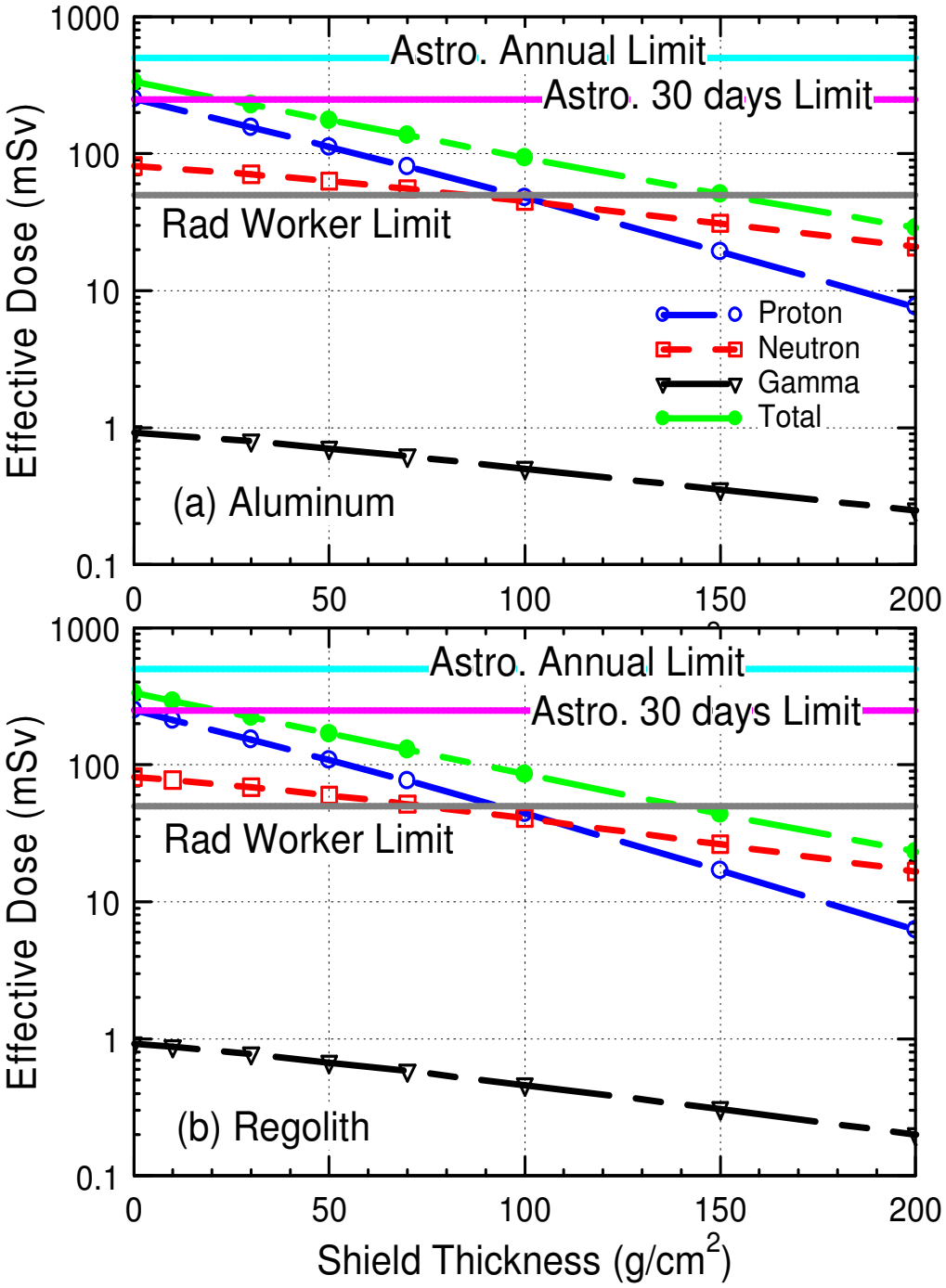

Figure 5.7. Dose Estimates Inside the Shelter as Function of Aluminum and Regolith Shield Thickness, Assuming Center Seeking Incidence of Source Protons.

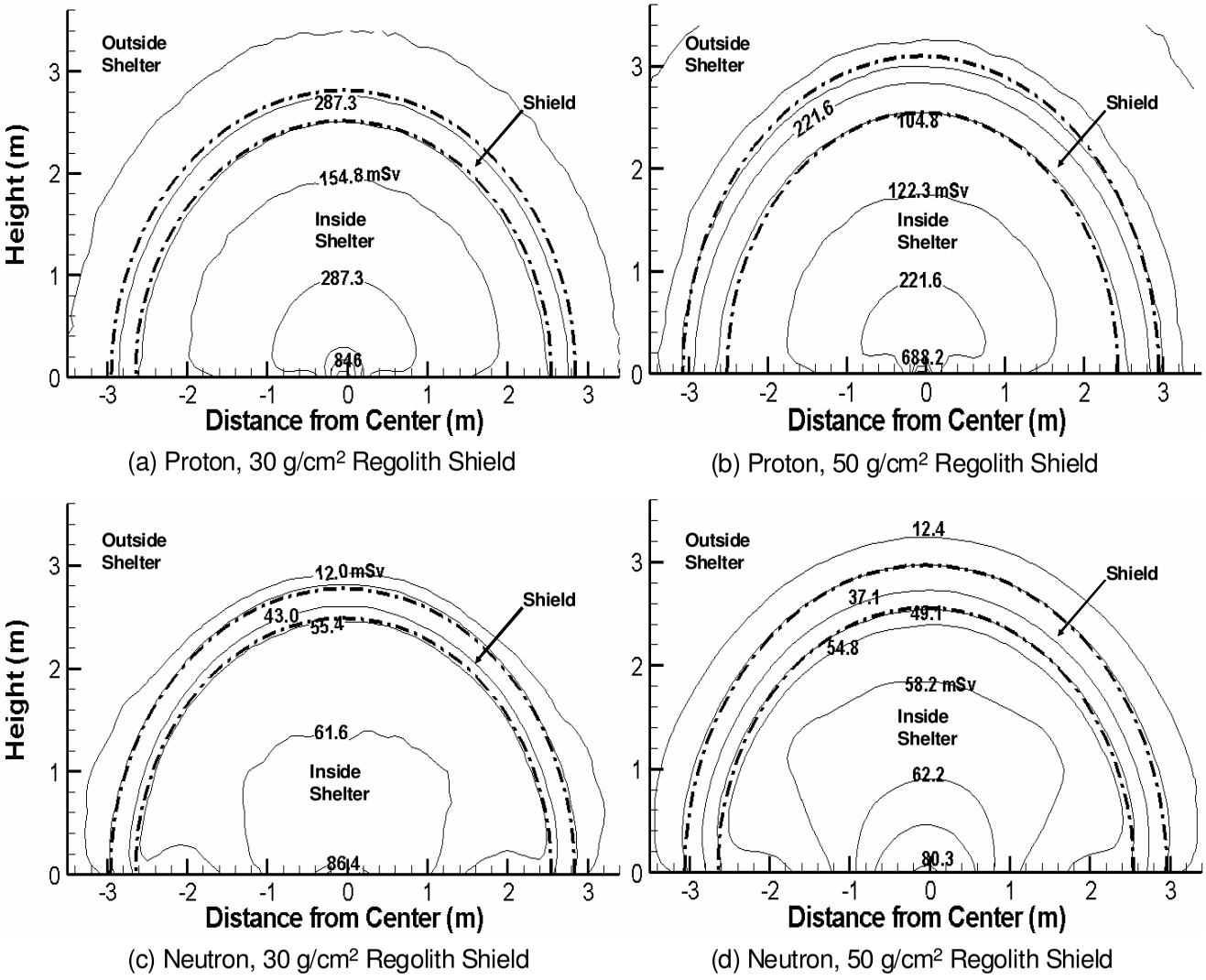

Figure 5.8. Spatial Distribution of the Dose Estimates Inside the Shelter due to Protons and Secondary Neutrons, Assuming Center Seeking Source Protons.

recommended 30-day limit for astronauts. For tourists and associated workers, this research assumes a radiation dose limit of 50 mSv in any given year or mission. The International Atomic Agency and current guidelines recommend 50 mSv for exposed workers in nuclear research facilities and nuclear power plants in any single year. This indicates the need to establish effective dose exposure limits in the future for space travel of members of the public, workers and astronauts. To reduce the estimated dose inside the lunar shelter for a February 1956 like solar event below 50 mSv, the required aluminum and lunar regolith shield thicknesses are 150 and 145 g/cm^2, respectively. These thicknesses translate into ~ 0.56 m of aluminum and 1.20 m of regolith, respectively (Figs. 5.7a and 5.7b). The contribution of the secondary neutrons to the estimated dose inside the shelter is the highest, followed by that of the protons. The contribution of the secondary gamma rays is negligible.

5.8.1.b Spatial distribution of estimated dose inside the lunar shelter

The spatial distribution of the estimated dose inside the shelter helps identify potential hotspots. It depends not only on the fluence and the energy spectrum of the incident solar protons, but also on the regolith shield thickness and the assumed mode of incidence of the source protons. With a center seeking incidence of the source protons, Figures 5.8a – 5.8d show the protons and neutrons dose distributions inside the shelter with 30 g/cm^2 and 50 g/cm^2 of regolith on top of the aluminum support structure. The dash-lines in these figures represent the shield thicknesses including the aluminum structure. With a 30 g/cm^2 regolith shield, the estimated dose due to the secondary and primary protons near the inside of the aluminum support structure is 155 mSv. The dose estimate increases toward the center of the shelter floor, where it reaches ~ 850 mSv (Fig. 5.8a). It is significantly higher than at the outer surface of the regolith shield, because of the assumed center seeking incidence of the source protons, thus excessively conservative. With all incident particles moving inward toward the center of the shelter, the cumulative fluence and the corresponding dose estimate increases. With 50 g/cm^2 of regolith shield, the largest dose estimate is at the centerline of the floor of the shelter (688 mSv). It decreases to ~105 mSv on the inside surface of the aluminum support structure. With a center seeking incidence of source particles, the estimated dose inside the shelter

is independent of angular orientation, only depends on the distance from the inside of the aluminum support structure (Figs. 5.8a – 5.8d).

The estimated dose distributions due to the secondary neutrons inside the shelter with 30 and 50 g/cm^2 of regolith are delineated in Figures 5.8c and 5.8d. The neutrons dose distribution exhibits the same behavior as the primary and secondary protons (Figs. 5.8a and 5.8b), but the dose estimates are much lower, for the same shield thickness. With 30 g/cm^2 of regolith shielding, the smallest neutrons dose of 55 mSv is on the inside of the aluminum support structure, increasing to 86 mSv at the center of the floor of the shelter. Increasing the shield thickness to 50 g/cm^2 reduces the estimated dose due to the secondary neutrons on the inside of the aluminum support structure to 49 mSv and that at the center of the shelter floor to 80 mSv. With a center seeking incidence of the source protons, the estimated dose on the inside of the aluminum support structure is the lowest. It is also constant regardless of the angular position (0 – 180^o), because the penetrated thicknesses of the shield and the aluminum support structure are the same regardless of the angular orientation.

5.8.1.c Relative attenuation using lunar regolith shielding and center-seeking incidence of source protons

Figures 5.9a presents the dose estimates at the outer surface of the aluminum support structure of the lunar shelter and Figure 5.9b compares the relative attenuation by the regolith shield, assuming a center seeking incidence of the source protons. The relative attenuation is defined as 1 minus the ratio of the decrease in the estimated dose at the outer surface of the aluminum support structure of the shelter with and without regolith shield ($1 – D/D_0$). The contributions of the secondary and primary protons to the estimated dose are by far the highest, followed by that due to secondary neutrons; the contribution of the secondary photons is negligibly small < 1%. The dose estimates due to the source and secondary protons in Figure 5.9a are almost independent of the angular orientation, decreasing monotonically as the thickness of the regolith shield increases. The dose attributed to the secondary neutrons increases initially as the thickness of the

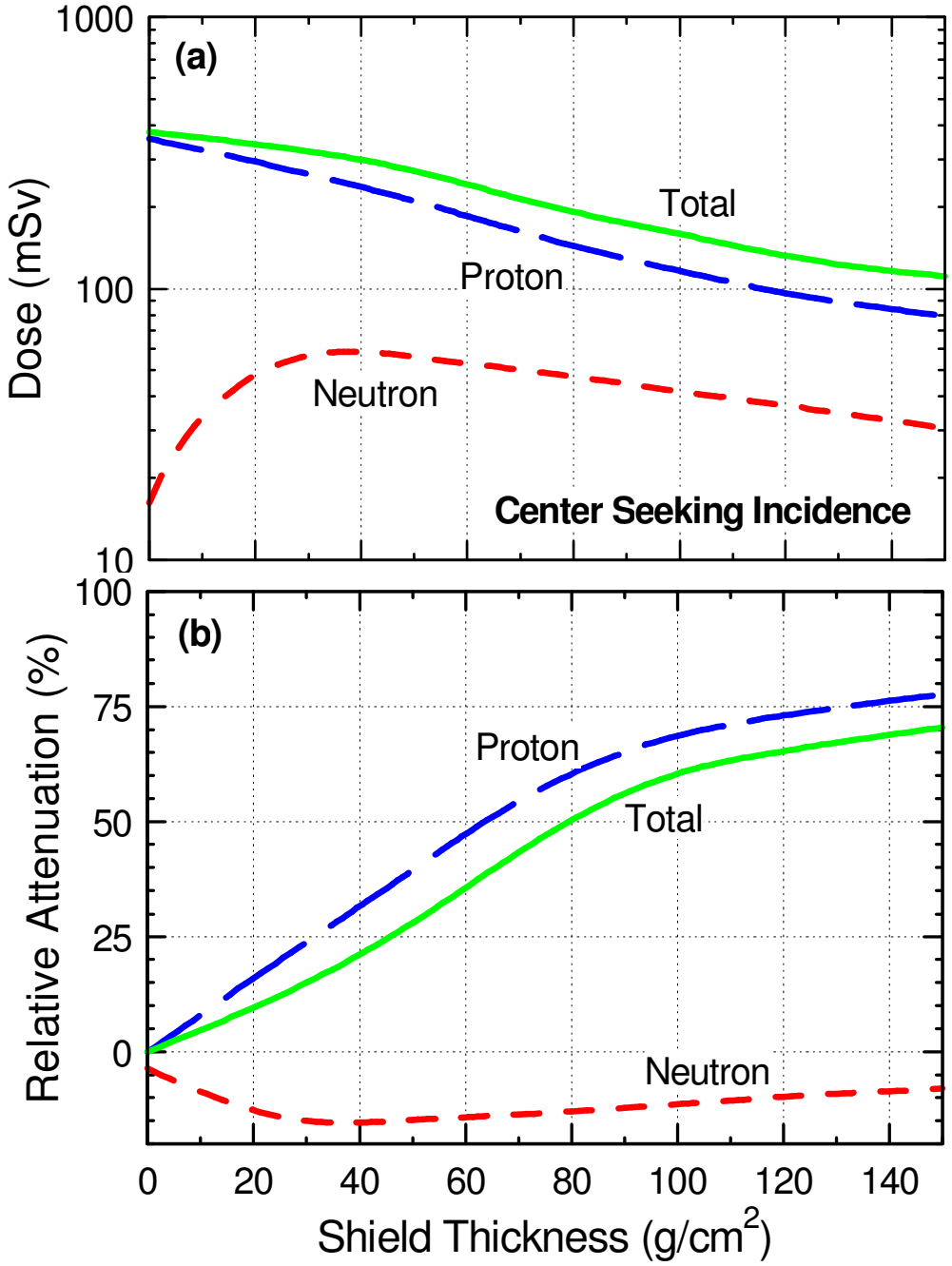

Figure 5.9. Dose Estimates and Relative Attenuation of Primary and Secondary Particles, Assuming Center Seeking Incidence of Source Protons.

regolith shield increases up to ~ 35 g/cm^2, then decreases with further increase in the shield thickness.

Since the estimated dose is the collective contribution of the particles fluences and energies, the initial increase in the secondary neutrons' dose is indicative of both the high fluence and energy of the neutrons generated by the spallation reactions of the high energy protons with the nuclei of the various elements in the regolith (Table 5.1). Similarly, the decreases in the neutron dose with regolith thicknesses > 35 g/cm^2 are indicative of the reduction in the fluence and energy of the secondary neutrons. The peak dose of the secondary neutrons corresponds to the minimum relative attenuation in Figure 5.9b. Note that the secondary neutrons practically decrease the relative attenuation of the regolith shield below that for the primary and secondary protons. The relative attenuation is 15% with 50 g/cm^2 of regolith and increases to 43% as the regolith shield thickness increases to 70 g/cm^2. Doubling the regolith thickness to 140 g/cm^2 increases the relative attenuation from 43% to only 70%. These values of the regolith relative attenuation is about 10 percentage points lower than that of the primary and secondary protons, because of the increase in the dose caused by the secondary neutrons (Figure 5.9b).

5.8.2 Planar Incidence of Source Protons

Planar incidence of the source protons results in the lowest dose estimates inside the lunar shelter. Figure 5.10 compares the calculated contributions of the source and secondary protons, as well as the secondary neutrons and gammas to the estimated dose on the inside surface of the aluminum support structure of the shelter, assuming a planar incidence of the source protons. The contributions and the dose estimates are significantly lower than in Figure 5.7b, assuming a center seeking incidence of the source protons. The results in both figures are for lunar regolith shield on top of the aluminum support structure of the shelter.

5.8.2.a Dose estimates inside the lunar shelter

With only the aluminum support structure, or zero regolith shield (Fig 5.10), the source and secondary protons are the dominant contributors to the dose of ~ 177 mSv on the inside of the aluminum support structure along the central vertical plane. The

secondary neutrons contribute less than 50 mSv and the contribution of the secondary gamma rays is negligible. The dose estimate with only the aluminum support structure is lower than the recommended 30-day limit for the astronauts of 250 mSv, but higher than that assumed for the radiation workers of 50 mSv. To reduce the dose estimate on the inside of the aluminum support structure below that for the radiation workers, a regolith shield thickness of ~ 110 g/cm^2 would be needed (Fig. 5.10), compared to 145 g/cm^2 when assuming a center seeking incidence. Increasing the regolith shield thickness to 120 g/cm^2 reduces the estimated dose at the same location inside the shelter to ~ 40 mSv.

The results in Figure 5.10 indicate that the dominant contributor to the dose estimates inside the lunar shelter are the primary and secondary protons up to a regolith shield thickness of ~ 90 g/cm^2. With larger thicknesses, the secondary neutrons are the major contributor to the dose estimates inside the shelter. The contribution of the secondary gammas is very small, regardless of the regolith shield thickness. The contribution of the protons to the dose estimates inside the shelter decreases faster than those due to the secondary neutrons and the secondary gammas with increased thickness of the regolith. With a planar incidence of the source particles, the penetration length and the attenuation of the primary and secondary particles increase with distance on either sides of the vertical central plane. Therefore, the highest dose estimate inside the shelter is that on the inside of the aluminum support structure along the central vertical plane (Figs. 5.10 and 5.11).

5.8.2.b Spatial distribution of estimated dose inside the lunar shelter

Figures 5.11a – 5.11d show the spatial distributions of the dose estimates inside the shelter due to the source and secondary protons with 0 – 100 g/cm^2 of regolith shield, assuming a planar incidence of the source protons. The estimated dose due to the source protons at the outer surface of the aluminum support structure without a shield is ~ 400 mSv. The corresponding value on the inside of the aluminum structure along the central vertical plane is 177 mSv. This dose estimate decreases with distance on either sides of the central vertical plane to < 78 mSv along the corner of the shelter, or at 2.5 m from the vertical central plane inside the shelter (Fig. 5.11a). Similar distributions of the estimated dose due to the primary and secondary protons inside the shelter with various thicknesses

of the regolith shield are obtained and delineated in Figs. 5.11b – 5.11d. The dose distributions in Figs. 5.11a – 5.11d are symmetric relative to the central vertical plane. The largest dose estimate due to the source and secondary protons on the inside of the aluminum support structure decreases to 140, 56 and 28 mSv as the thickness of the regolith shield increases to 30, 70 and 100 g/cm^2, respectively.

The estimated dose distributions inside the lunar shelter due to the secondary neutrons, without shield (0 g/cm^2) and with increasing regolith shield thickness up to 100 g/cm^2 are displayed in Figures 5.12a – 5.12d. The spatial distributions of the estimated dose inside the shelter are generally similar to those of the protons (Figs. 5.11a – 5.11d), but the values are much lower. The values at the outer surface of the shield include the contribution of the backscattered neutrons from the shield surface and the surface of the regolith on both sides of the shelter, are lower than the dose estimates inside the lunar shelter. Again, the highest dose estimates inside the shelter are on the inside surface of the aluminum support structure along the central vertical plane. With no shield, the highest estimated dose in the shelter due to the secondary neutrons is 48 mSv, though the estimated dose throughout the shelter is generally uniform and equal to 46 mSv. Increasing the thickness of the regolith shield decreases the dose estimates in the shelter (Figs. 5.10 and 5.11).

With 30 g/cm^2 of regolith (Fig. 5.12b), the highest estimated dose due to secondary neutrons on the inside of the aluminum support structure and within a small region at the top of the shelter is still 48 mSv. In most of the shelter, the estimated dose due to the secondary neutrons is almost uniform ~ 44 mSv. The lowest estimated dose at the corners of the shelter is < 41 mSv (Fig. 5.12b). Increasing the regolith thickness to 70 g/cm^2 reduces the estimated dose inside the shelter. It also generates distinct zones with different dose estimates. The estimated dose due to the secondary neutrons varies from 39 mSv on the inside of the aluminum structure at the central vertical plane to < 31 mSv at the corners of the shelter (Fig. 4.14c). With 100 g/cm^2 of regolith, the highest dose estimate is at the top of the shelter along the central vertical plane (~ 32 mSv), while the lowest estimated dose is at the corners of the shelter (< 27 mSv).

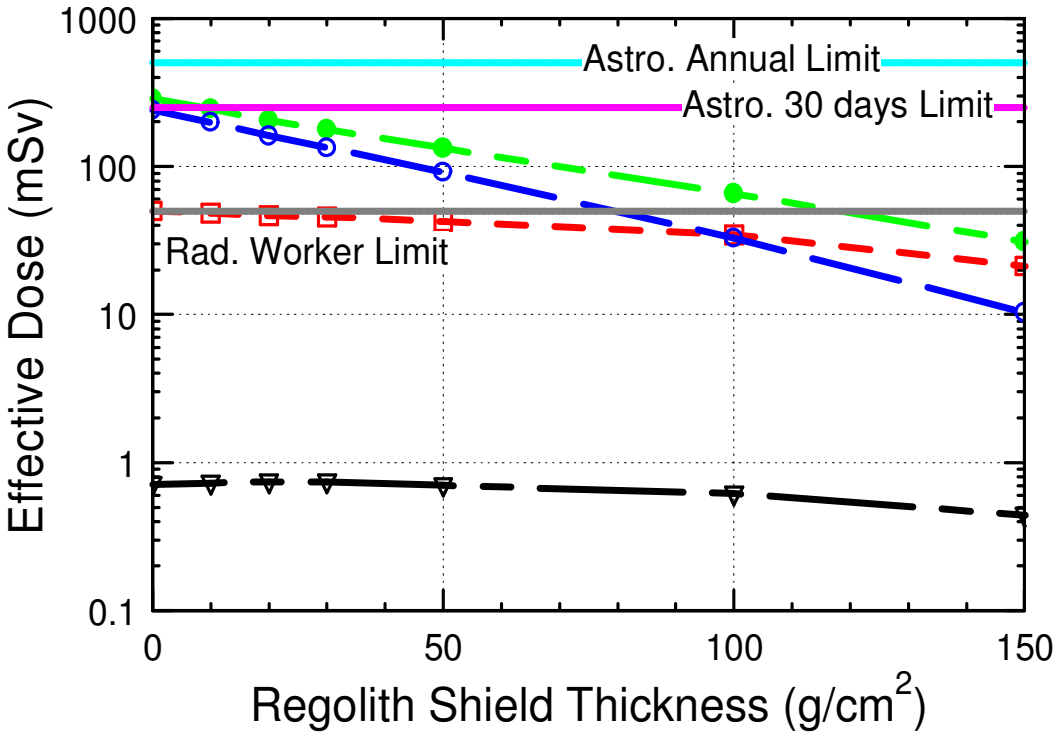

Figure 5.10. Dose Estimates inside the Lunar Shelter as Function of Regolith Shield Thickness, assuming a Planar Incident of Source Protons.

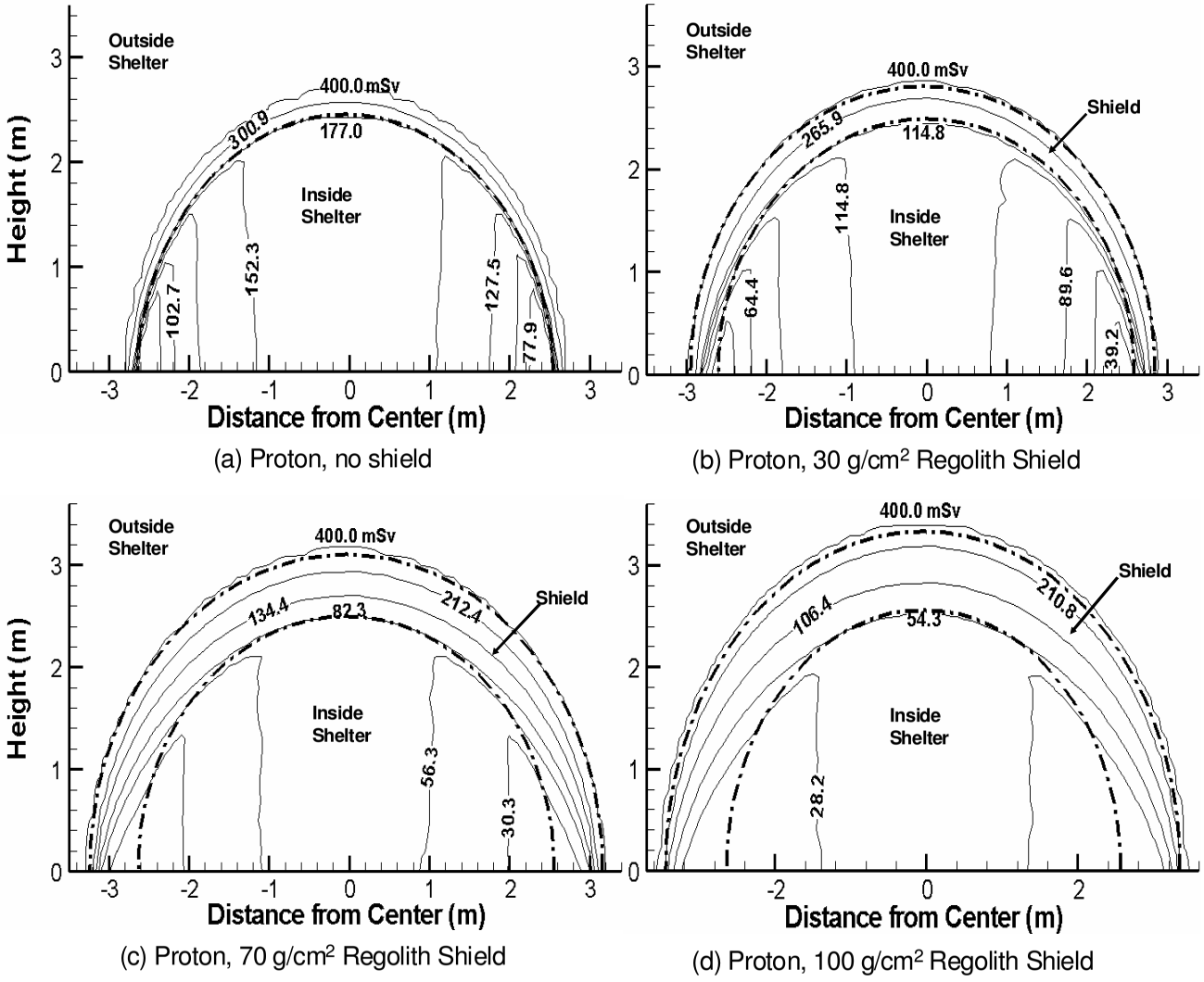

Figure 5.11. Protons' Dose Distribution Inside Lunar Shelter with Regolith Shield Thickness, assuming Planar Incidence of Source Protons.

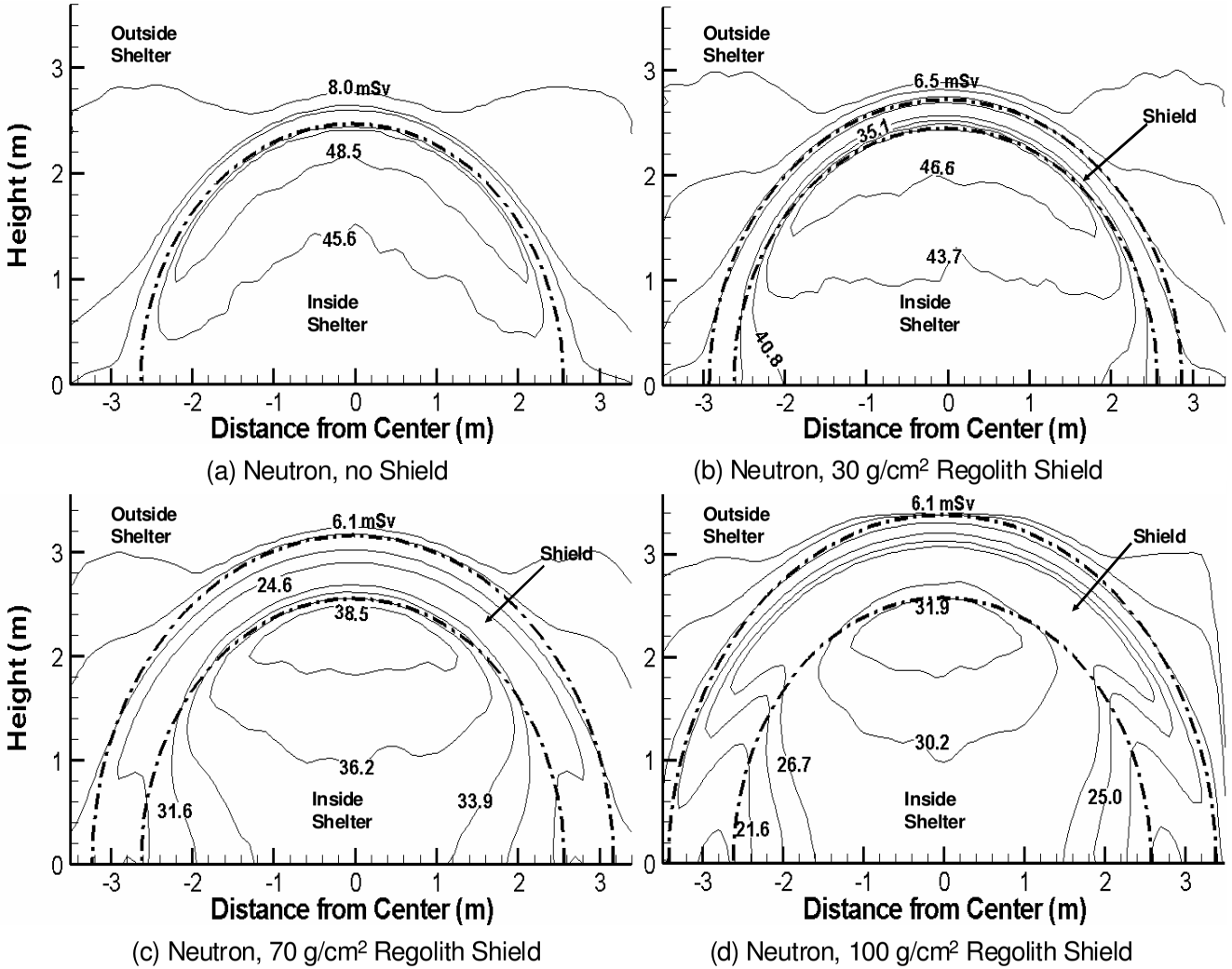

Figure 5.12. Secondary Neutrons' Dose Distribution Inside Lunar Shelter with Regolith Shield Thickness, assuming Planar Incidence of Source Protons.

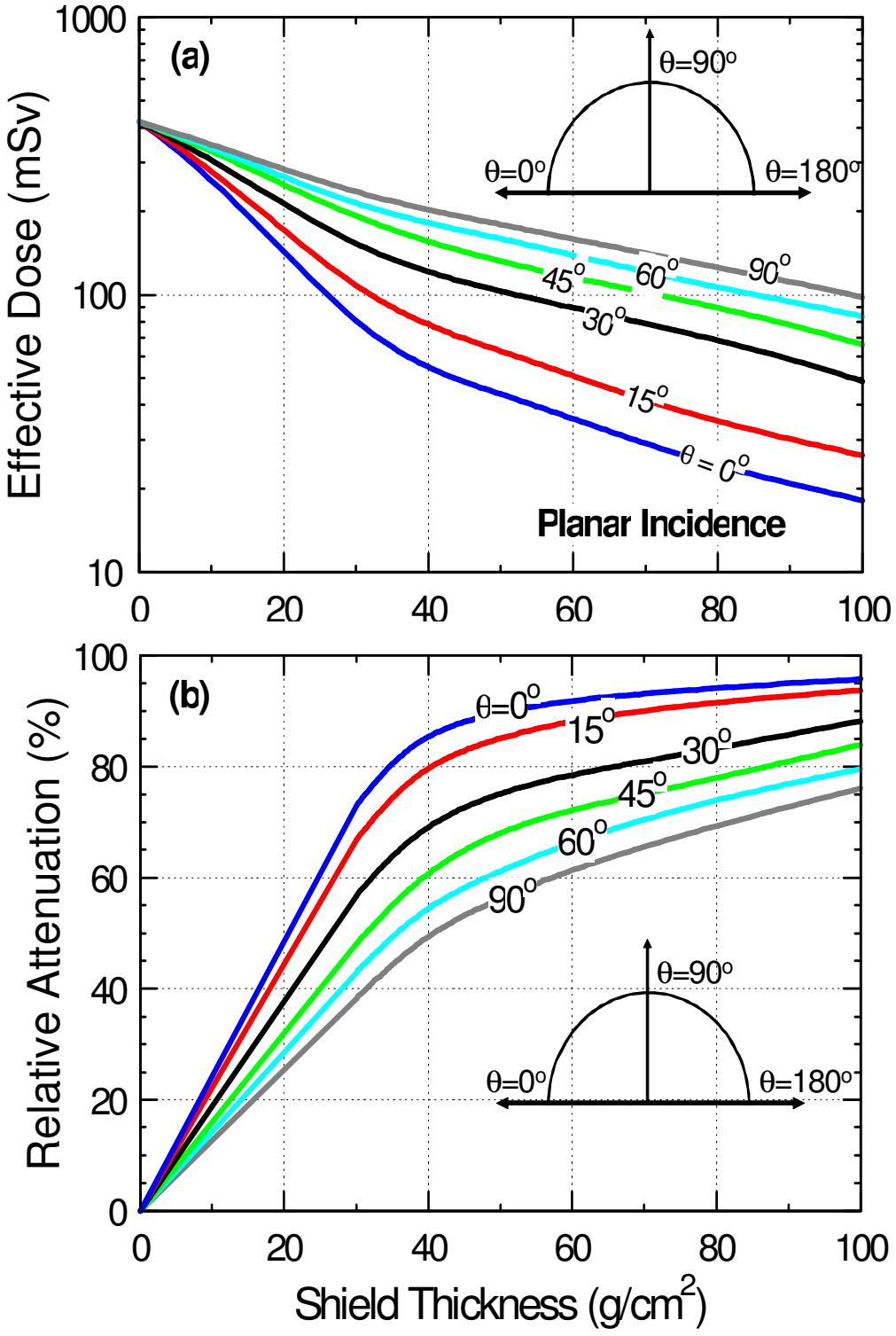

Figure 5.13. Angular Dependence of the Total Estimated Dose and Relative Attenuation of Primary and Secondary Particles using Regolith Shield, assuming a Planar Incidence of Source Protons.

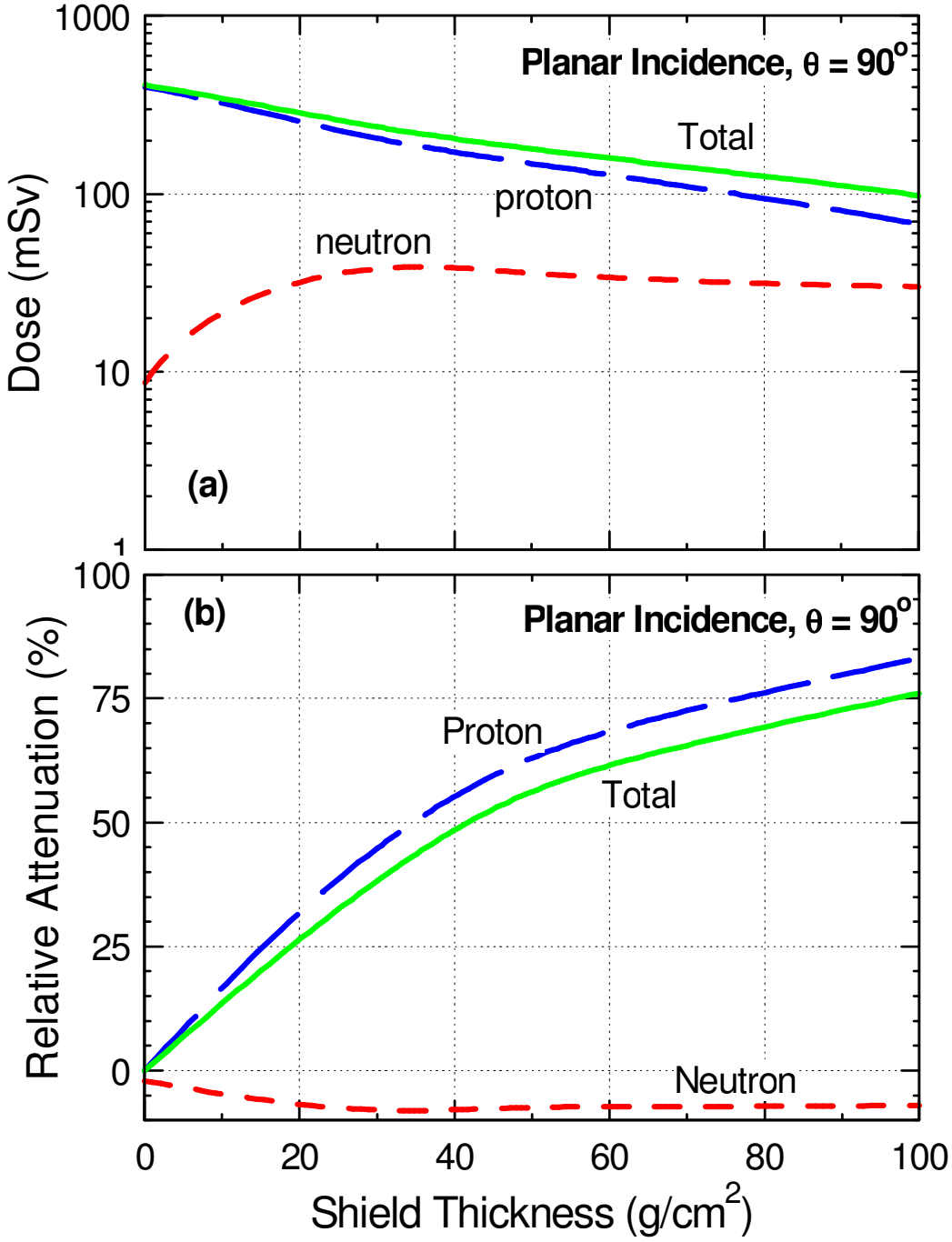

Figure 5.14. Contributions of the Protons and Secondary Neutrons to the Effective Dose and Relative Attenuation of Primary and Secondary Particles along the vertical plane in the Shelter with Regolith Shield, assuming Planar Incidence of Source Protons.

5.8.2.c Relative attenuation using lunar regolith shielding and planar incident of source protons

Figures 5.13a presents the estimated dose at the outer surface of the aluminum structure and Figure 5.13b compares the relative attenuation by the regolith shield as a function of the angular orientation, θ. For the vertical orientation ($\theta = 90^o$), the relative attenuation is the lowest and the estimated dose is the highest. Conversely, along the horizontal plane, $\theta = 0^o$ or 180^o, the estimated dose at the outer surface of the regolith shield is the lowest and the corresponding relative attenuation of the incident particle is the highest. Along the horizontal plane, with a regolith thickness of 40 g/cm^2, the relative attenuation is as much as 86%, but decreases with increasing angular orientation to its lowest value of 50% in the vertical orientation (Fig. 5.13b). With 100 g/cm^2 of regolith, the relative attenuation increase to 94% along the horizontal plane and 76% in the vertical orientation (Figure 5.13b). With 100 g/cm^2 of regolith, the estimated dose at the outer surface of the aluminum structure of the shelter is only 100 mSv in the vertical orientation, decreasing to its lowest value of < 19 mSv in the horizontal plane ($\theta = 0^o$ or 180^o).

Results in Figure 5.14a show that major contributor to the dose estimate in the lunar shelter are by far the primary and secondary protons, with the secondary neutrons contributing < 2% of the dose. Though the dose estimate due to the secondary neutrons peaks with ~ 30 g/cm^2 of regolith shield, it decreases slowly with further increase in the thickness of the regolith shield (Fig. 5.14a). This figure also shows that with 100 g/cm^2 of regolith, the estimated dose at the surface of the aluminum structure in the vertical orientation (90^o) is ~100 mSv, and the corresponding relative attenuation is more than 75% (Fig. 5.14b), compared to 65% when assuming a center seeking incidence of the source particles. These results show that the estimated dose at the surface of the aluminum structure, assuming a center seeking incidence of the sources particle is 10 – 15 % higher than when assuming a planar incidence of sources particle in the vertical orientation and more than 5 times higher at other orientations.

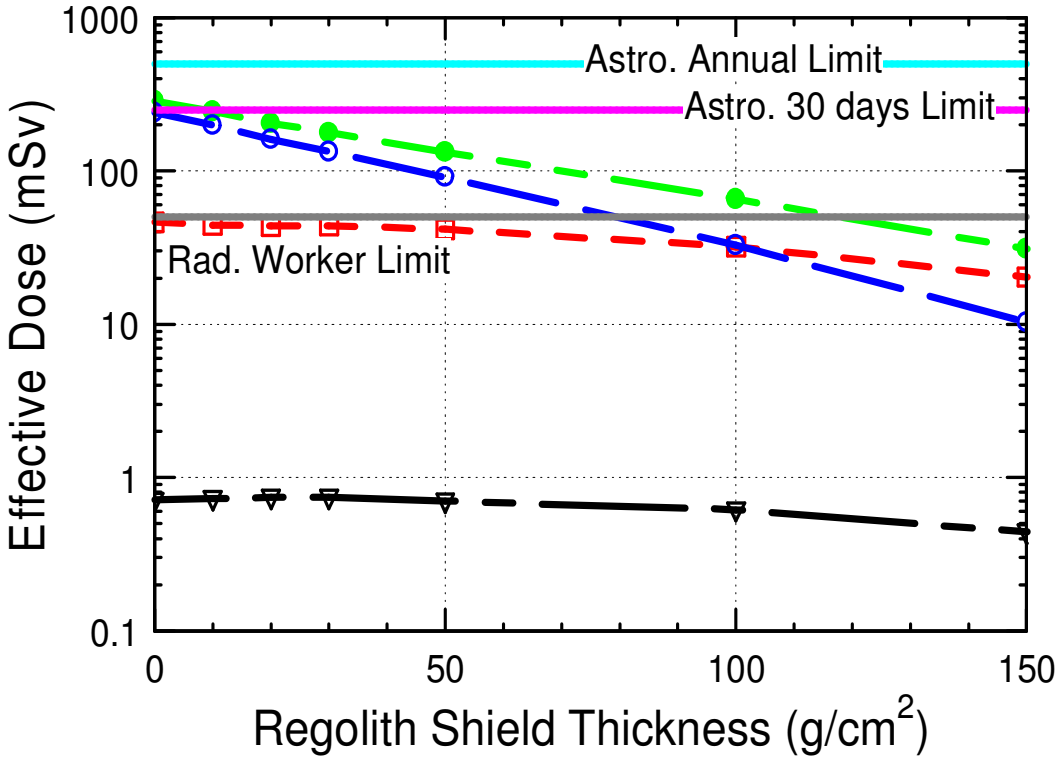

Figure 5.15. Dose Estimates inside Lunar Shelter as Function of Regolith Shield Thickness, assuming Isotropic Incidence of Source Protons.

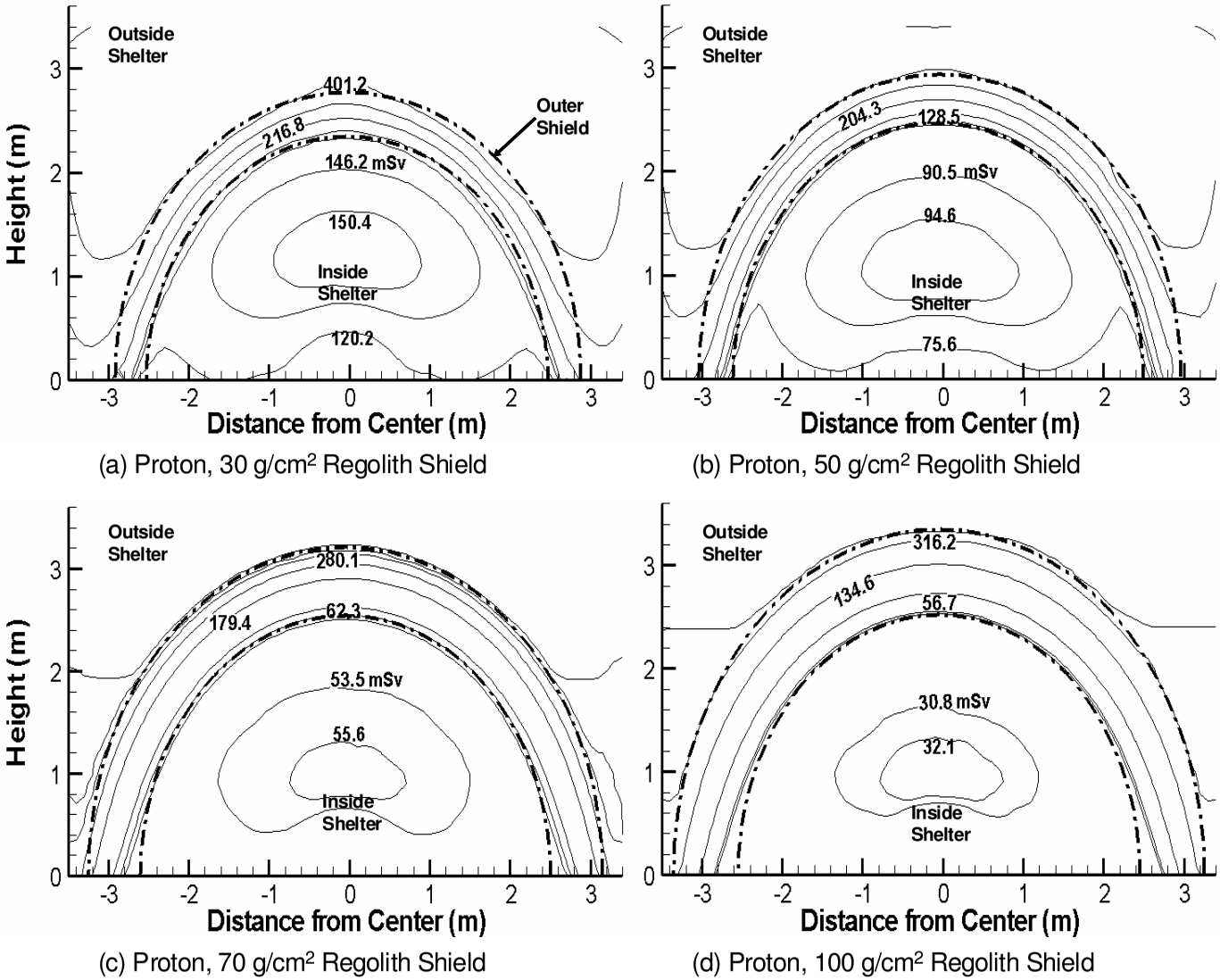

Figure 5.16. Protons Spatial Distributions of the Dose Estimates Inside the Shelter, assuming Isotropic Incidence of Source Protons.

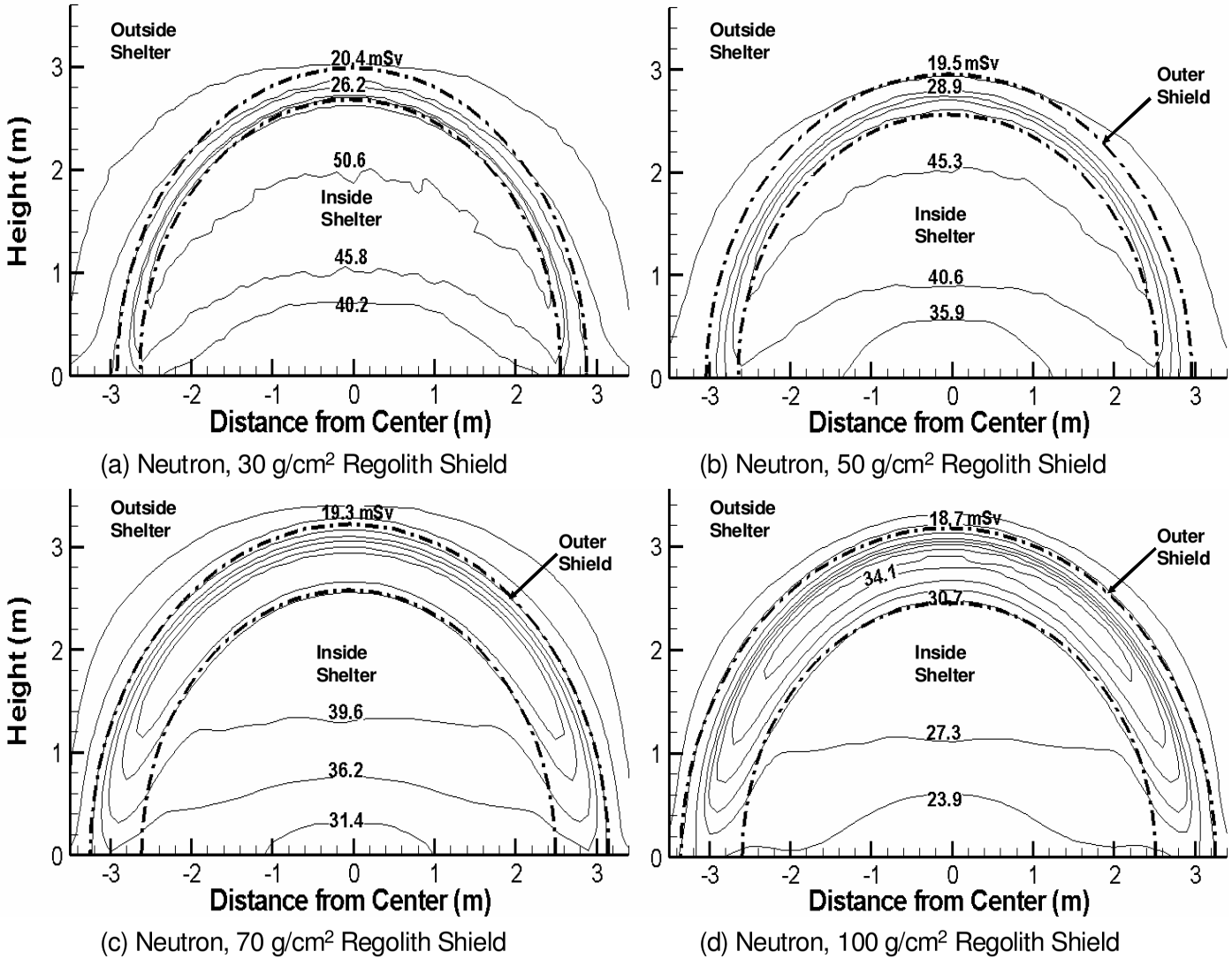

Figure 5.17. Neutrons Spatial Distributions of the Dose Estimates Inside the Shelter, assuming Isotropic Incidence of Source Protons.

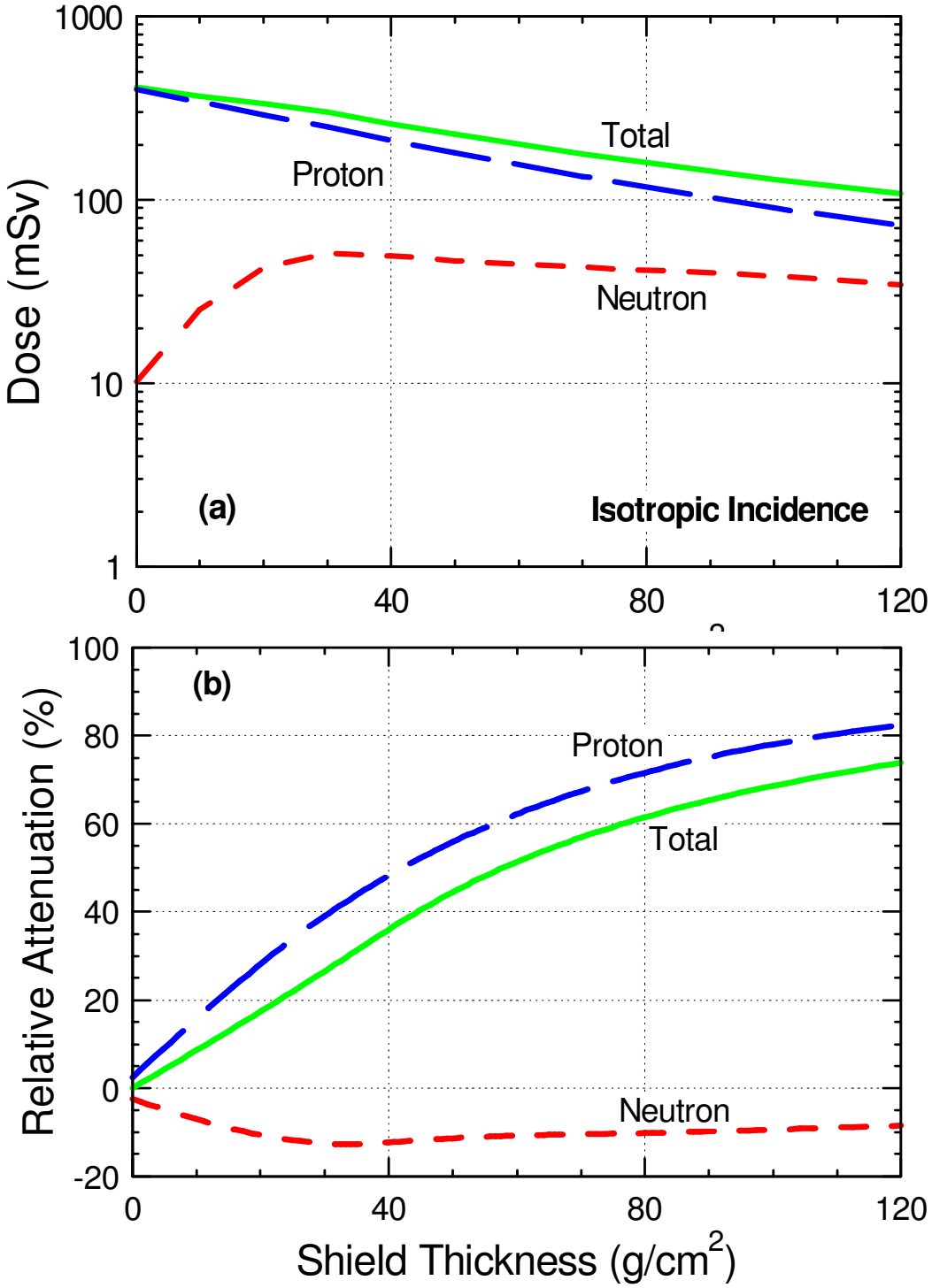

Figure 5.18. Contributions of the Protons and Secondary Neutrons to the Effective Dose and Relative Attenuation of Primary and Secondary Particles in the Shelter with Regolith Shield, assuming Isotropic Incidence of Source Protons.

5.8.3 Isotropic Incidence of Source Protons

The results presented in the following subsections show that ith isotropic incidence of source protons, the estimated dose estimate is always highest outside the lunar shelter, predominantly due to the incidence protons. The estimates as well as the spatial distribution of the dose inside the lunar shelter are also presented and discussed.

5.8.3.a Dose estimates inside the lunar shelter

The dose estimates inside the lunar shelter with zero regolith shield thickness is higher than the recommended 30-days limit for astronauts of 250 mSv (Fig. 5.15). To reduce the dose estimate inside the lunar shelter below the recommended 30-days limit for astronauts, an additional 10 g/cm^2 of regolith shield is needed on top of the aluminum support structure. The primary and secondary protons are the most dominant contributors to the dose estimates inside the lunar shelter, up to a regolith shield thickness of ~ 100 g/cm^2, when the secondary neutrons become the dominant contributor to the dose estimate. Increasing the regolith shield thickness to ~ 120 g/cm^2 reduces the dose estimate inside the lunar shelter below the 50 mSv limit for radiation worker.

5.8.3.b Spatial distribution of estimated dose inside the lunar shelter

The spatial distributions of the estimated dose inside the lunar shelter due the primary and secondary protons with 30, 50, 70 and 100 g/cm^2 of regolith shield are shown in Figure 5.16a – 5.16d. With 30 g/cm^2 (Fig. 5.16a), the lowest dose is that close to the floor of the lunar shelter of ~ 120 mSv. Unlike planar incidence of source protons, the random direction of the incidence source protons generates only small variation in the dose inside the lunar shelter. The dose distributions are primary uniform around 146.2 mSv, with the highest dose near the center zone in the shelter. With 50 g/cm^2 regolith shield (Fig. 5.16b), the dose estimates inside the habitat decrease, though the lowest dose is that close to the floor of the shelter ~ 75.6 mSv. The dose inside the shelter is generally uniform ~ 90.5 mSv, with the highest dose ~ 94.6 mSv. Increasing the regolith thickness to 100 g/cm^2 reduces the dose inside the lunar shelter to ~ 30.8, and the highest dose to ~ 32.1 mSv.

Figures 5.17a – 5.17d show the spatial distributions of the dose estimates inside the lunar shelter due to the secondary neutrons. With 30 g/cm^2, the highest neutrons dose estimate inside the shelter is ~ 50.6 mSv and decrease to ~ 40.2 mSv near the floor of the shelter. Increasing the shield thickness to 50, 70, and 100 g/cm^2 reduces the highest neutrons dose estimates inside the lunar shelter to ~ 45.3, 39.6, and 27.3 mSv respectively.

5.8.3.c Relative attenuation using lunar regolith shielding and isotropic incident of source protons

Figure 5.18 compare the contributions of the protons and secondary neutrons to the effective dose and the relative attenuation of the primary and secondary particles outside the aluminum support structure. The neutrons dose with a zero shield thickness is due to those backscattered off the aluminum structure and the lunar surface. Increasing the shield thickness initially increase the neutrons dose, as more neutrons are generated inside the shield, peaking at ~ 30 g/cm^2 then decreasing with further increase of the regolith shield thickness. The results in Figure 20 indicate that the primary dose inside the shelter are due to the primary and secondary protons, however, these particles are easier to shield than the secondary neutrons. With an isotropic incidence of source protons, a regolith shield thickness of ~ 100 g/cm^2 attenuates about 70% of the primary and secondary particles. The estimated dose inside the shelter is between those assuming center seeking and planar incidence of source protons.

5.9 Summary

This research investigated the interaction of source protons from solar events, like those of February 1956 with particle energy up to 1000 MeV and October 1989 with lower protons energy, but higher fluence. The study assumed the lunar shelter is 5 m in diameter and has a rectangular footprint of 5 m x 8 m and 10-cm thick aluminum support structure. However, the actual thickness of the aluminum support frame could be much smaller (~1 – 2 cm), depending on the weight of the regolith piled on top. Nonetheless, the presented results would apply, by replacing the reduced aluminum thickness with the equivalent (or same mass) thickness of the regolith. Results show that the regolith is

slightly more effective as shielding material than aluminum for energetic solar protons. In the future, using a frame structure fabricated from lighter or indigenous materials would save the high cost of bringing aluminum from Eath.

The shielding thicknesses to reduce the dose solely due to SEPs in the shelter to or below those recommended for astronauts for 30 day in space (250 mSv) and for radiation workers (50 mSv) in nuclear installations in any given year are determined. The exposure limits, however, need future investigation and validation of their applicability to future space travel of members of the public, workers and astronauts. The dose estimates presented in this work are for relative comparison, considering the uncertainties due to the simplified geometrical model of the lunar shelter and those in the input spectra and the Monte Carlo calculations, as well as in the fluence to dose conversion factors.

The estimated dose inside the shelter is calculated for three modes of incidence of the primary sources protons: center seeking, planar, and isotropic. The calculations are conducted using three-dimensional, general purpose Monte Carlo radiation transport code, MCNPX version 2.6C. The code tracks the primary and secondary protons, and secondary neutrons, gammas, deuterons, alphas and pions, within the shielding materials and the aluminum support structure of the shelter. The secondary particles and photons are generated by spallation reactions of the primary high energy protons with the nuclei of the shield material and the shelter's aluminum support structure. The dose is calculated as the product of the fluence inside the shelter times the fluence-to-dose conversion coefficients for each particle type. Results show that a February 1956 like event results in a much higher dose than an October 1989 like event, thus for a conservative consideration the former is used for the shelter shielding calculations.

For the same mass thickness, the lunar regolith is slightly more effective than aluminum for shielding SEPs. The major contributor to the estimated dose inside the shelter is by far the primary and secondary protons, followed by the secondary neutrons. The contribution of all other secondary particles and photons is negligible. The center seeking incidence of the source protons results in the highest dose estimates, followed by the isotropic incidence, while the planar incidence results in the lowest dose estimates.

With a center seeking incidence, the dose estimates inside the shelter drop below the recommended 30-day limit for the astronauts (250 mSv) with an aluminum and regolith shield thickness of ~ 25 g/cm^2 and ~ 20 g/cm^2. The source and secondary protons contribute ~ 180 mSv (72%), while the secondary neutrons contribute ~ 70 mSv (28%) to the dose estimates. With a planar incidence of source protons, the aluminum support structure alone (10 cm or 27g/cm^2 thick) reduces the dose estimates inside the shelter below the recommended 30-day limit (250 mSv). To reduce the dose estimates inside the shelter below the radiation worker limit (50 mSv) ~ 110 g/cm^2 of regolith shielding is needed. With an isotropic incidence of source protons and a regolith shield of ~ 10 g/cm^2, the dose estimates inside the lunar shelter fall below the recommended 30 days limit for astronaut (250 mSv) and below 50 mSv with ~ 120 g/cm^2 of regolith shield.

6. COMPARISONS OF PHITS AND MCNPX TRANSPORT CODES

The interactions of the incident primary radiation with target nuclei result in a modified radiation fields in the shielding materials. The propagation of these radiation fields and their alterations by atomic nuclear interactions are modeled using the radiation transport codes Monte-Carlo N-Particle transport code (MCNPX) and Particle and Heavy Ion Transport System (PHITS). This section presents the results of parametric studies using the two three-dimensional transport codes PHITS and MCNPX. The two codes will be cross-examined to determine their applicability for simulating space radiations and how the results can influence the absorbed dose rate estimates.

6.1 Monte-Carlo N-Particle Transport Code

The Monte-Carlo N-Particle Transport Code (MCNPX), developed at Los Alamos National Laboratory (LANL) and is a three-dimensional, general purpose Monte Carlo transport code. It is the results of combining the Los-Alamos High Energy Transport (LAHET) physics models and coupled high energy transport to the MCNP neutron, photon, electron code [Waters et. al. 2007, Briesmeister et. al. 2000]. The coupling allows for continuous transport of 34 different particles (neutron, photon, electron, 5 leptons, 11 baryons, 11 mesons, and 4 light ions) over a wide range of energy up to 1GeV/n. The code has an extensive statistical analysis package for tally results. It allows the user to selectively turn on and off specific particle physics. The code utilizes nuclear cross section libraries for the transport of protons, neutrons, photons, and electrons where measured data is available, typically < 20 MeV. For particles and energies where data tables are not available (typically > 20 MeV), the code uses physics models. The energy threshold for the transition from the nuclear cross-section library to the physics models is nuclide dependent and handled automatically by a mix-match algorithm in the code.

In 2008, the Los-Alamos Quark-Gluon String Model (LAQGSM) and Cascade-Exciton Model (CEM) were added to the MCNPX code package. The implementation of the LAQGSM physics model improved the interactions model of light ions and permitted the code to perform transport of over 2200 isotopes, ranging from ^{5}He up to ^{259}Fm. The maximum energy limits are also increased to 1 TeV/n, making the model useful for a

wide class of nuclear interaction problems, including reactions with protons, neutrons, pions, and photons, as well as ions [Waters et. al. 2008]. The new heavy ion transport physics along with a variety of sources, tally options, and the statistical analysis package make MCNPX a powerful tool for investigating space radiation interactions. The MCNPX code is well benchmarked and currently maintained by Los-Alamos MCNP team and RSICC.

6.2 Particle and Heavy Ion Transport code System

The Particle and Heavy Ion Transport System (PHITS) code is a three dimensional Monte Carlo code that simulates the transport of nuclei and other particles in complicated geometries and calculates fluxes, doses, energy deposition distributions and many other observables [Iwase et. al. 2002]. The code, developed at Japan Atomic Energy Research Institute (JAERI), couples the high-energy particle transport code Nucleon-Meson Transport Code (NMTC)/Jet AA Microscopic transport model (JAM) with JAERI Quantum Molecular Dynamics (JQMD) and SPAR heavy ion transport code [Iwase et. al. 2002]. The incorporation of the JQMD model makes it possible to model nucleus-nucleus interactions and estimate atoms fragmentation up to energies of 200 GeV/n. For low energy transport, the code can process tabulated cross-sections and data tables [Breismeister, 2000]. The generalized-geometry description system, treats problem geometry primarily in terms of surface, regions, and volumes, similar to that in the MCNP code system, is incorporated as the PHITS geometry input. The source types of cylinder, rectangular, Gaussian, generic parabola, sphere and spherical shell, and a user definition subroutine are supported for any energy distribution [Sato et. al. 2006]. The PHITS code had been under rigorous benchmarking and is currently supported by the Research Organization for Information Science and Technology (RIST), Japan Atomic Energy Agency (JAEA) and High Energy Accelerator Research (KEK) in Japan and Chalmers University in Sweden.

6.3 Simulation Approach

To compare the results of the PHITS and MCNPX transport codes, a simplified spherical space station and spherical phantom are employed. The spherical tissue

equivalent phantom has an outer diameter of 35 cm and a mass of 32 kg. It is composed of 8.63% Hydrogen, 2.6% Nitrogen, 32.3% Oxygen, and 56.5% Carbon; similar to the spherical MATROSHKA phantom aboard the ISS experiment [Kartsev et. al. 2005; Akatov et. al. 2007]. The spherical phantom is positioned concentric with a spherical aluminum structure, simulating that of a space station. The spherical aluminum station is 400 cm in diameter. The structure has an aluminum mass shielding thickness of 12.5 g/cm^2, and the station interior is filled with Air at atmospheric pressure.

The spectra of the Trapped Protons and GCRs source used in the simulations are obtained from CREME96 (Cosmic Ray Effect on Micro Electronics 1996) [Tylka et al. 1997; Sihver et al. 2009]. The Trapped Protons spectra used in the simulations are based on the average orbit parameters of the International Space Station, with orbit inclination ~51.6^0 and an altitude of 370 km [Kartsev et al. 2005]. The GCR spectra are based on the pre-calculated spectrum implemented in CREME96 [Tylka et al. 1997]. So far only two orbits are implemented in CREME96; the geomagnetic transmission for the ISS orbits and the general orbit for Shuttle mission at either solar minimum or maximum conditions. The ISS orbit model at a solar minimum condition is used here as the GCR source. No Trapped Electrons are included in the simulations since they are expected to be absorbed in the walls of the ISS module because of their low energies [Wilson et. al. 2001]. The trapped protons and GCRs spectra are incident as spherical external isotropic source, on a surface of a sphere that is 600 cm in diameter. Figure 6.1 show the layout of the simplified geometry used for the parametric studies of the two transport codes. The secondary spectra of protons and neutrons, calculated at different positions, are intercompared in PHITS and MCNPX. The trapped protons and GCRs simulations are performed separately. Each simulation is performed with 500 millions source particles in order to ensure good simulation statistics, particularly for the secondary spectrum inside the phantom.

6.4 Results and Discussion

The incident trapped protons and the calculated secondary protons spectra simulated with PHITS and MCNPX are shown in Figure 6.2. The calculated spectra of the secondary protons at the different location inside a simulated ISS module and

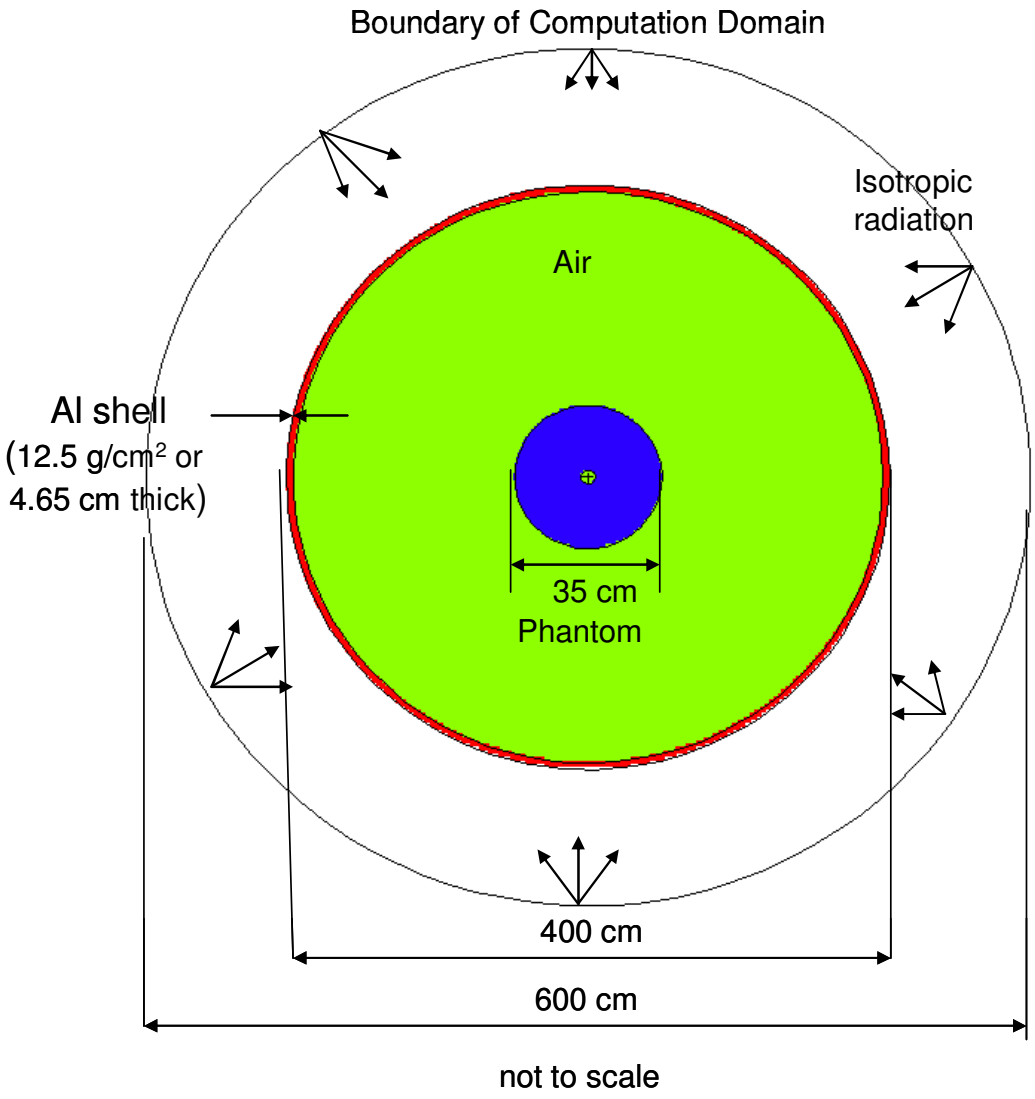

Figure 6.1. Schematic of simplified geometry for comparison of PHITS and MCNPX.

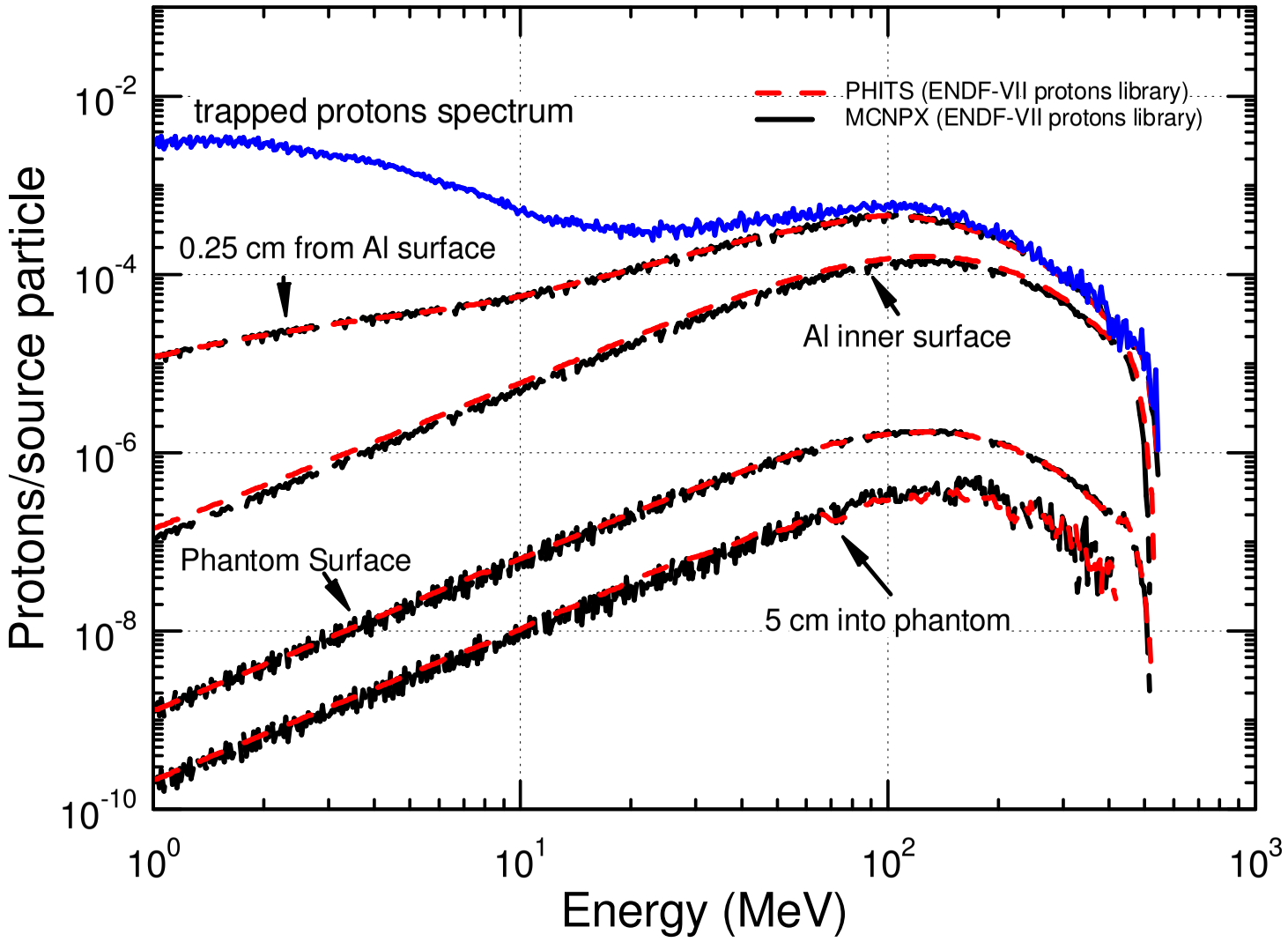

Figure 6.2. Incident trapped protons and calculated secondary protons spectra using PHITS and MCNPX codes.

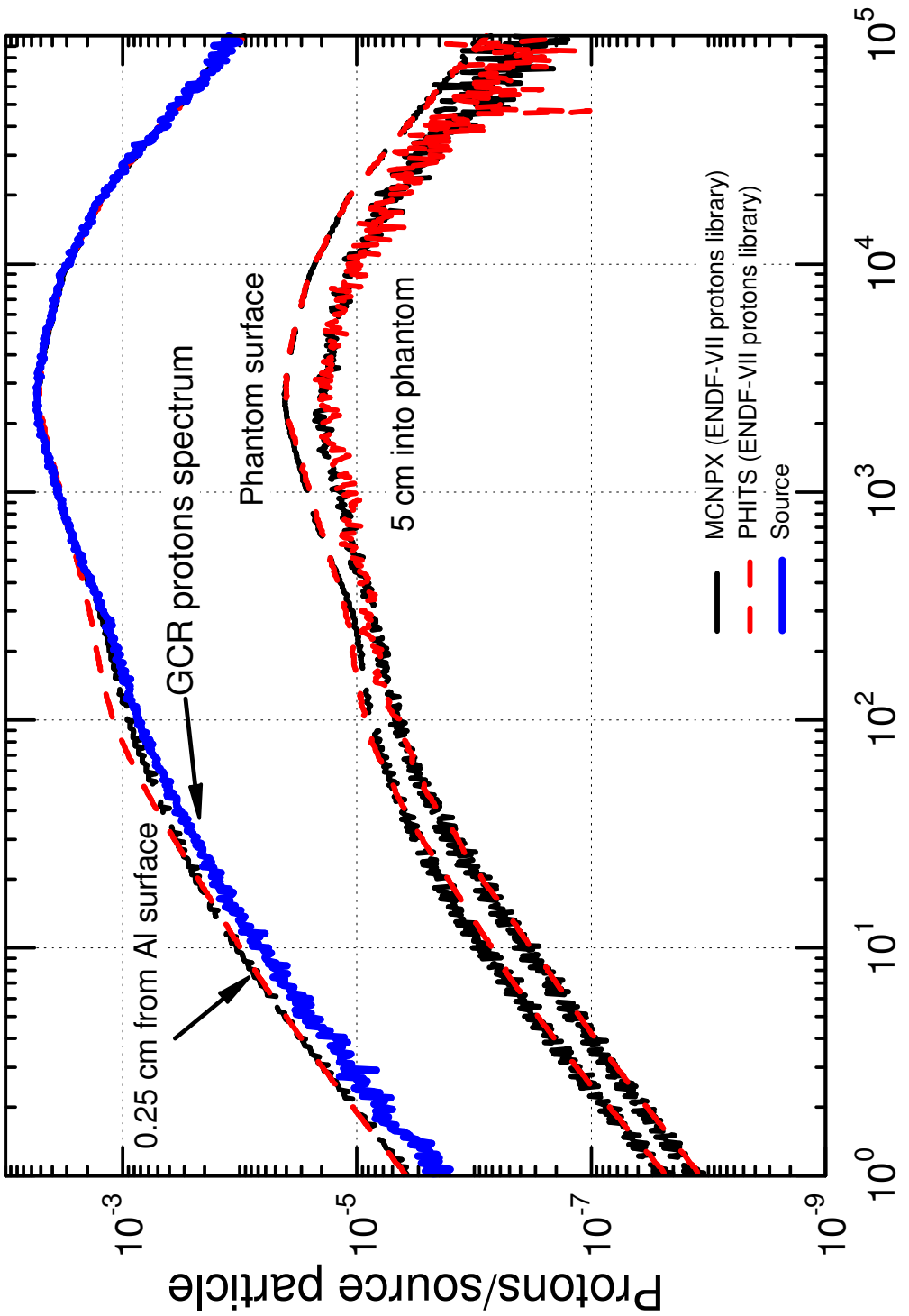

Figure 6.3. Incident GCR protons and calculated secondary protons spectra using PHITS and MCNPX codes.

phantom are compared. At position of 0.25 cm into the Aluminum structure outer surface, the low energies tail of the incident trapped protons spectrum has already been significantly attenuated, decreasing by an order of magnitude. Though the high energy end >100 MeV are largely unaffected. At the inner surface of the Aluminum structure (12.5 g/cm^2), the protons spectrum is significantly altered, with reductions in both the number of protons, as well as those with energies > 100 MeV. The low energy tail of the spectrum of the protons is further reduced by an order of magnitude, while the difference in the high energy end evidently more altered. Moving inward to the phantom surface, a large reduction in the numbers of protons occurs, largely due to the reduction in the surface area. The difference between the protons' spectra at the station inner aluminum surface and the phantom surface is about two-orders of magnitude. The air between the structure and phantom does not significantly affect the protons energies, nor the protons' spectrum. Further in, at 5 cm into the phantom (~ the body depth of radiosensitive organs and blood-forming organ), the protons' spectrum further soften, with a reduction in both the high energy particle in the spectrum and the overall number of protons. Such reductions are particularly due to the decrease in surface area and the effects of stopping power of the phantom material composition. The stopping powers of the lighter elements composing the tissue equivalent phantom are more prominent, as the difference in area between the phantom surface and at a position 5 cm into the phantom is < 2.

Figure 6.3 show a similar comparison of the caculated protons spectra for the incident GCR source particles. The GCR protons spectrum is shown alongside of the calculated spectra at the different locations for comparisons. It can be seen that the high energy end of the GCR protons spectrum is largely unimpeded by the Aluminum structure of the station. At energy approximately > 400 MeV, the protons' spectrum in the aluminum structure and that of the incident GCR protons practically overlapped. It is interesting to note, that unlike trapped protons, the spallation interactions of the high energy GCRs particles builds up a low energy tail, beyond that of the incident protons spectrum; particularly for energies < 100 MeV. Based on a previous study [Pham & El-Genk 2008], for protons with energies < 100 MeV, a shield mass thickness of ~10 g/cm^2 should've been sufficient to stop the protons. The buildup of the low energy protons suggested significant spallation interactions between the incident high energy GCR with

aluminum, in which additional secondary protons are produced. At the phantom surface, there is a large reduction in the protons' number, approximately two-orders of magnitude less than the calculated spectrum at the aluminum surface. Again, this is due primarily to the differences in surface areas at the two locations. Beside the large reduction in the protons' number, the spectrum remained practically the same, as the air between the structure and phantom does not change the spectrum. At 5.0 cm into the phantom, there is a further reduction in the protons' number, though this difference is much smaller than that of the trapped protons in Figure 6.2. The protons' number is approximately ½ that at the phantom surface, about the difference in surface area. This indicates that the high energy GCR particles are capable of penetrating deep into the phantom, beyond 5 cm of tissue equivalent materials. This is particularly important for the absorbed dose rate estimates, which depend upon the numbers (or flux, fluence) of the particles and the corresponding energy spectra. The relatively flat distribution of the protons' number, and the largely preserved GCR energy spectra, can lead to a flat distribution of the energy deposition or absorbed doses inside the phantom.

The results in Figure 6.2 and Figure 6.3 demonstrate the relative difference in results between the simulation using PHITS and MCNPX codes. The results are very comparable. Even after transported through the aluminum structure and 5 cm into the phantom, the calculated normalized protons' spectra agree with each other, except for a small difference at the low energy ends of the calculated spectra for the trapped protons'. The difference between the simulation results of PHITS and MCNPX increases for the secondary neutrons spectra at different locations within the simulation domain. Figures 6.4a – 6.4d compared the secondary neutrons spectra for the incident trapped protons, at the locations: (a) 0.25 cm from station aluminum surface (b) inner aluminum surface (c) the phantom surface and (d) 5 cm into the phantom. As can be seen, the results of the simulations using MCNPX and PHITS codes are in agreement with each other for energies > 20 MeV. Below 20 MeV, the results of the codes are different, both in the magnitude of the normalized secondary neutrons, as well as the trend. The PHITS results show a smooth reduction in the neutrons number with decreasing energy < 20 MeV. While the results of MCNPX simulations are much lower than those of PHITS for energies < 100 eV, they increase with increasing energy, exceeding those of PHITS for

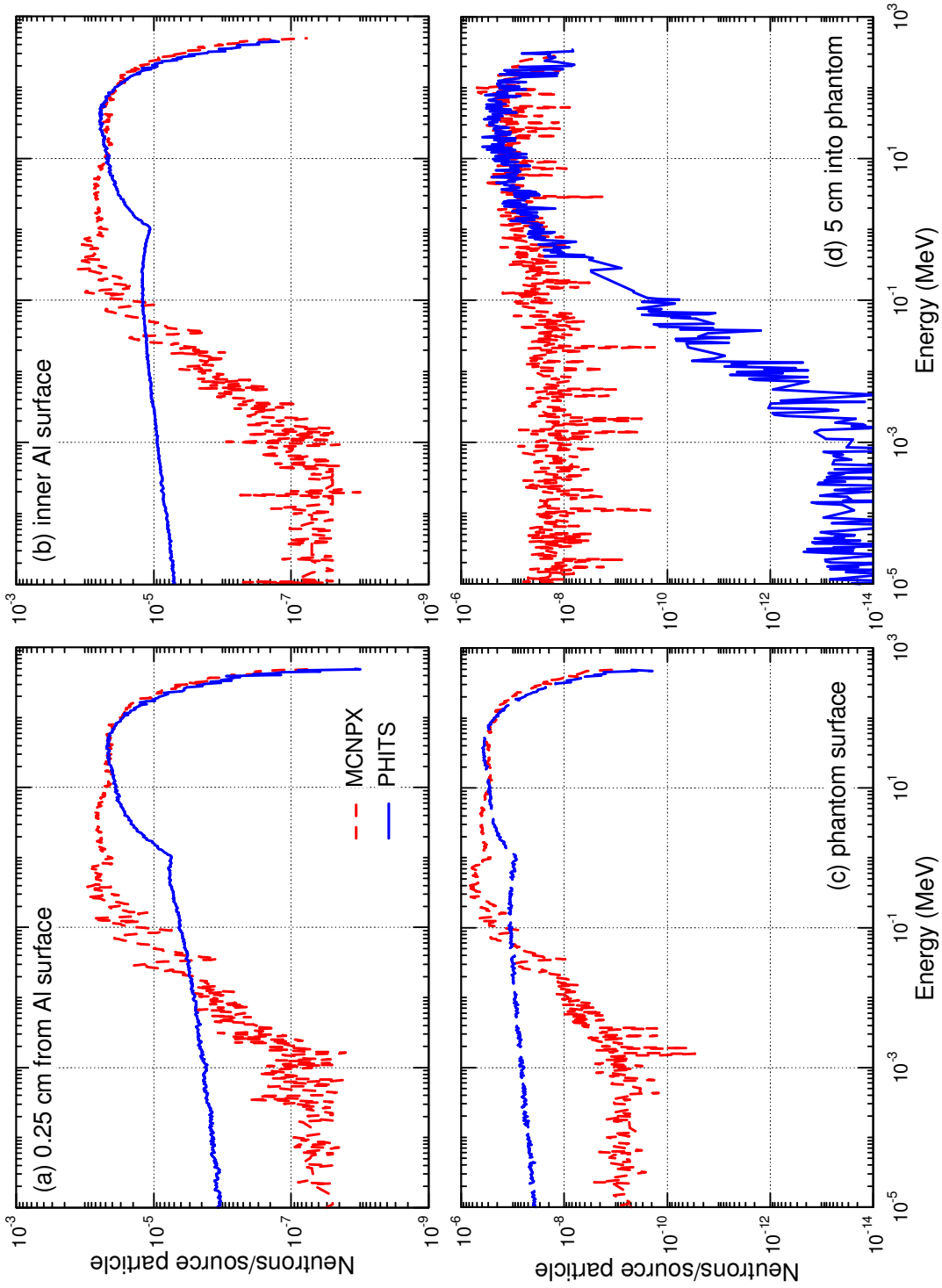

Figure 6.4. Secondary neutrons spectra resulted from Incident trapped protons.

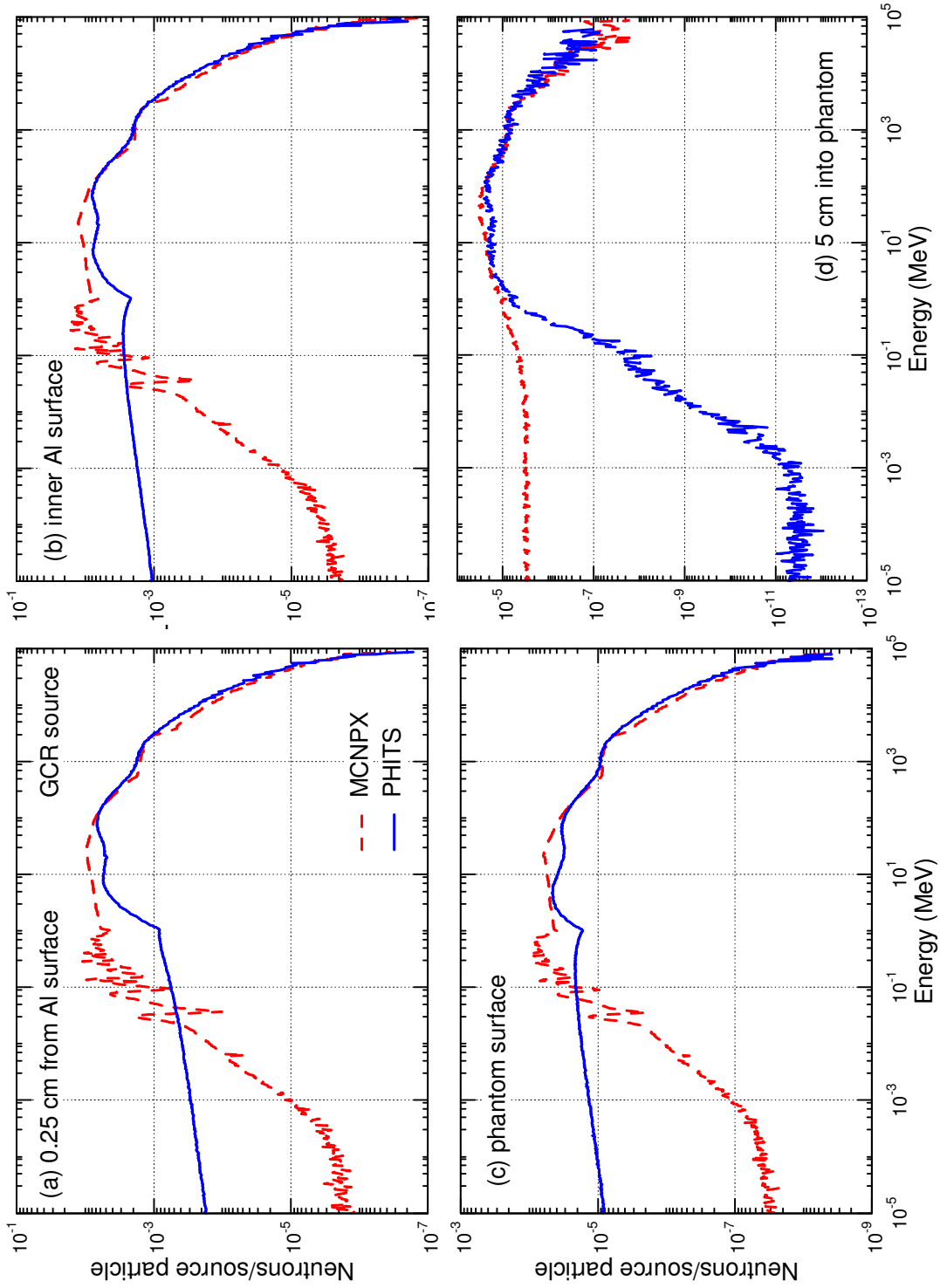

Figure 6.5. Secondary neutrons spectra resulted from Incident GCRs.

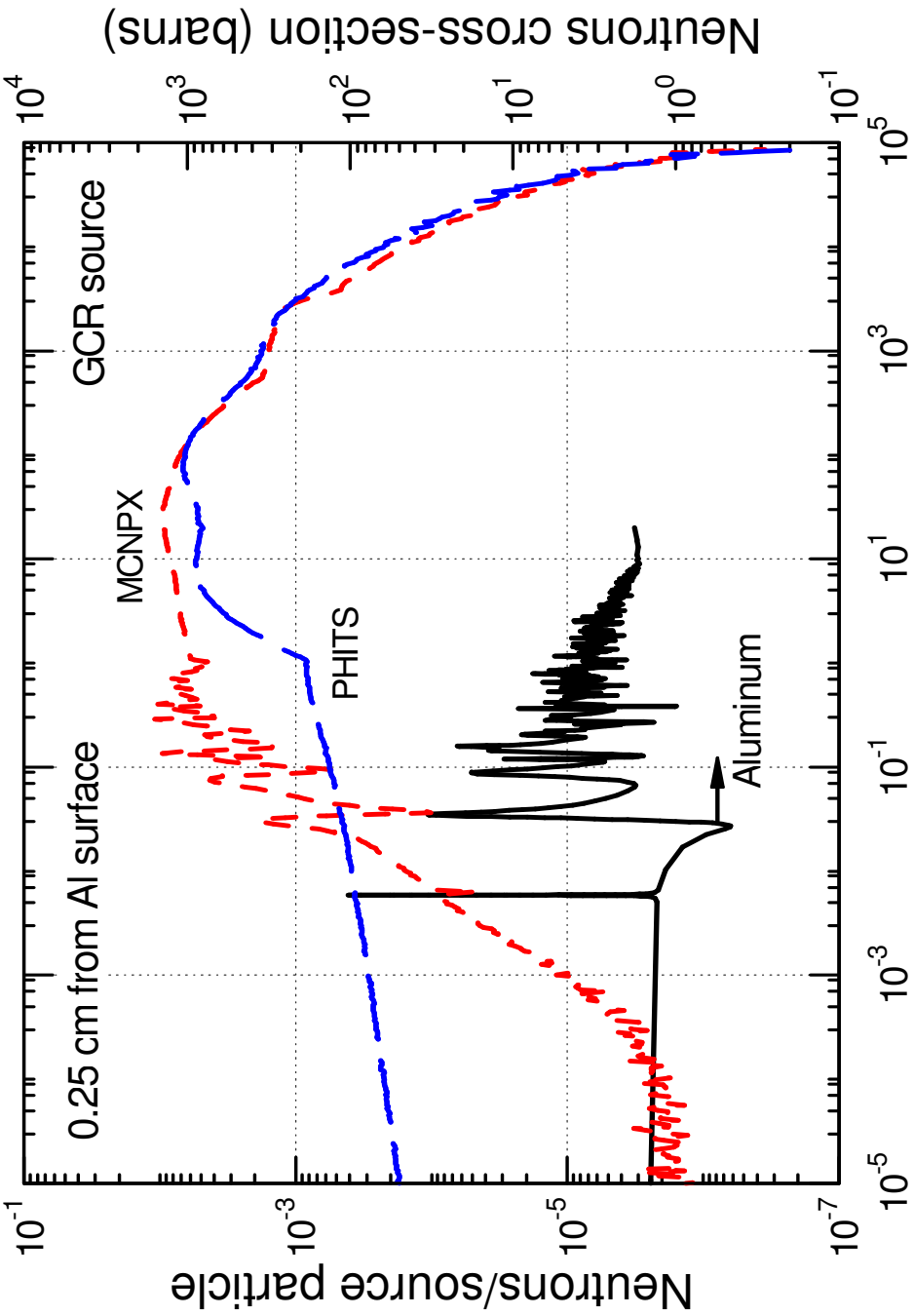

Figure 6.6. Comparison of the calculated spectra using incident GCRs with the Aluminum cross-section (ENDF-VII).

energies between 100 eV and 10 MeV. At higher energies, the results of PHITS and MCNPX are almost identical. The results of MCNPX also show a lot of scattering unlike the smooth reduction of the PHITS simulation results. Similar trends can be seen at the inner aluminum surface (Figs. 6.4b) and at the phantom surface (Figs. 6.4c). At 5 cm into the phantom, the calculated secondary neutrons spectrum using PHITS is significantly higher than that calculated using MCNPX for energies < 1 MeV, and similar at higher energies.

The calculated energy spectra for secondary neutrons from GCRs incident particles using PHITS and MCNPX are compared in Figure 6.5a – 6.5d. The results are similar to those for the incident trapped protons simulations in Figs. 6.4a – 6.4d. For neutrons energies > 20 MeV, the calculated neutrons spectra using both the PHITS and MCNPX codes agree well with each other. At lower energies (< 20 MeV), the results of PHITS are consistently higher than those of MCNPX.

To investigate the difference in the calculated neutrons spectra using PHITS and MCNPX, the Aluminum neutrons cross-section is plotted with the PHITS and MCNPX calculated neutrons spectra at 0.25 cm from the surface of the Aluminum structure of the station (Figure 6.6). Note that the peaks and troughs of the MCNPX calculated neutrons spectrum match the troughs and peaks in the resonance region of the Aluminum neutrons cross-section. Conversely, the PHITS simulation results show no such coincidence with the Aluminum neutrons cross-section, suggesting that the difference might due to PHITS default treatment of the data library available at low energy < 20 MeV.

In the initial simulations, the called up data are for high energy protons, since the incidents particles are high energy Trapped Protons and GCRs. Other secondary particles: such as neutrons, gammas, alphas, etc., are subject to the physics models at high energies (> 20 MeV). In MCNPX, the data selection and call-up are by default, so secondary particles (in this case neutrons) are automatically treated with cross-section data library ENDF-VII for energy < 20 MeV. The PHITS code, on the other hand, by default treats the secondary particles directly by the physics model. Using physics model for low energy neutrons (< 20 MeV) is not appropriate, leading to erroneous results as demonstrated in Figures 6.4 and 6.5 [Sato et al. 2004; Sihver et al. 2010].

To rectify this issue, for the same simulation conditions, the ENDF-VII neutrons library is called specifically for all available atoms, while the protons are, by default, treated with physics models in the two codes. The secondary protons and neutrons spectra are calculated using the two codes for trapped protons and GCRs incident spectra. The obtained results are compared in Figure 6.7 and 6.8. Comparisons are shown at three different locations: 0.25 cm from Aluminum structure surface, inner Aluminum surface, and the phantom surface. As can be seen, the calculated protons spectra using PHITS and MCNPX are very similar. In both PHITS and MCNPX simulations, the results of the physics models and those using ENDF-VII protons library result in practically overlapping protons spectrum. However, there is a clear difference in the secondary neutrons spectra, using the two codes (Fig. 6.9). The calculated secondary neutrons spectra using PHITS at 0.25 cm from Aluminum structure surface, inner Aluminum surface, phantom surface, and 5 cm from phantom surface are compared in Figure 6.9a – 6.9d. When using the ENDF-VII protons library, the calculated secondary neutrons spectrum by PHITS shows relatively smooth transitions from high energy to low energy, without any evidence of scattering effects. However, the calculated neutrons spectrum based on the ENDF-VII neutrons library are very similar to that calculated using MCNPX code. Both show peaks and troughs corresponding to the resonance scatterings of Aluminum in the energy regime < 20 MeV. At high energy > 20 MeV, the calculated secondary neutrons spectra using both PHITS and MCNPX are very similar, since both codes use similar physics model.

Figure 6.10a – 6.10b show similar comparisons for MCNPX simulations for incident GCRs. The MCNPX produced secondary neutrons spectra using either the neutrons or protons ENDF-VII libraries are the same, over the entire energy range. This is expected, since MCNPX, by default, applies cross-sections treatment where data library is available. In this case, ENDF-VII neutrons and protons library is used for energies < 20 MeV, while physics models are used for neutrons at higher energies, > 20 MeV.

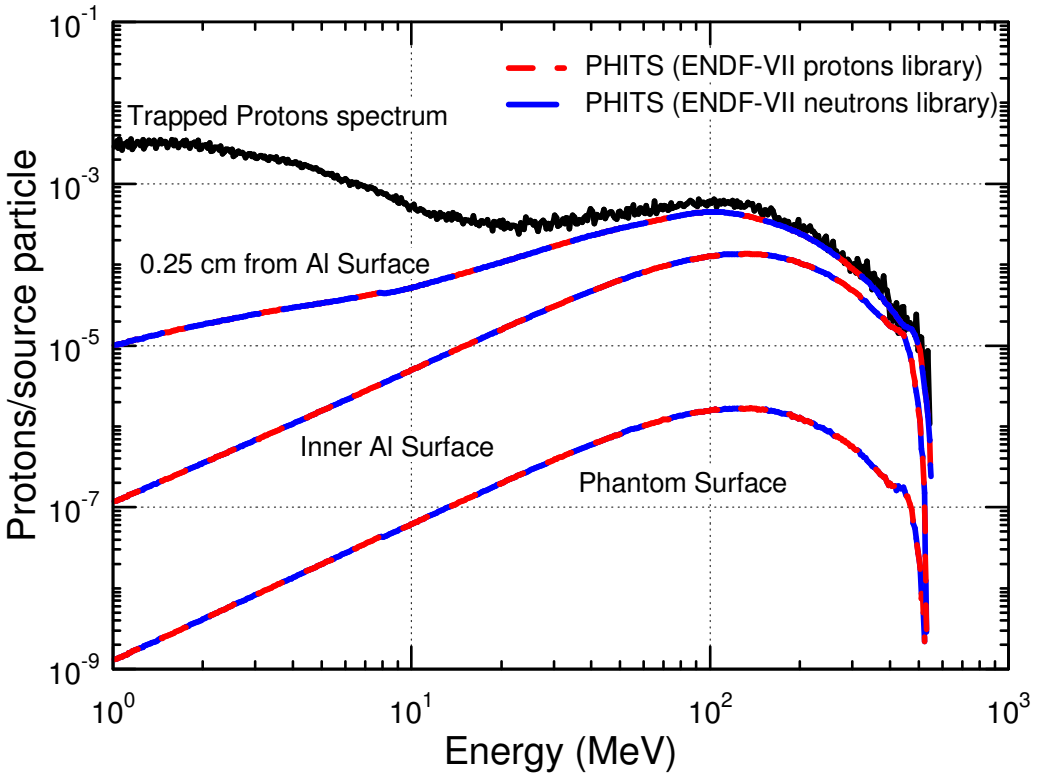

Figure 6.7. Secondary Protons spectra simulated in PHITS using ENDF-VII protons and neutrons library.

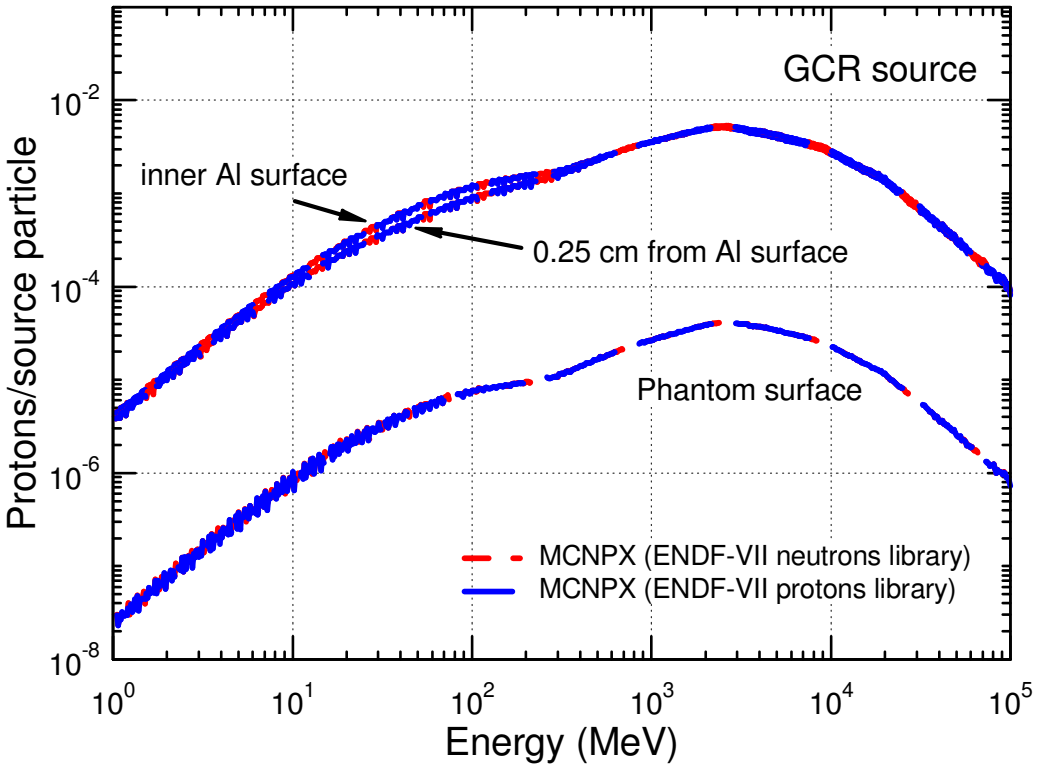

Figure 6.8. Secondary Protons spectra simulated in MCNPX using ENDF-VII protons and neutrons library.

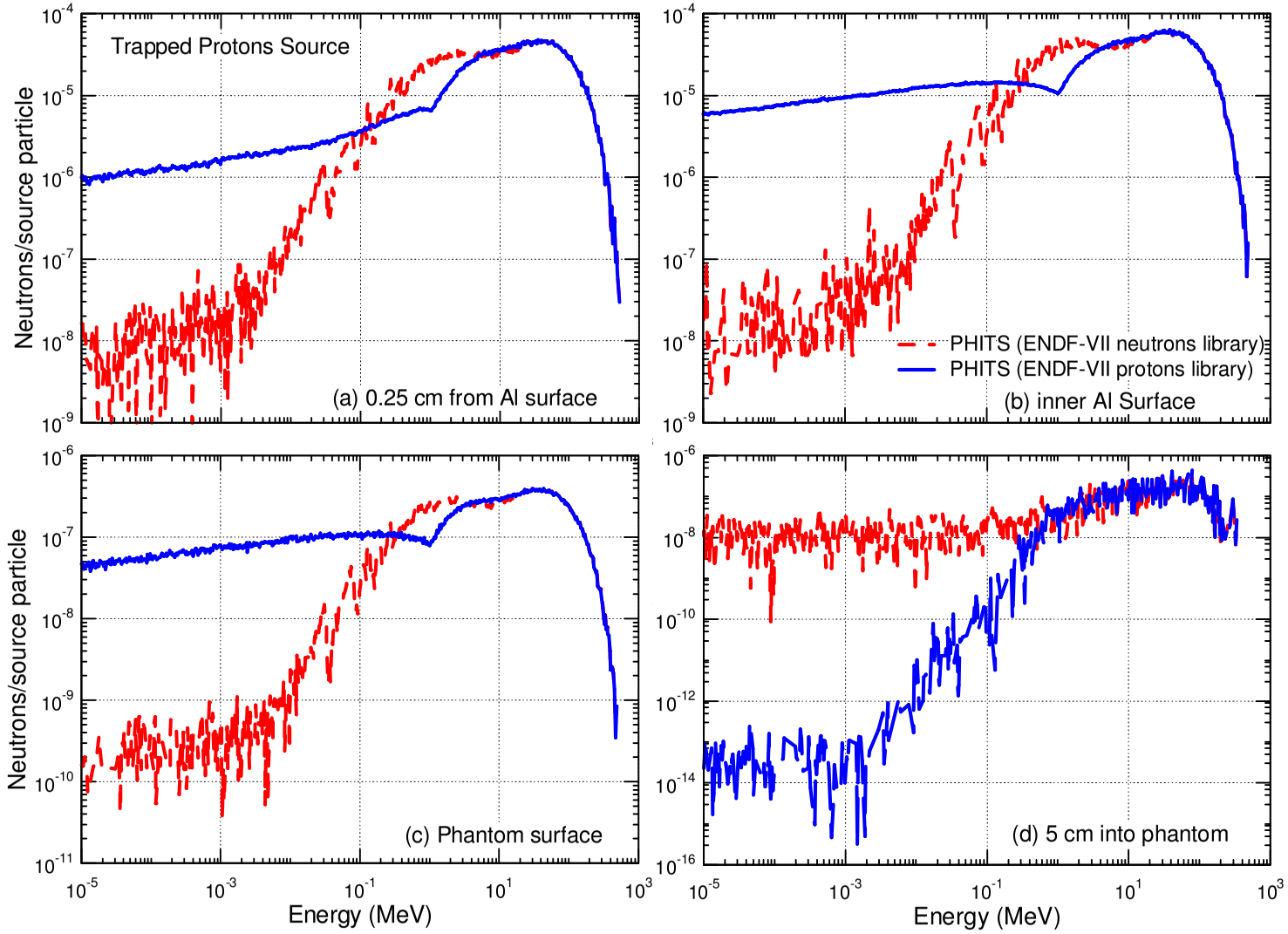

Figure 6.9. Calculated secondary neutrons spectra resulting from Trapped Protons Incident Source, using PHITS with ENDF-VII protons and neutrons library.

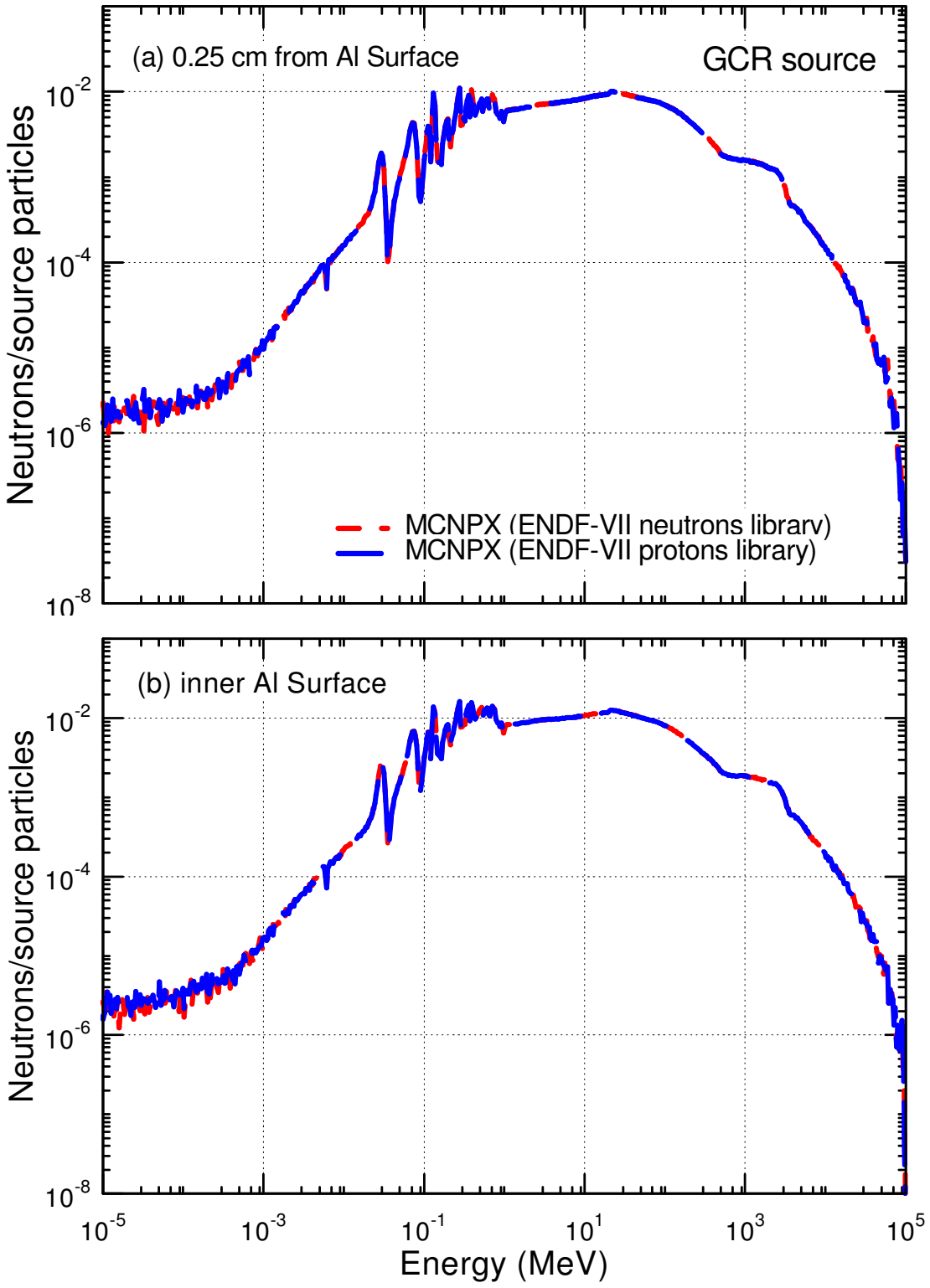

Figure 6.10. Calculated secondary neutrons spectra for Trapped Protons Incident Source, using MCNPX with ENDF-VII protons and neutrons library.

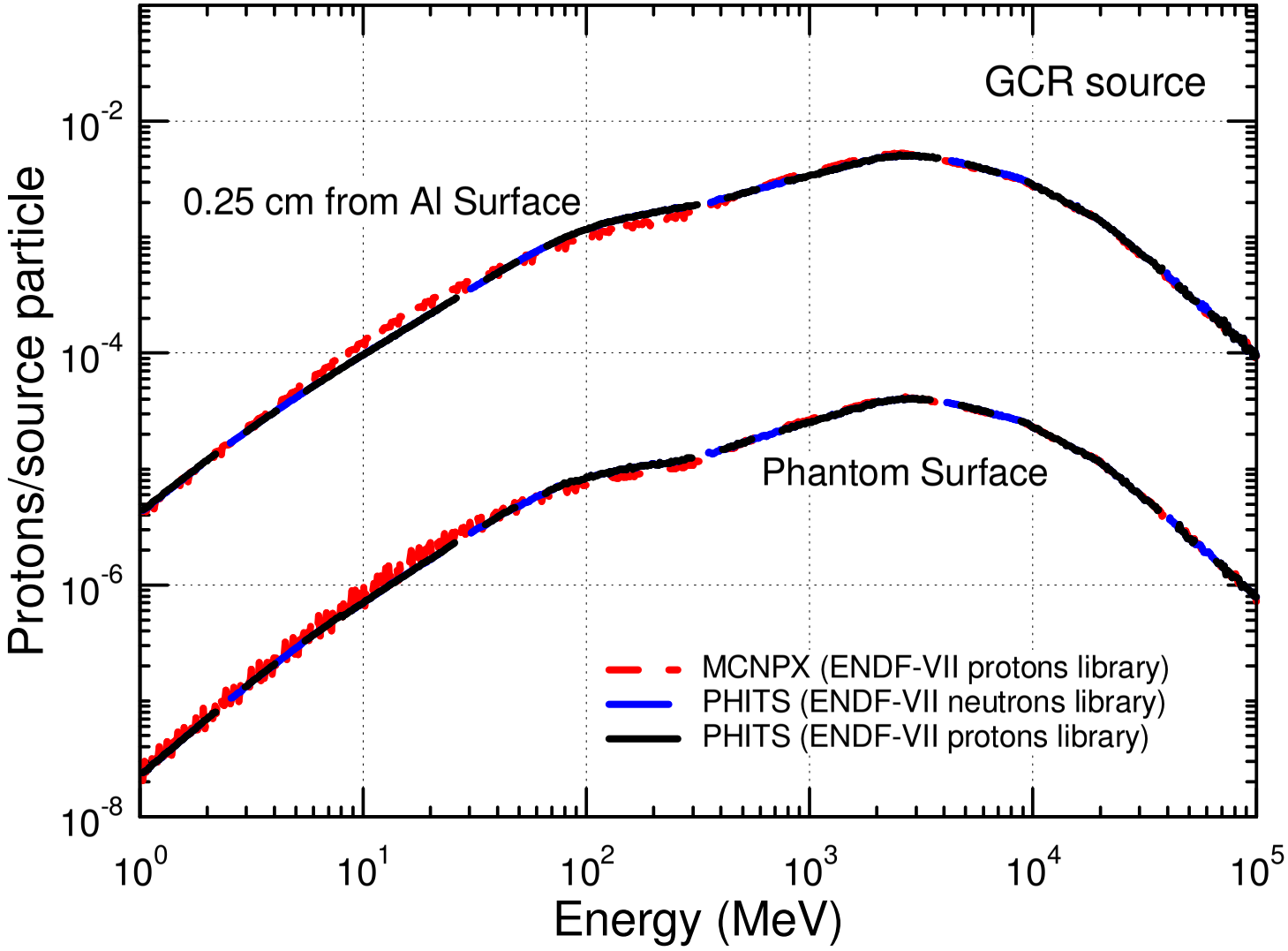

Figure 6.11. Comparison of PHITS and MCNPX for the calculated secondary protons spectra resulted from Incident GCRs.

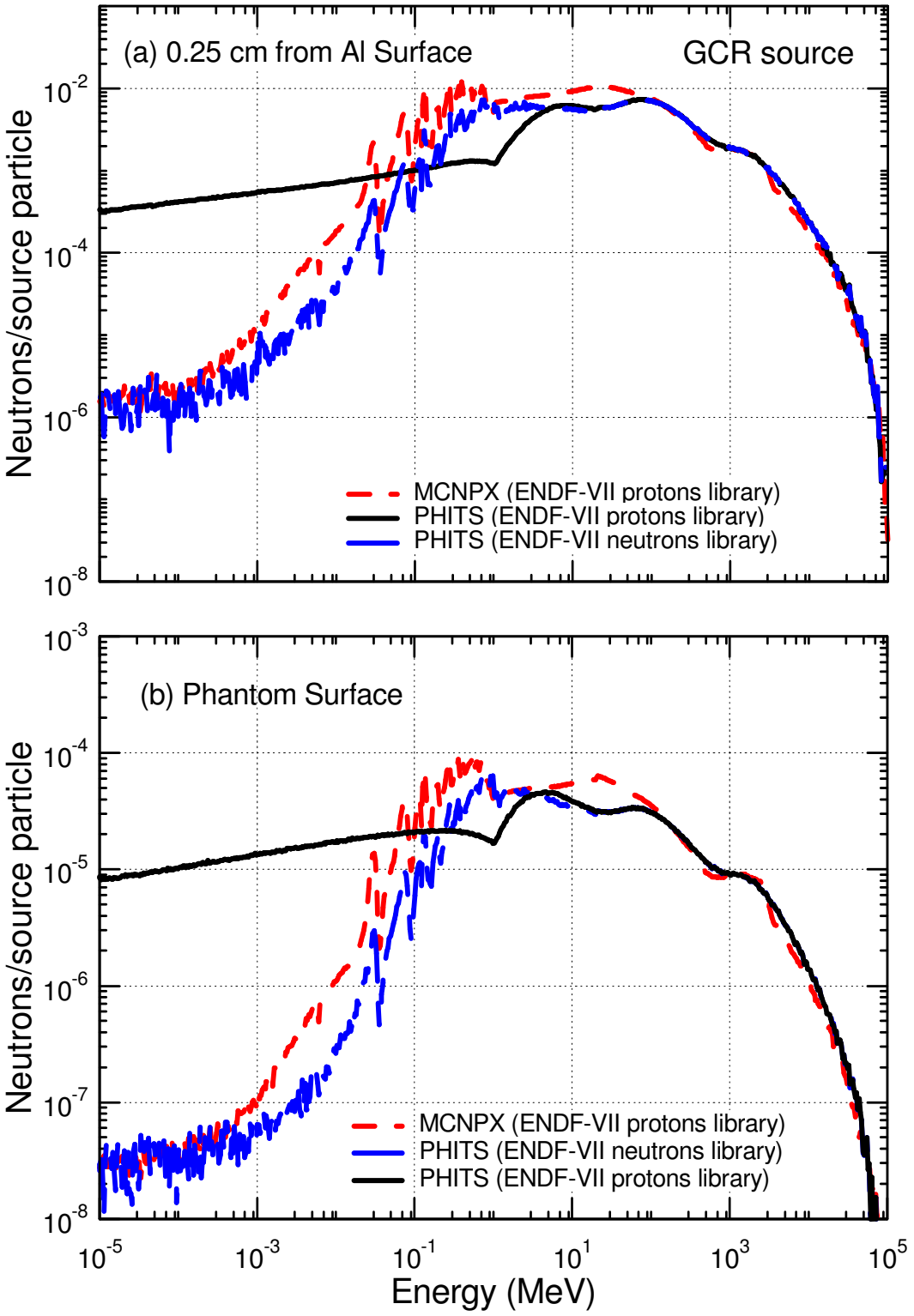

Figure 6.12. Comparison of Calculated secondary neutrons spectra using PHITS and MCNPX for Incident GCRs.

Figure 6.11 compares the results of simulations for the secondary protons spectra, using PHITS with ENDF-VII protons and neutrons library, along with those of MCNPX using the protons cross-section library. The protons spectra calculated by both codes are very similar over the entire energy range from 1 MeV to 10^5 MeV. Only a slight difference can be seen between the results of PHITS and MCNPX of the protons spectrum at energies < 400 MeV.

Figure 6.12a – 6.12b compares the calculated spectra of the secondary neutrons using PHITS with protons and neutrons cross-section libraries, and those using MCNPX but with the protons cross-section library. As mentioned before, using the protons library in PHITS resulted in a default physics model treatment for secondary particles such as neutrons. Conversely, MCNPX uses the cross-section library for both neutrons and protons with energies < 20 MeV, and physics models only at higher energies. Figs. 6.12a and 12b show that the results of PHITS are widely different from those of MCNPX. When the PHITS simulation uses ENDF-VII neutrons library, the calculated secondary neutrons spectrum shows more scattering effects for energies < 20 MeV. When using the ENDF-VII neutrons library for energies < 20 MeV, the peaks and troughs of the scattering effects in the calculated spectra by both PHITS and MCNPX corresponded with each others. Though showing the same trend, the MCNPX results consistently predict higher generation of low energy neutrons than PHITS. This difference, however, is primarily for energies < 1 MeV, which are not important for radiation dose estimates.

6.4 Summary

MCNPX and PHITS simulations produced identical results for incident trapped protons and GCR particles for energies > 20 MeV, since both codes use similar physics models. At lower energies, there was a large difference in the calculated secondary neutrons spectra. This is because in this energy range, MCNPX use cross-section library for both neutrons and protons, while the default treatment of PHITS uses cross-section library for protons and physics models for neutrons. Since physics model is not the appropriate treatment in this energy range, the calculated secondary neutron energy spectrum by PHITS is higher than that calculated with MCNPX and does not reflect the peaks and troughs of the continuous cross-section energy spectrum. Thus, MCNPX is

preferred choice for simulating space radiation and estimates of the dose rate. PHITS will give similar results, but only when the default changes to use neutrons and protons cross-section library, rather than physics model, at low energies (< 20 MeV). The next chapter uses MCNPX to calculate the dose rate in the phantom experiment onboard the ISS.

7. SIMULATIONS OF MATROSHKA-R PHANTOM ABOARD ISS

This chapter presents the experimental measurements of the MATROSHKA-R spherical phantom aboard the Russian segment of the International Space Station, and the efforts to simulate the experimental measurements using the state-of-art transport code MCNPX. The simulated absorbed dose rates inside the spherical phantom are calculated and compared directly with the experimental measurements.

7.1 Introduction

The radiation field inside a spacecraft is very complex. In low Earth orbit, it is composed mainly of galactic cosmic rays (GCRs), Solar Energetic Particles (SEPs), and Trapped Protons and Electrons in the Earth's radiation belts. The radiation field at a location, inside the spacecraft is affected both by the shielding and surrounding materials [Badhwar et al. 1998; Shurshakov et al. 1999; Benton and Benton 2001; NCRP 2000]. Dose characteristics during a space mission depend also on many parameters such as the phase of the solar cycle, spacecraft orbit parameters, and helio-and-geophysical parameters [Wilson et al. 2004; NCRP 2000; NCRP 2005]. The exposure level onboard spacecraft is several hundred times higher than at Earth surface and onboard an aircraft, representing a major health concern for astronauts [NCRP 2000]. To ensure the astronauts' safety and minimize risk, it is important to determine their exposure level as accurately as possible.

There are two principal methods to acquire information on the exposure level onboard spacecrafts: experimental measurements and theoretical simulations using Monte Carlo radiation transport codes [Badhwar et al. 2001; NCRP 2000; NCRP 2006]. Experiment on the ground to simulate space radiation and its influence on a human is a complicated problem. Space radiation includes a complex mix of ionizing radiations (protons, electrons, neutrons, and other heavy ions), over a wide range of energies, and whose composition and energy spectra vary temporally and spatially [Badhwar et al. 2001; Wilson et al. 2001]. In addition, shielding properties, geometry and material affect potential estimates of exposure. Currently, estimates onboard the International Space Station (ISS) are based on the data collected by a functioning set of radiation monitoring

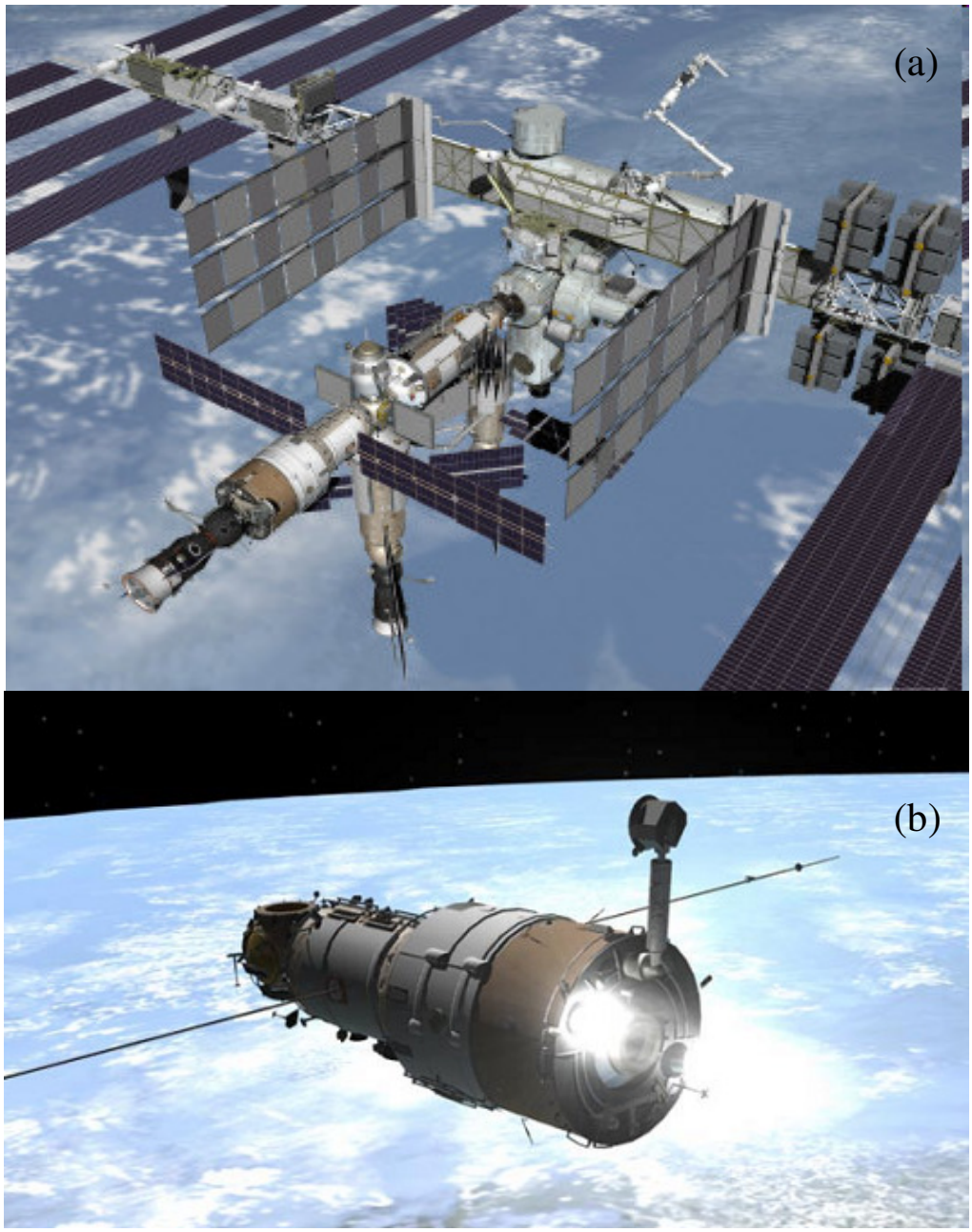

Figure 7.1. Image of the ISS and the Russian Module Zvezda. (a) Bird eye view of the ISS, and (b) Russian Module Zvezda.

devices distributed throughout different compartments [Badhwar et al. 1998; Wilson et al. 2004; NCRP 2000]. To record personal dose, crewmembers onboard are provided with passive detectors in the pockets of their flight suits [Badhwar et al. 1998; Wilson et al. 2004]. These monitoring devices, however, measure the dose at one point on the human body. No information is provided on the dose received inside the body [Badhwar 2000; Lyagushin et al. 2001; Jadrnickova et al. 2009; NCRP 2002].

The assessment of radiation exposure to astronauts is currently based on the combined dose from all radiation sources to the radiation sensitive and blood-forming organs (BFO) [ICRP 1993; NCRP 2000; ICRP 2003; NCRP 2002]. Accurate estimates require measurements of the dose distribution at various locations at the surface and inside the human body. However, direct dose measurements inside the organs of living subjects are not possible. To gain knowledge of the dose deposition and distribution inside a human body, phantom experiments, simulating the human body, have been conducted in-flight onboard the Space Shuttle and the ISS.

In 2004, the Institute for Biomedical Problems in Moscow (IBMP) has developed and flown an advanced spherical phantom MATROSHKA-R (MTR-R) aboard the Russian segment of the ISS. The dose distributions inside the spherical phantom were measured. The initial data recording was during space flights of crews ISS – 8, 9 (2004 – 2005) in the Russian Service/Crew Module cabin Zvezda of the ISS. This experiment is one of the first to study the radiation environment inside various compartments of the ISS over a long-duration mission. Figure 7.1a shows a bird view of the ISS, and Figure 7.1b shows an image of the Russian Module Zvezda.

While direct measurements are a necessity to assess the radiation hazard in space, it is impossible to perform experiments for all possible combinations of project-target and energy-geometry. Thus, to complement direct measurements, computer simulations are a useful tool for estimating radiation hazard. The focus of this section is therefore to simulate the experimental setup of the MATROSHKA-R spherical phantom used aboard the ISS, and benchmark the simulation methodology with measurements. The MATROSHKA-R spherical phantom is reproduced as described in the experimental setup, and absorbed dose rates are calculated using the state-of-art MCNPX transport

code. The absorbed dose rates estimates inside the phantom are directly compared to the measurements, validating the simulation methodology.

7.2 Experimental Setup

The MATROSHKA-R (MTR-R) phantom is a multi-user unit for studies of the accumulation and spatial distribution of the dose due to the exposure to different components of the onboard radiation field inside compartments of the ISS [Akatov et al. 2007]. The phantom consists of 13 slices made of the tissue equivalent prepolymer Diafor-TDI, with the following chemical composition, expressed by weight contribution: 8.63% Hydrogen, 2.6% Nitrogen, 32.3% Oxygen, and 56.5% Carbon [Kartsev et. al. 2005; Akatov et. al. 2007]. The slices stacked together form a spherical phantom with an outer diameter of 35 cm and an inner spherical air cavity of 10 cm diameter. Cylindrical channels are pierced through the phantom for placement of detectors. There are four main perpendicular channels across the equatorial plane. Passive Thermo-Luminescent Detectors (TLDs) and solid state Plastic Nuclear Track Detectors (PNTDs) installed inside tissue equivalent containers were inserted into channels within the phantom (Figs. 7.3 and 7.4). About 300 detectors are placed inside the phantom, at regular intervals, to measures the absorbed dose at their designated positions. The total weight of the phantom loaded with the detectors is about 32 kg [Kartsev et al. 2005; Akatov et al. 2007; Shurshakov et al. 2008].

Figure 7.2a shows a schematic of the MATROSHKA-R phantom and a cross-section view showing the detectors channels and Figure 7.2b shows the phantom covered with a working jacket [Kartsev et al. 2005; Akatov et al. 2007]. Figure 7.3 shows a picture of the actual phantom with detectors channels [Shurshakov et al. 2008]. The assembled phantom, covered in a working jacket (Fig. 7.2b), was installed on the starboard crew cabin floor of the Zvezda Module of ISS.

The Zvezda Module, the first Russian contribution to the International Space Station, served as the cornerstone for early human habitation of the station. The 42,000-pound module provides the station's living quarters, life support system, electrical power distribution, data processing system, flight-control and propulsion system. The module is

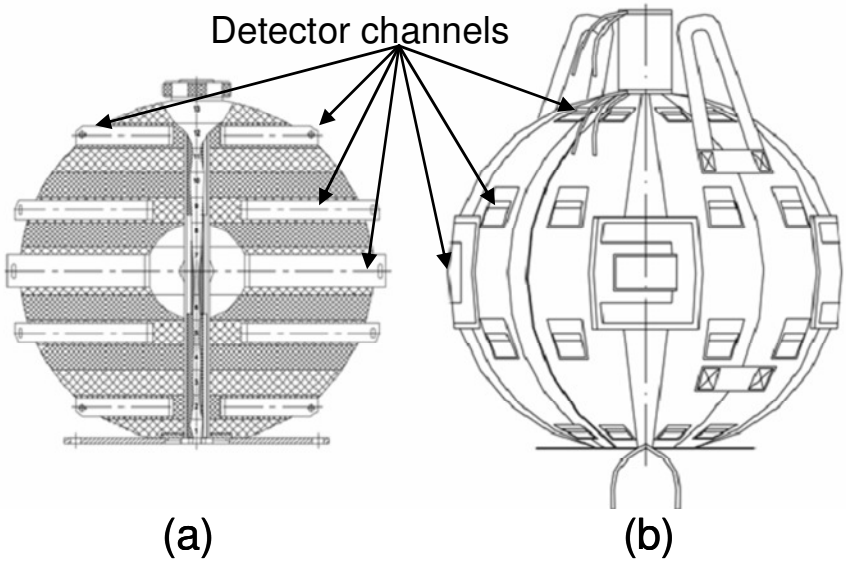

Figure 7.2. Schematic of the MATROSHKA-R phantom (a) cross-section view of phantom showing detector channel (b) phantom covered with working jacket [Akatov et al. 2007; Shurshakov et al. 2008].

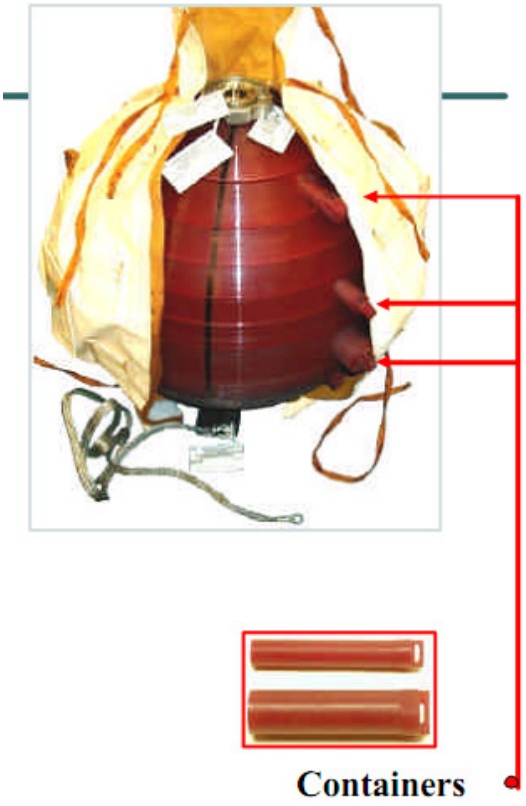

Figure 7.3. Picture of actual phantom with sample detector containers [Kartsev et al. 2005].

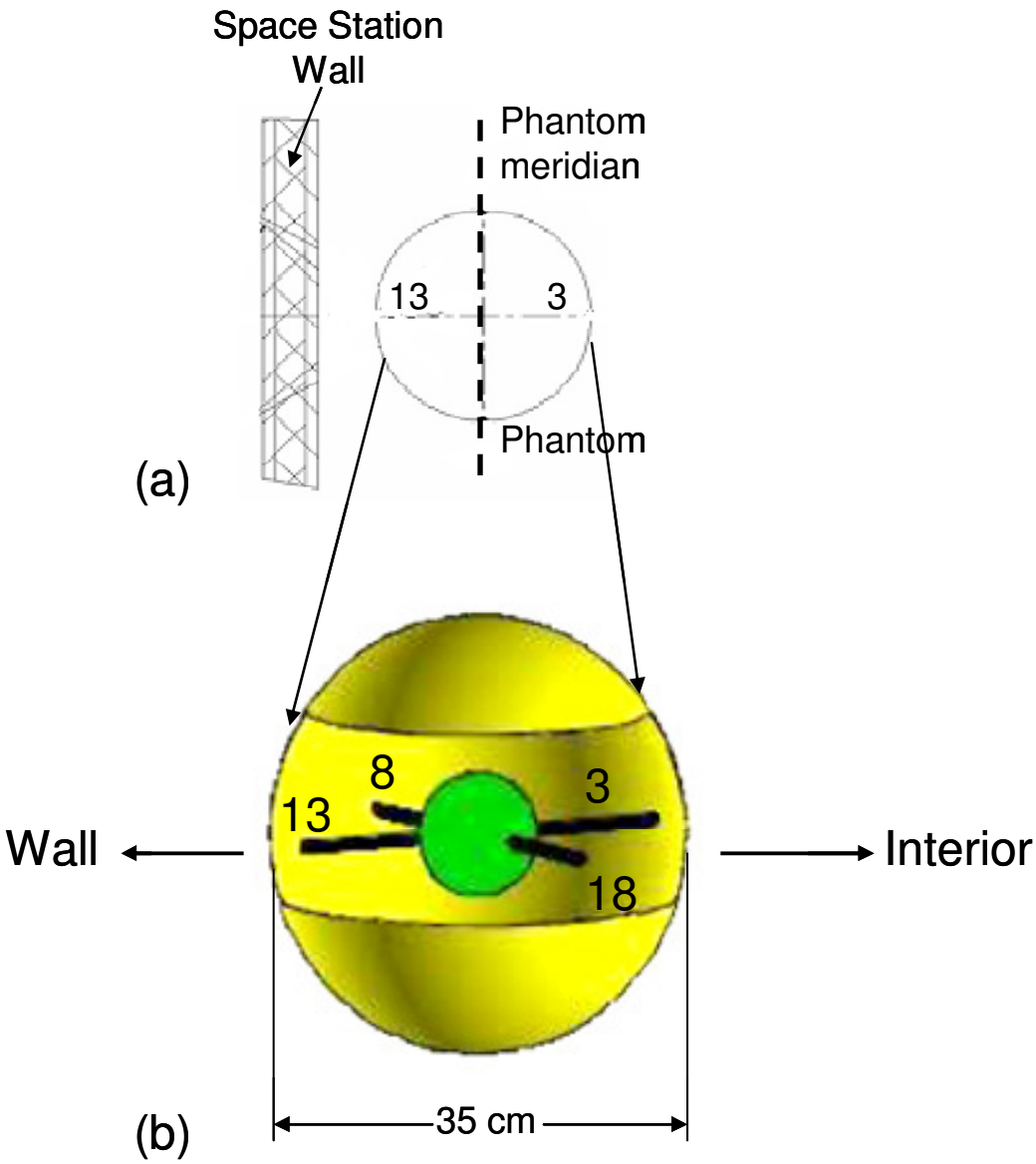

Figure 7.4. Schematic of Phantom (a) in relation to station wall (b) isometric view of simulated phantom.

13.1 m long from end to end, at 4.1 m in diameter. The Zvezda consists of three pressurized compartments: a small spherical transfer compartment at the forward end; a long, cylindrical main work compartment, where crews work and live; and a small cylindrical Transfer Chamber at the aft end. An unpressurized assembly compartment is wrapped around the exterior of the transfer chamber at the aft of the module, holds external equipment and communications antennas. The compartments are separated by airlocks, creating different working conditions. The main crew compartment is approximately 7 m long, houses living accommodations, such as: sleeping quarters for the crew, toilet and hygiene facilities, and a kitchen [NASA 2000].

For the period from August 2004 to October 2005, the MTR-R phantom was installed on the starboard floor in the crew cabin (main work compartment), with the four main detector channels located in the center of the phantom (3, 8, 13, and 18) directed toward and away from the wall of the ISS (Fig. 7.4). The closest distance between the surface of the MTR-R phantom and the inner wall of the ISS was 37.5 cm, with detector channel 13 pointing toward the wall, while detector channel 3 pointing toward the ISS interior [Kartsev et al 2005; Shurshakov et al. 2008]. Figure 7.4a shows the phantom in relation to the Space Station wall, and Figure 7.4b shows an isometric view of the MTR-R phantom with the four primary detector channels simulated in this research.

The phantom provided measurements for 425 days in the crew quarter. No powerful solar particle events were registered throughout this measurement period [Kartsev et al. 2005]. The mean orbits transmission parameters for the space station were about 355 km altitude at 52^0 inclination [Kartsev et al. 2005; Akatov et al. 2007; Shurshakov et al. 2008]. After the measurement period, passive detectors installed inside the phantom were removed, packaged and returned to Earth for post flight processing.

The detectors returned to the ground after the measurement showed that the dose rates on the phantom surface were as much as a factor of two higher than at the center of the phantom [Shurshakov et al. 2008; Jadrnickova et al. 2009]. The highest dose measurements in the phantom were those close to the outer wall of the space station.

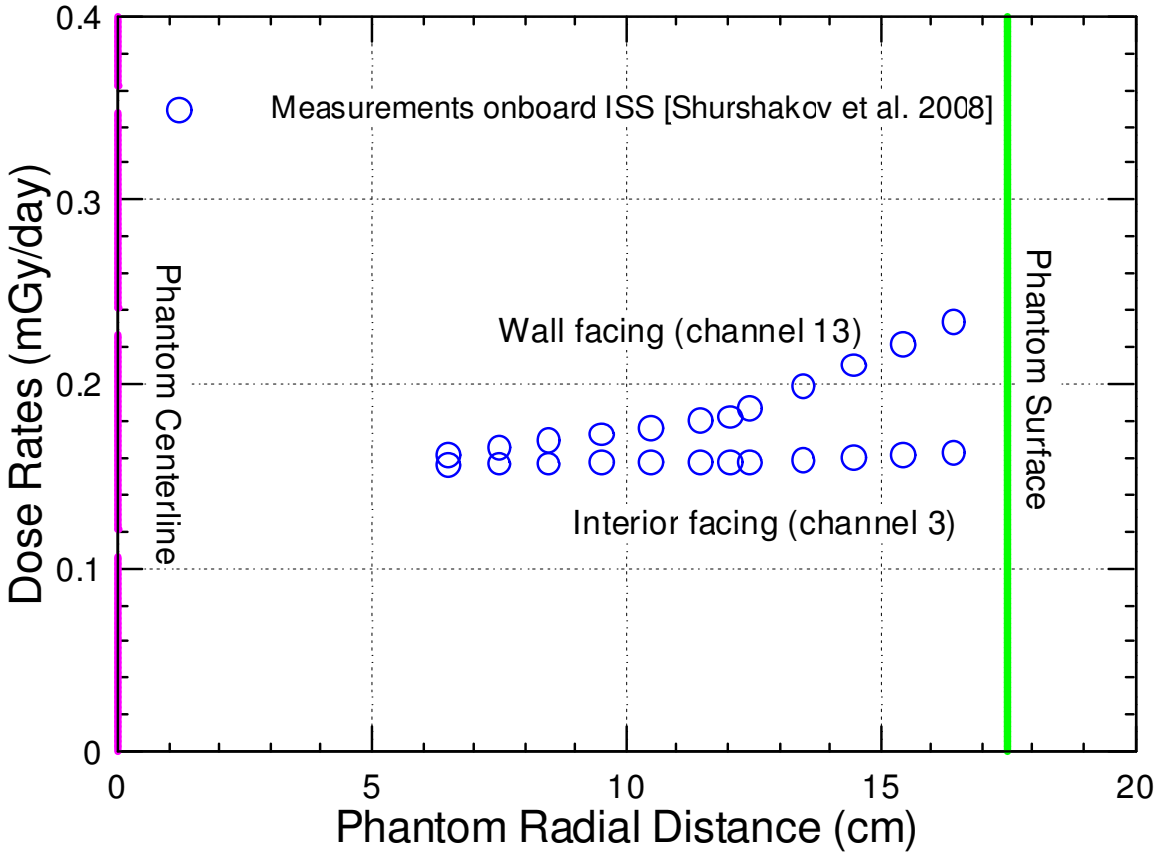

Figure 7.5. Measured absorbed dose rate inside the MATROSHKA-R phantom [Shurshakov et al. 2008].

This dose was ~0.253 mGy/day, likely due to both GCR and particles trapped in the Earth's radiation belt [Shurshakov et al. 2008; Jadrnickova et al. 2009]. Figure 7.5 show the dose rate distributions measurements inside the MATROSHKA-R phantom onboard the ISS. The measured absorbed dose rates dropped with increasing depth into the phantom, to ~0.16 mGy/day at the innermost position of 6.5 cm radial distance from phantom center (or 11 cm from phantom surface). The lowest measured dose rate was ~0.15 mGy/day at the inner most position (6.5 cm radial distance from phantom centerline) of the interior facing detectors channel 3 for more than 5 g/cm^2 tissue shielding [Shurshakov et al. 2008; Jadrnickova et al. 2009]. This is likely caused by the strongly penetrating high energetic GCR particles [Shurshakov et al. 2008; Jadrnickova et al. 2009]. The recorded absorbed dose rate distribution by interior facing detectors arrangement along channel 3 was found to be relatively flat, in contrast to that recorded by the wall facing detectors in channel 13. In channel 3, the dose rates at the deepest detector position (11 cm from phantom surface) and the detector near the phantom surface (1 cm from phantom surface) were ~0.15 mGy/day and ~0.16 mGy/day, differing only by ~0.01 mGy/day. In comparison, the wall facing detectors at these positions in channel 13 registered a difference of ~0.093 mGy/day.

7.3 Simulation of MATROSHKA-R Experiment

The MATROSHKA-R experiment was simulated using the MCNPX code, version 2.7E. The structure of the ISS Service Module Zvezda is too complicated and the detailed internal geometry is not readily available. Instead, the performed simulations used a simplified ISS module (Fig 7.6b). The simplified module in Figure 7.6b is compared with the schematic of the Zvezda model in Figure 7.6a. The geometry of the crew cabin of the Zvezda module was approximated by a cylindrical aluminum shell, with an inner diameter of 4 m and a length of 7 m [NASA 2000; Sihver et al. 2009]. The shielding mass thickness of the simplified module was estimated to be 12.5 g/cm^2 of aluminum [Reitz et al. 2009; Sihver et al. 2009; Gustafsson et. al. 2010]. The interior of the module is filled with air, and the phantom is situated in the same position on the starboard floor of the crew cabin. The MATROSHKA-R phantom is simulated as the real phantom, with an outer diameter of 35 cm and an inner air cavity of 10 cm in

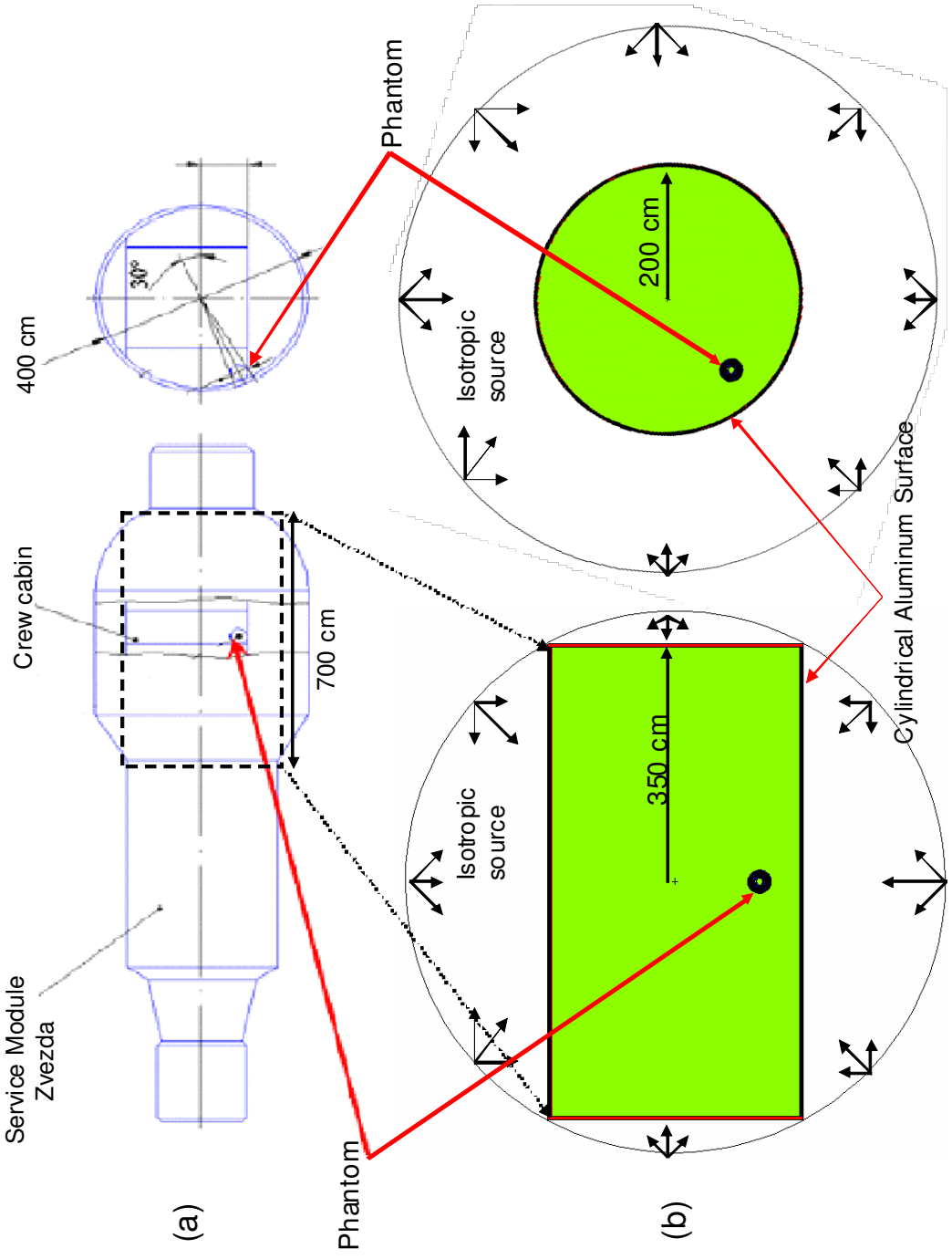

Figure 7.6. An illustration of the simplified module used in the present simulations using MCNPX and PHITS codes: (a) Schematic of Service Module Zvezda (b) Simplified module as simulated in PHITS and MCNPX.

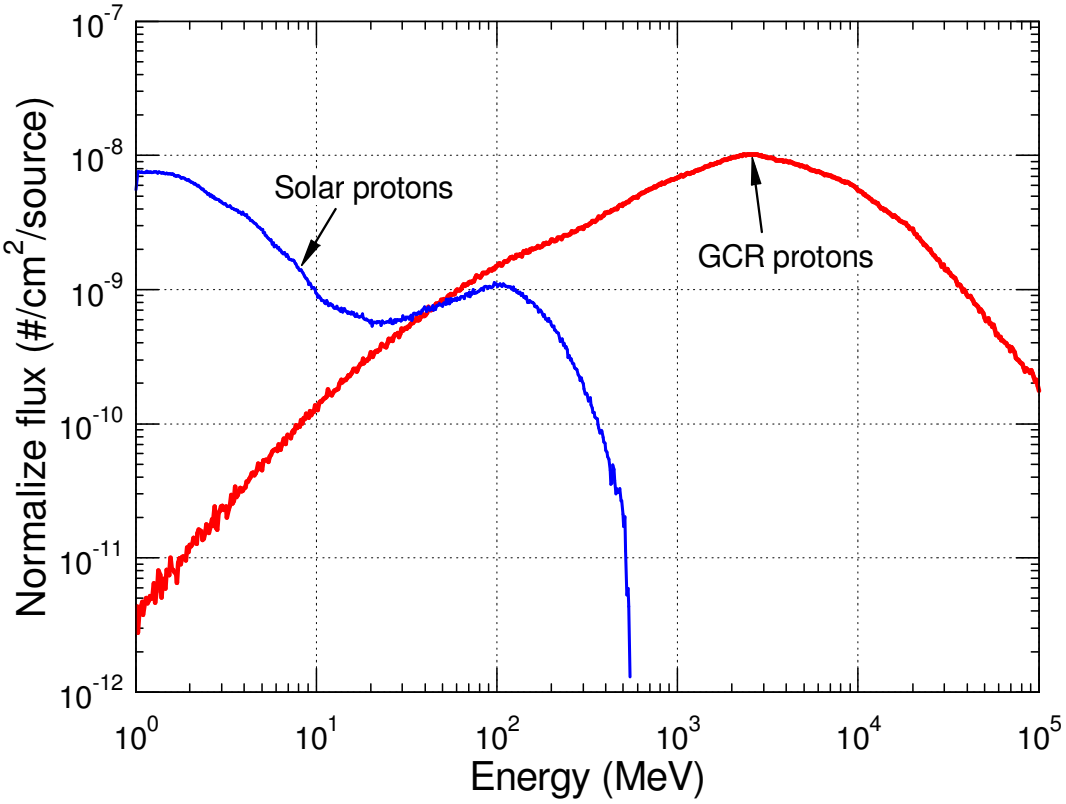

Figure 7.7. Trapped Protons and GCR protons spectra used in the present simulations.

diameter. The simulated phantom is composed of the same tissue equivalent material and same mass of 32 kg in the experimental setup. The simulated phantom is positioned as shown in Figure 7.6b, with 37.5 cm separating the phantom surface from the inner station wall.

In the simulations, the detectors and their channels are not explicitly modeled. Instead, the simulation employed a mesh function, discretizing the phantom into 5 mm rectangular volume elements, making up the simulated spherical phantom. The energy deposition or absorbed dose rates are calculated in each 5 mm mesh cell, providing the spatial dose distribution inside the phantom. The calculated absorbed dose rates at different positions within the spherical phantom are taken to correspond to the detectors position. The direction facing the station wall corresponded to the detectors in channel 13, while the module interior facing direction corresponds to detectors in channel 3. The simplified ISS module is surrounded by an arbitrary spherical radiation source, as shown in Figure 7.6b, to simulate the external isotropic radiation environment [Sihver et al. 2009; Reitz et al. 2009; Gustafsson et al. 2010].

The space radiation source is one of the most important parameters in determining the absorbed dose. At LEO, a spacecraft can experience a widely different environment, depending on the orbit parameters such as inclination, and the apogee and perigee altitudes. The time of the experiment (August 2004 – October 2005) was in the decreasing phase of the solar cycle, close to the solar minimum, and the radiation environment in the near Earth orbit was practically non-disturbed [Jadrnickova et al. 2009]. Thus, the radiation environment can be characterized based on the Trapped Protons in the Earth's radiation belt and the GCR source within the orbit parameters of the ISS. Thus, in the performed simulation, the used spectra of the trapped protons and GCRs are obtained from CREME96 (Cosmic Ray Effect on Micro Electronics 1996) [Tylka et al. 1997; Sihver et al. 2009]. The trapped protons spectrum used in the simulations is based on the orbit parameters from December 2004, which represent an average altitude of the ISS during the measurement period [Kartsev et al. 2005; Akatov et al. 2007; Shurshakov et al. 2008; Sihver et al. 2009]. The ISS orbit inclination is ~51.6^0 and the average apogee and perigee altitudes for this experiment were 364 and 347 km, respectively [Kartsev et al. 2005; Akatov et al. 2007; Jadrnickova et al. 2009]. The used

GCRs spectrum is defined using the pre-calculated geomagnetic transmission functions implemented in CREME96. So far, only two orbits are implemented in CREME96; these are the geomagnetic transmission for the ISS orbits and the general orbit for Shuttle mission at either solar minimum or maximum conditions. The ISS orbit model at the solar minimum condition is used here as the GCR source. Figure 7.7 shows the trapped protons and GCR protons spectra used in the present simulations. Trapped electrons are not included in the simulations, since they are expected to be absorbed in the walls of the ISS module due to their low energies.

For energies below 20 MeV, the performed simulations used the ENDF-VII evaluated data library. At higher energies, the simulations used MCNPX default physics models [Pelowitz et al. 2008]. The energy deposition or absorbed dose rates are tallies in the 5 mm mesh cell of the phantom, corresponding to the detectors in the experimental setup. Separate simulations are conducted for the trapped protons and GCRs, and the results are added to determine the total absorbed dose rates in the phantom. The simulations are performed with more than 500 millions source particles to enhance calculations' statistics. To further improve these statistics, the simulations also employed variance reduction technique, of increasing particles importance moving inward into the ISS structure and the phantom. For example, the importance of particles outside the Aluminum structure is 1, while the importance of the particles entering the phantom is increases to 10. This mean that every particle entering the phantom, splits into 10, reducing the weigh of each particle. This method keeps the particles' total contribution at unity, while effectively increasing the sample size of the Monte Carlo simulation, further increasing the simulation statistics beyond that of the 500 millions source particles [Pelowitz et al. 2010].

7.4 Simulation Results and Discussion

The calculated absorbed dose rates inside the simplified MATROSHKA-R spherical phantom (Fig. 7.6b) are compared in Figure 7.8. Shown are the experimental measurements for the wall facing detectors arrangement (detectors channel 13) and the interior facing detector arrangement (detectors channel 3), along with simulation results from PHITS (Sihver et al. 2009) and MCNPX. The PHITS and MCNPX simulations

show similar trends, with the dose rate highest near the surface of the phantom and decreases with increasing depth into the phantom. For the wall facing arrangement (detectors' channel 13), the highest dose rate of ~0.36 mGy/day is calculated near the phantom surface (1 cm from the surface). The lowest dose rate of ~0.25 mGy/day is that calculated at the deepest detector point of 6.5 cm radial distance from the surface (11.5 cm into the phantom) for the wall facing arrangement. The interior facing arrangement (detectors' channel 3) shows slightly lower, if not symmetric, absorbed dose rates compared with the wall facing arrangement. The highest dose rate of ~0.35 mGy/day is at the point near the phantom surface (at position -16.5 cm radial distance), and the lowest dose rate of ~0.24 mGy/day is at -6.5 cm radial distance (11 cm from the phantom surface). The simulation results of both PHITS (Sihver et al. 2009) and MCNPX are similar, showing decreasing dose rates from the phantom surface with distance into the phantom. The jaggedness of the simulation data using PHITS, reported by Sihver et al. (2009), are likely due to the statistics of the calculations (Fig. 7.8). In their simulations, they only used 30 million source particles, compared to 500 million source particles along with the importance variance reduction technique used in the present MCNPX simulations. This improved the MCNPX calculation statistics and resulted in a smoother absorbed dose rate estimates in the phantom.

As can be seen in Figure 7.8, the absorbed dose rates estimates using both PHITS and MCNPX are 1.5 – 2 times higher than the measurements. The large discrepancies are partially due to the absence of a detector efficiency correction in the simulations [Sihver et al. 2009]. When compared with experimental measurements, the absorbed dose rates estimates assuming a detector efficiency of 63.5%, agree well with the measurements for the wall facing arrangement (detectors' channel 13). As shown in Figure 7.8, the corrected simulation results for a constant detector efficiency, closely match the measurements throughout the phantom depth distribution; capturing well the trend of the absorbed dose rates distribution inside the phantom. However, with the same detector average efficiency, the interior facing detector arrangement (detectors' channel 3) shows large discrepancies between the measurements and simulated values, especially

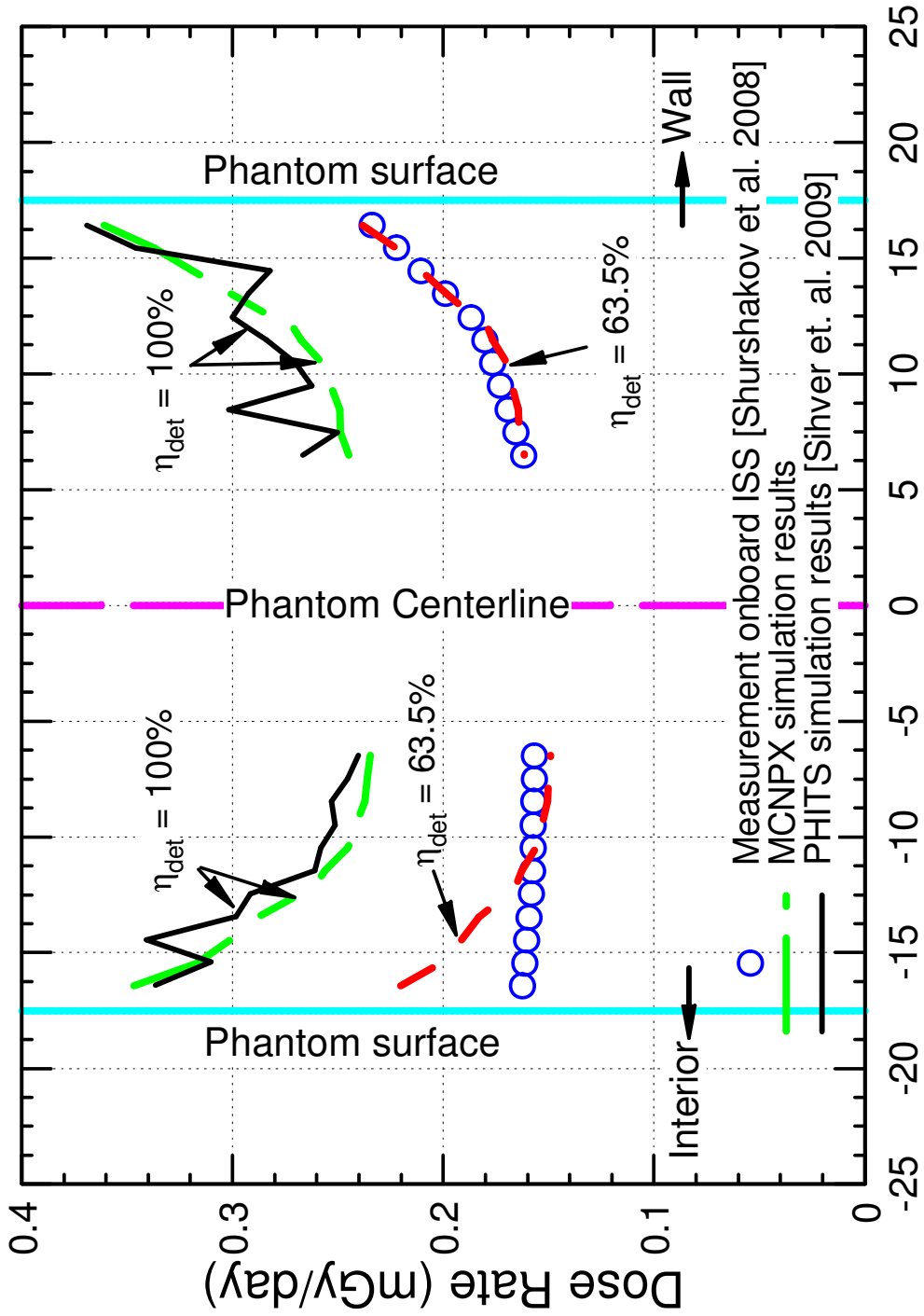

Figure 7.8. Simulated Absorbed Dose Rate Estimates inside the simplified MATROSHKA-R spherical phantom (Fig. 7.6), compared with experimental measurement and the PHITS simulation of Sihver et. al. (2009).

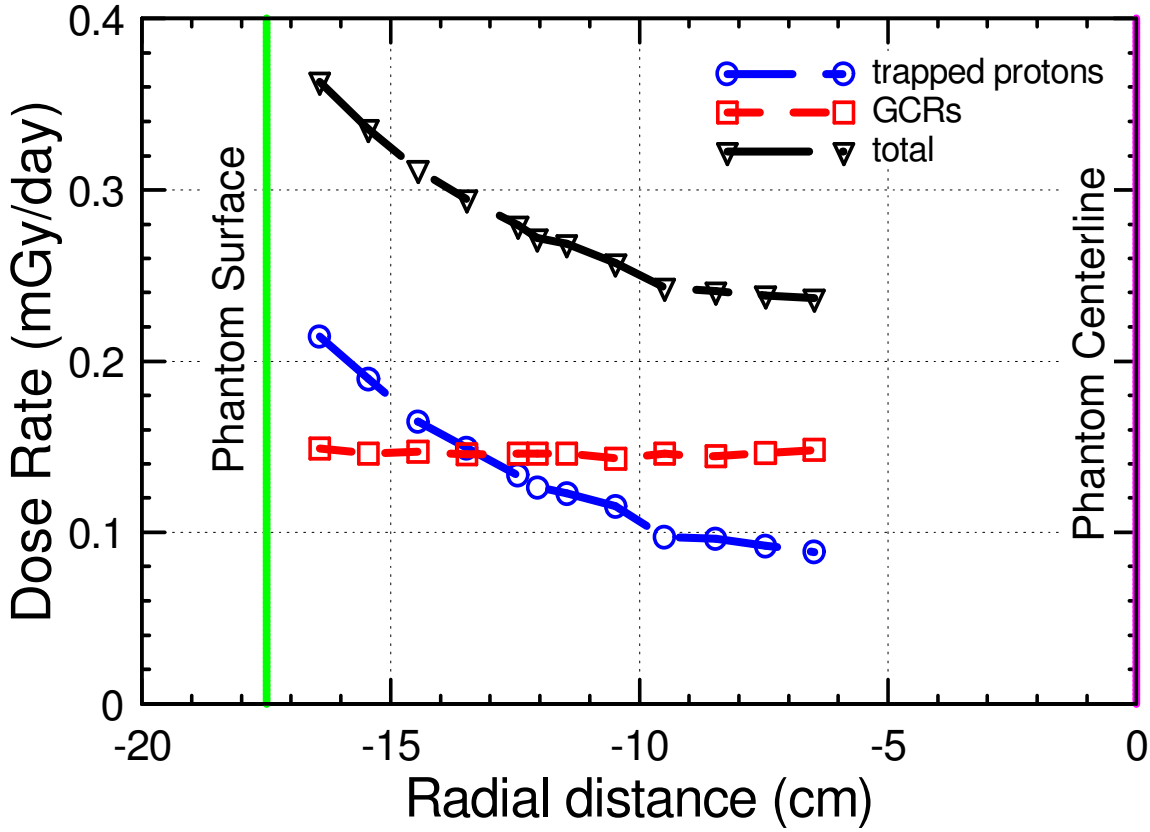

Figure 7.9. Relative contribution of the trapped protons and GCRs to the total absorbed dose rates estimates inside the phantom using MCNPX code and spherical source domain.

for the detectors near the phantom surface. The simulation results of both PHITS and MCNPX show a large decrease in the dose distribution with depth into the phantom, while the measurements have a relatively flat distribution throughout the phantom. The estimated dose rate near the phantom surface, corrected for detector efficiency, is up to ~1.4 times higher than the measurements. Only for detector points at -11 cm to -6.5 cm radial distance into the phantom, the estimates of the absorbed dose rates are comparable to the experimental measurements.

Figure 7.9 show the relative contribution of the trapped protons and GCRs to the estimated total dose rates using MCNPX code with the spherical domain of source particles (Fig 7.6), for the Interior facing detector arrangement (detectors channel 3). As shown, the dose rates estimates are calculated separately for the Trapped Protons and GCRs, and the results are added to get the total estimates absorbed dose rates inside the phantom for the respective detector positions. It can be seen that, the GCRs dose rate estimates are relatively constant throughout the phantom; depositing ~15 mGy/day. The dose rate estimates due to trapped protons, having lower energies, are more depth dependence. The highest dose rate is near the phantom surface and decreasing with increasing thickness into the phantom. For the detector point near the phantom surface, the trapped protons estimated dose rate is ~1.5 times that of the GCRs. At ~5 cm into the phantom, the trapped protons dose rate drops below that of GCRs and continues to decrease with distance into the phantom. At > 5 cm into the phantom, the GCRs are the dominant dose contributor, represnteing ~65% of the total dose rate at the deepest detector position.

7.5 Effect of Changing Simulation Domain

In the simulations presented and discussed in the previous section, the isotropic radiation environment is simulated as a sphere with a radius of ~400 cm, surrounding the simplified cylindrical aluminum space station module in Fig. 7.6b [Sihver et al. 2009; Reitz et al. 2009]. Results showed in section 7.4 that this domain overestimates the absorbed dose rates by the detectors facing away from the station wall (Figure 7.8). The largest difference in the absorbed dose rates are primarily near the phantom surface, indicating the contributions are likely from scattered lower energies particle onto the

phantom. The simulation domain can largely influence the dose estimates inside the simulated phantom. This section investigates the effect of changing the simulation domain radius on the simulated absorbed dose rates estimates, compared to the experimental measurements inside the phantom; particularly for the interior facing detectors arrangement.

7.5.1 Approach

The simulations in section 7.4 are performed using a spherical domain ~400 cm in radius, surrounding the simplified cylindrical aluminum space station module in Fig. 7.6b. The incident particles are simulated as isotropic radiation starting at the spherical surface of the calculation domain, simulating the isotropic radiation environment in LEO [Sihver et al. 2009; Reitz et al. 2009]. The cylindrical aluminum structure is assumed 12.5 g/cm^2 thick, 400 cm in diameter and 700 cm in long, as in section 7.4. The simplified spherical phantom (Fig. 7.6b), simulated as described in the experiment, is placed inside the station on the starboard floor, with the closest distance between the phantom and the station wall surface is 37.5 cm, as shown in Figure 7.6. In this arrangement, the cylindrical space station module is assumed a free standing structure in a fully enveloped isotropic radiation environment. Though, as can be seen in Figure 7.1, the Crew Cabin is attached to other structures and compartments on either ends. These structures and compartments could effectively provide more shielding mass thickness around the Crew Cabin, in which the phantom is situated. This limits the amounts of radiations entering through the two ends of the Module, in contrasts to a free standing structure with a fully enveloped isotropic radiation environment, as simulated in section 7.4. Thus, the radiation environment inside the module is likely due to the radiation traversing the cylindrical surface of the Crew Cabin, where there is the least amounts of shielding. With that in mind, the simulation domain is modified from the free standing structure in a spherical isotropic source, to a cylindrical source, using the cylindrical aluminum structure as the radiation initiation surface. The random isotropic nature of the incident radiations is kept the same, while varying the extend of the cylindrical source to investigate the effects on the absorbed dose rates inside the phantom. Figure 7.10 compares the spherical domain used in section 7.4 with the cylindrical domain used in

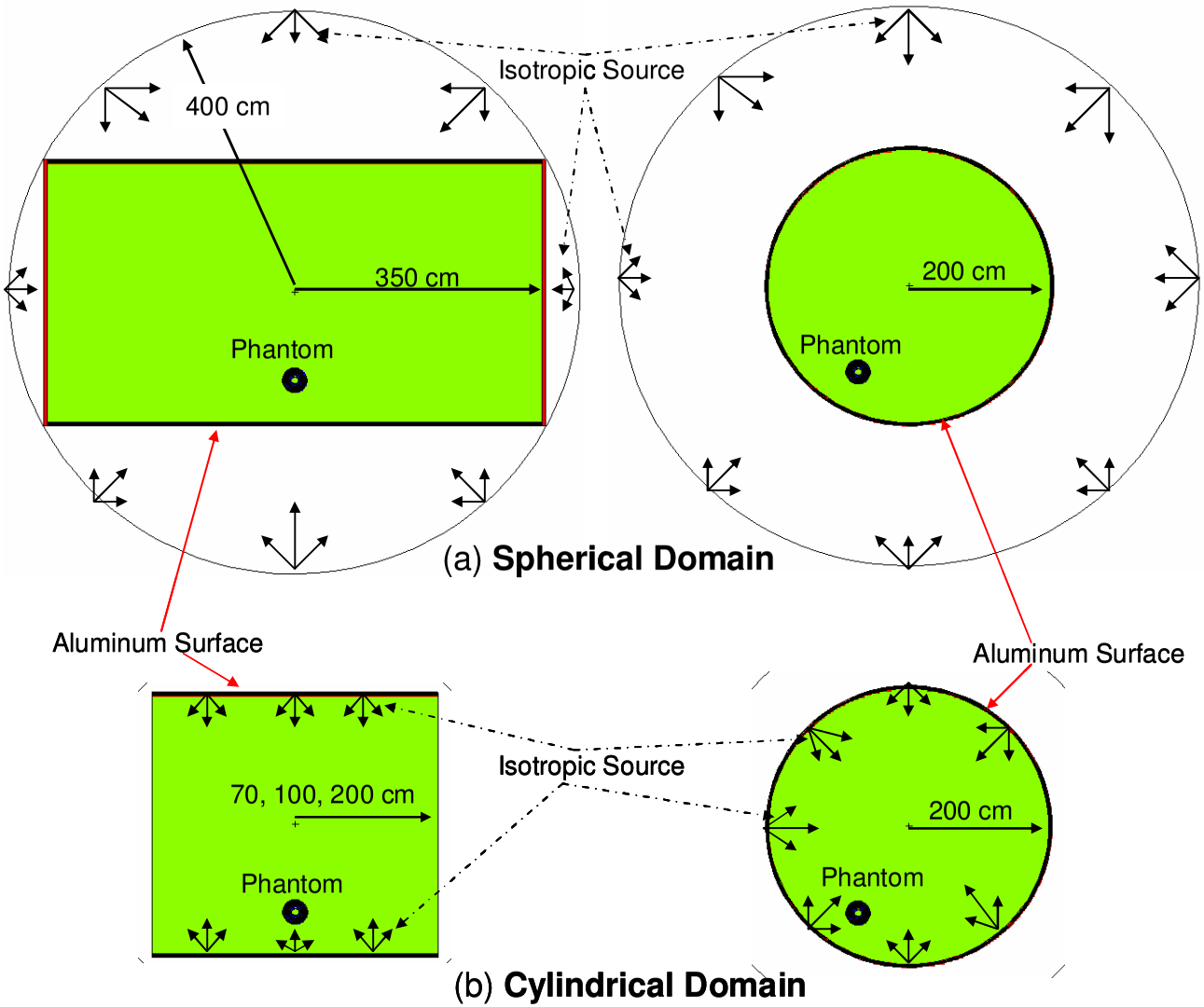

Figure 7.10. Schematic of the simulated domain for estimating the dose rate distribution inside the phantom inside the simplified module (a) Spherical domain (simulations in section 7.4) (b) cylindrical domain (current simulations).

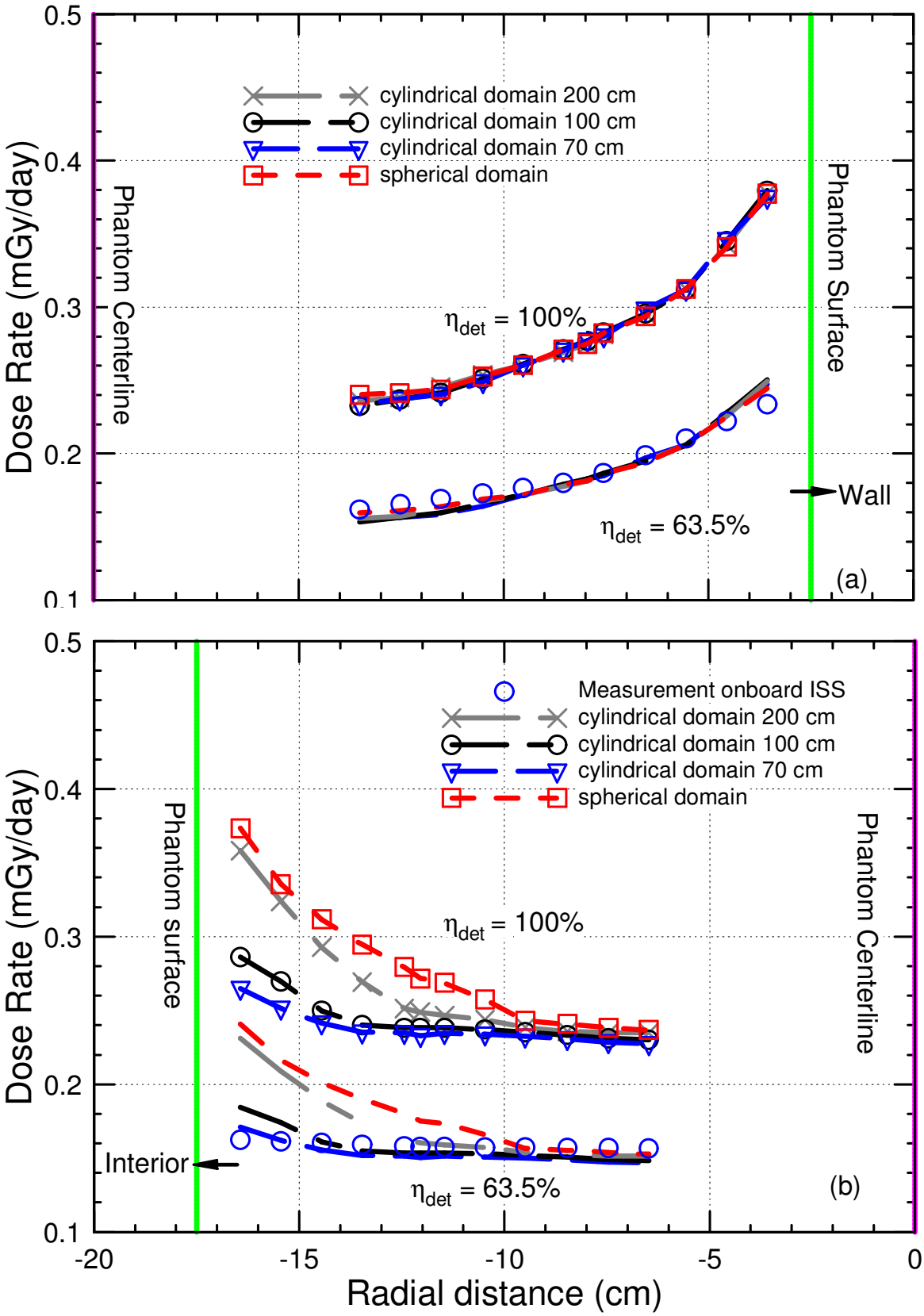

Figure 7.11. Absorbed Dose Rate Estimates using spherical and cylindrical domains, compared with experimental measurements.

this section. The spherical phantom position and orientation, as well as the trapped protons and GCRs spectra of incident source particles, are the same as in section 7.4. The simulations employed 500 millions source particles and increasing importance variance reduction technique, as mentioned in section 7.4.

7.5.2 Results and Discussion

The estimated dose rates using MCNPX code with the spherical and cylindrical domains are compared with the experimental measurements in Figure 7.11a – 7.11b. For clarity, the simulation results for the wall facing arrangement are shown in Figure 7.11a, and those for the Interior facing arrangement are shown in Figure 7.11b, corresponding to the experimental detectors channels 13 and 3, respectively. The dose rates estimates in Figure 7.11a are highest near the phantom surface, decreasing with increasing distance into the phantom. The highest dose rate of ~0.38 mGy/day is at a detector point of approximately 1 cm from the phantom surface (16.5 cm radial distance). The lowest absorbed dose rate ~0.23 mGy/day is approximately 11 cm from the phantom surface (6.5 cm radial distance). The dose rate estimates for three different cylindrical source particles domains that are 200 cm, 100 cm, and 70 cm long. Figure 7.11a show that the absorbed dose rates estimates from the wall facing detectors arrangement are independent of the length of the simulated domain. They are also the same for both the spherical and cylindrical source domain. The proximity to the wall restraint the amount of particles scattered into the phantom, insignificantly affecting the dose rate estimates. As demonstrated, the absorbed dose rate estimates not corrected for efficiency, are ~1.5 times higher than the experimental measurements. When the absorbed dose rate estimates are adjusted for an average detector efficiency of 63.5%, they almost overlap the experimental measurements, regardless of the length of the simulation cylindrical source particles domain (Fig. 7.10a).

Figure 7.11b compares the dose rate estimates in the phantom for the interior facing detectors' arrangement (detectors channel 3). The spherical source particles domain gives the highest dose rate estimates near the phantom surface of ~0.37 mGy/day, dropping to ~0.23 mGy/day at detector point deepest inside the phantom (-6.5 cm radial distance). This is almost a symmetric trend with the wall facing dose rate estimates,

though the phantom is not located at the center of the cylindrical station. When adjusted with the same detector average efficiency of 63.5%, the highest and lowest estimates dose rates drop to ~0.24 mGy/day and ~0.15 mGy/day at their respective positions. The absorbed dose rate estimates near the phantom surface are much higher than the experimental measurements. The dose decreases inward with distance into the phantom, in contrast to the relatively flat distribution of the measurements.

With a cylindrical source particles domain, the absorbed dose rate estimates for the interior facing arrangement decrease significantly in contrast to those calculated with the spherical domain. With a 200 cm long cylindrical source particle domain (Fig. 7.10b), the simulated absorbed dose rate estimates decrease to ~0.35 mGy/day at -16.5 cm radial distance (1 cm from phantom surface), while that at -6.5 cm radial distance (11 cm from the phantom surface) is not affected. More notable is the flattening of the dose rate distribution inside the phantom, compared to that with the spherical source particles simulation domain. With this domain, a relatively flat absorbed dose rate occurs only at radial distance of -6.5 cm to -10 cm in the phantom. With a 200 cm long cylindrical source particles domain, the flat radial distribution of the absorbed dose rate estimates extends from -6.5 cm to -13 cm in the phantom; with a dose rate difference of only ~0.02 mGy/day. Reducing the length of the cylindrical source particles domain further to 100 cm, decreases the absorbed dose rate estimates near the phantom surface. The highest dose rate is ~0.29 mGy/day at a radial distance of -16.5 cm (1 cm from phantom surface) which quickly decrease to ~0.24 mGy/day at radial position of -13.5 cm (4 cm from phantom surface) and to its lowest value of ~0.23 mGy/day at a radial position of -6.5 cm (11 cm from phantom surface) (Fig. 7.11b). In addition, the dose rate distribution inside the phantom becomes flatter (compared to the 200 cm long cylindrical source particles domain and the spherical source particles domain), with a difference of ~0.01 mGy/day from radial positions of -6.5 cm to -13.5 cm. Decreasing the length of the cylindrical source particles domain to 70 cm, further reduces the dose rate estimates near the phantom surface. The dose rate at radial distance of -16.5 cm (1 cm from phantom surface) is ~0.27 mGy/day. It decreases to ~0.24 mGy/day at a radial position of -14.5 cm in the phantom, before dropping to ~0.23 mGy/day at phantom radial position of -6.5 cm (11 cm from phantom surface) (Fig. 7.11b).

Figure 7.11b also shows that with a constant average detector efficiency of 63.5%. The absorbed dose rate estimates in the phantom are slightly lower than the experimental measurements, though this difference is small relative that near the phantom surface. With the spherical source particles domain, the dose rate estimates are comparable to the experimental measurements only at phantom radial distance of < -10 cm. Closer to the phantom surface, the lower energy trapped protons are more dominant, increasing the absorbed dose rate.

The spherical isotropic source particles domain seems to increase the low energy scattering into the phantom, resulting in a high dose rate near the phantom surface (Fig. 7.9a). Changing the source particles domain to a cylindrical eliminates the radiation scattering coming from the two ends of the cylindrical station, thus leading to an overall reduction in the absorbed dose rates in the phantom, for the interior facing arrangement of the detectors (detectors channel 3). Decreasing the length of the cylindrical source particles domain reduces the amount of low-energy secondary particles scattering into the phantom, lowering the dose rate at the phantom surface and flattening the dose rate distributions inside the phantom (Fig. 7.11b).

7.6 Summary

The MATROSHKA-R spherical phantom experiment aboard the Russian segment Zvezda of the ISS, for the duration period from August 2004 – October 2005, is simulated using the transport code MCNPX. Results show that the absorbed dose rate estimates have a similar trend to the measurements, with the dose rates are highest near the phantom surface and decrease with radial distance into the phantom. Without accounting for detectors efficiency, the absorbed dose rate estimates using a spherical source particles domain are approximately 1.5 – 2 times higher than the measurements. When corrected for an average detector efficiency of 63.5%, the calculated dose rate estimates agree well with the measurements, only for the wall facing detectors' arrangement. For the interior facing detectors' arrangement, the dose rate estimates are much higher than the measurements near the phantom surface. At a detector point of ~1 cm from the phantom surface, the dose rate estimate is ~40% higher than the experimental measurements. In addition, the dose rate distribution inside the phantom,

decreases with increasing depth, while the experimental measurements had flat distribution. This discrepancy has been eliminated by switching from a spherical to a cylindrical source particles domain.

Changing the radiation source particles domain does not alter the absorbed dose rate estimates and distribution inside the phantom for the wall facing arrangement. For the interior facing arrangement, however, the cylindrical source particles domain significantly reduces the absorbed dose rate at the surface of the phantom and flattens the radial distribution inside the phantom, closely matching the experimental measurements.

The analysis performed in this chapter clearly show the strong dependence of the calculated dose rate estimates for the detectors focusing away from the station wall on the selected dimension and geometry of the source particles domain. Based on the presented results, it is recommended that cylindrical source particles domain be used for accurate estimates of the dose rate in ISS and future space flights. Such a domain provides better estimates of the dose rate to interior organs as well as at the surface of the astronaut body. This finding is important for future space flights to Mars, for which no direct measurements for a phantom are available.

8. SUMMARY AND CONCLUSIONS

This research performed simulations using the state-of-art three dimensional MCNPX and PHITS Monte Carlo particles transport codes to investigate the interactions of space radiation with materials and quantify the dose rates onboard the International Space Station (ISS) and in a lunar shelter for future missions. High-energy space radiation of trapped protons, Solar Particle Events, and GCRs particles interactions are simulated using MCNPX and PHITS. The energy loss and energy deposition within the shielding materials and in the phantom are calculated. The contributions of secondary particles produced through spallation reactions are identified. Recent phantom experiment onboard the ISS was simulated, and the methodology to best reproduce experimental measurements is presented.

The interactions of high energy particles with shielding materials generate large amounts of secondary particles including: secondary protons, neutrons, deuterons, alphas, etc. Depending on the shield thickness, secondary particles such as neutrons, can contribute significantly to the dose estimates. For protons energy < 100 MeV, a mass shielding thickness of ~10 g/cm^2 is likely sufficient to shield incident particles. Beyond such thickness, secondary neutrons dominate. The energetic solar protons can penetrate deep into the shield, producing additional secondary particles. Analysis using a spherical space station with 12.5 g/cm^2 shield thickness shows that the dose inside the station is due almost entirely to primary and secondary protons.

For long duration missions on the lunar surface, a radiation shelter is a must for emergency protection, in case of solar events. Large solar events are rare, though their high energy fluence of incident particles is capable of delivering lethal radiation doses. Two typical solar particle events are investigated and the shielding thickness to reduce the dose estimates inside the lunar shelter below the 30-days limit for astronauts are calculated. For a typical solar event with high fluence and moderately low-energy, such as that of the October 1989, a regolith shield thickness of < 20 g/cm^2 can sufficiently reduces the dose inside the structure below the 30-days limit of 250 mSv. For solar event with large concentration of high-energy protons, such as the February 1956 event, ~30 – 40 g/cm^2 of regolith shielding may be required. Results also show that the incident mode of the source particles can significantly influence the dose estimates inside the lunar

shelter. With the February 1956 solar event, dose estimates are calculated for three incidence modes of primary source particles: center-seeking, planar, and isotropic. The center-seeking is overly conservative, with the largest shielding requirement to reduce estimated dose inside the shelter to below the 30-days limit. The planar incidence mode of source particles required the least shielding.

Recent experimental measurements of the MATROSHKA-R spherical phantom aboard the Russian segment Zvezda of the ISS, is simulated using the transport codes PHITS and MCNPX. The spherical phantom is positioned inside the cylindrical ISS module. Radiation environment from the ISS orbital parameters, during the solar minimum conditions, are simulated as a spherical source envelope the cylindrical aluminum module. Absorbed dose rates calculated inside the phantom are compared with experimental measurements. Results show that the simulated absorbed dose rates have a similar trend to the experimental values, though they are 1.5 – 2 times higher. When corrected with an average detector efficiency of 63.5%, they are in good agreement with experimental measurements. Particularly, for the Wall facing detector arrangement (corresponding to detector cylinder 13 in the experiment), the simulation results agree well with experimental measurements. For the Interior facing detector arrangement (corresponding to detector cylinder 3 in experiment), however, the dose rate estimates are much higher than the experimental values near the phantom surface. The simulated dose rates inside the phantom decreases almost exponentially with distance into the phantom; though the experimental measurements had a relatively flat distribution inside the phantom.

The simulation domain is modified to a cylindrical source domain, using the outer cylindrical surface as the main source particles surface, though the isotropic nature of the radiation is kept unchanged. Changing the radiation source particles domain, does not alter the absorbed dose rate estimates and distributions inside the phantom for the Wall facing arrangement. The proximity of the phantom to the wall surface, limits the relative amount of particles scattered into that area of the phantom. For the interior facing arrangement, however, the source particles domain significantly altered the absorbed dose rate estimates and distribution inside the phantom. Changing the source particles domain from the spherical to cylindrical that is 200 cm, 100 cm, and 70 cm long,

systematically reduced the absorbed dose rate estimates near the phantom surface from ~0.24 mGy/day to ~0.22 mGy/day, ~0.18 mGy/day, and ~0.17 mGy/day, respectively. With the 70 cm long cylindrical source particles domain, the difference between the inner and outer dose rates in the phantom is ~0.02 mGy/day; compared with ~0.01 mGy/day for the experimental measurements. The simulations using a cylindrical particles domain gave the best comparison with the experimental measurements.

The results show the strong dependence of the calculated dose rate estimates for the detectors facing away from the station wall on the selected dimension and geometry of the source particles domain. Based on the present results, it is recommended that cylindrical source particles domain be used for accurate estimates of the dose rate estimates in ISS and future space flights. Such a domain also provides better estimates of the dose rate to interior organs as well as at the surface of the astronaut body. This finding is important for future space flights to Mars, for which no direct measurements for a phantom are available.

APPENDIX A – Reactions of Energetic Protons and Neutrons with Shielding Materials

This appendix lists the spallation reactions of high energy protons and neutrons with the elements in the shield materials investigated in this paper. Tables A.1 to A.4 list the most probable reactions of the protons with Aluminum, Carbon, Silicon, and Oxygen. The data in these table are from ENDF and EXFOR libraries [Young and Chadwick 1997; Kitazawa et. al. 2002]. The listed reactions show the type of secondary particles generated. The energy thresholds for these reactions to occur are calculated. The lowest value represents the lowest energy of the incoming proton for the spallation reaction to occur. The most probable spallation reactions of high energy neutrons with the elements in the shielding materials are listed in A.5 – A.9. The calculated energy thresholds for these reactions are also listed in tables A.1 to A.4.

A.1. Reactions of high energy Protons with Aluminum

$$^{27}_{13}Al + ^{1}_{1}p \rightarrow ^{22}_{11}Na + X_1 \quad \text{(A1)}$$

$$^{27}_{13}Al + ^{1}_{1}p \rightarrow ^{24}_{11}Na + X_2 \quad \text{(A2)}$$

$$^{27}_{13}Al + ^{1}_{1}p \rightarrow ^{22}_{11}Ne + X_3 \quad \text{(A3)}$$

$$^{27}_{13}Al + ^{1}_{1}p \rightarrow ^{26}_{13}Al + X_4 \quad \text{(A4)}$$

The reaction products of protons, neutrons, alphas ($^{4}_{2}He$) and Deuterons ($^{2}_{1}D$) are listed in Table A-1.

A.2. Reactions of high energy Protons with Carbon

The following are the spallation reactions of energetic protons with Carbon in shield materials.

$$^{12}_{6}C + ^{1}_{1}p \rightarrow ^{7}_{4}Be + X_1 \quad \text{(A5)}$$

$$^{12}_{6}C + ^{1}_{1}p \rightarrow ^{9}_{4}Be + X_2 \quad \text{(A6)}$$

$$^{12}_{6}C + ^{1}_{1}p \rightarrow ^{10}_{4}Be + X_3 \quad \text{(A7)}$$

$$^{12}_{6}C + ^{1}_{1}p \rightarrow ^{11}_{6}C + X_4 \quad \text{(A8)}$$

The reaction products of protons, neutrons, alphas ($^{4}_{2}He$) and Deuterons ($^{2}_{1}D$) are listed in Table A-2.

A.3. Reactions of high energy Protons with Silicon

The following are the spallation reactions of the energetic protons with Silicon in the regolith shield.

$$^{28}_{14}Si+^{1}_{1}p\rightarrow^{22}_{10}Ne+X_1 \quad \text{(A9)}$$

$$^{28}_{14}Si+^{1}_{1}p\rightarrow^{24}_{11}Na+X_2 \quad \text{(A10)}$$

$$^{28}_{14}Si+^{1}_{1}p\rightarrow^{26}_{13}Al+X_3 \quad \text{(A11)}$$

The reaction products of protons, neutrons, alphas ($^{4}_{2}He$) and Deuterons ($^{2}_{1}D$) are listed in Table A-3.

A.4. Reactions of high energy Protons with Oxygen

The following are the spallation reactions of energetic protons with Oxygen in the regolith shield.

$$^{16}_{8}O+^{1}_{1}p\rightarrow^{7}_{4}Be+X_3 \quad \text{(A12)}$$

$$^{16}_{8}O+^{1}_{1}p\rightarrow^{15}_{6}O+X_2 \quad \text{(A13)}$$

$$^{16}_{8}O+^{1}_{1}p\rightarrow^{10}_{4}Be+X_1 \quad \text{(A14)}$$

The reaction products of protons, neutrons, alphas ($^{4}_{2}He$) and Deuterons ($^{2}_{1}D$) are listed in Table A-4.

A.5. Reactions of high energy Neutrons with Aluminum

The following are the reactions of energetic neutrons with Aluminum Shield.

$$^{27}_{13}Al+^{1}_{0}n\rightarrow^{26m}_{13}Al+(2)^{1}_{0}n \quad (E_{th} = 13.545 \text{ MeV}) \quad \text{(A15)}$$

$$^{27}_{13}Al+^{1}_{0}n\rightarrow^{26g}_{13}Al+(2)^{1}_{0}n \quad (E_{th} = 13.057 \text{ MeV}) \quad \text{(A16)}$$

$$^{27}_{13}Al+^{1}_{0}n\rightarrow^{27}_{12}Mg+^{1}_{1}p \quad (E_{th} = 1.896 \text{ MeV}) \quad \text{(A17)}$$

$$^{27}_{13}Al+^{1}_{0}n\rightarrow^{26}_{12}Mg+^{1}_{0}n+^{1}_{1}p \quad (E_{th} = 8.580 \text{ MeV}) \quad \text{(A18)}$$

A.6. Reactions of high energy Neutrons with Boron

$$^{10}_{5}B+^{1}_{0}n\rightarrow^{7}_{3}Li+\alpha \quad (E_{th} = 0.00 \text{ MeV}) \quad \text{(A19)}$$

$$^{10}_{5}B+^{1}_{0}n\rightarrow^{9}_{5}B+(2)^{1}_{0}n \quad (E_{th} = 9.286 \text{ MeV}) \quad \text{(A20)}$$

$$^{10}_{5}B+^{1}_{0}n\rightarrow^{6}_{3}Li+^{1}_{0}n+\alpha \quad (E_{th} = 4.910 \text{ MeV}) \quad \text{(A21)}$$

$$^{10}_{5}B+^{1}_{0}n\rightarrow^{9}_{4}Be+^{1}_{0}n+^{1}_{1}p \quad (E_{th} = 7.249 \text{ MeV}) \quad \text{(A22)}$$

$$^{10}_{5}B+^{1}_{0}n\rightarrow^{8}_{4}Be+^{1}_{0}n+^{2}_{1}D \quad (E_{th} = 9.082 \text{ MeV}) \quad \text{(A23)}$$

A.7. Reactions of high energy Neutrons with Silicon

The following are the reactions of energetic neutrons with Silicon, in the regolith shield.

$$^{28}_{14}Si+^{1}_{0}n\rightarrow^{27}_{13}Al+^{1}_{0}n+^{1}_{1}p \quad (E_{th} = 12.002 \text{ MeV})$$ (A24)

$$^{28}_{14}Si+^{1}_{0}n\rightarrow^{28}_{13}Al+^{1}_{1}p \quad (E_{th} = 3.999 \text{ MeV})$$
(A25)

$$^{28}_{14}Si+^{1}_{0}n\rightarrow^{27}_{14}Si+(2)^{1}_{0}n \quad (E_{th} = 17.799 \text{ MeV})$$ (A26)

$$^{28}_{14}Si+^{1}_{0}n\rightarrow^{24}_{12}Mg+^{1}_{0}n+\alpha \quad (E_{th} = 10.034 \text{ MeV})$$ (A27)

$$^{28}_{14}Si+^{1}_{0}n\rightarrow^{25}_{12}Mg+\alpha \quad (E_{th} = 2.749 \text{ MeV})$$ (A28)

A.8. Reactions of high energy Neutrons with Oxygen

The following are the reactions of energetic neutrons with Oxygen, in the regolith shield.

$$^{16}_{8}O+^{1}_{0}n\rightarrow^{16}_{7}N+^{1}_{1}p \quad (E_{th} = 10.246 \text{ MeV})$$
(A29)

$$^{16}_{8}O+^{1}_{0}n\rightarrow^{15}_{8}O+(2)^{1}_{0}n \quad (E_{th} = 16.651 \text{ MeV})$$ (A30)

$$^{16}_{8}O+^{1}_{0}n\rightarrow^{12}_{6}C+^{1}_{0}n+\alpha \quad (E_{th} = 7.613 \text{ MeV})$$ (A31)

$$^{16}_{8}O+^{1}_{0}n\rightarrow^{15}_{7}N+^{1}_{1}p+^{1}_{0}n \quad (E_{th} = 12.892 \text{ MeV})$$ (A32)

A.9. Reactions of high energy Neutrons with Carbon

$$^{12}_{6}C+^{1}_{0}n\rightarrow^{11}_{5}B+^{1}_{1}p+^{1}_{0}n \quad (E_{th} = 17.298 \text{ MeV})$$ (A33)

$$^{12}_{6}C+^{1}_{0}n\rightarrow^{12}_{5}B+^{1}_{1}p \quad (E_{th} = 13.644 \text{ MeV})$$ (A34)

Table A-1. Products and Energy Thresholds of Protons Reactions with Aluminum.

Reaction (A1)		Reaction (A2)		Reaction (A3)		Reaction (A4)	
X_1	E_{th} (MeV)	X_2	E_{th} (MeV)	X_3	E_{th} (MeV)	X_4	E_{th} (MeV)
${}_2^4He+{}_1^2D$	21.043	${}_1^2D+(2)_1^1p$	30.293	${}_2^4He+(2)_1^1p$	19.591	${}_1^2D$	11.237
${}_2^4He+{}_1^1p+{}_0^1n$	23.351	$(3)_1^1p+{}_0^1n$	32.601	${}_1^2D+(3)_1^1p+{}_0^1n$	46.635	${}_1^2p+{}_0^1n$	13.454
$(2)_1^2D+{}_1^1p+{}_0^1n$	48.088			$(4)_1^1p+(2)_0^1n$	48.943		
${}_1^2D+(2)_1^1p+(2)_0^1n$	50.395						
$(3)_1^1p+(3)_0^1n$	52.703						

Table A-2. Products and Energy Thresholds of Protons Reactions with Carbon.

Reaction (A5)		Reaction (A6)		Reaction (A7)		Reaction (A8)	
X_1	E_{th} (MeV)	X_2	E_{th} (MeV)	X_3	E_{th} (MeV)	X_4	E_{th} (MeV)
${}_2^4He+{}_1^2D$	26.060	$(3)_1^1p+{}_0^1n$	36.851	$(3)_1^1p$	29.467	${}_1^2D$	17.882
${}_2^4He+{}_1^1p+{}_0^1n$	28.471	${}_1^2D+(2)_1^1p$	34.440			${}_1^1p+{}_0^1n$	20.292
$(3)_1^1p+(3)_0^1n$	59.143						
$(3)_1^2D$	51.909						

Table A-3. Products and Energy Thresholds of Protons Reactions with Silicon.

Reaction (A9)		Reaction (A10)		Reaction (A11)	
X_1	E_{th} (MeV)	X_2	E_{th} (MeV)	X_3	E_{th} (MeV)
$(2)_1^2D+(3)_1^1p$	56.273	${}_1^2D+(3)_1^1p$	42.257	${}_1^2D+{}_1^1p$	23.225
${}_1^2D+(4)_1^1p+{}_0^1n$	58.576	$(4)_1^1p+{}_0^1n$	44.561	$(2)_1^1p+{}_0^1n$	25.530
$(5)_1^1p+(2)_0^1n$	62.926				
${}_2^4He+(3)_1^1p$	31.568				

Table A-4. Products and Energy Thresholds of Protons Reactions with Oxygen.

Reaction (A12)		Reaction (A13)		Reaction (A14)	
X_1	E_{th} (MeV)	X_2	E_{th} (MeV)	X_3	E_{th} (MeV)
$(2)_2^4He+{}_1^2D$	33.168	${}_1^2D$	14.280	${}_2^4He+(3)_1^1p$	36.510
$(2)_2^4He+{}_1^1p+{}_0^1n$	35.530	${}_1^1p+{}_0^1n$	16.600	$(2)_1^2D+(3)_1^1p$	61.858
${}_2^4He+(3)_1^2D$	58.515			${}_1^2D+(4)_1^1p+{}_0^1n$	64.220
${}_2^4He+{}_1^2D+(2)_1^1p+(2)_0^1n$	63.245			$(5)_1^1p+(2)_0^1n$	65.558
${}_2^4He+(2)_1^2D+{}_1^1p+{}_0^1n$	60.880				

APPENDIX – B: Non-Ionizing Energy Loss (NIEL)

For charged particles such as protons, deuterons, and alphas, the NIELs are the sum of the contributions of both the coulombic and nuclear interactions, while for neutrons the energy loss is solely by nuclear elastic/inelastic interactions. Thus, the NIEL for protons, deuterons, and alpha particlesis calculated as [Jun et al. 2003]:

$$NIEL = \left(\frac{N}{A}\right)\left(\sigma_{d,coulomb} + \sigma_{d,nuclear}\right) \tag{B1}$$

The charged particles, such as protons, deuterons and alphas, when traversing a target material, undergo both coulombic and nuclear interactions. The later is an important contribution to the energy loss at energies greater than a threshold value that depends on the atomic number of target material and is typically > 10 MeV (see Appendix A).

The contribution of nuclear interactions to the NIEL is estimated using the thin target approximation method in MCNPX [Jun 2001]. The damage energy tally is used to calculate the portion of the energy transferred to the lattice nuclei, T_{dam}. The damage energy cross section used for the nuclear interactions is then given by [Jun 2001]:

$$\sigma_d = \frac{T_{dam}}{N_v\, x}. \tag{B2}$$

The cross-section for displacement damage by the coulombic interactions in equation (B1) is described as:

$$\sigma_{d,coulomb}(E) = \int_{T_d}^{T_{\max}} L(T)\, T\, d\sigma(E,T). \tag{B3}$$

where T_d and T_{max} are the threshold and the maximum permissible energy transferred to the lattice atoms of the target. T_{max}, which depend on the type, energy and mass of the incident particles and atom mass of the recoiling particle, can be expressed as:

$$T_{\max} = \frac{2E(E + 2m_1c^2)}{\left(1 + \frac{m_1}{M}\right)^2 Mc^2 + 2E}. \tag{B4}$$

The fraction of the incident particle energy transferred to the recoil atoms of the target material during the displacement process is calculated using the Lindhard energy partition function L(T) as [Summers et. al. 1993]:

$$L(T) = \left[1 + F_L \left(3.4008 \left(\frac{T}{E_L} \right)^{1/6} + 0.40244 \left(\frac{T}{E_L} \right)^{3/4} + \left(\frac{T}{E_L} \right) \right) \right]^{-1}, \quad \text{(B5)}$$

where,

$$F_L = \frac{0.0793\, z_1^{2/3}\, z_2^{1/2}\, (A_1 + A_2)^{3/2}}{\left(z_1^{2/3} + z_2^{2/3} \right)^{3/4} A_1^{3/2}\, A_2^{1/2}}, \quad \text{(B6)}$$

$$E_L = 30.724\, z_1\, z_2 \left(z_1^{2/3} + z_2^{2/3} \right)^{1/2} \left(\frac{A_1 + A_2}{A_2} \right). \quad \text{(B7)}$$

The relativistic differential cross-section for the Coulombic scattering contribution to the displacement energy loss in equation (B3) is computed as [Jun, Xapsos, and Burke 2004]:

$$d\sigma(E,T) = \frac{\pi b^2 T_{\max}}{4 \gamma^2 T^2} \left[1 - \beta^2 \left(\frac{T}{T_{\max}} \right) + \pi \alpha \beta \left(\sqrt{\frac{T}{T_{\max}}} - \left(\frac{T}{T_{\max}} \right) \right) \right] dT, \quad \text{(B8)}$$

where,

$$\alpha = \frac{z e^2}{\hbar c}, \quad b = \frac{2 z_1 z_2 e^2}{m_1 c^2 \beta^2}, \quad \gamma = \frac{1}{\sqrt{1 - \beta^2}}, \quad \textit{and } \beta = \sqrt{1 - \left(\frac{m_1 c^2}{m_1 c^2 + E} \right)^2}. \quad \text{(B9)}$$

The values of the NIEL used in this work for protons, neutrons, electrons, deuterons, and alphas are compiled from many different sources [Summers et al. 1993; Jun and McAlpine 2001; Jun, Xapsos, and Burke 2004; Messenger et al. 1999; Akkerman et al. 2001]. Additional calculation are performed using the method described above, are to confirm the continuity of the data and generate values to fill the voids in the reported data.

REFERENCES

Abbey G. and Lane N., 2004. "United State Space Policy: Challenges and Opportunities," American Academy of Arts and Sciences.

Akkerman, A., Barak, J., Chadwick, M.B., Levinson, J., Murat, M., Lifshitz, Y., 2001. "Updated NIEL calculations for estimating the damage induced by particles and γ-rays in Si and GaAs," Radiat. Phys. Chem., **62**, 301-310.

Ambrozova, I., Brabcova, K., Spurny, F., Shurshakov, V.A., Kartsev, I.S., Tolochek, V., 2011. "Monitoring onboard Spacecraft by means of passive detectors," Radiat. Prot. Dosim., **144**, 605-610.

Badhwar, G.D., 1997. "The Radiation Environment in Low-Earth Orbit," Radiat. Res., **143**, S3-S10.

Badhwar, G.D., 2000. "Radiation measurement in low-earth orbit: US and Russian results," Health Phys., **79**, 507-514.

Badhwar, G.D., Keith, J.E., Cleghorn, T.F., 2001. "Neutron measurements onboard the space shuttle," Radiat. Meas., **33**, 235-241.

Badhwar, G.D., 2002. "Shuttle radiation dose measurements in the International Space Station orbits," Radiat. Res., **157**, 69-75.

Badhwar, G.D., Cucinotta, F.A., 2000. "A comparison of depth dependence of dose and linear energy transfer spectra in aluminum and polyethylene," Radiat. Res., **153**, 1-8.

Badhwar, G.D., Atwell, W., Cash, B., Petrov, V.M., Akatov, Y.A., Tchernykh, I.V., Shurshakov, V.A., and Arkhangelsky, V.A., 1998. "Radiation environment on the Mir orbital station during solar minimum," Adv. Space Res., **22**, 501-510.

Badhwar, G.D., Atwell, W., Badavi, F.F., Yang, T.C., and Cleghorn, T.F., 2002. "Space radiation absorbed dose distribution in a human phantom," Radiat. Res., **157**, 76-91.

Badhwar, G. D. and O'Neill, P. M., "Galactic Cosmic Radiation Model and Its Applications," *Adv. Space Res.*, **17**, no. 2, pp. 7-17, 1996.

Ballarini, F., Battistoni, G., Cerutti, F., Fasso, A., Ferrari, A., Gadioli, E., Garzelli, M.V., Mairani, A., Ottolenghi, A., Paretzke, H.G., Parini, V., Pelliccioni, M., Pinsky, L., Sala, P.R., Scannicchio, D., Trovati, S., Zankl, M., 2006. "GCR and SPE organ doses in deep space with different shielding. Monte Carlo simulations based on the FLUKA code coupled to anthropomorphic phantoms," Adv. Space Res., **37**, 1791-1797.

Benton, E.R., Benton, E.V., Frank, A.L., Moyers, M.F., 2006. "Characterization of the radiation shielding properties of US and Russian EVA suits using passive detectors," Radiat. Meas., **41**, 1191-1201.

Chadwick, M.B., Young, P.G., 1997. ENDF/B-VI MOD 2 Evaluation.

Colborn, B. L., Ringler, S. J., Potter, D. W., and Armstrong, T. W., 1995. "CADrays 3-D Mass Model of International Space Station Alpha," Science Applications International Corporation Report SAIC-TN-9502.

Copeland, K., Parker, D.E., Friedberg, W., 2010. "Alpha Particles at energies of 10 MeV to 1 TeV: Conversion coefficients for Fluence-to-Absorbed Dose, Effective Dose, and Gray Equivalent, Calculated using Monte Carlo Radiation Transport Code MCNPX 2.7A," Radiat. Prot. Dosim., **138**, 310-319.

Copeland, K., Parker, D.E., Friedberg, W., 2010. "Fluence-to-Absorbed Dose, Effective Dose, and Gray Equivalent Conversion Coefficients for Iron Nuclei from 10 MeV to 1 TeV, Calculated using Monte Carlo Radiation Transport Code MCNPX 2.7A," Radiat. Prot. Dosim., **138**, 353-362.

Copeland, K., Parker, D.E., Friedberg, W., 2010. "Helions at energies of 10 MeV to 1 TeV: Conversion coefficients for Fluence-to-Absorbed Dose, Effective Dose, and Gray Equivalent, Calculated using Monte Carlo Radiation Transport Code MCNPX 2.7A," Radiat. Prot. Dosim., **142**, 99-109.

Copeland, K., Friedberg, W., Sato, T., Niita, K., 2011. "Comparisons of Fluence-to-Dose Conversion Coefficients for Deuterons, Tritons, and Helions," Radiat. Prot. Dosim., 1-8.

Cucinotta, F.A., Badhwar, G.D., Saganti, P.B., Schimmerling, W., Wilson, J.W., Peterson, L.E., and Dicello, J.F., 2002. *Space Radiation Cancer Risk Projections for Exploration Missions: Uncertainty Reduction and Mitigation*, NASA/TP-2002-210777 (Center for AeroSpace Information, Hanover, Maryland).

Cucinotta, F.A., Schimmerling, W., Wilson, J.W., Peterson, I.E., Saganti, P.B., and Dicello, J.F., 2004. "Uncertainties in estimates of the risks of late effects from space radiation," Adv. Space Res., **34**, 1383-1389.

Cucinotta, F.A., Kim, M.Y., Willingham, V., George, K.A., 2008. "Physical and Biological Organ Dosimetry Analysis for International Space Station Astronauts," Radiat. Res., **170**, 127-138.

Day, S., 2009. "Everyone's Going to the Moon", NASA.

Dettmann, J., Reitz, G., Gianfiglio, G., 2007. "MATROSKA-The first ESA external payload on the International Space Station," Acta Astro., **60,** 17-23.

Dordain J. J., 2010. "Space Exploration in the 21st Century: Global Opportunities and Challenges" *Insight,* Ask Magazine.

Ferrari, A., Pelliccioni, M., and Pillon, M., 1996. "Fluence to Effective Dose Conversion Coefficients for Photons From 50 keV to 10 TeV," *Radiation Protection Dosimetry,* **67,** no. 4, pp. 245-251.

Ferrari, A., Pelliccioni, M., and Pillon, M., 1997. "Fluence to Effective Dose Conversion Coefficients for Protons From 5 MeV to 10 TeV," *Radiation Protection Dosimetry,* **71,** no. 2, pp. 85-91.

Ferrari, A., Pelliccioni, M., and Pillon, M., 1998. "Fluence to Effective Dose Conversion Coefficients for Negatively and Positively Charged Pions," *Radiation Protection Dosimetry,* **80,** no. 4, pp. 361-370.

Ferrari, A., Pelliccioni, M., and Pillon, M., 1997. "Fluence to Effective Dose Conversion Coefficients for Neutrons Up To 10 TeV," *Radiation Protection Dosimetry,* **71,** no. 3, pp. 165-173.

Foelsche, T., Mendell, R. B., Wilson, J. W., and Adams, R. R., 1974. *Measured and Calculated Neutron Spectra and Dose Equivalent Rates at High Altitudes; Relevance to SST Operations and Space Research*, NASA TN D-7715.

Gustaffson, K., Sihver, L., Mancusi, D., Sato, T., Reitz, G., Berger, T., 2010. "PHITS simulations of the Matroshka experiment," Adv. Space Res., **46**, 1266-1272.

Harrison, C., Burgett, E., Hertel, N., Grulke, E., 2008. "Polyethylene/Boron Composites for Radiation Shielding Applications," In: El-Genk, M.S. (Ed.), Space Technology and Applications International Forum (STAIF-2008), Conference Proceeding 969. American Institute of Physics, Melville, New York, pp. 484-491.

Hawari, A.I., Al-Qasir, I.I., Ougouag, A.M, 2007. "Investigation of the Impact of Simple Carbon Interstitial formations on Thermal Neutron Scattering in Graphite," Nucl. Sci. and Eng., **155**, 449-462.

Hayatsu, K., Hareyama, M., Kobayashi, S., Yamashita, N., Miyajima, M., Sakurai, K., Hasebe, N., 2008. "Radiation Doses for Human Exposed to Galactic Cosmic Rays and Their Secondary Products on the Lunar Surface," Biological Sciences in Space, **22**, (2) 59-66.

Hendricks, J.S., MCNPX, Version 2.5.0., Los Alamos National Laboratory, 2005, LA-UR-05-2675.

Hufner, J., 1985. "Heavy fragments produced in proton-nucleus and nucleus-nucleus collisions at relativistic energies," Phys. Rep., **125**, 129-185.

ICRP, 1991. International Commission on Radiological Protection. *1990 Recommendation of the International Commission on Radiological Protection*, ICRP Publication 60, Ann. ICRP21 (1-3) (Elsevier Science, New York).

ICRP, 2003. International Commission on Radiological Protection. *Relative Biological Effectiveness (RBE), Quality Factors (Q), and Radiation Weighting Factor (w_R)*, ICRP Publication 92, Ann. ICRP33 (4) (Elsevier Science, New York).

Iwase, H., Niita, K., and Nakamura, T., 2002. "Development of General-Purpose Particle and Heavy-Ion Transport Monte Carlo code," Nucl. Sci. and Tech., **39**, no 11, 1142-1151.

Iwase, H., Wiegel, B., Fehrenbacher G., Schardt, D., Nakamura, T., Niita, K., Radon, T., 2005. "Comparison between calculation and measured data on secondary neutron energy spectra by Heavy-Ion reactions from different thick targets," Radiat. Prot., Dos., **116**, no 1-4, 640-646.

Jadrnickova, I., Tateyama, R., Yasuda, N., Kawashima, H., Kurano, M., Uchihori, Y., Kitamura, H., Akatov, Yu., Shurshakov, V., Kobayashi, I., Ohguchi, H., Koguchi, Y., Spurny, F., 2009. "Variation of absorbed doses onboard of ISS Russian Service Module as measured with passive detectors," Radiat. Meas., **44**, 901-904.

Jadrnickova, I., Brabcova, K., Mrazova, Z., Spurny, F., Shurshakov, V.A., Kartsev, I.S., Tolochek, R.V., 2010. "Dose characteristics and LET spectra on and inside the spherical phantom onboard ISS," Radiat. Meas., **45**, 1536-1540.

Jun I., 2001. "Effects of secondary particles on the total dose and the displacement damage in space protons environments," IEEE Trans. Nucl. Sci., **48**, no 1, 162-175.

Jun, I. and McAlpine, W., 2001. "Displacement damage in silicon due to secondary neutrons, pions, deuterons, and alphas from proton interactions with materials," IEEE Trans. Nucl. Sci., **48**, no 6, 2034 – 2038.

Jun, I, Xapsos, M.A., Burke, E.A., 2004. "Alpha particle nonionizing energy loss (NIEL)," IEEE Trans. Nucl. Sci., **51**, no 6, 3207-3210.

Jun, I., Xapsos, M.A., Messenger, S.R., Burke, E.A., Walters, R.J., Summers, G.P., Jordan, T., 2003. "Proton nonionizing energy loss (NIEL) for device applications," IEEE Trans. Nucl. Sci., **50**, no 6, 1924-1928.

Kang, S., Lipinski, R., McAlpine, W., 2006. "Lunar surface reactor shielding study," In: El-Genk, M.S. (Ed.), Space Technology and Applications International Forum

(STAIF-2006), Conference Proceeding 813. American Institute of Physics, Melville, New York, pp. 707-715.

Kireeva, S.A., Benghin, V.V., Kolomensky, A.V., Petrov, V.M., 2007. "Phantom-dosimeter for estimating effective dose onboard International Space Station," Acta Astro., **60**, 547-553.

Kitazawa, H., Harima, Y., Fukahori, T., 2002. JENDL-3.3 Incident Neutron Data, Tit-Jaeri, DIST-MAR02.

Kartsev, I.S., Tolochek, R.V., Shurshakov, V.A., Akatov, Yu.A., 2009. "Calculation of Radiation Doses in Cosmonaut's Body in Long-Term Flight Onboard the ISS Using the Data Obtained in Spherical Phantom," Fundamental Space Res., 80-83.

Littmark, U., and Ziegler J.F., 1980. Range Distribution for Energetic Ions in All Elements, Pergammon Press, New York.

Lyagushin, V.I., Dudkin, V.E., Potapov, Yu.V., Svastianov, V.D., 2001. "Russian measurements of neutron energy spectra on the Mir orbital station," Radiation Measurements, **33**, 313-319.

Machrafi, R., Garrow, K., Ing, H., Smith, M.B., Andrews, H.R., Akatov, Yu., Arkhangelsky, V., Chernykh, I., Mitrikas, I., Petrov, V., Shushakov, V., Tomi, L., Kartsev, I., and Lyagushin, V., 2009. "Neutron Dose Study with Bubble Detectors Aboard the International Space Station as Part of the Matroshka-R Experiment," *Radiation Protection Dosimetry*, **133**, 4, 200.

Mancusi, D., Bertucci, A., Gialanella, G., Grossi, G., Manti, L., Pugliese, M., Rusek, A., Scampoli, P., Sihver, L., Durante, M., 2007. "Comparison of aluminum and Lucite for shielding against 1GeV protons," Adv. Space Res., **40**, 581-585.

Messenger, S.R., Burke, E.A., Summers, G.P., Xapsos, M.A., Walters, R.J., Jackson, E.M., Weaver, B.D., 1999. "Nonionizing energy loss (NIEL) for heavy ions," IEEE Trans. Nucl. Sci., **46**, no 6, 1595-1602.

McKay D. S., et. al., "JSC-1: A New Lunar Soil Simulant, 1994. " *Engineering, Construction, and Operation in Space IV,* vol. 2, edited by R. G. Galloway and S. Lokaj, American Society of Civil Engineers, New York, New York, 1994, pp. 857 – 866.

McKinney, G.W., Hendricks, J.S., Waters, L.S., 2002. "Using MCNPX for Space Applications," LA-UR-02-740.

McKinney, G.W., James, M.R., Hendricks, J.S., Moyers, M., 2006. "Recent enhancements in MCNPX: Heavy-ion transport and the LAQGSM physics model," Nucl. Inst. Meth. in Phys. Res. A, **562**, 819-822.

McKinney, G.W., Lawrence, D.J., Prettyman, T.H., Elphic, R.C., Feldman, W.C., Hagerty, J.J., 2008. "MCNPX benchmark for cosmic ray interactions with the Moon," Geophysical Res., **111**, E06004.

NASA, 2004. *The Vision for Space Exploration, February 2004*, NP-2004-01-334-HQ, NASA, Washington, D.C.

NCRP, 1989. National Council on Radiation Protection and Measurements. *Guidance on Radiation Received in Space Activities*, NCRP Report No. 98 (National Council on Radiation Protection and Measurements, Bethesda, Maryland).

NCRP, 1993. National Council on Radiation Protection and Measurements. *Limitation of Exposure to Ionizing Radiation*, NCRP Report No. 116 (National Council on Radiation Protection and Measurements, Bethesda, Maryland).

NCRP, 2000. National Council on Radiation Protection and Measurements. *Radiation Protection and Guidance for Activities in Low-Earth Orbit*, NCRP Report No. 132 (National Council on Radiation Protection and Measurements, Bethesda, Maryland).

NCRP, 2002. National Council on Radiation Protection and Measurements. *Operational Radiation Safety Program for Astronauts in Low-Earth Orbit: A Basic Framework*, NCRP Report No. 142 (National Council on Radiation Protection and Measurements, Bethesda, Maryland).

Niita, K., Matsuda, N., Iwamoto, Y., Sakamoto, Y., Nakashima, H., Sato, T., Iwase, H., Sihver, L., Mancusi, D., 2007. "PHITS Overview," *Hadronic Shower Simulation Workshop*, edited by Albrow M. and Raja R., CP896.

Papike, J. J., Simon, S. B., and Laul, J. C., 1982. "The Lunar Regolith: Chemistry, Mineralogy, and Petrology," *Rev. Geophys. Space Phys.,* **20,** pp. 761-826.

Pelowitz, D. B., Ed., *MCNPX™ User's Manual: Version 2.6.0:* Los Alamos National Laboratory, April. 2008, LA-CP-07-1473.

Pelowitz, D. B., Ed., *MCNPX™ User's Manual: Version 2.7.0:* Los Alamos National Laboratory, April. 2011, LA-CP-11-00438.

Pelowitz, D. B., Ed., MCNPX, Version 2.7.C, Los Alamos National Laboratory, 2010, LA-UR-10-00481.

Pelowitz, D. B., Ed., MCNPX, Version 2.7.D, Los Alamos National Laboratory, 2010, LA-UR-10-07031.

Pelowitz, D. B., Ed., MCNPX, Version 2.7.E, Los Alamos National Laboratory, 2011, LA-UR-11-01502.

Petrov, V.M., Kartashov D.A., Akatov, Yu.A., Kolomensky, A.V., Shurshakov, V.A., 2011. "Comparison of space radiation doses inside the Matroshka-torso phantom installed outside the ISS with the doses in a cosmonaut body in Orlan-M spacesuit during EVA," Acta. Astro., **68**, 1448-1453.

Pham, T. T., El-Genk, M. S., and Al-Haik, M., 2006. "Aluminum, B_4C and Polymer Shielding for 100 MeV Protons," *Transactions of the American Nuclear Society*, **95,** pp. 597-598.

Pham, T.T., and El-Genk, M.S., 2010. "Shielding Electronic Devices from Monoenergetic 100 MeV protons," Nucl. Sci. and Eng., **166,** 58-72.

Pham, T.T., and El-Genk, M.S., 2009. "Dose estimates in a Lunar Shelter with Regolith Shielding," Acta Astronautica, **64**, 697-713.

Qualls, G.D., Wilson, J.W., Sandridge, C., Cucinotta, F.A., Nealy, J.E., Heinbockel, J.H., Hugger, C.P., Verhage, J., Anderson, B.M., Atwell, W., Zapp, N., Barber, R., 2001. "International Space Station Radiation Shielding Model Development," *Proceedings of the 31st International Conference on Environmental Systems*, (Orlando, Florida).

Reitz, G., and Berger, T., 2006. "The MATROSKA facility-Dose determination during an EVA," Radiat. Prot. Dosim., **120**, 442-445.

Reitz, G., Berger, T., Bilski, P., Facius, R., Hajek, M., Petrov, V., Puchalska, M., et. al., 2009. "Astronaut's Organ Doses Inferred from Measurements in a Human Phantom outside the International Space Station," Radiat. Res., **171**, 225-235.

Saganti, P.B., Cucinotta, F.A., Wilson, J.W., Schimmerling, W., 2002. "Visualization of Particle flux in the human body on the surface of Mars," J. Radiat. Res., **43**, S119.

Sato, T., Niita, K., Iwase, H., Nakashima, H., Yamaguchi, Y., and Sihver, L., 2004. "Calculation of Neutron Spectra Inside Spacecraft by 3-Dimensional Particle and Heavy Ion Transport Code System PHITS," in the proceedings of *the 6th International Workshop on Radiation Effects on Semiconductor Devices for Space Application,* Tsukuba, pp. 25-28.

Sato, T., Tsuda, S., Sakamoto, Y., Yamaguchi, Y., Niita, K., 2003. "Conversion Coefficients from Fluence to Effective Dose for Heavy Ions with Energies up to 3GeV/A," Radiat. Prot. Dos., **106**, 137-144.

Sato, T., Niita, K., Iwase, H., Nakashima, H., Yamaguchi, Y., Sihver, L., 2006. "Applicability of particle and heavy ion transport code PHITS to the shielding design of spacecrafts," Radiat. Meas., **41**, 1142-1146.

Sato, T., Endo, A., Zankl, M., Petoussi-Henss, N., Niita, K., 2009. "Fluence-to-dose conversion coefficients for neutrons and protons calculated using the PHITS code and ICRP/ICRU adult reference computational phantoms," Phys. Med. Biol., **54**, 1997-2014.

Sato, T., Endo, A., N., Niita, K., 2010. "Fluence-to-dose conversion coefficients for heavy-ions calculated using the PHITS code and ICRP/ICRU adult refernce computational phantoms," Phys. Med. Biol., **55**, 2235-2246.

Satoh, D., Takahashi, F., Endo, A., Ohmachi, Y., Miyahara, N., 2009. "Calculation of Dose contributions of electron and charged heavy particles inside phantoms irradiated by Monoenergetic Neutron," Radiat. Res., **49**, 503-508.

Sauer, H. H., Zwicki, R. D., and Ness, M. J., 1990. "Summary Data for the Solar Energetic Particle Events of August through December 1989," Space Environment Laboratory, National Oceanic and Atmospheric Adm.

Semkova, J., Koleva, R., Todorova, G., Kanchev, N., Petrov, V., Shurshakov, V., Benghin, V., Tchhernykh, I., Kireeva, S., 2004. "Instrumentation for investigation of the depth dose distribution by the Liulin-5 instrument of a human phantom on the Russian segment of ISS for estimation of the radiation risk during long term space flights," Adv. Space Res., **34**, 1297-1301.

Semkova, J., Koleva, R., Todorova, G., Kanchev, N., Petrov, V., Shurshakov, V., Benghin, V., Tchhernykh, I., Akatov, Yu., Redko, V., 2003. "Invesitigation of dose and flux dynamics in the Liulin-5 dosimeter of the tissue-equivalent phantom onboard the Russian segment of the International Space Station," Adv. Space Res., **31**, no. 5, 1383-1388.

Shea, M. A. and Smart, D. F., 1990. "A Summary of Major Solar Proton Events," *Solar Physics*, **127**, 297-320.

Shurshakov V.A.., Akatov Yu.A., Kartsev I.S., Petrov V.M., Tolochek R.V., Petrov V.I., Polenov B.V., Lyagushin V.I., 2008. "Study of Dose Distribution in a Human Body in Space Station Compartments with the Spherical Tissue-Equivalent Phantom," Fundamentals Space Research.

Sihver, L, Sato, T., Gustafsson, K., Shurshakov, V.A., Reitz, G., 2009. "Simulations of the MTR-R and MTR experiments at ISS, and shielding properties using PHITS," Proc. of 2009 IEEE Aerospace Conf. paper #1015, 1-8.

Sihver, L., Sato, T., Gustafsson, K., Mancusi, D., Iwase, H., Niita, K., Nakashima, H., Sakamoto, Y., Iwamoto, Y., Matsuda, N., 2010. "An update about recent development of the PHITS code," Adv. Space Res., **45**, 892-899.

Sihver, L, Sato, T., Puchalska, M., Reitz G., 2010. "Simulations of the MATROSHKA experiment at the international space station using PHITS," Radiat. Environ. Biophys., **49**, 351-357.

Simonsen, L., Nealy, J., John, E., Sauer, H.H., and Townsend, L.W., 1991. "Solar Flare protection for Manned Lunar Missions. Analysis of the October 1989 Proton Flare Event," SAE Tech. Paper Ser. 911351.

Slaba, T.C., Blattnig, S.R., and Clowdsley, M.S., 2011. "Variation in Lunar Neutron Dose Estimates," Radiat. Res., **176**, 827-841.

Summers G.P., Burke, E.A., Shapiro, P., Messenger, S.R., Walters, R.J., 1993. "Damage correlations in semiconductors exposed to gamma, electron, and proton radiations," IEEE Trans. Nucl. Sci., **40**, no. 6, 1372-1379.

Taylor, G. J., 1989. *The Environment at the Lunar Surface, Lunar Base Agriculture: Soils for Plant Growth*, edited by Ming D. W. and Henninger, D. L., Madison, WI.

Trovati, S., Ballarini, F., Battistoni, G., Cerutti, F., Fasso, A., Ferrari, A., Gadioli, E., Garzelli, M.V., Mairani, A., Ottolenghi, A., Paretzke, H.G., Parini, V., Pelliccioni, M., Pinsky, L., Sala, P.R., Scannicchio, D., and Zankl, M., 2006. "Human Exposure to space radiation: Role of primary and secondary particles," Radiat. Prot. Dos., **122**, no 1-4, 362-366.

Tylka, A.J., Adams, J.H., JR, Boberg, P.R., Brownstein, B., Dietrich, W.F., Flueciger, E.O., Petersen, E.I., Shea, M.A., Smart, D.F., and Smith, E.C., 1997. "CREME96: A revision of the cosmic ray effects on micro-electronics code," IEEE Trans. Nucl. Sci. **44**, 2150-2160.

Tylka, A.J., Dietrich, W.F., and Boberg, P.R., 1997. "Observations of very high energy solar heavy ions from IMP-8,"*Proceedings of the 25th International Cosmic Ray Conference* (World Scientific, Hackensack, New Jersey).

Vana, N., Hajek, M., Berger, T., Fugger, M., Hofmann, P., 2006. "Novel Shielding Materials for Space and Air Travel," Radiat. Prot. Dosim., **120**, 405-409.

Wilson, J. W., Miller J., Konradi A., and Cucinotta, F. A., (1997). *Shielding Strategies for Human Space Exploration,* NASA CP 3360 (Center for Aerospace Information, Hannover, Maryland)

Wilson, J.W., 2000. "Overview of Radiation Environments and Human Exposures," *Health Physics*, **79**, 5, 470.

Wilson, J.W., Shinn, J.L., Tripathi, R.K., Singleterry, R.C., Clowdsley, M.S., Thibeault, S.A., Cheatwood, F.M., Cucinotta, F.A., Badhwar, G.D., Noor, A.K., Kim, M.Y., Badavi, F.F., Heinbockel, J.H., Miller, J., Zeitlin, C., Heilbronn, L., 2001. "Issues in Deep Space Radiation Protection," Acta Astro., **49**, 3-10, 289.

Wilson, J.W., Clowdsley, M.S., Cucinotta, F.A., Tripathi, R.K., Nealy, J.E., DeAngelis, G., 2004. "Deep Space Environment for Human Exploration," *Advances in Space Research,* **34**, 6, 1281.

Wilson, J. W., Tripathi, R.K., Badavi, F.F., Cucinotta, F.A., 2006. "Standardized Radiation Shield Design Method: 2005 HZETRN," *Proceeding of the International Conference on Environmental Systems (ICES)*, (Norfolk, VA).

Wilson, J.W., Cucinotta, F.A., Golightly, M.J., Nealy, J.E., Qualls, G.D., Badavi, F.F., DeAngelis, G., Anderson, B.M., Clowdsley, M.S., Luetke, N., Zapp, N., Shaveers, M.R., Semones, E., Hunter, A., 2006. "International Space Station: A Test Bed for Experimental and Computational Dosimetry," Adv. Space. Res., **37**, 1656-1663.

Wilson, J.W., Townsend, L.W., Schimmerling, W., Khandelwal, G.S., Khan, F., Nealy J.E., Cucinotta, F.A., Tweed, J., Heinbockel, J.H., Walker, S.A., Nealy, J.E., 2005. *Verification and Validation: High Charge and Energy (HZE) Transport Codes and Future Development,* NASA Technical Paper 213784.

Yasuda, H., Badhwar, G.D., Komiyama, T., Fujitaka, K., 2000. "Effective Dose Equivalent on the Ninth Shuttle-Mir Mission (STS-91)," Radiat. Res., **154**, 705-713.

Yasuda, H., 2009. "Effective Dose Measured with a Life Size Human Phantom in Low Earth Orbit Mission," Radiat. Res., **50**, 89-96.

Yoshizawa, N., Sato, O., Takagi, S., Furihata, S., Iwai, S., Uehara, T., Tanaka, S., Sakamoto, Y., 1998. "External Radiation Conversion Coefficients using Radiation Weighting Factor and Quality Factor for Neutron and Proton from 20 MeV to 10 GeV," Nucl. Sci. and Tech., **35**, 928-942.

Ziegler, J. F., Biersack, J. P. and Littmark, U., 1985. "The Stopping Range of Ions in Solids", **1**, Pergammon Press, New York, 1985, pp. 37-44.

Zhou, D., Semones, E., O'Sullivan, D., Zapp, N., Weyland, M., Reitz, G., Berger, T., Benton, E.R., 2010. "Radiation Measurement for MATROSKA-1 experiment with passive dosimeters," Acta Astro., **66**, 301-308.